UC Berkeley

UC Berkeley Electronic Theses and Dissertations

Title

Slow Magnetic Relaxation in Multinuclear Coordination Clusters and Low-Coordinate Transition Metal Complexes

Permalink

https://escholarship.org/uc/item/2mv3w4wq

Author

Zadrozny, Joseph Mercer

Publication Date

2013

Peer reviewed|Thesis/dissertation

eScholarship.org Powered by the California Digital Library
University of California

Slow Magnetic Relaxation in Multinuclear Coordination Clusters and Low-Coordinate Transition Metal Complexes

by

Joseph Mercer Zadrozny

A dissertation submitted in partial satisfaction of the

requirements for the degree of

Doctor of Philosophy

in

Chemistry

in the

Graduate Division

of the

University of California, Berkeley

Committee in charge:

Professor Jeffrey R. Long, Chair
Professor Kenneth N. Raymond
Professor Irfan Siddiqi

Spring 2013

Slow Magnetic Relaxation in Multinuclear Coordination Clusters

and Low-Coordinate Transition Metal Complexes

© 2013

Joseph Mercer Zadrozny

Abstract

Slow Magnetic Relaxation in Multinuclear Coordination Clusters and Low-Coordinate Transition Metal Complexes

By

Joseph Mercer Zadrozny

Doctor of Philosophy in Chemistry

University of California, Berkeley

Professor Jeffrey R. Long, Chair

Contained in the following dissertation are detailed investigations of the syntheses, structures, and magnetic properties of a series of paramagnetic molecules. A wide range of magnetic behavior is reported, including interionic magnetic exchange coupling, magnetic anisotropy, molecular magnetic relaxation mechanisms, and ultimately their respective origins on the basis of fundamental concepts in coordination chemistry. Chapter One provides a brief background of the origins of single-molecule magnet behavior with a review of basic molecular magnetism concepts and techniques and is geared toward the comprehension level of a first-year graduate student fluent in the basics of coordination chemistry.

In Chapter Two, the syntheses, structures, and magnetic properties of pentanuclear cyanide-bridged clusters are presented. The complexes are based upon the highly anisotropic building unit $[Re(CN)_7]^{4-}$, which possesses an $S = {}^1/_2$ Re^{IV} ion with an associated unquenched orbital angular momentum. Further, the clusters produce a variety of magnetic behaviors, including $Ni^{II}\cdots Re^{IV}$ ferromagnetic interactions in $[(PY5Me_2)_4Ni_4Re(CN)_7](PF_6)_5$ and intermolecular $Co^{III}\leftarrow Re^{III}$ charge transfer in $[(PY5Me_2)_4Co_4Re(CN)_7](PF_6)_5$. Notably, $[(PY5Me_2)_4Ni_4Re(CN)_7]^{5+}$ is a single molecule magnet that is stable at room temperature in contrast to $[(PY5Me_2)_4Mn_4Re(CN)_7]^{5+}$, which is spontaneously reduced in solution at room temperature to $[(PY5Me_2)_4Mn_4Re(CN)_7]^{4+}$, the latter of which contains a diamagnetic Re^{III} ion. Like this Mn-containing cluster, however, the complex $[(PY5Me_2)_4Cu_4Re(CN)_7]^{5+}$ is temperature sensitive and is reduced in solution at room temperature to provide $[(PY5Me_2)Cu_4Re(CN)_7]^{4+}$. In the former of these two species, ferromagnetic $Cu^{II}\cdots Re^{IV}$ interactions are observed in addition to slow magnetic relaxation, while the magnetic behavior of the latter complex is consistent with four noninteracting Cu^{II} centers. The observation of slow magnetic relaxation in $[(PY5Me_2)Cu_4Re(CN)_7]^{4+}$ thus categorizes this molecule as a redox-switchable single-molecule magnet.

Chapters Three through Seven are shifted in focus to the investigation of the magnetic properties of complexes with only one paramagnetic ion, for reasons detailed in Chapter One.

Chapter Three describes the synthesis and characterization of a pseudotetrahedral complex of cobalt(II) and the tri-dentate, nitrogen-donor ligand 1,1,1-tris[2*N*-(1,1,3,3-tetramethylguanidino)methyl]ethane (3G). Up until this point, most of the literature for single-molecule magnetism focuses on the fact that a negative zero-field splitting value is essential for the observation of slow magnetic relaxation. In this chapter, however, slow magnetic relaxation under applied dc field by the complex $[(3G)CoCl]^{+}$ is presented, despite being shown by HF-EPR to possess a positive zero-field splitting. The reported results importantly refute the idea that slow magnetic relaxation is only possible in systems with negative axial anisotropy, but further suggest that systems with easy plane magnetic anisotropy need not be omitted from the search for large magnetic relaxation barriers.

Chapter Four details the first observation of slow magnetic relaxation in the mononuclear transition metal complex $[Co(SPh)_4]^{2-}$ without the typical required static dc field, providing a U_{eff} of 21(1) cm^{-1}. The observation of slow magnetic relaxation at zero dc field for this species is attributed to both the large, negative, zero-field splitting, as well as the half-integer spin. All previous accounts of slow magnetic relaxation in mononuclear complexes invoked nonzero transverse anisotropies (E) as the source of fast zero field tunneling, as this parameter leads to mixing of the bistable $\pm M_S$ levels. However, by Kramers' theorem, E should not mix the bistable $M_S = \pm^3/_2$ levels in $[Co(SPh)_4]^{2-}$, and indeed it does not, as evidenced by the slow magnetic relaxation detected at zero applied dc field. Notably, a lingering influence of tunneling is still detected for this molecule, and dilution studies show that the mechanism of tunneling at low temperature is intermolecular in origin.

The large zero-field splitting (D) in $[Co(SPh)_4]^{2-}$ is likely attributed to the nearly degenerate d_{xy} and d_{x2-y2} orbitals, which provide a low-lying excited state with a large negative contribution to D. As detailed in Chapter Five, the preparation and characterization of the series of complexes $[Co(EPh)_4]^{2-}$ (E = O, S, Se) were performed to see how a simple modification of the ligand field would influence D and U_{eff}. Of note were the isolation and structural characterization of a relatively simple molecule, $[Co(OPh)_4]^{2-}$, a moiety which was hitherto unknown in the literature as a mononuclear species. The D values proved highly influenced by the ligand field, yet U_{eff} did not, in contrast to the expectation that the barrier to spin reversal should directly scale with D. Also discussed is a detailed analysis of the diffuse reflectance spectra for the series of complexes, which was pursued with the intent of gaining a deeper understanding of the mechanisms by which the ligand field adjusts both the magnetic anisotropy and the low temperature magnetization dynamics.

Chapter Six describes the magnetic investigation of two-coordinate, linear complexes of iron(II). Unlike the $[Co(EPh)_4]^{2-}$ species in Chapters Four and Five, the d-orbital splitting diagrams for two-coordinate transition metal ions in linear geometries feature degenerate (or as close as reasonably possible) d_{xy} and d_{x2-y2} orbitals, which are predominately nonbonding in character. These complexes display magnetic relaxation barriers up to 181 cm^{-1} under applied dc field and fast tunneling of the magnetization at zero applied dc field. *Ab initio* studies, initiated to elucidate the influence of the ligands on the slow magnetic relaxation, revealed that though the d_{xy} and d_{x2-y2} orbitals were not rigorously degenerate (due to molecular symmetries lower than $D_{\infty h}$), the spin-orbit coupling was strong enough to engender electronic ground states corresponding to orbital angular momentum that is essentially unquenched by the ligand field. Thus, these complexes contain transition metal ions that magnetically mimic lanthanide ions,

where the spin-orbit coupling is strong enough to override the quenching influence of the very weak ligand-field felt by the spin-bearing 4f orbitals. The calculated barriers are close to the experimental ones for $Fe[N(SiMe_3)(Dipp)]_2$ and $Fe[C(SiMe_3)_3]_2$, but differ strongly for the other investigated complexes, the reasons for which are attributed to a possible vibronic model.

Chapter Seven meshes the ideas presented in Chapters Four through Six while describing the magnetic properties of a two-coordinate, linear complex of iron(I). This species, obtained by a one-electron reduction of the iron(II) complex $Fe[C(SiMe_3)_3]_2$, possesses both a half-integer spin and unquenched orbital angular momentum. As a result of these two characteristics, $[Fe(C(SiMe_3)_3)_2]^-$ displays the largest spin reversal barrier yet observed for all transition-metal-containing species (226(4) cm^{-1}) by an order of magnitude. As a consequence of such a large magnetization reversal barrier, $[Fe(C(SiMe_3)_3)_2]^-$ possesses a molecular magnetic moment that is blocked from reversal at low temperature, giving rise to magnetic hysteresis, a phenomenon typically associated with bulk magnetic materials, but here due to an individual transition metal ion.

Table of Contents

	Page
Table of Figures	iii
Acknowledgements	v
Dedication	ix
Chapter 1: Single-Molecule Magnet Behavior in Multi- and Mononuclear Transition Metal Complexes	1
Section 1.1. Introduction	1
Section 1.2. Multinuclear Single-Molecule Magnets and the Spin-Reversal Barrier	3
Section 1.3. Origins of Large Magnetic Anisotropy in Transition Metal Complexes	4
Section 1.4. Characterization of Magnetic Anisotropy in Single-Molecule Magnets	7
Section 1.5. Characterization of Magnetization Reversal Barriers in Single-Molecule Magnets	9
Section 1.6. Lanthanide-Based Single-Molecule Magnets	10
Section 1.7. Mononuclear Transition Metal Single-Molecule Magnets	11
Section 1.8. Outlook	14
Section 1.9. References and Notes	15
Chapter 2: Slow Magnetic Relaxation and Charge Transfer in Cyano-Bridged Coordination Clusters Incorporating $[Re(CN)_7]^{3-/4-}$	17
Section 2.1. Introduction	17
Section 2.2. Experimental	18
Section 2.3. Results and Discussion	23
Section 2.4. Outlook and Conclusions	32
Section 2.5. Acknowledgements	33
Section 2.6. References, Notes, and Supplementary Information	33
Chapter 3: Slow Magnetic Relaxation in a Pseudotetrahedral Cobalt(II) Complex With Easy-Plane Anisotropy	45
Section 3.1. Introduction	45
Section 3.2. Experimental	45
Section 3.3. Results and Discussion	47
Section 3.4. Outlook and Conclusions	51
Section 3.5. Acknowledgements	52
Section 3.6. References, Notes, and Supplementary Information	52
Chapter 4: Slow Magnetic Relaxation at Zero Field in the Tetrahedral Complex $[Co(SPh)_4]^{2-}$	61
Section 4.1. Introduction	61
Section 4.2. Experimental	61
Section 4.3. Results and Discussion	63

Section 4.4. Outlook and Conclusions..... 66
Section 4.5. Acknowledgements..... 66
Section 4.6. References, Notes, and Supplementary Information..... 66

Chapter 5: Slow Magnetic Relaxation in the Tetrahedral Cobalt(II) Complexes $[Co(EPh)_4]^{2-}$ (E = O, S, Se) 74
Section 5.1. Introduction..... 74
Section 5.2. Experimental..... 75
Section 5.3. Results and Discussion..... 78
Section 5.4. Outlook and Conclusions..... 87
Section 5.5. Acknowledgements..... 87
Section 5.6. References, Notes, and Supplementary Information..... 87

Chapter 6: Slow Magnetization Dynamics in a Series of Two-Coordinate Iron(II) Complexes..... 104
Section 6.1. Introduction..... 104
Section 6.2. Experimental..... 106
Section 6.3. Results and Discussion..... 109
Section 6.4. Outlook and Conclusions..... 122
Section 6.5. Acknowledgements..... 123
Section 6.6. References, Notes, and Supplementary Information..... 123

Chapter 7: Magnetic Blocking in a Linear Iron(I) Complex..... 140
Section 7.1. Introduction..... 140
Section 7.2. Experimental..... 141
Section 7.3. Results and Discussion..... 143
Section 7.4. Outlook and Conclusions..... 149
Section 7.5. Acknowledgements..... 149
Section 7.6. References, Notes, and Supplementary Information..... 149

Appendices
Appendix A.1. Additional Crystallographic Tables for Chapter 2..... 158
Appendix A.2. Additional EPR Interpretive Details for Chapter 3..... 163
Appendix A.3. Additional AOM and Ligand Field Analysis Details for Chapter 5.... 165
Appendix A.4. Magnetization Fitting Details for Chapter 6..... 174
Appendix A.5. Additional Mössbauer Interpretation and Computational Details for $[Fe(C(SiMe_3)_3)_2]^-$ for Chapter 7..... 175

Table of Figures

Page

Chapter 1. Single-Molecule Magnet Behavior in Multi- and Mononuclear Transition Metal Complexes 1
Figure 1.1 Depiction of M_S levels and spin reversal barrier for an $S = 2$ system 2
Figure 1.2. Crystal structures of notable multinuclear single-molecule magnets 3
Figure 1.3. Crystal structure of $[Mn_{19}O_8(N_3)_8(HL)_{12}(CH_3CN)_6]^{2+}$ 4
Figure 1.4. Relative d-orbital energies for several iron(II) and cobalt(II) geometries 5
Figure 1.5. Example traces of in-phase and out-of-phase magnetic susceptibility as a function of frequency 10
Figure 1.6. Examples of lanthanide-based single-molecule magnets 11
Figure 1.7. Molecular structure and magnetic parameters for the $[(tpa^R)Fe]^-$ complexes 12
Figure 1.8. Molecular structures and spin reversal barriers for three species that display slow magnetic relaxation from a single paramagnetic ion at zero dc field 13

Chapter 2. Slow Magnetic Relaxation and Charge Transfer in Cyano-Bridged Coordination Clusters Incorporating $[Re(CN)_7]^{3-/4-}$ 17
Figure 2.1. Crystal structures of $[(PY5Me_2)_4Co_4Re(CN)_7]^{5+}$ and $[(PY5Me_2)_4Ni_4Re(CN)_7]^{5+}$ as observed in **7** and **8**, respectively 24
Figure 2.2. Crystal structure of $(PY5Me_2)_4Cu_4Re(CN)_7]^{4+}$ as observed in **9** 25
Figure 2.3. Dc susceptibility data of **7**-**9** and $[(PY5Me_2)_4Cu_4Re(CN)_7](PF_6)_5$ (**10**) 27
Figure 2.4. Variable-temperature, variable-field magnetization data for **8** and **10** 28
Figure 2.5. Variable-temperature out-of-phase ac magnetic susceptibility data for **8** and **10**. 29
Figure 2.6. Cyclic voltammogram of **7** in acetonitrile 30
Figure 2.7. Spectroelectrochemical data for **7** in acetonitrile 31
Supplementary Figures for Chapter 2 39

Chapter 3. Slow Magnetic Relaxation in a Pseudotetrahedral Cobalt(II) Complex with Easy-Plane Anisotropy 45
Figure 3.1. Crystal structure and d-orbital splitting diagram for $[(3G)CoCl]^+$ 48
Figure 3.2. Variable-temperature dc magnetic susceptibility data for $[(3G)CoCl](CF_3SO_3)$.. 48
Figure 3.3. High-field EPR spectra and analysis of $[(3G)CoCl](CF_3SO_3)$ 49
Figure 3.4. Variable-temperature ac susceptibility data for $[(3G)CoCl](CF_3SO_3)$ 50
Figure 3.5. Zeeman energy diagram and relaxation mechanism for $[(3G)CoCl](CF_3SO_3)$.... 51
Supplementary Figures for Chapter 3 55

Chapter 4. Slow Magnetic Relaxation at Zero Field in the Tetrahedral Complex $[Co(SPh)_4]^{2-}$ 61
Figure 4.1. Crystal structure and d-orbital splitting diagram for $[Co(SPh)_4]^{2-}$ 62
Figure 4.2. Out-of-phase ac susceptibility data for $(Ph_4P)_2[Co(SPh)_4]$ 64
Figure 4.3. Variable-field ac susceptibility data and Arrhenius plot for $(Ph_4P)_2[Co(SPh)_4]$... 65
Supplementary Figures for Chapter 4 69

Chapter 5. Slow Magnetic Relaxation in the Tetrahedral Cobalt(II) Complexes $[Co(EPh)_4]^{2-}$ (E = O, S, Se) 74
Figure 5.1. Crystal structures for $(Ph_4P)K[Co(OPh)_4]$ (**1**), $(Ph_4P)_2[Co(OPh)_4]$ (**2**), $(Ph_4P)_2[Co(SPh)_4]$ (**3**), and $(Ph_4P)_2[Co(SePh)_4]$ (**4**) 78
Figure 5.2. Chain-like extended structure observed in **2** 79
Figure 5.3. Variable-temperature dc magnetic susceptibility data for **1**-**4** 80
Figure 5.4. Arrhenius plots of **1**-**4** and $(Ph_4P)_2[Co_{0.06}Zn_{0.94}(OPh)_4]$ (**5**) 82
Figure 5.5. Diffuse reflectance spectra for **1**-**4** 83
Figure 5.6. Selected d-orbital energies for **1**-**4** resulting from ligand-field analysis 84
Supplementary Figures for Chapter 5 96

Chapter 6. Slow Magnetization Dynamics in a Series of Two-Coordinate Iron(II) Complexes 104
Figure 6.1. Crystal structures of the studied complexes 105
Figure 6.2. Variable-temperature dc magnetic susceptibility data of the studied complexes .. 111
Figure 6.3. Field-dependence of the magnetic relaxation times for the studied complexes 113
Figure 6.4. Field-dependence of the magnetic relaxation time for $Fe[N(H)Ar^*]_2$ 114
Figure 6.5. Variable-temperature ac susceptibility for $Fe[N(SiMe_3)(Dipp)]_2$ 115
Figure 6.6. Arrhenius plots for the studied complexes 117
Figure 6.7. Calculated quintet energy states for the studied complexes and $Fe[N(t\text{-}Bu)_2]_2$ 118
Figure 6.8. Calculated spin-orbit coupled splittings of the ground ^5E states for the studied complexes and $Fe[N(t\text{-}Bu)_2]_2$ 119
Supplementary Figures for Chapter 6 130

Chapter 7. Magnetic Blocking in a Linear Iron(I) Complex 139
Figure 7.1. Preparation, structure, and d-orbital energies for $[Fe(C(SiMe_3)_3)_2]^-$ 143
Figure 7.2. Mössbauer spectra of $Fe(C(SiMe_3)_3)_2$ and $[Fe(C(SiMe_3)_3)_2]^-$ 144
Figure 7.3. Variable-temperature dc magnetization and magnetic susceptibility data for $[(crypt\text{-}222)K][Fe(C(SiMe_3)_3)_2]$ 146
Figure 7.4. Dynamic magnetic susceptibility data for $[(crypt\text{-}222)K][Fe(C(SiMe_3)_3)_2]$ 147
Figure 7.5. Variable-field magnetization data for $[(crypt\text{-}222)K][Fe(C(SiMe_3)_3)_2]$ 148
Supplementary Figures for Chapter 7 154

Acknowledgements

Six years were spent working on the results presented in this manuscript. Six years! To many of the students who come fresh out of their undergraduate institution full of life and the nauseating eagerness to change the world, the prospect of a six-year graduate degree would likely not seem appealing. Of course, at the beginning, I had no idea it would take six years. At the end, however, I appreciated the length, and I would not have felt as comfortable with my thesis had I left after a more standard PhD timelength of 4 or 5 years. I did not work in isolation, and from a personal and science standpoint, much of the work contained herein would not have been possible were it not for the long list of people with whom I had the joy of working. Everyone I worked with before and during graduate school contributed in some way to my success.

I will begin by thanking my graduate advisor, Jeff, for several reasons, foremost of which is for providing me the resources and guidance to pursue scientific questions I thought worth investigation, as well as giving me a pep talk in my third year, without which I would probably still be bumbling around to a greater extent than I do today. I furthermore am thankful because somehow he managed to hire people that I would love working with over the next few years. I don't think I can stress enough that my day to day work was made brighter due to the people I worked with; over time I began to look less and less at my labmates as "coworkers" and more as friends or even as a family, though a clearly dysfunctional one.

My climb to graduate school began during several semesters of high school chemistry, and during this time my teacher Steve Moore portrayed chemistry in such a way that I was immediately grasped. As an undergraduate, my first laboratory research experience was performed under the auspices of Prof. Gordon Yee. To both I am indebted for giving me my first tastes of what would become a very fulfilling career choice.

I left Virginia Tech with the experience of working in a lab of four people. Arriving in Berkeley, I flirted with the idea of working in other labs, but I was almost certain that I wanted to work for Jeff. I was somewhat intimidated by the large lab size, but the six graduate students at the time made the lab feel small (some of them even made it feel "intimate"), and the fourteen or so postdocs were nothing but helpful. Steven Kaye provided me some initial guidance, as well as a desk area that I inhabited the majority of my PhD. Mircea Dincă was a great resource during that first year, and was in general fun to be around. My memory of him that first year was that of the grumpy senior graduate student. Now I find myself in a similar role, which I find amusing.

Danna Freedman oversaw my initial training in the lab, and I remember the initial reaction we did together; it failed, and she said "OK, there you go, now you have a reaction to study!" thus providing me my first push to become an independent researcher. Over the next year she was always willing to talk science with me, which assisted my understanding of magnetism and chemistry in general. I am extremely grateful to have worked with her as a graduate student and I am very excited to continue the next phase of my career in her lab at Northwestern.

There were several initial postdocs who I also found extremely helpful. Deanna D'Alessandro helped me learn the concepts of mixed valency and especially the technique of solution electrochemistry. David Jenkins and Bart Bartlett helped me on my way into magnetism and taught me the synthetic techniques necessary for cluster synthesis. I also must thank David for establishing the eternal "AG" label for the brown box, and must thank Bart for always being a joy to drink around. I cannot finish this paragraph unless I thank the famous Kentaro Tamaki,

who taught me so much beyond the realm of chemistry, and created my (egg salad and smoked ham) and meg's (meg salad) nicknames, the latter of which I particularly cherish.

Dave Harris was instrumental during and past the initial year, from both a scientific and social standpoint. Aside from an initial tirade against a delinquent prospective student (which ultimately convinced me, also a prospective at that time, that I would survive at UC Berkeley), various interactions with Dave proved worthwhile over the years. I particularly appreciated his speeches, given at all times, which were simultaneously cheesy, sincere, and occasionally moving.

Hema Karunadasa I found extremely knowledgeable about synthesis and a great coworker. For all of the crap she would give me about playing loud music while working at the gloveboxes in 210, I am grateful that, defying most indications, she had a great appreciation for Snoop Dogg, which allowed me to get around the oppressive noise ordnances of 210 Lewis.

Two very important postdoctoral associates, Leslie Murray and Hye Jin Choi, were also present during the first few years, and each made my time at UCB special. Hye-Jin was a senior magnetism postdoc and had been working on magnetism since before I had arrived, thus, she was a great information bank for me. Leslie I consider a close friend who I am consistently impressed with, and I always appreciated going on runs up the hill with him. I especially loved how he would run ahead of me, seemingly trying to have me murdered via isolation of my fat self in the realm of mountain lions.

I am grateful to Jeff Rinehart for many things, including passing on many magnetism ideas at the outset of my work on mononuclear transition metal complexes. I was obsessed with his doodles, and loved how he could start from one or two lines and end up with some sort of bulbous monster.

Kenji Sumida is worthy of a significant amount of thanks for being my comrade at arms for many years. Notably, I owe him thanks for graduating before me, which helped me internalize the fact that I needed to buck up and get on with my life.

The year after Kenji and I were hired, Jeff brought in a relatively big class of students, including Curtis, Zoey, Tom, and Brian. Each of them impacted my graduate career. Zoey and Curtis I always found super helpful, and Tom always willing to get a drink and Brian always willing to point me to some awesome new thing he found. Collectively, I was actually always impressed by now nice they are, and think that they probably constitute the nicest recruiting class I've known for the Long group.

The year after that, Jeff brought in four excellent people who I would get to know closely over the coming years: Eric Bloch, Katie Meihaus, Xiaowen Feng, and Dana Levine. Eric Bloch has been a phenomenal labmate over the years. His most notable skill is the uncanny ability to make me behave about 15 years my junior at the drop of a hat. By merely walking into lab, my maturity level dropped significantly regarding almost anything that involved Eric. That I was at a neighboring desk meant that at any given time, I was less likely behave as a nearly 30 year old professional person and more like a 15 year old with a penchant for bathroom humor. Seriously, it's been real.

The two students who joined the magnetism subgroup, Katie Meihaus and Xiaowen Feng (Spanky), immediately made their mark on the culture of the subgroup. I've never seen someone take his or her science as personally as Katie, and because of that I think she is destined for high success. More than simply a hard worker, Katie has been a great labmate and always willing to lend an ear when I was ready to rant about the myriad things that made me grumpy in my later years. Xiaowen has been highly efficient in graduate school, and I will always miss how, with

his help, we deconstructed the English language, ultimately creating an enjoyable and entertaining lab vernacular which I will take with me to my future ventures. Zurss. I will also fondly recall our wing-loaded trips to the NHMFL, and his drunk willingness to go fight dudes at the ICMM who were trashing my poster.

During my later years, there were a string of awesome postdocs. I think the world of Michael Nippe and Selly Demir, who taught me many things, from basic synthetic ideas, to proper box protocol, to lab safety, to the difference between proper german and schwäbisch. More than educating me about simple lab techniques, I found them to be extremely good friends, always willing to go grab a drink or coffee and let me vent about the myriad of issues that confront a sixth year graduate student trying to get moving with his life. Of Michael I will always remember his infectious bad moods, while of Selly I will instead remember her infectious laugh. I will miss them both dearly and hope that we find the opportunity to meet up in the future. I was also consistently impressed with Wendy Queen (not really a postdoc in our lab, but I'm putting her mention here regardless), Paulina Gomora-Figueroa, Keith Keitz, Rob Ameloot and Jeff Van Humbeck, who to me all seemed like bottomless pits of useful information and smart things to say.

As I passed toward my later years Jeff continued to hire amazing people with whom I could work. Jarad Mason, David Zee and Jordan Axelson were always fun to talk to in lab. I will forever admire the good humour Jarad could maintain in light of the crushing oppresion that Eric and I leveled on him. I am also thankful to David and Jordan for their willingness to brave the 7th circle of hell (bourbon street) with me during my last hurrah at the New Orleans ACS meeting this last semester.

The following year we had several new members, who are great for lab. Dianne Xiao I will never forget, especially her tendency to say markedly mean things (to Jarad, mostly) despite her affable demeanor. She was ultimately crucial for a specific chapter of my thesis and I have the highest expectations for her in the future. Miguel Gonzalez and I shared many a drunk bus ride home. In truth, I was usually the drunk one, on the way home from the bar right as he was soberly leaving work, and I appreciate that he sat there and laughed while I babbled on. The bus ride home some evenings can be quite dull, and Miguel made them much more enjoyable. I always enjoyed the sense of humor from Mike Aubrey, and a particular interaction between him and Brian regarding a cold, hard dose of reality and a pumpkin bowl remains one of my favorite stories from graduate school.

Much of my time in lab occurred in tandem with several great undergraduate researchers. I was consistently impressed by them; Kaitlyn Weeber, Mary Anne Manumpil, and David Gygi. I look forward to moving on from Berkeley at the same time as Kaitlyn and Mary Anne, and I am excited to see what Geeg does when he finally moves on from UCB.

Toward the end of my PhD, some particularly promising blue-chippers came onto the magnetism project, Phil Bunting and Lucy Darago. I have the utmost expectations for them, and am happy to see the influx of talent right as I leave! I look forward to seeing great results from them both! Matt Kapelewski and Douglas A. Fresh I also particurlarly enjoy, and am excited to see what they do after I leave.

A lot of the work done was accomplished with the help of some very competent facility staff at UCB as well as staff at companies. Much of what I know about the inner workings of the SQUID are due to extensive interactions with James O'Brien at Quantum Design. For crystallography, I learned heavily from Fred Hollander and Antonio DiPasquale. I appreciated their complementary, but slightly adversarial, attitudes toward small molecule crystallography. I

acquired the here reported mass spectra with the assistance of Tony Iavarone and Rita Nichiporuk, and I am grateful for their assistance in characterizing my compounds.

I have a list of collaborators outside the department without whom I likely would not understand my science nearly to the level that I do now. I collected high-field EPR data with the assistance of Junjie Liu and Stephen Hill at the NHMFL in Tallahassee; both schooled me well in the basics of EPR, magnetic anisotropy and slow magnetic relaxation. Josh Telser I found very helpful during my work for chapter 5, and particularly enjoy his emails. Our computational collaborators, Mihail Atanasov and Frank Neese, helped me develop a fundamental understanding of unquenched orbital angular momentum in transition metal complexes, for which I am grateful.

Through the ups and downs of my graduate career, I had the never ending support of my family and friends outside of chemistry (gasp!), Katie, Mom, Dad, Kaneil, Tylyn, my aunt Jenni, as well as my grandparents Flo, Forest, and Amanda, who never neglected to tell me how proud they were of me. I have no doubt I would have heard the same thing from my Dad's parents were they around during this time. My closest friends from home, Andrew McKeegan, Adrian Cubbage, and Joel Parker, were always supportive, and always assisted in my enjoyment of my visits back home. Likewise, Meg's family, including Lanie, Joejoe, Taylor, Nick, and Joycee, were always welcoming of me and I'm grateful for their feigned enthusiasm when I decided I wanted to talk science.

Much like the professor whose name sits at the end of the author list because he or she oversaw the whole mess, I save the last bit of these acknowledgements for a very special person: Dr. Meg E. Fasulo. Whenever I had problems in lab, she was almost always the first person I would go to, and she was never short of great advice. Her synthetic knowledge was always extremely useful, and her prowess at passing that information on also made the student she trained, Mike Lipschutz, also supremely useful. During the darkest phases of my PhD, she had nothing for me but support. Furthermore, even after she graduated, she still had great advice for me and was willing to listen to my rants! Truly, her contributions to all phases of my studies can not be overstated. In addition to the science, it has been a phenomenal joy sharing the existence of Berkeley with her, from the introductory seminar for prospectives (where we first met), to my being called out by Ken Raymond for writing "love notes" in X-ray class, to eventually a wedding and everything great that has come afterward.

In summary, to all of you who contributed to this thesis, or my personal growth over the past six years, you have my eternal thanks and friendship/love. If I have not explicitly mentioned you herein, please accept my apology, and know that such oversight was not intentional!

To my friends and family

Chapter 1: Single-Molecule Magnet Behavior in Multi- and Mononuclear Transition Metal Complexes

1.1. Introduction

A magnetically isolated transition metal ion with unpaired electrons will possess a ground state spin that is quantized to achieve only certain orientations, denoted as M_S levels. Bearing in mind that the spin is precessing about a particular reference frame axis (typically taken as the *z*-axis), then the greater the value of $|M_S|$, the closer the spin precesses about the *z*-axis. For example, the M_S levels for an $S = 2$ ion will feature values of $M_S = \pm 2, \pm 1$ and 0. Qualitatively, the $M_S = \pm 2$ levels can be thought of as "up" and "down" within this example, since they precess closest to the reference frame *z*-axis, while the $M_S = 0$ level precesses orthogonal to *z*-axis, and is thus completely in the *xy* plane. For a half integer spin, $S = {}^3/_2$ for example, the $M_S = \pm {}^3/_2$ levels are "up" and "down" within this spin system, while the $M_S = \pm {}^1/_2$ are the M_S levels that precess closest to the *xy* plane.

In many systems, the energies of these M_S levels are approximately degenerate, producing a spin that has no stabilization associated with orientation along a particular direction. For reasons that will be discussed in section 1.3, these energies can be split, leading to a directional preference for the spin, which is a property referred to as magnetic anisotropy. For example, if the energies of the $S = 2$ species are split such that the $M_S = \pm 2$ levels are lowest in energy and the $M_S = \pm 1$ levels are higher in energy with the $M_S = 0$ level highest in energy (see Figure 1.1), then the magnetic moment of this spin will be stabilized when aligned parallel or antiparallel to the *z*-axis, while destabilized if aligned perpendicular to the *z*-axis. A similar but opposite situation can also be found where the M_S levels of lowest $|M_S|$ value ($M_S = 0$ or $M_S = {}^1/_2$) are stabilized and the spin aligns in the *xy*-plane. When the cartesian axes of the reference frame are associated with a molecule or a crystalline lattice, the system is said to possess magnetic anisotropy, and will display different magnetic properties as a function of direction. This thesis focuses upon molecules that possess large magnetic anisotropies of the axial type, where the M_S levels of large $|M_S|$ are stabilized, a class of molecules referred to as single-molecule magnets.[1]

By virtue of the bistable magnetic moments, which by and large possess magnetic properties similar to the examples depicted in Figure 1.1, single-molecule magnets could potentially be used to store information.[2] In such an application, for example, a bit of information could be contained in an individual molecule where the "up" M_S level is labeled as "1" while the "down" M_S level would correspond to "0" (see Figure 1.1). At an average width of 1 nm or less, single-molecule magnets would allow for data densities of up to 200,000 gigabits per square inch on a surface and thus would offer substantial improvement over current technologies. This assessment does not acknowledge the challenge of developing the necessary technology for arranging and addressing single molecules on a surface; however, note that application of single-molecule magnets for information storage devices would require a suitably large energy penalty for inversion of the spin from "up" to "down", because only very large spin-reversal barriers would make data storage practical in light of facile randomization by environmental influences

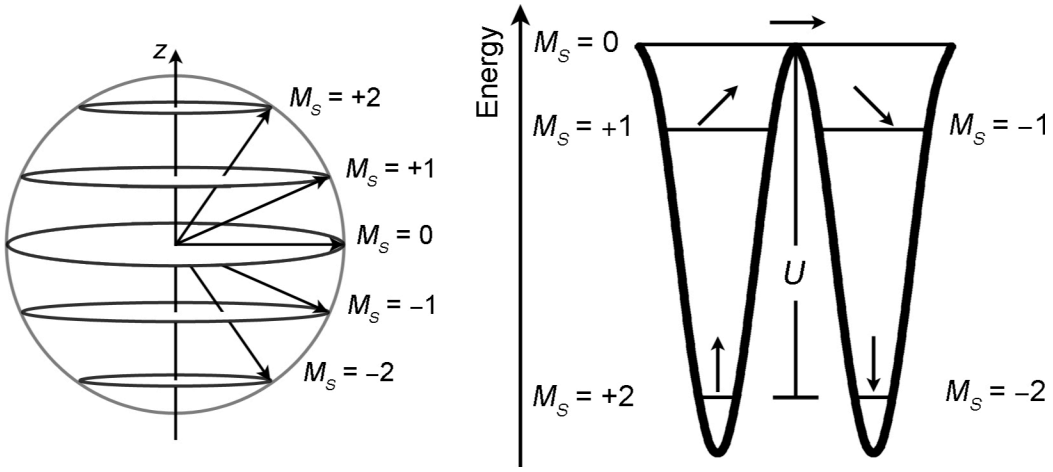


Figure 1.1. Left: depiction of the M_S levels for an $S = 2$ species. Right: relative energy scheme of the M_S levels for an $S = 2$ species under the influence of negative axial anisotropy, with relative orientations of the spin for the various M_S levels denoted. The barrier height for spin reversal, U, is labeled.

such as thermal fluctuations. This barrier, denoted U, is the current figure of merit for the field, and its maximization has been the subject of intense research by inorganic chemists.

For nearly ten years, the first discovered single-molecule magnet, which was composed of multiple transition metal ions linked together, possessed the record barrier (see section 1.2). While the results of subsequent synthetic and theoretical studies elucidated much of the underlying physics of the magnetic behavior of single-molecule magnets, the main figure of merit for information storage application, U, was not appreciably enhanced until 2001 with the discovery of single-molecule magnet behavior in complexes incorporating one lanthanide metal ion. A similar discovery was not made for the transition metals until 2013, and developing this latter discovery is the focus of the research reported in this thesis. In particular, the overarching goal was to explore the origins of single-molecule magnet behavior in transition metal complexes incorporating one transition metal ion. The elemental forms of some transition metals, such as iron, are known for their magnetic properties, which typically originate from cooperative effects and lead to bulk magnetic behavior as a solid. Contained within this thesis are studies exploring systems with analogous magnetic behavior, but here the behaviors are intrinsic to a single ion. As will be shown, such complexes can possess spin-reversal barriers an order of magnitude greater than any other known transition-metal containing species. Also of note is that study of the electronic structures of transition metal complexes containing one transition metal ion is a broad field, and necessarily many different techniques were developed to facilitate analysis and understanding. The development of single-molecule magnets composed of one transition metal ion allowed such techniques (for example Mössbauer spectroscopy or electron paramagnetic resonance spectroscopy) to find immediate utility, and the subsequency analyses are relatively simplified compared to studies of lanthanide or multi-nuclear single-molecule magnets.

In the following chapter, the study of single-molecule magnets is given some historical context and the underlying reasons for shifting from the study of multinuclear to mononuclear species is given. Then, the origins of the spin reversal barrier are discussed, and followed by an

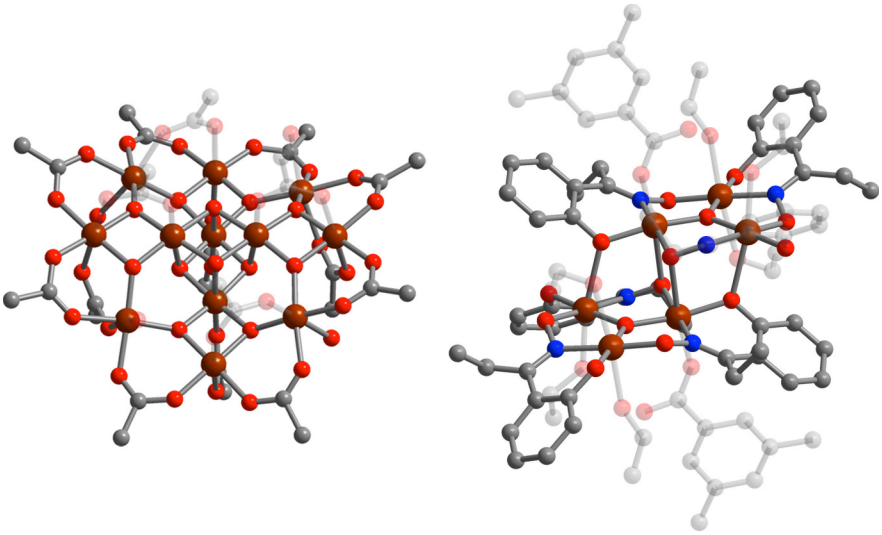


Figure 1.2 Crystal structures of notable multinuclear single-molecule magnets. Left: $Mn_{12}O_{12}(O_2CCH_3)_{16}(H_2O)_4$, Right: $Mn_6O_2(Et\text{-}sao)_6(O_2CPh(Me)_2)_2(EtOH)_6$. Brown, red, blue, and gray spheres represent manganese, oxygen, nitrogen, and carbon atoms, respectively. Hydrogen atoms have been omitted and select ligand scaffolding has been made partially transparent for clarity.

explanation of the most common experimental techniques used to characterize magnetic anisotropy in molecular species. Following those sections, a brief summary of the most notable mononuclear lanthanide single-molecule magnets is given, which includes, on the basis of fundamental physical inorganic chemistry principles, why they are so promising for large U_{eff} values. The final section of this introduction details the theory behind the design of mononuclear transition metal complexes with lanthanide-like magnetism, as well as a brief summary of some notable examples in this regard.

1.2. Multinuclear Single-Molecule Magnets and the Spin-Reversal Barrier

The expression for the magnitude of the spin reversal barrier, U, is $U = S^2|D|$ for integer-spin systems and $U = (S^2 - {}^1/_4)|D|$ for half-integer spin systems, where S is the spin of the magnetic moment and D the zero-field splitting, and these equations apply for systems lacking unquenched orbital angular momentum. In $Mn_{12}O_{12}(O_2CCH_3)_{16}(H_2O)_4$, the first single-molecule magnet (see Fig 1.2), the incorporated eight Mn^{III} (S = 2) and four Mn^{IV} ($S = {}^3/_2$) ions are magnetically coupled to give an S = 10 ground state, and in combination with the non-zero D (–0.5 cm^{-1}), a large theoretical U = 50 cm^{-1} is determined that is reasonably close to the experimental, or effective U_{eff} = 42 cm^{-1}.[3] Importantly, in many multinuclear systems the observed D values are less than a few wavenumbers in magnitude. Thus, over the next decade, the most promising route toward large U_{eff} values seemed to involve the preparation of systems with larger and larger spin ground states via the targeting of oxo-bridged coordination clusters incorporating ever increasing numbers of magnetically-coupled transition metal ions. Despite all

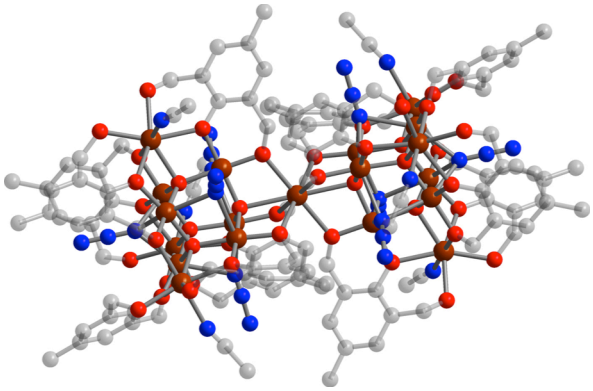


Figure 1.3. Crystal structure of $[Mn_{19}O_8(N_3)_8(HL)_{12}(CH_3CN)_6]^{2+}$ which has an $S = {}^{83}/_2$ ground state. Solvents of crystallization, counterions, hydrogen atoms have been omitted, and select ligand scaffolding has been rendered transparent for clarity.

of the efforts, the barrier of a $Mn_{12}O_{12}$-type cluster, $Mn_{12}O_{12}(O_2CCH_2Br)_{16}(H_2O)_4$, ($U_{eff}$ = 52 cm^{-1}) remained the record for nearly two decades.[4] In light of the trend toward larger nuclearity species, the breaking of this record barrier in 2006 by a lower-nuclearity complex, Mn_6O_2(Et-sao)$_6$(O_2CPh(Me)$_2$)$_2$(EtOH)$_6$ (Et-saoH$_2$ = 2-hydroxyphenylpropanone oxime, see Figure 1.2), U_{eff} = 60 cm^{-1}, seems unexpected.[5] Further, a rigorous development of the theory of zero-field splitting had shown the magnitude of D to be inversely proportional to S^2,[6] though this theoretical argument seemed to go largely ignored by the community as evidenced by the large numbers of studies on multinuclear species. The somewhat negative influence of the overall spin state on the magnitude of U_{eff} via the hidden relation between S^2 and D was studied in depth for a few molecular systems,[7] but is most dramatically demonstrated by the enneakaidecanuclear oxy-bridged complex $[Mn_{19}O_8(N_3)_8(HL)_{12}(CH_3CN)_6]^{2+}$ (H_3L = 2,6-bis(hydroxymethyl)-4-methylphenol) , see Figure 1.3.) which has an $S = {}^{83}/_2$ ground state.[8] If this complex possessed a negative D with a magnitude of a fraction of a wavenumber, it would possess a giant spin reversal barrier (for example, with $|D|$ = 0.1 cm^{-1}, U = 172 cm^{-1}). However, this complex displays negligble magnetic anisotropy and does not exhibit any indications of possessing a spin reversal barrier. Taken together, the theoretical and experimental developments discussed here suggest that research efforts to create a complex with a large barrier should not focus solely on the preparation of high-spin ground states in multinuclear species.

1.3. Origins of Large Magnetic Anisotropy in Transition Metal Complexes

Low-nuclearity transition metal complexes (containing 3 or fewer transition metal ions) have been of interest for many years as model complexes for the active sites of biologically relevant enzymes.[9] As the crystallographic identification of the active sites of transition metal containing enzymes remains a difficult task even today, various spectroscopic methods were established to help derive information about the transition metal oxidation states and coordination geometries.[10] Correlations between the spectra of the enzymes and those of small model complexes allowed for general conclusions about the oxidiation states, coordination numbers, and coordination geometries of the transition metal ions in the active sites to be made. As a result of the further application of these analytical techniques, large D values (on the order of tens of wavenumbers) were discovered in simple transition metal complexes, in contrast to the

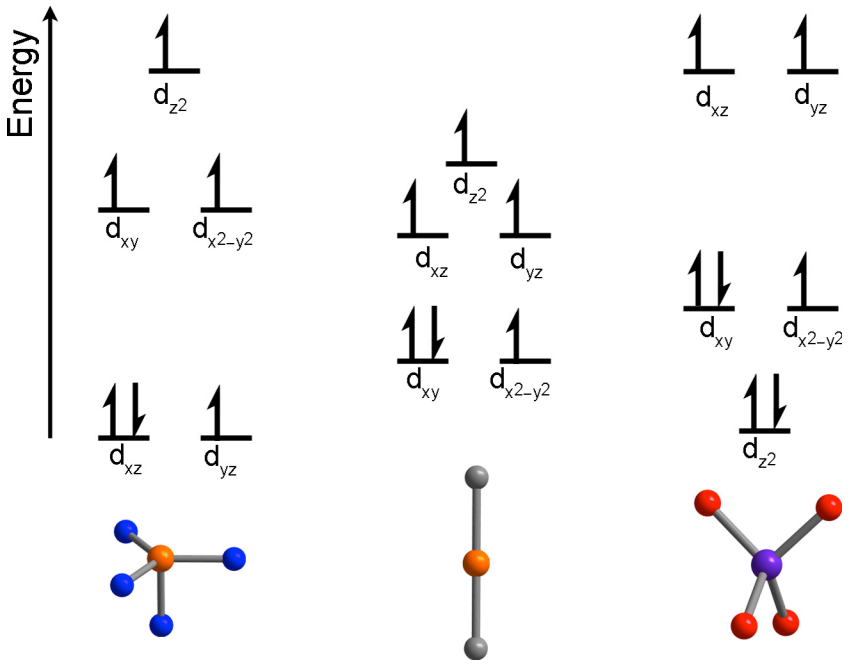


Figure 1.4. Electron configurations and relative d-orbital energies for idealized iron (II) and cobalt(II) complexes of C_{3v} (left, iron), $D_{\infty h}$ (middle, iron), and D_{2d} (right, cobalt) symmetry. Energies are approximately to scale; note that a smaller ligand-field splitting is expected for lower coordination numbers. Relative energy spacings are based upon the geometries of molecules discussed in this chapter and in chapters 4-6 of this thesis.

often-small *D* values exhibited by large multinuclear species. The origin of this discrepancy lies in the fact that the total molecular *D* for a multinuclear species is created by the vector addition of the *D* tensors of the constituent paramagnetic centers.[6c,11] Thus, if one wanted a large *D* in the multinuclear species, then one would target a complex where the *D* tensors of the spin centers are nearly parallel. In practice, however, it is extremely difficult to impart this amount of control during cluster synthesis. Fortuitously, $Mn_{12}O_{12}$-type molecular architectures, as well as $Mn_6O_2(Et\text{-}sao)_6(O_2CPh(Me)_2)_2(EtOH)_6$, possess a near parallel alignment of the *D* tensors of the manganese ions.[11] A variety of cyanide-bridged coordination clusters have also been pursued with the idea that one could magnetically-couple high-magnetic anisotropy cyanometallate species and thus also achieve a large *D*.[12] None of these design principles is necessarily straightforward, and there are also other sources of anisotropy for multinuclear paramagnetic complexes[13] that can complicate the design of large-*D* systems. In contrast, the sources of magnetic anisotropy for mononuclear systems are comparatively simple.

The magnetic anisotropy in mononuclear transition metal systems is fundamentally tied to the coupling of the spin to the orbital angular momentum, which can be readily tuned by manipulation of the ligand field. As the orbital angular momentum in first-row transition metal complexes originates from the spin-bearing 3d-orbitals, and since these 3d-orbitals interact strongly with the surrounding ligand field, the orbital angular momentum generates an inherent directionality for the spin with respect to the arrangement of the ligands and thus the coordination environment. This transitive-like interaction between spins and the environment is the basis for the directional magnetic anisotropy observed for single-molecule magnets and enables the manipulation of the anisotropy via the ligand field. Orbital angular momentum

originates in systems that possess an odd number of electrons occupying an even number of degenerate orbitals. Depicted in Figure 1.4 are several example 3d-orbital splittings and electron configurations for a few idealized geometries (as relevant to this thesis) that would be expected to possess orbital angular momentum. In a system with unquenched orbital angular momentum, the total angular momentum quantum number J results from the addition of the spin angular momentum S and the orbital angular momentum L. Rather than M_S levels, as possessed by spin-only systems, the quantized orientations of the total angular momentum are given by M_J levels. Here, the energy splittings between the M_J levels are dictated by the spin-orbit coupling constant, ζ, of the spin center. Thus, the spin-reversal barrier is proportional to ζ, not D, as is the case for most single-molecule magnets. It is important to note that ζ is often orders of magnitude greater than the largest D values,[14] therefore complexes which have unquenched orbital angular momentum possess an inherent advantage toward the creation of a large magnetization reversal barrier. Indeed, this is particularly true for the lanthanides, which feature very large ζ values.

On account of the strong interaction between the d-orbitals and ligand orbitals, however, there is often a stabilization energy associated with splitting the orbital degeneracy (the Jahn-Teller distortion) and quenching the orbital angular momentum. This tendency directs many coordinatively saturated transition metal complexes (those with five or more ligands) toward magnetic properties attributable only to their spin (so-called spin-only behavior). Further, geometric distortions of the coordination sphere of the transition metal ion on account of crystal packing or steric strain of the ligands can also split the degenerate orbitals and effectively quench the orbital angular momentum.

In most transition metal complexes, which lack the exact degeneracy required for unquenched orbital angular momentum, the split orbitals are still close enough in energy that the spin-orbit coupling of the ion resuscitates some of the orbital angular momentum. This situation gives rise to a second-order magnetic anisotropy, the zero-field splitting (D), and is the source of energy splitting of the M_S levels in most transition metal complexes. To describe the energy of the M_S levels in the presence of zero-field splitting, the following Hamilonian is applied, using the $|M_S\rangle$ wavefunctions as the basis set.

$$\hat{H} = D\hat{S}_z^2 + E(\hat{S}_x^2 - \hat{S}_y^2) \quad (1)$$

Here, E is the transverse anisotropy, and $\hat{S}_i$ represent the spin operators. The transverse anisotropy describes an energy difference between alignment in the x and y directions of a spin. Further, E can mix $|M_S\rangle$ levels and thus eliminate the bistable ground state necessary for single-molecule magnet behavior in mononuclear species, as discussed later in the manuscript for integer-spin systems. Note that this Hamiltonian can be augmented depending on the system by the inclusion of terms that describe other magnetic interactions, such as superexchange between neighboring atoms, or the Zeeman interaction an external dc applied magnetic field.[15]

According to the Hamiltonian in eq (1), when D is non-zero, the M_S levels of a spin S are split by amounts proportional to D. However, the sign of D is important because it dictates whether the M_S levels of maximum $|M_S|$ value are stabilized or destabilized. If D is positive, the stabilized M_S values are either $M_S = 0$ (integer spin systems only) or $M_S = \pm{}^1/_2$ (half-integer spin systems). This creates easy-plane anisotropy, where the spin is stabilized upon alignment in the xy plane of the system. In contrast, when D is negative (easy-axis anisotropy), the M_S levels of largest $|M_S|$ value are stabilized. Thus, a bistable "up" and "down" ground state, like the kind depicted in Figure 1.1, is only possible for a system with a negative D state. Note that a positive

D, half integer spin system also possesses a bistable ground state of $M_S = \pm^1/_2$. As is discussed in Chapter 3, such a bistability is not the ideal case needed for single-molecule magnet behavior due to the ease of the direct transition between the $M_S = \pm^1/_2$ levels rather than over a spin reversal barrier.

The magnitude and sign of *D* are a result of a sum of second-order interactions between the ground magnetic state (where the orbital angular momentum is quenched) and excited states. The lowest lying excited states in transition metal complexes are often d-d excitations, thus, these are the strongest contributing factors to *D*, and therefore are most useful in determining *a priori* whether or not a complex will have a large *D*. The second order nature of the ground-excited state interaction indicates a proportional relationship between the contribution to *D* and an inversely proportional relationship to energy gap between the two states. Thus, the contribution to *D* from an interaction between the ground state and a specific excited state will be larger in magnitude if the excited state is close in energy to the ground state. With regard to the observation of single-molecule magnet properties, the second important aspect of *D* is its sign. Here, the sign for a specific contribution to *D* arises from the product $\langle \Psi_a | \hat{L}_i | \Psi_b \rangle \langle \Psi_b | \hat{L}_i | \Psi_a \rangle$, where Ψ_a represents the ground state wavefunction, Ψ_b the excited state wavefunction $\hat{L}_i$ the orbital angular momentum operator for a given axis in the system ($\hat{L}_i$ can be $\hat{L}_x$, $\hat{L}_y$, and $\hat{L}_z$). Qualitatively, the products of these operators represent the direction of the resurrected orbital angular momentum by the interaction between the ground and excited states, while the inverse relationship with the energy gap determines the magnitude. For a transition metal ion, where the lowest lying excited states are as a result of one-electron d-d excitations, the above product can be qualitatively thought of by replacing Ψ_a and Ψ_b with the m_l values of the d-orbitals that the electron involved in the d-d excitation is excited *from* and *to*, respectively. When the m_l values of the two orbitals involved in the excitation differ in $|m_l|$, the value of the product is zero for $\hat{L}_z$ but may be nonzero for $\hat{L}_x$ and $\hat{L}_y$. In contrast, when the excitation instead involves two orbitals with the same $|m_l|$ values, the product is *negative* for $\hat{L}_z$ but zero for $\hat{L}_x$ and $\hat{L}_y$. Thus, one can achieve a maximum, negative *D* value when the lowest lying excited that contributes to *D* involves a d-d transition between orbitals of the same $|m_l|$. However, given the complexity of d-orbital splittings in the plethora of paramagnetic transition metal complexes known, and their sensitivity to tiny distortions of the coordination sphere of the transition metal ion, it is no surprise that the determination of *D* can be difficult without a detailed knowledge of the electronic structure of a given paramagnetic ion. In particular, nonzero products with $\hat{L}_x$ and $\hat{L}_y$ can lead to positive *D* values and easy-plane anisotropy, but also can lead to negative *D* values where the axis of preferred orientation for the spin deviates from the molecular *z*-axis. In terms of the design of systems with large magnetic anisotropy, it appears that large *D* values are more likely in systems with low lying excited states than those with high-lying excited states. However, given that *D* arises from the contributions over *all* the excited states, if there are multiple low-lying excited states with opposing contributions, *D* could still be small in magnitude.

1.4 Characterization of Magnetic Anisotropy in Single-Molecule Magnets

The principal characterization of the magnetic anisotropy for a complex comes from the temperature dependence of the molar magnetic susceptibility (χ_M) under a dc applied field. The fundamental concepts that enable the utility of this technique are three-fold. Firstly, different M_S values contribute different amounts to the measured magnetic moment. Second, the possession of

appreciable magnetic anisotropy for a given spin system implies that the resultant M_S levels will be split in energy. Finally, in most transition metal systems, the splitting energies between the M_S or M_J levels (whether from D or ζ) are comparable in magnitude to $k_B T$ over the common temperature ranges of investigation (from 2 to 300 K, or 1.4 to 208.5 cm^{-1}). Thus, the temperature dependence of the magnetic susceptibility reflects the changing moment as a function of the changing populations of the M_S or M_J sublevels with temperature.

One typically creates a model spin hamiltonian which constrains the relative ordering of the relevant M_S and M_J sublevels, then fits the molar magnetic susceptibility data by altering the magnitude of the splitting of these levels. To perform this fit, the Van-Vleck equation is utilized to fit the data.

$$\chi_M = \frac{N}{H} \frac{\sum_i \mu_i \exp\left(\frac{-E_i}{k_B T}\right)}{\sum_i \exp\left(\frac{-E_i}{k_B T}\right)} \qquad (2)$$

Here, N is Avogadro's number, H is the applied dc magnetic field, μ_i is the magnetic moment of a specific state i (herein these i-states represent the wavefunctions of either M_S or M_J levels), E_i is the energy of that state, k_B is Boltzmann's constant, and T is temperature. The exponential terms here account for the temperature-dependent populations of state i, while μ_i provides the contribution that the individual M_S or M_J levels provide to the magnetic moment of the sample. This equation can also be used to fit magnetization data.

In the limit that all of the i states in eq (2) are degenerate, or the system is at a high enough temperature to ensure nearly equal population of the i states, then eq (2) reduces to eq (3), the Curie Law.

$$\chi_M = \frac{C}{T} = \frac{N\mu_B^2}{3k_B T} g^2 S(S+1) \qquad (3)$$

Here, N is Avogadro's number, μ_B is the Bohr magneton, k_B is the Boltzmann constant, T is temperature, g is the Landé g-factor, and S is the spin. There are several important aspects of this formula to note. Firstly, at room temperature, the value of $\chi_M T$ can be used to obtain information about S for a species, given that the rest of the terms in eq (3) are constants and the value of g should be 2.0023. Second, the deviation of g from 2.0023 can help give further information about the deviation from spin-only magnetic properties in a given system. Thirdly, note that eq (2) is a function of spin, thus it assumes that the magnetic moment depends on the spin only. With respect to this last note, eq (3) can be easily modified to incorporate unquenched orbital angular momentum, but is nevertheless typically applied in the spin-only form for transition metal species. Thus, deviations of g from 2.0023 further indicate deviations of the magnetic properties of the measured system from spin-only behavior. The most important aspect of eq (3), as relevant to the work contained in this thesis, is that the product $\chi_M T$ will be temperature independent when the M_S or M_J levels are degenerate for a measured system. This is not the case for magnetically anisotropic systems, which can feature significant splitting of their respective M_S and M_J levels. Application of eq (2) is then required, which can provide the exact energy differences between the levels, as these energy differences ultimately dictate the shape of the $\chi_M T$ *vs*. T plot.

The splittings between the M_S or M_J levels are typically parameterized by terms in a spin-Hamiltonian. This Hamiltonian is then used to determine a relative ordering for the relevant magnetic states and thus provide quantitative information about the degree of energy splitting between the M_S or M_J levels. Specific parameterizations for transition metal species describe the magnetic anisotropy as it arises from first-order unquenched orbital angular momentum (ζ, the spin-orbit coupling constant) and second-order magnetic anisotropy (D), and the origins of and differences between these two factors are discussed throughout this thesis. Though fitting susceptibility data to a spin-Hamiltonian is a common way of evaluating the magnetic anisotropy in a molecular complex, ideally this method is complemented with spectroscopic techniques, such as electron paramagnetic resonance (EPR), luminescence (for some f-element compounds), and even low-energy infrared spectroscopy. Further, computational analyses can provide all of the information needed for eq (2), and in such cases, close agreement between the experimental data and simulated data (based on computational results) can be used to verify spin-Hamiltonian parameters.

1.5. Characterization of Magnetization Reversal Barriers in Single-Molecule Magnets

As a consequence of the magnetic anisotropy, there may be a spin reversal barrier in a molecule, and if large enough, then the magnetic moment will lag behind an applied ac magnetic field. Measurement of the ac susceptibility of a single-molecule magnet is the principal method for determining experimentally the magnitude of the barrier to magnetization reversal. In the presence of an oscillating magnetic field, the molar magnetic susceptibility of a compound becomes a summation of a real (in-phase) component, designated χ_M', and an imaginary (out-of-phase) component, χ_M''. The temperature dependence of χ_M'' yields crucial information about both the height of the magnetic relaxation barrier as well as mechanisms for spin reversal. In a typical measurement, the sample is held at a constant temperature and dc field while the ac susceptibility is measured as a function of frequency (ν) of the applied ac magnetic field. For a sample with a barrier with respect to spin reversal, the value of χ_M' will fall once the ac field switching frequency becomes too fast for the magnetic moment of the sample to follow it (see Figure 1.5). Simultaneously with the decrease in χ_M', a peak will appear in the trace of χ_M'' versus ac field frequency. The frequency at which the peak maximum occurs yields the magnetic relaxation time (τ) via the relation $\nu = (2\pi\tau)^{-1}$. Though τ can be approximated through a inspection of the χ_M'' versus frequency trace, a more exact value can be obtained through fitting the ac susceptibility data with a Debye model. This model utilizes the following two equations for χ_M' and χ_M''.

$$\chi'(\nu) = \chi_S + (\chi_T - \chi_S)\frac{1 + (2\pi\nu\tau)^{1-\alpha}\sin\left(\pi\alpha/2\right)}{1 + (4\pi\nu\tau)^{1-\alpha}\sin\left(\pi\alpha/2\right) + (2\pi\nu\tau)^{2-2\alpha}} \qquad (3)$$

$$\chi''(\nu) = (\chi_T - \chi_S)\frac{(2\pi\nu\tau)^{1-\alpha}\cos\left(\pi\alpha/2\right)}{1 + (4\pi\nu\tau)^{1-\alpha}\sin\left(\pi\alpha/2\right) + (2\pi\nu\tau)^{2-2\alpha}} \qquad (4)$$

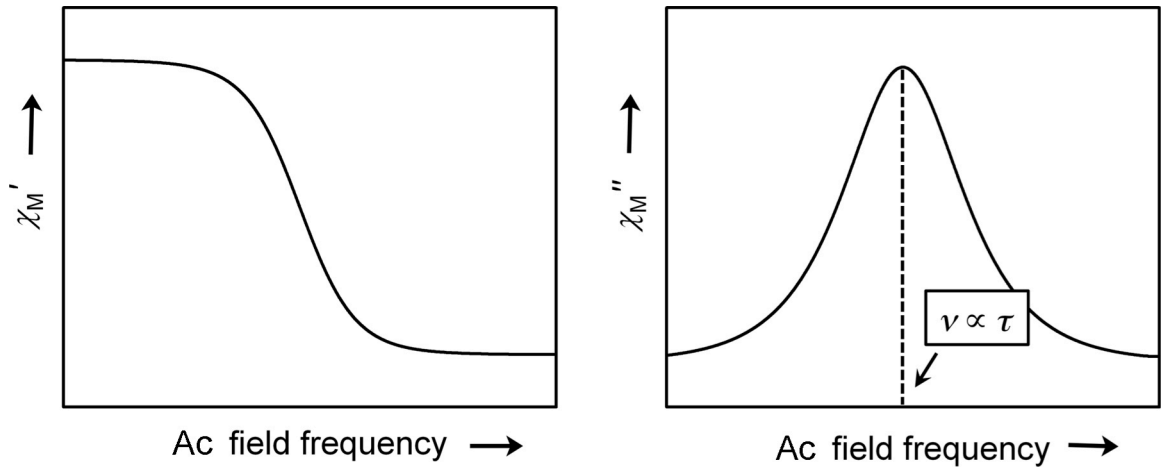


Figure 1.5. Depiction of frequency (ν) dependence of the in-phase (χ_M'', left) and out-of-phase (χ_M'', right) susceptibility in the frequency regime where the spin reversal barrier blocks the magnetic moment from following the applied ac magnetic field. Note that the maximum of χ_M'' occurs at a ν that is proportional to the magnetic relaxation time (τ) under the experimental conditions.

Here, χ_T and χ_S are the isothermal and adiabatic susceptibilities respectively, ν and τ have already been defined, and α is a parameter that allows for a distribution of relaxation times about τ for the sample. χ_T corresponds to the value of χ_M' at frequencies where χ_M' is at a maximum, i.e. the magnetic moment is following in-phase with the ac field. χ_S, in contrast, represents the value of χ_M' at the blocked limit, where the moment is unable to follow the ac field. Note that χ_S need not be exactly zero if a small portion of the sample is not blocked by the barrier; in practice such behavior can be due to a minor paramagnetic impurity but can also be observed in compounds with multiple magnetic relaxation pathways.

1.6. Lanthanide-Based Single-Molecule Magnets

In 2001, the first mononuclear lanthanide complex was shown to display single-molecule magnet behavior.[16] This complex, $[Tb(Pc)_2]^-$ (Pc^{2-} = phthalocyanine dianion) is depicted in Figure 1.6 along with some other notable lanthanide-based single-molecule magnet species and their respective barriers.[17] The exceptional single-molecule magnet activity from these species is tied to fundamental aspects of lanthanide electronic structure. The first important facet of lanthanide electronic structure results from the contracted 4f orbitals, which experience a very weak ligand field. This weak ligand field results in a relatively large spin per ion ratio that one does not find in the first row of the transition metals; further, there are no known low-spin configurations for lanthanide ions, nor are there any reported instances of spin crossover. This near degeneracy of the 4f-orbitals also facilitates the development of unquenched orbital angular momentum in most of the ions and strong deviations from spin-only behavior. For the systems with unquenched orbital angular momentum, the coupling of the spin and orbital angular momenta is further strengthened by the very heavy nuclei. In fact, the influence of the spin-orbit coupling on the energies of the electronic states of a lanthanide ion is much stronger than imparted by the ligand field. As a result, even though the ligand field around a lanthanide may be

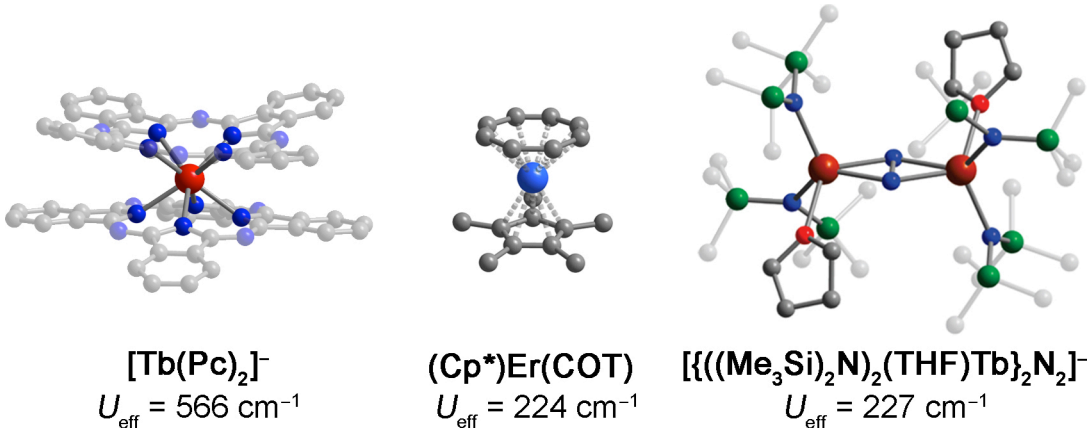


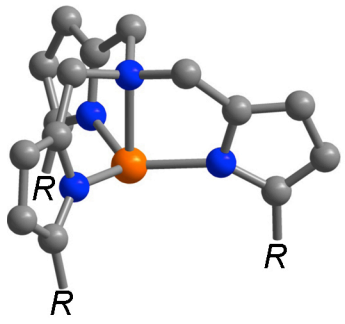
Figure 1.6. Examples of lanthanide-based mono- and multinuclear single-molecule magnets (Pc^{2-} = phthalocyanine dianion, Cp^{*-} = pentamethylcyclopentadiene anion, COT^{2-} = cyclooctatetraene dianion, THF = tetrahydrofuran).

very asymmetric, the orbital angular momentum will remain unquenched and thus the magnetic anisotropy very big. This is in contrast to the first row transition metals for which a distortion of the coordination sphere can readily quench any orbital angular momentum and anisotropy.

1.7. Mononuclear Transition Metal Single-Molecule Magnets

Isolating comparable anisotropy to the lanthanides in a transition metal complex requires approximating the electronic structure that gives the lanthanides such characteristically strong magnetic anisotropy. It was highlighted earlier that the spin-orbit coupling in lanthanides is so strong that it will override quenching effects of the ligand field. Enhancement of the spin-orbit coupling for a transition metal ion is not straightforward synthetically; however, the manipulation of the ligand field is. Note that the weak ligand field of the 4f-orbitals can be nearly approximated for the 3d-orbitals in a low-coordinate transition metal complex. Here, the low number of coordinating ligands creates a relatively weak the ligand field that engenders a situation where the spin-orbit coupling contribution to the electronic structure is comparable to that of the ligand field (*i.e.* an electronic structure similar to the lanthanides and 5d transition metals, but here for a first row transition metal ion).

In these lower-coordinate geometries, the coordinatively unsaturated metal ions are likely to have d-orbitals with lobes extending in directions not occupied by ligands. Thus, low-coordinate transition metal species tend to have d-orbitals with significant non-bonding character, as dramatically exemplified in the complexes presented in Chapters 6 and 7 of this thesis. This has important consequences with regard to the two forms of anisotropy covered in section 1.3. Such low-coordinate transition metal ions (for example, those depicted in Figure 1.4) with the requisite electronic configuration for unquenched orbital angular momentum can possess rigorously unquenched orbital angular momentum because the stabilization energy afforded by a Jahn-Teller distortion is so small. However, as is the case with most transition metal complexes, the orbitals are usually split. If the splitting is small enough, the spin-orbit coupling can fully resurrect the orbital angular momentum, as is shown in Chapters 6 and 7. In the cases where the splitting is too large, however, the significant nonbonding character of the



[(TPA^R)Fe]$^-$

R =	*D* (cm^{-1})	U_{eff} (cm^{-1})	|*E*| (cm^{-1})
t-Bu[a]	–48	60	0.0001
Mes	–40	42	0.4
Trip	–36	[b]	6
Ph	–26	25	0.3
DFP	–6.2	-	0.1

[a]Iron(II) ion resides on crystallographic 3-fold axis

[b]Relaxation dominated by tunneling, possibly due to large *E*

Figure 1.7. Molecular structure and magnetic parameters for the [(tpa^R)Fe]$^-$ series of complexes.

orbitals in a low-coordinate species can ensure that the d orbitals are still close enough in energy to facilitate a strong second-order interaction and give rise to a large *D* relative to higher-coordinate species, as covered in Chapters 4 and 5.

A large magnetic anisotropy is not a sufficient condition for creating a large spin reversal barrier; the anisotropy must be axial. This considerably limits the desirable geometries if one wants to create a transition metal complex with a large spin-reversal barrier. In order to create an axial anisotropy, the system must feature 1 or 3 electrons in a degenerate or nearly-so set of (d_{xy}, d_{x2-y2}) or (d_{xz}, d_{yz}) orbitals, which respectively share the same $|m_l|$ value. With respect to unquenched orbital angular momentum, such rigorous degeneracies will create an addition of L = 2 and L = 1 contribution, respectively, to the magnetic moment and a strong deviation from spin-only behavior. Note that degeneracies between orbitals of differing $|m_l|$ values instead engender anisotropy analogous to a positive *D*, but here due to orbital angular momentum. Conveniently, this same design principle extends to systems that do not feature rigorously degenerate sets of (d_{xy}, d_{x2-y2}) and (d_{xz}, d_{yz}) orbitals. Here, the orbital angular momentum may be quenched; however, the near-degeneracy of the (d_{xy}, d_{x2-y2}) or (d_{xz}, d_{yz}) orbitals ensures that the inter-pair d-d excitation is very low energy and thus contributes significantly to the magnitude of *D*. Further, the contribution to *D* from a d-d excitation between two orbitals of the same $|m_l|$ value is always negative. Thus, a simple structural motif for a large, negative axial anisotropy appears to be coordination geometries with a principal rotation axis of order greater than 3. However, as displayed in Figure 1.4, other coordination geometries are also well suited toward having the appropriate d-orbital splitting for a large magnetic anisotropy.

The first transition metal systems studied as mononuclear single-molecule magnets were trigonal pyramidal iron(II) complexes of the tris(pyrrolyl-α-methyl)amine ligand tpa^R (R = *tert*-butyl, phenyl, mesityl, 2,4,6-triisopropylphenyl, and 2,6-difluorophenyl) (see Figure 1.7).[18] The d-orbital splitting for the idealized geometry (depicted in Figure 1.4) reveals 3 electrons in the (d_{xz}, d_{yz}) set of orbitals. Consistent with the above discussion, these species display large, negative *D* values. Here, small distortions of the coordination geometry from strict C_{3v} symmetry serve to quench the orbital angular momentum, leading to second-order anisotropy. The magnetic anisotropy for these complexes was demonstrated to be very sensitive to the ligand

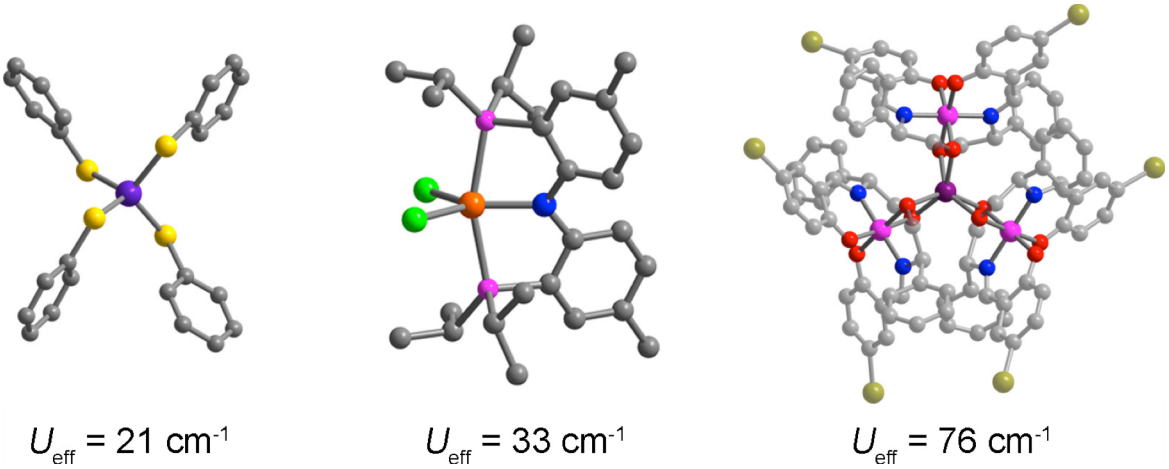


Figure 1.8. Molecular structures and observed barriers for three species that display slow magnetic relaxation at zero applied field attributable to a single transition metal ion. Left, $[Co(SPh)_4]^{2-}$, middle, (PNP)$FeCl_2$, right, $[L_6Co^{III}{}_3Co^{II}]^-$.

field, with small changes in the electron donating properties of the pyrrolyl-nitrogen (*via* inductive effects of the *R*-group) appreciably manipulating the observed *D* values. Furthermore, the complex closest to rigorous 3-fold symmetry, $[(tpa^{tbu})Fe]^-$, which achieved such a high symmetry geometry via crystallization with an iron(II) on a crystallographic 3-fold rotation axis, was shown to possess the largest *D*. Most importantly, these complexes displayed a temperature-dependent peak in the out-of-phase ac susceptibility at low temperature, indicative of slow magnetic relaxation and a barrier with respect to spin reversal. In the series, however, the application of a static dc field was necessary to subjugate fast ground-state magnetic tunneling between the $M_S = \pm 2$ sublevels and give rise to slow magnetic relaxation. Given that ref 14a and 14b were the first studies of mononuclear transition metal complexes as single-molecule magnets, it is particularly noteworthy that the largest barrier observed for this family of complexes, U_{eff} = 62 cm^{-1} for $[(tpa^{tbu})Fe]^-$, was already comparable to the largest U_{eff} values demonstrated for multinuclear transition metal species. Several other mononuclear iron(II) species with other coordination numbers were subsequently shown to display slow magnetic relaxation. A four-coordinate organometallic complex, ($C_5{}^iPr_5$)Fe(2,6-*i*Pr-C_6H_3),[19] displayed a quite large spin reversal barrier under applied barrier (U_{eff} = 100 cm^{-1}) and an additional study revealed slow magnetic relaxation for the three-coordinate iron(II) species $Fe(N(SiMe_3)_2)_2(P(C_6H_{10})_3)$ with U_{eff} = 29 cm^{-1}.[20]

The aforementioned drawback of these species, the requirement of an applied field to see a peak in the out-of-phase ac susceptibility, necessitated an investigation of the origin of the ground-state magnetization tunneling and subsequent experimental efforts to observe slow magnetic relaxation at zero applied dc field. Magnetization tunneling in a molecular species can be engendered by a variety of interactions that serve to mix the ground $\pm M_S$ levels.[21] Foremost among these is transverse anisotropy (*E*). As noted some time ago by H. A. Kramers, the ground states of half-integer spin systems will not be mixed by *E*, and thus will remain bistable even for species with nonzero *E*. Thus, cobalt(II) seemed particularly promising for zero-dc-field slow magnetic relaxation, not only because of the large magnetic anisotropy for which it is historically known,[22] but also because of the half-integer spin. However, note that the first few studies of cobalt(II) did not reveal slow magnetic relaxation under zero applied dc field. The first reported

example of slow-magnetic relaxation in a mononuclear cobalt(II) complex was demonstrated with the complexes $L_1Co(NCS)_2$ and $L_2Co(NCS)_2$ (L_1 = 2,6-bis[1-((2,6-diisopropylphenyl)imino)ethyl]pyridine and L_2 = 2,6-bis[1-((2,6-diisopropylphenyl)imino)benzyl]pyridine), with U_{eff} = 11.2 and 16.68 cm^{-1}, respectively.[23] In this original publication, the anisotropy in the complex was only characterized by susceptibility fitting, a technique that can sometimes be unreliable for determining the sign of *D*. To further complicate matters, shortly after this initial report, the complex $[(3G)CoCl]^+$ (3G = 1,1,1-tris-[2*N*-(1,1,3,3-tetramethylduanidino)methyl]ethane), which has a positive *D* value, was discovered to display slow magnetic relaxation under applied field, and this complex is the focus of Chapter 3. Thus, the observation of slow magnetic relaxation under an applied field is not an indication that *D* is negative for half-integer spin systems. In the time since this publication, several other species have been shown to display slow magnetic relaxation despite having positive *D* values.[24]

A survey of the literature revealed a particular promising candidate for slow magnetic relaxation at zero-field, $[Co(SPh)_4]^{2-}$. Importantly, EPR characterization revealed a substantial negative *D* value on the order of –70 cm^{-1}.[25] Coupled with the half-integer spin, this complex was the first to display slow magnetic relaxation at zero applied field with U_{eff} = 21 cm^{-1}. Shortly after this initial observation, an intermediate spin, trigonal bipyramidal iron(III) complex, $(PNP)FeCl_2$ (PNP^- = *N*-[2-$P(CHMe_2)_2$-4-methylphenyl]$_2^-$), was also shown to display slow magnetic relaxation at zero applied field with a larger U_{eff} = 33 cm^{-1}.[26] Very recently, the complex $(L_6Co^{III}{}_3Co^{II})^-$ (H_2L = R-4-bromo-2-((2-hydroxy-1-phenylethylimino)methyl)phenol), which incorporates one high-spin six-coordinate cobalt(II) ion, was discovered to display a large spin reversal barrier at zero applied dc field, with U_{eff} = 76 cm^{-1}.[27] Importantly, all three of these complexes (see Figure 1.8) feature d-orbital splittings that engender a lowest-energy d-d excitation between two orbitals of the same $|m_l|$ values: in $(PNP)FeCl_2$, this transition is $d_{yz} \rightarrow d_{xz}$, while in $[Co(SPh)_4]^{2-}$ and $(L_6Co^{III}{}_3Co^{II})^-$ the transition is between the d_{x2-y2} and d_{xy} orbitals.

1.8 Outlook

Over a decade of fervent research effort passed before the U_{eff} of the first single-molecule magnet was eclipsed by a different multinuclear transition metal species. During that effort, a plethora of beautiful complexes were made, many of which possessed interesting properties that extend beyond their spin reversal barriers. Nevertheless, in terms of the figure of merit for single-molecule magnets, progress was incremental. The discovery of slow magnetic relaxation in mononuclear lanthanide systems illuminated the possibility of very large magnetic barriers in systems with only one magnetic ion. However, the observation of single-molecule magnet behavior in complexes with one magnetic ion was restricted to the lanthanides for the following decade, presumably because of a wide held belief that the magnetic anisotropies of mononuclear transition metal systems would be too small to generate a significant spin-reversal barrier, thus there was no choice but to target large U_{eff} by seeking systems with high-spin ground states. Note that the benefits of the lanthanides with respect to single-molecule magnetism also engender their limits; the contracted 4f-orbitals can lead to relatively less tunability of their magnetic anisotropies through the ligand field, as compared to 3d systems. Further, the kind of deep understanding that can develop from electronic structure calculations is far more likely with transition metal systems than those of lanthanides or even actinides.

In this brief survey of the nascent field of mononuclear transition single-molecule magnets, I have laid down a few guiding principles for the design of transition metal ions with large single-ion anisotropies. Given the success highlighted in this introduction and the rest of this thesis, I suspect that the tip of the iceberg has only been observed, and that there is a wealth of new information to be gleaned from the study of the magnetic properties of low-coordinate transition metal complexes, some of which is detailed in this thesis.

1.9 References and notes

(1) (a) Leuenberger, M. N.; Loss, D. *Nature* **2001**, *410*, 789. (b) Gatteschi, D.; Sessoli, R.; Villain, J. *Molecular Nanomagnets*; Oxford University Press, Oxford, 2006.

(2) Mannini, M.; Pineider, F.; Sainctavit, P.; Danieli, C.; Otero, E.; Sciancalepore, C.; Talarico, A. M.; Arrio, M.-A.; Cornia, A.; Gatteschi, D.; Sessoli, R. *Nat. Mater.* **2009**, *8*, 194.

(3) (a) Lis, T. *Acta Crystallogr., Sect. B: Struct. Sci* **1980**, *36*, 2042. (b) Sessoli, R.; Hui, L.; Schake, A. R.; Wang, S.; Vincent, J. B.; Folting, J.; Gatteschi, D.; Christou, G.; Hendrickson, D. N. *J. Am. Chem. Soc.* **1993**, *115*, 1804. (c) Sessoli, R.; Gatteschi, D.; Caneschi, A.; Novak, M. A. *Nature* **1993**, *365*, 141.

(4) Chakov, N. E.; Lee, S.-C.; Harter, A. G.; Kuhns, P. L.; Reyes, A. P.; Hill, S. O.; Dalal, N. S.; Wernsdorfer, W.; Abboud, K. A.; Christou, G. *J. Am. Chem. Soc.* **2006**, *128*, 6975.

(5) Milios, C. J.; Vinslava, A.; Wernsdorfer, W.; Moggach, S.; Parsons, S.; Perlepes, S. P.; Christou, G.; Brechin, E. K. *J. Am. Chem. Soc.* **2007**, *129*, 2754.

(6) (a) Neese, F.; Solomon, E. I. *Inorg. Chem.* **1998**, *37*, 6568. (b) Waldmann, O. *Inorg. Chem.* **2007**, *46*, 10035. (b) Ruiz, E.; Cirera, J.; Cano, J.; Alvarez, S.; Loose, C.; Kortus, J. *Chem. Commun.* **2008**, *1*, 52. (d) Cirera, J.; Ruiz, E.; Alvarez, S.; Neese, F.; Kortus, J. *Chem. Eur. J.* **2009**, *15*, 4078. (e) Neese, F.; Pantazis, D. A. *Farad. Discuss.* 2011, *148*, 229.

(7) Hill, S.; Datta, S.; Liu, J.; Inglis, R.; Milios, C. J.; Feng, P. L.; Henderson, J. J.; del Barco, E.; Brechin, E. K.; Hendrickson, D. N. *Dalton Trans.* **2010**, *39*, 4693.

(8) Ako, A. M.; Hewitt, I. J.; Mereacre, V.; Clérac, R.; Werndorfer, W.; Anson, C. E.; Powell, A. K. *Angew. Chem. Int. Ed.* **2006**, *45*, 4926.

(9) Lippard, S. J.; Berg, J. M. *Principles of Bioinorganic Chemistry*; University Science Books, Mill Valley, 1994.

(10) Drago, R. S. *Physical Methods For Chemists*; Surfside Scientific Publishers, Gainesville, 1992.

(11) Nakano, M.; Oshio, H. *Chem. Soc. Rev.* **2011**, *40*, 3239.

(12) (a) Long, J. R. Molecular Cluster Magnets. In *Chemistry of Nanostructured* Materials; Yang, P., Ed.; World Scientific: Hong Kong, 2003; pp 291-315 and references therein. (b) Beltran, L. M. C.; Long, J. R. *Acc. Chem. Res.* **2005**, *38,* 325. (c) Shatruk, M.; Avendano, C.; Dunbar, K. In *Progress in Inorganic Chemistry*; Karlin, K. D., Ed.; John Wiley & Sons: Amsterdam, 2009, Vol *56*, p 155 and references therein.

(13) Palii, A.; Tsukerblat, B.; Klokishner, S.; Dunbar, K. R.; Clemente-Juan, J. M.; Coronado, E. *Chem. Soc. Rev.* **2011**, *40*, 3130.

(14) D = –120 to –190 cm^{-1} for [(Me_6tren)NiCl](ClO_4) (Me_6tren = tris((*N*,*N*-dimethylamino)ethyl)amine: Ruamps, R.; Maurice, R.; Batchelor, L.; Boggio-Pasqua, M.;

Guillot, R.; Barra, A. L.; Liu, J.; Bendeif, E.-E.; Pillet, S.; Hill, S.; Mallah, T.; Guihéry N. *J. Am. Chem. Soc.* **2013**, *135*, 3017. (b) $D = -70$ cm^{-1} for $(Ph_4P)_2[Co(SPh)_4]$: see ref 22. (c) $|D| = 76$ cm^{-1}, $[(^{H}L)_2Fe_6(NCMe)_6](PF_6)_3$: Zhao, Q.; Harris, T. D.; Betley, T. A. *J. Am. Chem. Soc.* **2011**, *133*, 8293. (d) $D = 70$ cm^{-1}, mixed-valence di-ruthenium tetracarboxylate complexes: see for example: Telser, J.; Drago, R. S. *Inorg. Chem.* **1984**, *23*, 3114.

(15) Kahn, O. *Molecular Magnetism*; John Wiley & Sons, New York,1993.

(16) (a) Ishikawa, N.; Sugita, M.; Ishikiawa, T.; Koshihara, S.-Y.; Kaizu, S. *J. Am. Chem. Soc.* **2003**, *125*, 8694. (b) Ishikawa, N.; Sugita, M.; Ishikawa, T.; Koshihara, S.; Kaizu, S. *J. Phys. Chem. B* **2004**, *108*, 11265.

(17) (a) Jiang, S.-D.; Wang, B.-W. Wang, Sun, H.-L.; Wang, Z.-M.; Gao, S. *J. Am. Chem. Soc.* **2011**, *133*, 4730. (b) Rinehart, J. D.; Fang, M.; Evans, W. J.; Long, J. R. *Nat. Chem.* **2011**, *3*, 538. (c) Rinehart, J. D.; Fang, M.; Evan, W. J.; Long, J. R. *J. Am. Chem. Soc.* **2011**, *133*, 14236.

(18) (a) Freedman, D. E.; Harman, W. H.; Harris, T. D.; Long, G. J.; Chang, C. J.; Long, J. R. *J. Am. Chem. Soc.* **2010**, *132*, 1224. (b) Harman, W. H.; Harris, T. D.; Freedman, D. E.; Fong, H.; Chang, A.; Rinehart, J. D.; Ozarowski, A.; Sougrati, M. T.; Grandjean, F.; Long, G. J.; Long, J. R.; Chang, C. J. *J. Am. Chem. Soc.* **2010**, *132*, 18115.

(19) Weissmann, D.; Sun, Y.; Lan, Y.; Wolmerhauser, G.; Powell, A. K.; Sitzmann, H. *Chem.-Eur. J.* **2011**, *17*, 4700.

(20) Lin, P.-H.; Smythe, N. C.; Gorelsky, S. L.; Maguire, S.; Henson, N. J.; Korobkov, I.; Scott, B. L.; Gordon, J. C.; Baker, R. T.; Murugesu, M. *J. Am. Chem. Soc.* **2011**, *133*, 15806.

(21) Gatteschi, D.; Sessoli, R. *Angew. Chem. Int. Ed.* **2003**, *42*, 268.

(22) Kahn, O. *Molecular Magnetism*; John Wiley & Sons, New York,1993.

(23) Jurca, T.; Farghal, A.; Lin, P.-H.; Korobkov, I.; Murugesu, M.; Richeson, D. S. *J. Am. Chem. Soc.* **2011**, *133*, 15814.

(24) (a) Vallejo, J.; Castro, I.; Ruiz-Garcia, R.; Cano, J.; Julve, M.; Lloret, F.; De Munno, G.; Wernsdorfer, W.; Pardo, E. *J. Am. Chem. Soc.* **2012**, *134*, 15704. (b) Feng, X.; Liu, J.; Harris, T. D.; Hill, S.; Long, J. R. *J. Am. Chem. Soc.* **2012**, *134*, 7521.

(25) (a) Fukui, K.; Ohya-Nishiguchi, H.; Hirota, N. *Bull. Chem. Soc. Jpn.* **1991**, *64*, 1205. (b) Fukui, K.; Kojima, N.; Ohya-Nishiguchi, H.; Hirota, N. *Inorg. Chem.* **1992**, *31*, 1338. (c) Fukui, K.; Masuda, H.; Ohya-Nishiguchi, H.; Kamada, H. *Inorg. Chim. Acta* **1995**, *238*, 73.

(26) Mossin, S.; Tran, B. L.; Adhikari, D.; Pink, M.; Heinemann, F. W.; Sutter, J.; Szilagyi, R.; Meyer, K.; Mindiola, D. J. *J. Am. Chem. Soc.* **2012**, *134*, 13651.

(27) Zhu, Y.-Y.; Cui, C.; Zhang, Y.-Q.; Jia, J.-H.; Guo, X.; Gao, C.; Qian, K.; Jiang, S.-D. Wang, B.-W.; Wang, Z.-M.; Gao, S. *Chem. Sci.* **2013**, *4*, 1802.

Chapter 2: Slow Magnetic Relaxation and Charge-Transfer in Cyano-Bridged Coordination Clusters Incorporating $[Re(CN)_7]^{3-/4-}$

2.1. Introduction

In the early 1990s, the molecular cluster $Mn_{12}O_{12}(O_2CCH_3)_{16}(H_2O)_4$ was shown to display slow magnetic relaxation at low temperatures, similar to the behavior of a superparamagnet below its blocking temperature.[1] As discussed in the previous chapter, such complexes, known as single-molecule magnets, could ultimately utilize their magnetic bistability for potential applications in high-density information storage or quantum computing.[2]

One method for synthesizing new single-molecule magnets centers on the use of a building-block approach to target high-nuclearity clusters where the metal ions are linked by cyanide bridging ligands.[3,4] This method exploits the predictable coordination chemistry of the cyanide ion, where one cyanide ligand is expected to bridge only two metals in an approximate linear geometry. Typical cluster preparation involves two building units, where one unit features one or more terminal cyanide ligands and the other unit bears one or more coordination sites occupied by labile solvent molecules. In solution, the nucleophilic nitrogen ends of the terminal cyanide ligands displace these solvent molecules, thereby leading to a multinuclear assembly. By judicious selection of polydentate capping ligands for either of the two building units, one can direct the formation of a variety of molecular structures. In addition to this structural control, qualitative rules for predicting the nature of the magnetic superexchange coupling between two cyano-bridged metal centers are well established via exhaustive studies on Prussian Blue analogues.[5] This combination of structural and magnetic predictability has led to the rational design of a wide variety of cyano-bridged magnetic molecules.[3,4]

In 2003, the homoleptic cyanometalate complex $[Re(CN)_7]^{3-}$ was prepared and shown to exhibit strong magnetic anisotropy.[6] This anisotropy can be attributed to a combination of the unquenched orbital angular momentum afforded by the $^2E_1''$ electronic ground state and the large spin-orbit coupling associated with the heavy rhenium atom.[7] Freedman and coworkers thus hypothesized that incorporating $[Re(CN)_7]^{3-}$ into a high-spin cluster would impart magnetic anisotropy to the magnetic moment of the assembly, thereby leading to slow magnetic relaxation. Indeed, the pentanuclear cyano-bridged cluster $[(PY5Me_2)_4Mn_4Re(CN)_7]^{5+}$ ($PY5Me_2$ = 2,6-bis(1,1-bis(2-pyridyl)ethyl)pyridine)) was prepared and shown to exhibit the highest relaxation barrier (U_{eff} = 33 cm^{-1}) yet observed for a cyano-bridged single-molecule magnet.[8] One considerable drawback to the preparation of this cluster, however, is that it requires low-temperature conditions, as the 4+ oxidation state of the rhenium ion becomes destabilized upon cluster formation. Indeed, upon warming to room temperature, the paramagnetic Re^{IV} ion undergoes a spontaneous, solvent-assisted, one-electron reduction to the diamagnetic Re^{III} ion. This thermal instability has precluded significant study of the Mn_4Re cluster, owing to preparative and handling difficulties.

Electrochemical investigations of Prussian Blue analogues have shown that the reduction potential of ferricyanide is shifted toward a more positive potential as other metals are appended to it, a consequence of polarization effects by M′.[9] Furthermore, these studies have revealed that this general effect becomes more pronounced as the charge/radius ratio of the M′ ion increases.

In view of this trend, I sought to substitute more electron-rich metal ions (Co^{II}, Ni^{II}, Cu^{II}) in place of Mn^{II} in the synthesis of clusters of formulae $[(PY5Me_2)_4M_4Re(CN)_7]^{5+}$ with the expectation that such a substitution would stabilize the Re^{IV} ion toward reduction.

The selection of Co^{II}, Ni^{II}, and Cu^{II} for incorporation into the M_4Re clusters was not driven simply due their electron density relative to Mn^{II}. For instance, the unquenched orbital angular momentum present in octahedrally-coordinated Co^{II} ion should enhance the anisotropy of the overall cluster. Furthermore, the unpaired electron of Re^{IV} in $[Re(CN)_7]^{3-}$ lies in an orbital of π-type symmetry.[7] Exchange coupling with high-spin Mn^{II} is therefore expected to be weak due to competing ferromagnetic and antiferromagnetic contributions from electrons residing in d_σ and d_π-type orbitals of the Mn^{II} ion.[10] Indeed, fits to the magnetic susceptibility data obtained for the Mn_4Re cluster reveal a coupling constant of only J = 2.3 cm^{-1}. In contrast, the octahedral coordination geometry of a $[(PY5Me_2)M(NC)]^{2+}$ fragment should promote strictly ferromagnetic Re•••M exchange for Ni^{II} and Cu^{II} ions, which both bear unpaired electrons in only σ-type orbitals. In fact, a recent report has demonstrated very strong ferromagnetic coupling between Re^{IV} and Cu^{II} ions through a cyanide ligand.[11] Herein, are reported the syntheses of the building units $[(PY5Me_2)M(MeCN)](PF_6)_2$ (M = Co (**4**), Ni (**5**), Cu (**6**)) and their subsequent incorporation into the cyano-bridged cluster compounds $[(PY5Me_2)M_4Re(CN)_7](PF_6)_5$ (M = Co (**7**), Ni (**8**), Cu (**10**)) and $[(PY5Me_2)_4Cu_4Re(CN)_7](PF_6)_4$ (**9**). Notably, the use of **5** enables preparation of the Ni_4Re cluster, where the Re^{IV} ion is stable toward reduction. In contrast, **9** is thermally unstable, and preparation at room temperature triggers a reduction of the Re^{IV} ion. Moreover, slow magnetic relaxation is observed for clusters **8** and **10**, where the Re ion remains in the 4+ oxidation state. Finally, an intramolecular charge-transfer occurs during the synthesis of **7**, yielding a $Co^{II}_3Co^{III}Re^{III}$ cluster.

2.2. Experimental

Preparation of Compounds. Unless otherwise noted, all procedures were performed under an inert N_2 atmosphere using standard glove box techniques. The ligand 2,6-bis(1,1-bis(2-pyridyl)ethyl)pyridine ($PY5Me_2$)[12] and the compound $(Bu_4N)_3[Re(CN)_7]$[6] were synthesized as previously described. Acetonitrile (MeCN), diethylether (Et_2O), and tetrahydrofuran (THF) were dried by circulation over alumina for 16 h prior to use, and were then deoxygenated by sparging with N_2 for at least 1 h. Propionitrile (EtCN) and diisopropylether (*i*-Pr_2O) were distilled over CaH_2 and degassed prior to use. Diatomaceous earth (Celite® 545) was purchased from Fisher Scientific and dried by heating under vacuum. All other reagents were obtained from commercial vendors and used without further purification.

$[(PY5Me_2)CoI]I$ (1). Solid $PY5Me_2$ (1.0 g, 2.3 mmol) and CoI_2 (0.72 g, 2.3 mmol) were added to 100 mL of THF and stirred for 48 h, giving a yellow solid. The precipitate was collected on a fine fritted glass filter, washed with successive aliquots of THF (2 × 30 mL) and Et_2O (2 × 30 mL), and dried *in vacuo* for 2 h to give 1.6 g (96%) of product. IR (neat): 1594(s), 1477(m), 1464(s), 1450(m), 1435(s), 1294(m), 1253(w), 1230(w), 1201(w), 1066(w), 1078(w), 1061(m), 1015(m), 865(m), 792(m), 751(s) cm^{-1}. ESI-MS (m/z): $\{[(PY5Me_2)CoI]\}^+$, 629.1. UV-vis (MeCN): λ_{max} (ε_M, $M^{-1}cm^{-1}$) 366 (110), 500 (9), 900 (11) nm. Anal. Calcd. for $C_{29}H_{25}CoI_2N_5$: C, 46.05; H, 3.33; N, 9.26 %. Found: C, 45.89; H, 3.54; N, 9.65 %.

$[(PY5Me_2)NiI]I$ (2). Solid $PY5Me_2$ (1.1 g, 2.4 mmol) and NiI_2 (0.77 g, 2.5 mmol) were added to 100 mL of THF and stirred for 48 h, giving a gray solid. The precipitate was collected

on a fine fritted glass filter, washed with successive aliquots of THF (2 × 30 mL) and Et_2O (2 × 30 mL), and dried *in vacuo* for 2 h to give 1.5 g (83%) of product. IR (neat): 1595(s), 1478(m), 1464(s), 1452(m), 1437(s), 1386(m), 1295(m), 1166(w), 1063(m), 1017(m), 863(m), 791(m), 766(m), 752(s) cm^{-1}. ESI-MS (m/z): $\{[(PY5Me_2)Ni]\}^{2+}$, 251.0; $\{[(PY5Me_2)NiI]\}^{+}$, 628.0. UV-vis (MeCN): λ_{max} (ε_M, $M^{-1}cm^{-1}$) 320 (1197), 430 (37), 524 (18), 802 (17), 877 (15) nm. Anal. Calcd. for $C_{29}H_{25}I_2N_5Ni$: C, 46.07; H, 3.33; N, 9.27 %. Found: C, 46.38; H, 3.51; N, 8.93 %.

$[(PY5Me_2)CuCl]Cl$ (3). Solid $CuCl_2$ (0.15 g, 1.1 mmol) and $PY5Me_2$ (0.49 g, 1.1 mmol) were added to 20 mL of THF and stirred for 48 h, giving a blue solid. The precipitate was collected on a fine fritted glass filter, washed with successive aliquots of THF (2 × 30 mL) and Et_2O (2 × 30 mL), and dried *in vacuo* for 2 h to give 0.59 g (93%) of product. IR (neat): 1598(s), 1588(s), 1580(s), 1471(s), 1463(s), 1456(s), 1438(s), 1424(s), 1370(m), 1296(m), 1223(w), 1202(w), 1173(m), 1153(m), 1104(m), 1068(m), 1057(m), 1029(m), 1011(m), 993(m), 869(m), 842(m), 779(s), 755(s), 749(s), 655(m) cm^{-1}. ESI-MS (m/z): $\{[(PY5Me_2)CuCl]\}^{+}$, 541; $\{[(PY5Me_2)Cu]\}^{2+}$, 253. UV-vis (MeCN): λ_{max} (ε_M, $M^{-1}cm^{-1}$) 468 (18), 616 (74), 950 (11) nm. Anal. Calcd. for $C_{29}H_{25}Cl_2CuN_5$: C, 60.26; H, 4.36; N, 12.12 %. Found: C, 59.92; H, 4.54; N, 11.83 %.

$[(PY5Me_2)Co(MeCN)](PF_6)_2$ (4). Solid $TlPF_6$ (0.29 g, 0.83 mmol) was added to a solution containing **1** (0.29 g, 0.39 mmol) in 9 mL of MeCN, resulting in an orange solution and a yellow precipitate. After stirring for 48 h, the orange mixture was filtered through diatomaceous earth to remove the yellow solid. Vapor diffusion of Et_2O into the orange filtrate gave 0.22 g (69%) of product as orange, block-shaped crystals suitable for X-ray analysis. IR (neat): 2302(m), 2275(m), 1599(s), 1591(s), 1484(m), 1470(s), 1457(m), 1441(m), 1110(w), 1063(m), 1022(m), 828(vs), 758(s), 635(m) cm^{-1}. ESI-MS (m/z): $\{[(PY5Me_2)Co]\}^{2+}$, 249.1; $\{[(PY5Me_2)Co](PF_6)\}^{+}$, 643.1; $\{[(PY5Me_2)Co(MeCN)](PF_6)\}^{+}$, 685.1. UV-vis (MeCN): λ_{max} (ε_M, $M^{-1}cm^{-1}$) 257 (43100), 308 (sh) (4300), 450 (48) nm. Anal. Calcd. for $C_{31}H_{28}CoF_{12}N_6P_2$: C, 44.67; H, 3.39 ; N, 10.09 %. Found: C, 44.52; H, 3.36; N, 10.02 %.

$[(PY5Me_2)Ni(MeCN)](PF_6)_2$ (5). Solid $TlPF_6$ (0.38 g, 1.1 mmol) was added to a solution containing **2** (0.40 g, 0.53 mmol) in 14 mL of MeCN, resulting in an orange solution and yellow precipitate. After stirring for 48 h, the orange mixture was filtered through diatomaceous earth to remove the yellow solid. Vapor diffusion of Et_2O into the orange filtrate gave 0.30 g (65%) of product as pink, block-shaped crystals suitable for X-ray analysis. IR (neat): 2273(w), 1596(s), 1484(m), 1469(s), 1457(m), 1441(m), 1064(m), 1021(m), 881(m), 827(vs), 795(m), 757(s), 652(m), 629(m) cm^{-1}. ESI-MS (m/z): $\{[(PY5Me_2)Ni]\}^{2+}$, 250.6. UV-vis (MeCN): λ_{max} (ε_M, $M^{-1}cm^{-1}$) 307 (1350), 432 (4), 529 (8), 863 (17), 794 (18) nm. Anal. Calcd. for $C_{31}H_{28}F_{12}N_6NiP_2$: C, 44.69; H, 3.39; N, 10.09 %. Found: C, 44.38; H, 3.24; N, 10.13 %.

$[(PY5Me_2)Cu(MeCN)](PF_6)_2$ (6). Solid $TlPF_6$ (0.27 g, 0.77 mmol) was added to a solution containing **3** (0.21 g, 0.36 mmol) in 16 mL of MeCN, resulting in a blue solution and a white precipitate. After stirring for 48 h, the blue mixture was filtered through diatomaceous earth to remove the white solid. Vapor diffusion of Et_2O into the blue filtrate gave 0.22 g (70%) of product as blue, block-shaped crystals suitable for X-ray analysis. IR (neat): 2312(w), 2284(w), 1596(s), 1586(s), 1468(s), 1456(s), 1441(m), 1398(m), 1303(w), 1064(m), 1018(m), 828(vs), 792(m), 775(m), 758(s) cm^{-1}. ESI-MS (m/z): $\{[(PY5Me_2)Cu](PF_6)\}^{+}$, 652; $\{[(PY5Me_2)Cu]\}^{2+}$, 254. UV-vis (MeCN): λ_{max} (ε_M, $M^{-1}cm^{-1}$) 605 (75), 928 (13) nm. Anal. Calcd. for $C_{31}H_{28}CuF_{12}N_6P_2$: C, 44.43; H, 3.37; N, 10.03 %. Found: C, 44.26; H, 3.30; N, 9.89 %.

$[(PY5Me_2)_4Co_4Re(CN)_7](PF_6)_5$ (7). A solution containing $(Bu_4N)_3[Re(CN)_7]$ (21 mg, 0.019 mmol) in 3 mL of MeCN was added to a solution containing **4** (63 mg, 0.075 mmol) in 3 mL of

MeCN to give a purple solution. Vapor diffusion of Et_2O into this solution afforded 45 mg (77%) of product as red, plate-shaped crystals suitable for X-ray analysis. IR (neat): 2102(s), 2056(s), 1640(w), 1594(s), 1480(w), 1467(s), 1440(m), 1393(m), 1253(w), 1170(w), 1058(w), 1019(w), 830(vs), 757(s) cm^{-1}. ESI-MS (m/z): $\{[(PY5Me_2)_4Co_4Re(CN)_7](PF_6)_3\}^{2+}$, 1406; $\{[(PY5Me_2)_3Co_3Re(CN)_7]\}^{3+}$, 625 (base peak); $\{[(PY5Me_2)_3Co_3Re(CN)_7](PF_6)\}^{2+}$, 1009.5; $\{[(PY5Me_2)_3Co_3Re(CN)_7](PF_6)_2\}^{+}$, 2164; $\{[(PY5Me_2)_3Co_3Re(CN)_7]\}^{2+}$, 937; $\{[(PY5Me_2)_2Co_2Re(CN)_7]\}^{+}$, 1372; $\{[(PY5Me_2)_2Co_2Re(CN)_7]\}^{2+}$, 686; $\{[(PY5Me_2)_2Co_2Re(CN)_7](PF_6)\}^{+}$, 1517. UV-vis (MeCN): λ_{max} (ε_M, $M^{-1}cm^{-1}$) 510 (1680), 854 (1600) nm. Anal. Calcd. for $C_{123}H_{100}Co_4F_{30}N_{27}P_5Re$: C, 47.61; H, 3.25; N, 12.19 %. Found: C, 47.27; H, 3.36; N, 12.49 %.

$[(PY5Me_2)_4Ni_4Re(CN)_7](PF_6)_5$ (8). A solution containing $(Bu_4N)_3[Re(CN)_7]$ (16 mg, 0.015 mmol) in 1 mL of MeCN was added to a solution containing **5** (50 mg, 0.06 mmol) in 2 mL of MeCN to give a dark yellow-brown solution. Vapor diffusion of Et_2O into this solution afforded 18 mg (40%) of product as dark yellow, needle-shaped crystals suitable for X-ray analysis. IR (neat): 2120(w), 2089(w), 1596(s), 1480(m), 1468(m), 1454(m), 1441(m), 1390(w), 1169(w), 1111(w), 1062(m), 1021(m), 834(s), 792(m), 757(s) cm^{-1}. ESI-MS (m/z): $\{[(PY5Me_2)_4Ni_4Re(CN)_7](PF_6)_3\}^{2+}$, 1406; $\{[(PY5Me_2)_4Ni_4Re(CN)_7](PF_6)_2\}^{3+}$, 888; $\{[(PY5Me_2)_3Ni_3Re(CN)_7](PF_6)\}^{2+}$, 1008; $\{[(PY5Me_2)_3Ni_3Re(CN)_7]\}^{3+}$, 623 (base peak). Anal. Calcd. for $C_{123}H_{100}F_{30}N_{27}Ni_4P_5Re$: C, 47.62; H, 3.24; N, 12.19 %. Found; C, 47.39; H, 3.56; N, 12.11 %.

$[(PY5Me_2)_4Cu_4Re(CN)_7](PF_6)_4$ (9). A solution containing $(Bu_4N)_3[Re(CN)_7]$ (17 mg, 0.016 mmol) in 1 mL of EtCN was added to a solution containing **6** (53 mg, 0.063 mmol) in 3 mL of EtCN to give a dark blue solution, which was stirred for 48 h. Vapor diffusion of *i*-Pr_2O into this solution produced 40 mg (87%) of product as dark blue, plate-shaped crystals suitable for X-ray analysis. IR (neat): 2287(w), 2256(w), 1587(m), 1467(m), 1456(m), 1441(m), 1397(w), 1303(w), 1202(w), 1172(w), 1092(w), 1062(w), 1018(w), 993(w), 907(w), 832(s), 788(m), 773(m), 758(m), 655(m), 632(m), 618(m), 606(m), 581(m), 572(m), 556(s), 538(w) cm^{-1}. ESI-MS (m/z): $\{[(PY5Me_2)_4Cu_4Re(CN)_7](PF_6)_2\}^{2+}$, 1343; $\{[(PY5Me_2)_4Cu_4Re(CN)_7](PF_6)\}^{3+}$, 847; $\{[(PY5Me_2)_4Cu_4Re(CN)_7]\}^{4+}$, 599; $\{[(PY5Me_2)_3Cu_3Re(CN)_7](PF_6)]\}^{2+}$, 1017; $\{[(PY5Me_2)_3Cu_3Re(CN)_7]\}^{3+}$, 630. Anal. Calcd. for $C_{123}H_{100}Cu_4F_{24}N_{27}P_4Re{\cdot}EtCN$: C, 48.73; H, 3.33; N, 12.47 %. Found: C, 48.48; H, 3.10; N, 12.14 %.

$[(PY5Me_2)_4Cu_4Re(CN)_7](PF_6)_5$ (10). A solution containing $(Bu_4N)_3[Re(CN)_7]$ (21 mg, 0.019 mmol) in 1 mL of MeCN and a solution containing **6** (63 mg, 0.075 mmol) in 2 mL of MeCN were chilled to –42 °C. The solution containing $(Bu_4N)_3[Re(CN)_7]$ was then added dropwise to the other stirred solution to give a dark green solution. The solvent was removed *in vacuo* to afford the product as an impure dark green solid mixed with $(Bu_4N)PF_6$. All analyses were performed on this mixture. IR (neat): n_{CN} = 2294(w), 2252(w), 2163(w), 2126(w), 2066(w) cm^{-1}. ESI-MS (m/z): $\{[(PY5Me_2)_4Cu_4Re(CN)_7](PF_6)_3\}^{2+}$, 1415.5; $\{[(PY5Me_2)_4Cu_4Re(CN)_7](PF_6)_2\}^{2+}$, 1343; $\{[(PY5Me_2)_4Cu_4Re(CN)_7](PF_6)\}^{3+}$, 847; $\{[(PY5Me_2)_4Cu_4Re(CN)_7]\}^{4+}$, 599; $\{[(PY5Me_2)_3Cu_3Re(CN)_7](PF_6)\}^{2+}$, 1017; $\{[(PY5Me_2)_3Cu_3Re(CN)_7]\}^{3+}$, 630; $\{[(PY5Me_2)_3Cu_3Re(CN)_7]\}^{2+}$, 944. Anal. Calcd. For $C_{123}H_{100}Cu_4F_{30}N_{27}P_5Re{\cdot}3(Bu_4N)PF_6$: C,47.94; H, 4.89; N, 9.81 %. Found: C, 47.65; H, 4.85; N, 9.89 %.

X-ray Structure Determinations. Structures were determined for compounds **4**, **5**, **6**, **7**, **8**, and **9**. X-ray diffraction analyses were performed on single crystals coated with Paratone-N oil and mounted on Kaptan loops. The crystals were frozen under a stream of N_2 during measurements. Data were collected using either a Bruker X8 APEX diffractometer equipped with a Bruker MICROSTAR X-ray source, APEX-II detector and a Cu anode (λ = 1.5406 Å) (**8**)

or a Bruker SMART diffractometer equipped with an APEX detector using MoKα (λ = 0.71073 Å) radiation (**4**, **5**, **6**, **7**, **9**). Raw data were integrated and corrected for Lorentz and polarization effects using Bruker APEX2 v. 2009.1.[13] Absorption corrections were applied using SADABS.[14] Space group assignments were determined by examination of systematic absences, E-statistics, and successive refinement of the structures. Crystal structures were solved by either direct methods (**4**, **5**, **6**, **8**, **9**) or Patterson techniques (**7**) with the aid of successive difference Fourier maps in SHELXL.[15] None of the crystals showed significant decay during data collection. Thermal parameters were refined anisotropically for all non-hydrogen atoms in the main body and PF_6^- counterions of **4**, **5**, **6**, **8**, and **9**. The quality of the collected data for **7** was not sufficient to justify an anisotropic refinement of the thermal parameters for all atoms, and as such anisotropic refinement was restricted to the metal, phosphorus, and fluorine atoms with full occupancy. Hydrogen atoms were placed in ideal positions and refined using a riding model for all structures. Heavy disorder of PF_6^- anions and solvents of crystallization were modeled with the use of free variables. Solvent disorder was extensive and in some cases impossible to model for the structures of **7**, **8**, and **9**. Note that attempts to model the disorder did not significantly alter the metrics for the clusters. For these structures, SQUEEZE[16] was used to account for the unassigned electron density. Refinement data is listed in Table 2.S1, and full crystal tables can be found in Appendix 1.

Magnetic and Photomagnetic Measurements. Magnetic data were collected using a Quantum Design MPMS-XL or PPMS magnetometer. Measurements for **4**-**9** were obtained on finely ground microcrystalline powders restrained in a frozen eicosane matrix within polycarbonate capsules. Dc magnetic susceptibility data were collected in the temperature range 2-300 K under an applied field of 1000 Oe. Ac susceptibility data were collected under zero applied dc field using a 4 Oe ac field oscillating at frequencies from 10 to 1488 Hz. Dc magnetization data were collected in the temperature range 1.8-10 K at fields from 1 to 15 T (**8**) or from 1 to 7 T (**10**). All data were corrected for diamagnetic contributions from the sample holder and eicosane, as well as for core diamagnetism (estimated using Pascal's constants).

A chilled sample of the reaction mixture containing **10** was isolated for measurement *in vacuo* and restrained in a frozen Et_2O matrix. Due to its thermal instability, the sample could not be completely separated from the diamagnetic side product $(Bu_4N)PF_6$. During the course of the measurements, the sample cavity of the magnetometer was not heated above 230 K in order to maintain the highest concentration of **10** and to limit the amount of **9** formed as an impurity.

Photomagnetic experiments were performed with a 150 W halogen lamp (LEICA CLS 150X) and different LED sources coupled through an optical fiber directed into the SQUID magnetometer cavity. Powdered samples (2 to 3 mg) were packed in a thermoformed plastic straw maintained at about 3-4 mm from the optical fiber. Data acquired in the absence of light were systematically subtracted from the data acquired after irradiation. This difference was added to dc measurements performed with a standard SQUID set-up in order to get final post-irradiation data.

Electrochemical and Spectroelectrochemical Measurements. Cyclic voltammograms were obtained with a Bioanalytical systems CV-50W voltammograph, a platinum wire counter electrode, a silver wire reference electrode, and a glassy carbon working electrode. Analyte solutions were prepared with 0.1 M solutions of $(Bu_4N)PF_6$ in MeCN. Ferrocene was used as an internal standard and all potentials reported here are referenced to the $Cp_2Fe/[Cp_2Fe]^+$ couple. UV-Vis-NIR spectroelectrochemistry over the range of 5000-30,000 cm^{-1} was performed using a CARY 5000 spectrophotometer interfaced to Varian WinUV software. The absorption spectra of

the electrogenerated species were obtained *in situ* by the use of an Optically Semi-Transparent Thin-Layer Electrosynthetic (OSTLE) cell, of path length 1.0 mm, mounted in the path of the spectrophotometer. Solutions for the spectroelectrochemical experiment contained 0.1 M $(Bu_4N)PF_6$/MeCN supporting electrolyte and ca. 1 mM of the analyte. All solutions were prepared under a dinitrogen atmosphere in the glove box. Appropriate potentials were applied by using a Bioanalytical Systems (BAS) CV 50W voltammograph, and the current was carefully monitored throughout the electrolysis. By this method, the electrogenerated species (which are otherwise unstable) were obtained *in situ*, and their absorption spectra were recorded at regular intervals throughout the electrolysis. The attainment of a steady-state spectrum and the decay of the current to a constant minimum at a potential appropriately beyond $E_{1/2}$ (for the redox process in question) was indicative of the complete conversion of the starting material. The reversibility of the spectral data was confirmed by the regeneration of the starting spectrum.

Mass Spectrometry. Mass spectra were acquired in positive ion mode using a quadrupole time-of-flight (Q-Tof) mass spectrometer equipped with a Z-spray electrospray ionization (ESI) source (Q-Tof Premier, Waters, Milford, MA). Sample solutions were withdrawn from glass vials using a 250 mL Gastight® syringe (Hamilton, Reno, NV) and immediately infused into the ESI probe at a flow rate of 5 mL/min using a syringe pump. Charged droplets of the sample solution were emitted from a stainless steel capillary (inner diameter 127 mm) with a nitrogen nebulizing gas flow of 800 L/h. The instrument parameters were as follows: capillary voltage 1.0 kV, sample cone 10 V, extraction cone 3 V, ion guide 3 V, source block temperature 80 °C, desolvation (nebulizing) gas temperature 150 °C, accelerating voltage into the argon-filled cell 2 V, first pumping stage pressure 1.2 mbar, ion transfer stage pressure 6×10^{-4} mbar, quadrupole analyzer pressure 2×10^{-5} mbar, argon-filled cell pressure 8×10^{-3} mbar, Tof analyzer pressure 9×10^{-7} mbar. No cone gas flow was used. For each sample, the sample cone and extraction cone voltages were adjusted to optimize signal for the ion(s) of interest, and the ESI capillary voltage was adjusted to maintain ion counts below the dead-time threshold (< 0.1 ions per push) to prevent spectral distortion effects due to detector saturation. The Tof analyzer was operated in "W" mode. Under these conditions, a mass resolving power, R, of 1.5×10^4 was achieved, where $R = m/\Delta m_{50\%}$, m is the mass-to-charge ratio of an ion, and $\Delta m_{50\%}$ is the full width of the mass spectral peak at half-maximum height. This was sufficient to resolve the isotopic distributions of the singly and multiply charged ions measured in this study. Thus, an ion's mass and charge could be determined independently, i.e., an ion's charge state can be determined from the reciprocal of the spacing between adjacent isotope peaks in the m/z spectrum. External mass calibration was performed using solutions of sodium formate immediately prior to measuring samples. Mass spectra were processed using MassLynx software (version 4.1, Waters). In the case of **10**, reactants were mixed immediately prior to injection and the syringe was stored at –4 ºC until immediately before use. In this way, the metastable forms of the analytes were maintained for measurement.

Irradiation Measurements. The optical studies were performed with a home-built reflectivity system. Operating temperatures range from 4.2 to 300 K. The spectrometric range runs from 300 to 1070 nm. The optical measurement chain is very sensitive in order to minimize the irradiation employed for spectrometry. This allowed for the independent collection of (i) the spectrometric information (by a high sensitivity Hamamatsu 10083CA spectrometer) and (ii) the photoinduced changes in the compound. The light source for spectrometric measurements was a halogen-tungsten light source (Leica CLS 150 XD tungsten halogen source adjustable from 0.5 mW/cm^2 to 1 W/cm^2 or Ocean Optic DT-MINI-2-GS deuterium tungsten halogen lamp that

delivers power as low as 0.05 mW/cm^2). To induce spectrometric changes in the compound, high power irradiations (up to several mW/cm^2) have been used from a set of photodiodes (Nichia for UV, Lumileds Luxeon V for visible, Roithner for near IR). The measurements were calibrated using a NIST traceable standard for reflectance (sphereOptics, ref. SG3054).

Other Physical Measurements. UV-vis-NIR diffuse reflectance and solution spectra were collected using a CARY 5000 spectrophotometer interfaced with Varian WinUV software. Infrared spectra were obtained on a Perkin-Elmer Spectrum 100 Optica FTIR spectrometer furnished with an attenuated total reflectance accessory (ATR). Elemental (C, H, and N) analyses were performed at the Microanalytical Laboratory of the University of California, Berkeley.

2.3. Results and Discussion

2.3.1. PY5Me$_2$ Precursor Complexes. Syntheses of the $[(PY5Me_2)M]^{2+}$ building units were carried out through a two-step reaction sequence. First, addition of solid $PY5Me_2$ to a stirred THF solution containing MX_2 (for M = Co and Ni, X = I; for M = Cu, X = Cl) led to isolation of the compounds $[(PY5Me_2)MI]I$ (M = Co (**1**), Ni (**2**)) and $[(PY5Me_2)CuCl]Cl$ (**3**). Subsequent addition of $TlPF_6$ to **1** and **2** or $AgPF_6$ to **3** in MeCN resulted in abstraction of the coordinated halide, giving the compounds $[(PY5Me_2)M(MeCN)](PF_6)_2$ (M = Co (**4**), Ni (**5**), Cu (**6**)).

X-ray crystallographic analyses of single crystals of complexes **4** and **5** revealed an octahedral coordination environment for each M^{II} center, featuring five coordination sites blocked by a $PY5Me_2$ ligand and the other bound by an MeCN ligand (see Figure 2.S1 and Table 2.S2). The mean $M-N_{py}$ bond distances (2.13(1) Å for **4** and 2.09(2) Å for **5**) are similar to those observed in complexes featuring Co^{II} and Ni^{II} centers coordinated to pyridyl ligands.[17,18] The crystal structure of **6** exhibits an asymmetric unit consisting of two distinct $[(PY5Me_2)Cu]^{2+}$ molecules (see Figure 2.S1), where both units feature a square pyramidal coordination geometry for the Cu^{II} ion. In one molecule, the coordination environment of the Cu^{II} ion consists solely of a pentacoordinate $PY5Me_2$ ligand, with the nitrogen atom of a weakly associated MeCN molecule positioned 2.514(6) Å from the open face of the basal plane. The other molecule features a Cu^{II} ion bound by a κ^4-$PY5Me_2$ ligand in a seesaw coordination, where the unbound pyridyl ring is canted away from the Cu^{II} ion. The Cu^{II} center is bound by an MeCN ligand in the remaining basal position, with a Cu–N bond distance of 2.015(6) Å, to complete the square pyramid. Variable-temperature dc magnetic susceptibility measurements performed on polycrystalline samples of **4**, **5**, and **6** gave values at 300 K of $\chi_M T$ = 3.17, 1.17, and 0.39 cm^{3}K/mol, respectively (see Figure 2.S2), confirming the expected presence of $S = {}^3/_2$, 1, and ${}^1/_2$ spin ground states with g values of 2.60, 2.16, and 2.05, respectively. In all cases, the $\chi_M T$ vs. T plots show no significant temperature dependence until reaching low temperature, consistent with Curie behavior and thus magnetically isolated spin carriers. In the case of **4**, the decrease in $\chi_M T$ at low temperature is associated with spin-orbit coupling of the high-spin Co^{II} ion.

In order to probe the range of accessible oxidation states in the precursor complexes, cyclic voltammograms (CVs) were collected for $PY5Me_2$ and **4**-**6** dissolved in MeCN. Importantly, the CV obtained for uncoordinated $PY5Me_2$ shows the absence of any redox events in the potential range −2.0 to +1.8 V vs. $Cp_2Fe/[Cp_2Fe]^+$, suggesting that redox processes observed for **4**-**6** are likely metal-centered. Indeed, CVs obtained for **4**-**6** reveal reversible processes (see Figure 2.S3). Specifically, the CV of **4** shows two reversible waves with $E_{1/2}$ = 0.168 and –1.466 V vs. $Cp_2Fe/[Cp_2Fe]^+$, likely corresponding to the $Co^{II/III}$ and $Co^{I/II}$ couples, respectively. Similarly, two events are present in the CV of **5**, with $E_{1/2}$ = 1.320 and –1.610 V, assigned to the $Ni^{II/III}$ and

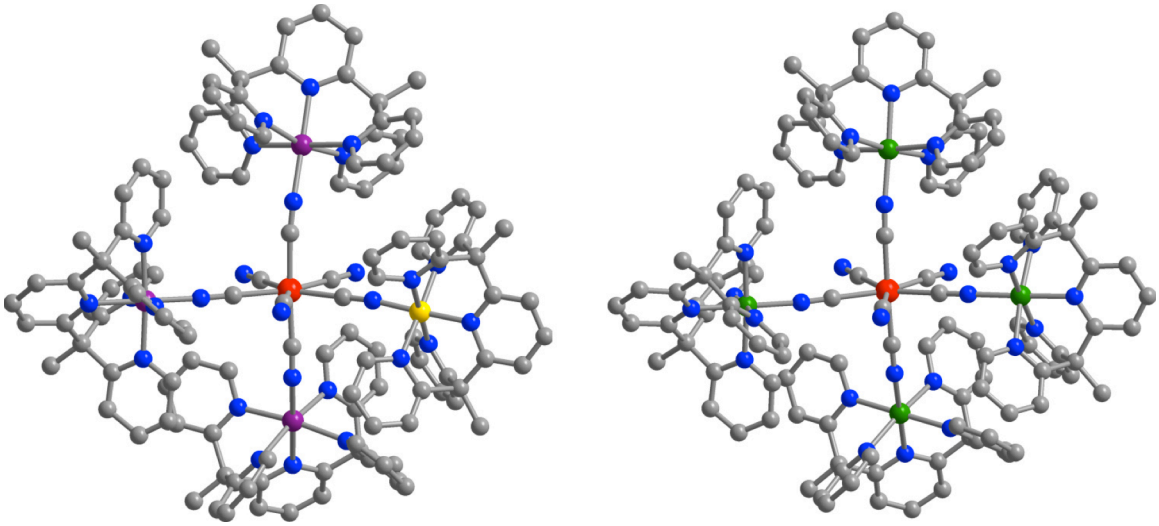


Figure 2.1. Left: Structure of $[(PY5Me_2)_4Co_4Re(CN)_7]^{5+}$ as observed in **7**. Red, yellow, purple, blue, and gray spheres represent Re, Co^{III}, Co^{II}, N, and C atoms/ion, respectively; hydrogen atoms are omitted for clarity. Right: Structure of $[(PY5Me_2)_4Ni_4Re(CN)_7]^{5+}$, as observed in **8**. Red, green, blue, and gray spheres represent Re, Ni, N, and C atoms, respectively; hydrogen atoms are omitted for clarity.

$Ni^{I/II}$ couples. In contrast, the CV of **6** displays a single quasireversible reduction at $E_{1/2} = -0.302$ V, likely corresponding to the $Cu^{I/II}$ redox couple.

2.3.2. Syntheses and Structures of the M_4Re Clusters. The pentanuclear cyano-bridged cluster compounds $[(PY5Me_2)_4M_4Re(CN)_7](PF_6)_5$ (M = Co (**7**), Ni (**8**), Cu (**10**)) and $[(PY5Me_2)_4Cu_4Re(CN)_7](PF_6)_4$ (**9**) were synthesized through the simple addition of a solution containing $[Re(CN)_7]^{3-}$ to a solution containing the appropriate precursor (**4**, **5**, or **6**). Notably, carrying out the reaction between $[Re(CN)_7]^{3-}$ and **6** at 25 °C produces a blue solution containing **9**, while performing the reaction at −42 °C gives a dark green solution containing **10**. Furthermore, within minutes upon standing at ambient temperature, the dark green solution undergoes a rapid color change to blue, associated with the spontaneous one-electron reduction of **10** to **9**. X-ray analyses on single crystals of **7**-**9** revealed the presence of a four-point star-like topology for each cluster, as depicted in Figures 2.1 and 2.2. In **7** and **8**, a $[Re(CN)_7]^{3-/4-}$ unit occupies the center of the star and is bridged through cyanide ligands to four pendant $[(PY5Me_2)M]^{2+/3+}$ units. The coordination environment of the $Re^{III/IV}$ ion approximates a pentagonal bipyramid and does not deviate significantly from that observed in $(Bu_4N)_3[Re(CN)_7]$[6] and $[(PY5Me_2)_4Mn_4Re(CN)_7]^{4+/5+}$ [8]. In contrast, the $[Re(CN)_7]^{4-}$ unit in **9** features $C_{eq}-M-C_{eq}$ angles ranging from 70.9(2)° to 74.7(2)°, representing significant distortions from the 72° angle expected for an idealized pentagonal bipyramid (see Figure 2.2). Additionally, the equatorial cyanide ligands are buckled out of the idealized pentagonal plane, as evidenced by $C_{ax}-Re-C_{eq}$ angles of a single pentagonal pyramid ranging from 82.2(2)° to 98.9(2)°. The axial cyanide ligands lie close to along the five-fold axis, with a $C_{ax}-Re-C_{ax}$ angle of 177.8(2)°.

In the structures of compounds **7**, **8**, and **9**, the coordination environments of the M^{II} ions differ considerably. In **7**, three of the cobalt ions feature a mean $Co-N_{py}$ distance of 2.13(3) Å,

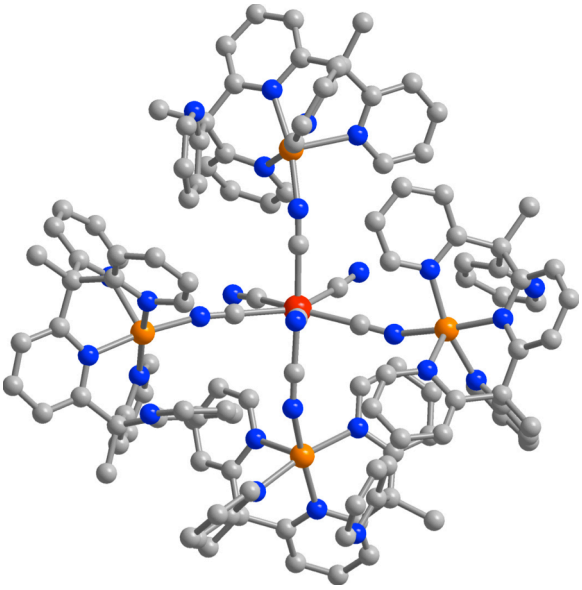


Figure 2.2. Structure of $[(PY5Me_2)_4Cu_4Re(CN)_7]^{4+}$, as observed in **9**. Red, orange, blue, and gray spheres represent Re, Cu, N, and C atoms, respectively; hydrogen atoms are omitted for clarity.

within the range usually observed for a Co^{II} ion bound by pyridyl ligands. [17] In stark contrast, the fourth cobalt center exhibits a significantly shorter mean distance of 1.93(4) Å. This short distance indicates the presence of a Co^{III} ion, in accordance with related pyridyl-bound Co^{III} compounds.[19] Considering charge balance in the compound, the presence of a Co^{III} ion suggests that the $[Re(CN)_7]^{3-}$ precursor has been reduced to a $[Re(CN)_7]^{4-}$ unit during the formation of **7**. In **8**, the Ni–N_{py} distances clearly correspond to four octahedral Ni^{II} ions, with mean distances ranging from 2.06(5) to 2.11(6) Å. Finally, the coordination environment of each Cu^{II} ion in **9** approximates a square pyramid, with the Cu-N≡C linkage lying in the basal plane and Cu–N_{py} distances not deviating significantly from those observed in **6**. The structures of **7**, **8**, and **9** all feature significantly bent M–N≡C angles, with mean angles ranging from 176.6(10)° in **7** to 152.3(4)° in **9**. Such bent angles are typical for M^{II} ions coordinated to the nitrogen end of cyanide ligands and likely arise from steric conflicts between $[(PY5Me_2)M]^{2+}$ units.[6,8,20] A summary of mean interatomic distances and angles for the structures of **7**, **8**, and **9** is given in Table 2.1.

Due to the propensity for spontaneous reduction of $[Re(CN)_7]^{3-}$ upon incorporation into a cluster, all syntheses were initially performed at –42° C. In the case of **7** and **8**, this low-temperature preparation led to products identical to those obtained from reactions conducted at ambient temperature. In the case of Cu^{II}, however, preparation at low temperature is necessary to forestall a reduction of the Re^{IV} center. Indeed, electrospray ionization mass spectrometry measurements of the chilled reaction mixture revealed the presence of an ion with a mass, charge and isotopic distribution corresponding to that of $[(PY5Me_2)_4Cu^{II}_4Re^{IV}(CN)_7]^{5+}$, consistent with **10**. In contrast, a similar measurement of a solution at 300 K revealed the presence of only **9** (see Figure 2.S4).

Table 2.1. Selected Mean Interatomic Distances (Å) and Angles (°) for $[(PY5Me_2)_4M_4Re(CN)_7](PF_6)_5$ (M = Co (**7**), Ni (**8**)) and $[(PY5Me_2)_4Cu_4Re(CN)_7](PF_6)_4$ (**9**).

	7	**8**	**9**
$M–N_{py}$	2.13(3), 1.93(4)	2.09(2)	2.05(8)
M–NC	2.00(13)	2.03(1)	1.95(1)
M•••Re	5.16(6)	5.22(4)	5.07(5)
M•••M	7.6(3)	7.6(3)	7.4(2)
Re–C	2.09(2)	2.10(2)	2.10(2)
M–N≡C	165(10)	168(8)	158(8)
Re–C≡N	176(2)	177(2)	178(5)
C_{eq}–Re–C_{eq}	72(2)	72(1)	73(2)
C_{ax}–Re–C_{ax}	176(1)	175(1)	178(1)

2.3.3. Static Magnetic Properties of the M_4Re Clusters. Variable-temperature dc susceptibility measurements were conducted to probe the magnetic exchange coupling in **7**, **8**, **9**, and **10**. A plot of $\chi_M T$ vs. T for **7**, collected under an applied field of 1000 Oe, is shown in Figure 2.3. At 300 K, $\chi_M T$ = 7.03 cm^3K/mol, higher than the expected value of 5.63 cm^3K/mol for diamagnetic Re^{III} and low-spin Co^{III} ions and three isolated high-spin Co^{II} centers ($S = {}^3/_2$) with g = 2.00. This high value stems from the spin-orbit coupling of the Co^{II} ions and leads to g = 2.24. Upon lowering the temperature, $\chi_M T$ remains essentially constant to 100 K, before dropping abruptly to a minimum value of 4.56 cm^3K/mol at 5 K. The constant value of $\chi_M T$ demonstrates the absence of any significant exchange coupling, as expected for one low-spin Co^{III} and three high-spin Co^{II} ions connected to a central diamagnetic Re^{III} center. The downturn in $\chi_M T$ below 100 K likely stems from spin-orbit coupling in the Co^{II} ions and very weak antiferromagnetic coupling between Co^{II} ions through the diamagnetic Re^{III} center.[10,21] Although intermolecular interactions could be possible in this temperature range, the metal ions of each cluster are insulated from surrounding clusters by the $PY5Me_2$ ligands, solvents of crystallization, and counterions, rendering long-range interactions unlikely in comparison to the spin-orbit effects.

The temperature dependence of $\chi_M T$ observed for **8** is markedly different than that of **7**, as illustrated in the left panel of Figure 2.2. At 300 K, $\chi_M T$ = 4.36 cm^3K/mol, close to the expected value of $\chi_M T$ = 4.38 cm^3K/mol for one isolated Re^{IV} center ($S = {}^1/_2$) and four isolated Ni^{II} centers (S = 1). As the temperature is decreased from 300 K, $\chi_M T$ increases monotonically to a maximum of 7.07 cm^3K/mol at 5 K. This increase in $\chi_M T$ with decreasing temperature is indicative of ferromagnetic coupling between the Re^{IV} and Ni^{II} centers, expected for superexchange through cyanide between Re^{IV} ($e_2'^3$) and Ni ($t_{2g}^6e_g^2$) ions, giving rise to a spin ground state of $S = {}^9/_2$. The maximum at low temperature falls short of the expected value of $\chi_M T$ = 12.38 cm^3K/mol for a spin ground state of $S = {}^9/_2$, owing in part to the strong magnetic anisotropy of the Re^{IV} center. The low magnitude of the exchange coupling constant (4.4 cm^{-1},

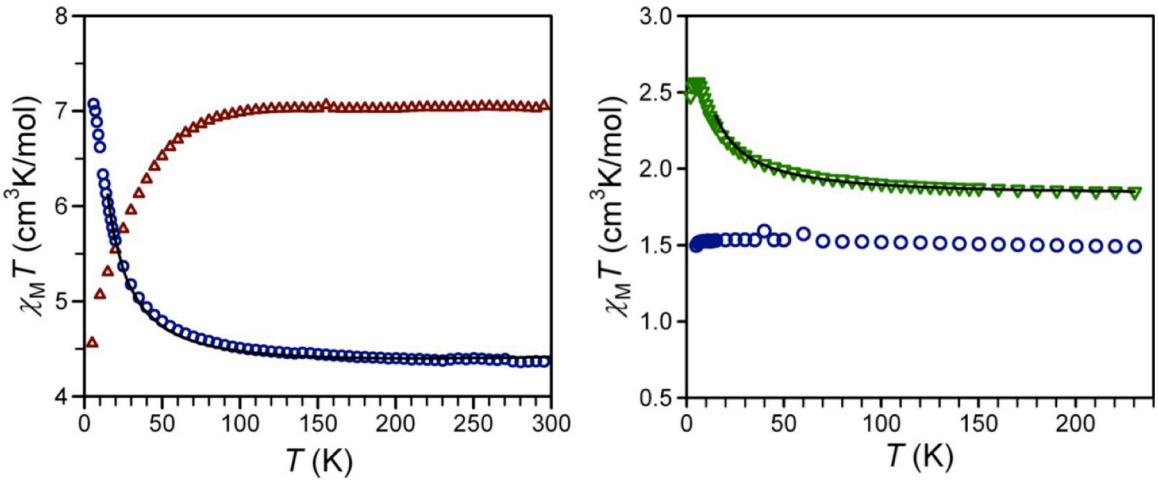


Figure 2.3. Left: Variable-temperature dc magnetic susceptibility data for **7** (red triangles) and **8** (blue circles), collected under an applied field of 1000 Oe. The solid black line corresponds to a fit to the data, as described in the text, giving $J = +4.4$ cm^{-1}. Right: Variable-temperature dc magnetic susceptibility data for **9** (blue circles) and **10** (green triangles), collected under an applied field of 1000 Oe. The black line represents a fit to the data, as described in the text, giving $J = +6.26$ cm^{-1}.

vide infra) suggests that a significant population of low lying excited spin states ($S \leq {}^7/_2$) also contributes to the unexpectedly low maximum observed in the susceptibility data.

In order to quantify the exchange coupling in **8**, the $\chi_M T$ data were modeled with the following isotropic spin Hamiltonian: $\hat{H} = -2J[\hat{S}_{Re} \bullet (\hat{S}_{Ni(1)} + \hat{S}_{Ni(2)} + \hat{S}_{Ni(3)} + \hat{S}_{Ni(4)})]$. In the temperature range 15-300 K, the data were fit using MAGFIT 3.1[22] to give a coupling constant of $J = +4.4$ cm^{-1} with $g = 1.85$. This value represents a nearly two-fold increase over the analogous Mn_4Re cluster, where competitive ferromagnetic and antiferromagnetic interactions lower the overall exchange strength.[8,10]

The plot of $\chi_M T$ vs. T for **9**, shown in the right panel of Figure 2.2, reveals a value of $\chi_M T = 1.48$ cm^{3}K/mol at 300 K, in agreement with the expected value of $\chi_M T = 1.50$ cm^{3}K/mol for four isolated Cu^{II} centers ($S = {}^1/_2$) and a diamagnetic Re^{III} ion. Upon lowering the temperature, $\chi_M T$ remains constant down to 5 K, as expected for negligible exchange interactions between isolated Cu^{II} centers. In stark contrast to those observed for **9**, the $\chi_M T$ data collected for **10** demonstrate a significant dependence on temperature. At 300 K, $\chi_M T = 1.85$ cm^{3}K/mol, consistent with the value of $\chi_M T = 1.88$ cm^{3}K/mol expected for one isolated Re^{IV} center ($S = {}^1/_2$) and four isolated Cu^{II} centers ($S = {}^1/_2$). As the temperature is lowered, the data increase monotonically to $\chi_M T = 2.57$ cm^{3}K/mol at 6 K, before falling sharply to $\chi_M T = 2.47$ cm^{3}K/mol at 2 K. The increase in $\chi_M T$ as the temperature is lowered demonstrates the presence of ferromagnetic exchange coupling between the Re^{IV} and Cu^{II} centers, as expected for Re^{IV} ($e_2'^3$) and Cu^{II} ($e^4b_2^2b_1^2a_1^1$). The maximum at 6 K falls short of the expected $\chi_M T = 4.375$ cm^{3}K/mol for an $S = {}^5/_2$ ground state, likely due to the magnetic anisotropy of the Re^{IV} ion and the presence of low lying excited states corresponding to $S < {}^5/_2$. Nevertheless, the data were fit analogously to those obtained for **8** to give parameters of $J = +6.26$ cm^{-1} and $g = 2.35$. This magnitude of J surpasses that observed in

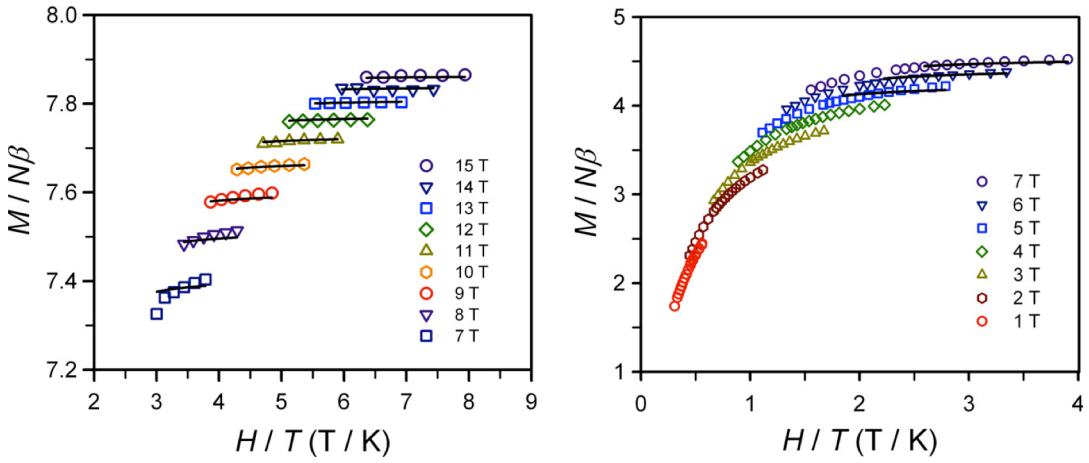


Figure 2.4. Low-temperature magnetization data recorded at various applied dc fields for **8** (left) and **10** (right). Solid black lines represent fits to the data as described in the text, giving $D = 0.93$ cm^{-1}, $|E| \leq 0.01$ cm^{-1}, and $g = 1.78$ for **8** and $D = -1.49$ cm^{-1}, $|E| \leq 0.01$ cm^{-1}, and $g = 1.95$ for **10**.

8, presumably from the localization of the unpaired electron in the d_{x2-y2} orbital along the direction of magnetic exchange.

To probe the magnetic anisotropy in **8** and **10**, variable-temperature magnetization data were collected under a range of applied dc fields. The resulting plots of reduced magnetization for the compounds reveal the presence of non-superimposable isofield curves (see Figure 2.4) as expected for molecules exhibiting significant zero-field splitting of the spin ground state. Indeed, best fits to the data obtained for **8** using ANISOFIT 2.0[23] gave axial and transverse zero-field splitting parameters of $D = 0.93$ cm^{-1} and $|E| \leq 0.01$ cm^{-1}, respectively, with $g = 1.78$. While the data were best modeled using a positive value of D, note that determination of the sign of D from magnetization data obtained for powder samples can be difficult for small D values.[10a] Indeed, ac susceptibility measurements indicate that the sign of D is in fact negative (*vide infra*). The best fits to the data obtained for **10** revealed parameters of $D = -1.33$ cm^{-1}, $|E| \leq 0.01$ cm^{-1}, and $g = 1.95$. This value of D is among the largest yet reported for cyano-bridged pentanuclear single-molecule magnets[4d,k,24] and the largest recorded for a homoleptic cyanometalate-based cluster.[8] Notably, the magnitude of D is also accompanied by the lowest spin ground state of the series, as D decreases from Cu_4Re to Ni_4Re to Mn_4Re.

2.3.4. Dynamic Magnetic Properties of the $M^{II}_4Re^{IV}$ Clusters. To probe the relaxation dynamics in **8** and **10**, variable-temperature ac magnetic susceptibility data were collected for the two clusters under zero applied dc field at various frequencies. As shown in Figure 2.5, the data for **8** reveal a substantial frequency dependence of the out-of-phase (χ_M'') component of the ac susceptibility. Relaxation times (τ) were extracted from the maxima observed in χ_M'' according to the expression $\tau = 1/2\pi\nu$, where ν is the oscillation frequency of the ac field. For a single-molecule magnet, the temperature dependence of the relaxation time follows the Arrhenius relationship $\tau = \tau_0 \exp(U_{eff}/kT)$, such that a plot of $\ln(\tau)$ vs. $1/T$ should be linear, with the slope giving U_{eff}. Indeed, an Arrhenius plot constructed for **8** reveals a linear relationship, with a fit to the data affording a relaxation barrier of $U_{eff} = 17$ cm^{-1} with $\tau_0 = 1.4 \times 10^{-7}$ s^{-1}. The magnitude of the energy barrier is close to the theoretical value of $U = 19$ cm^{-1} for an $S = {}^9/_2$ ground state with $D = -0.93$ cm^{-1}, suggesting that quantum tunneling of the magnetization is not a major relaxation

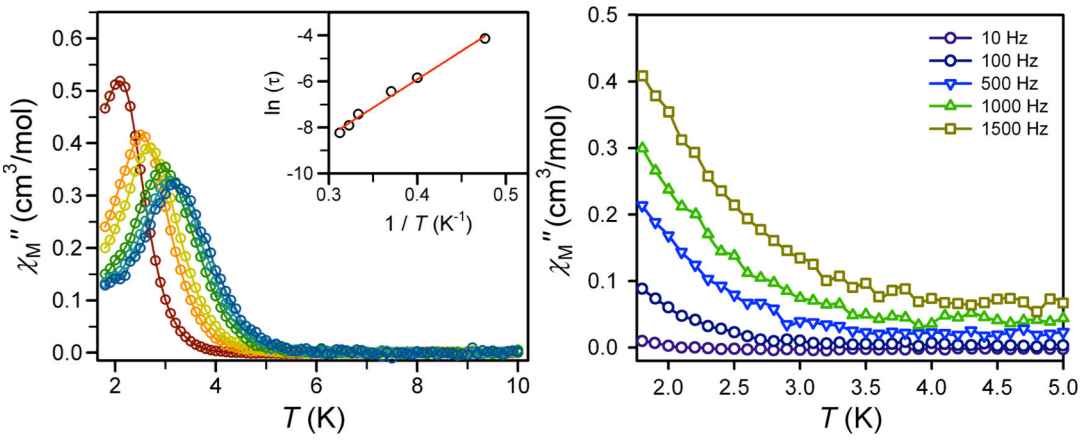


Figure 2.5. Left: Variable-temperature out-of-phase ac magnetic susceptibility data for **8**, collected in a 4 Oe oscillating field at frequencies of 10 (red), 55 (orange), 100 (yellow), 267 (green), 434 (turquoise) and 601 (blue) Hz. Inset: Arrhenius plot of the relaxation time, as determined through variable-temperature ac susceptibility measurements. The solid red line corresponds to a linear fit of the data, giving U_{eff} = 17 cm^{-1}. Right: Out-of-phase ac susceptibility of **10**. Data were recorded from 1.8 to 5 K under 5 different switching frequencies.

pathway in this case above 1.8 K. Additionally, the value of τ_0 gives a quantitative measure of the attempt frequency for magnetic relaxation, and the value obtained here is within the expected range for single–molecule magnets.[3,4]

Variable–temperature ac susceptibility data collected on **10** also show a frequency-dependent signal, however this signal occurs at lower temperature such that only tails are visible in χ_M'' at temperatures down to 1.8 K (see Figure 2.5, right panel). The spin ground state ($S = {}^5/_2$) and D value obtained from magnetization measurements give a theoretical barrier height of 8 cm^{-1}, consistent with the observation of only tails in the χ_M'' data.

2.3.5. Spectroelectrochemistry and Photomagnetic Measurements of the Co_4Re Cluster. The cyclic voltammogram of **7**, as shown in Figure 2.6, reveals the presence of multiple overlapping quasi–reversible peaks, the most prominent of which are situated near 0.050 and –1.8 V vs. $Cp_2Fe/[Cp_2Fe]^+$. The separation between the redox processes occurring in these regions (1.85 V) is comparable to the separation of the $Co^{II/III}$ and $Co^{I/II}$ transitions in the CV of **5** (1.63 V). In view of this similarity, these processes likely correspond to the $Co^{II/III}$ and $Co^{I/II}$ couples within the cluster, respectively. Additionally, the two quasireversible redox processes, with peak areas approximately one–third that of the other two processes, occur at $E_{1/2}$ = 0.762 and 1.341 V and likely correspond to $Re^{III/IV}$ and $Re^{IV/V}$ couples, respectively.

Electronic absorption spectroscopy was employed to analyze the absorption profile of **7**. The diffuse reflectance and solution spectra collected for **7** reveal the presence of two transitions, occurring at 12,500 cm^{-1} and 20,000 cm^{-1} (see Figure 2.S4). The acetonitrile solution measurements provided molar extinction coefficients (ε) of 2,030 $M^{-1}cm^{-1}$ and 1,930 $M^{-1}cm^{-1}$ for the bands at 12,500 and 20,000 cm^{-1}, respectively. Additionally, bandwidths at half height ($\Delta\nu_{1/2}$) for the two absorptions are 5363 cm^{-1} and 5395 cm^{-1}, respectively. Importantly, neither of these bands is observed in the spectra of the starting materials, indicating that the observed transitions are associated with cluster.

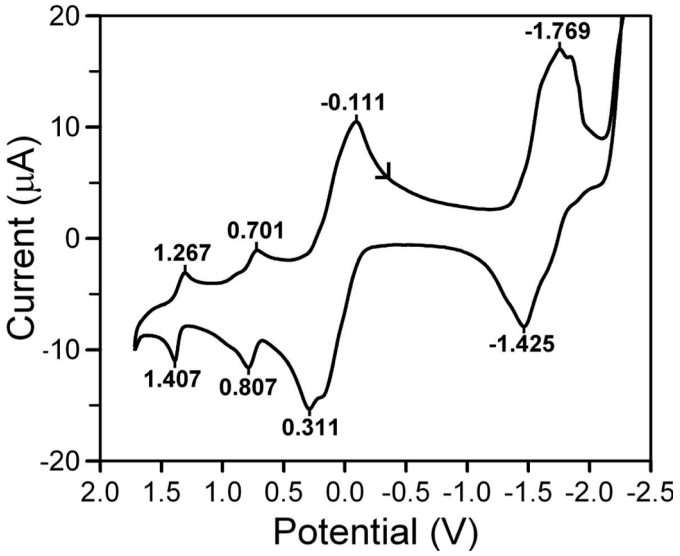


Figure 2.6. Electrochemical data obtained on an acetonitrile solution of **7** using a platinum electrode, 100 mV/s scan rate, and 0.1 M $(Bu_4N)PF_6$ supporting electrolyte. Potentials are reported vs. $Cp_2Fe/[Cp_2Fe]^+$.

UV–Vis–NIR spectroelectrochemical measurements were performed on an acetonitrile solution containing **7**, depicted in Figure 2.7, in order to characterize the absorption bands. The spectrum changes significantly as the potential of the solution is held at +0.5 V. The lower energy band intensifies by 1000 $M^{-1}cm^{-1}$, while the higher energy band weakens by 700 $M^{-1}cm^{-1}$. Both peaks experience a concomitant blueshift of 2000 cm^{-1}. As the voltage is further increased to +1.0 V, the lower energy band at 14,000 cm^{-1} weakens in intensity by 1742 $M^{-1}cm^{-1}$ as it shifts to a higher energy by 1650 cm^{-1}. A new transition appears at 23,000 cm^{-1} and grows to a maximum intensity of 2400 $M^{-1}cm^{-1}$. As the higher energy transition intensifies, it overlaps the weaker transition at 21,000 cm^{-1}, precluding a clear determination of whether the latter disappears completely during electrochemical oxidation. The lack of an isosbestic point associated with a +0.5 V applied potential is unsurprising considering the high degree of overlap observed in the CV for this potential. In contrast, an applied potential of +1.0 V is accompanied by an isosbestic point.

The presence of two bands at relatively low energy that are not observed in the spectra of the starting materials (see Figure 2.S4) suggests the occurrence of metal–to–metal charge-transfer. Indeed, the energies, intensities, and bandwidths of the two transitions are within the range expected for localized metal–to–metal charge-transfer transitions.[25] Both peaks are also highly solvatochromic. The spectroelectrochemistry experiment showed that changes to the redox states of the metal ions in the cluster caused significant changes in both the intensities and energies of the two transitions. On the basis of these observations, I hypothesize that the two low energy transitions are metal–to–metal charge-transfers (MMCTs).

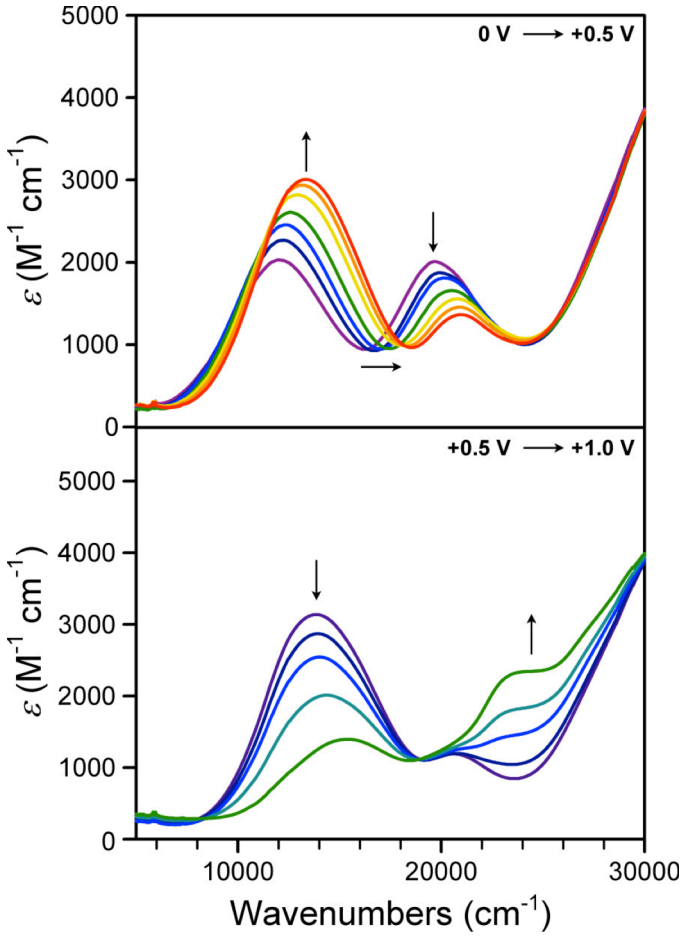


Figure 2.7. Spectroelectrochemical data for a 0.1 M $(Bu_4N)PF_6$ MeCN solution of **7**. The top panel displays the change in the spectrum as a +0.5 V potential is applied to the solution. The bottom graph corresponds to an applied potential of +1.0 V. Arrows indicate direction of change.

While experimental evidence strongly suggests the presence of a metal–to–metal charge-transfer, assignment of the direction of the MMCT is more tentative. The reduction of Re^{IV} by one of the $[(PY5Me_2)Co]^{2+}$ units during cluster assembly suggests that perhaps one of the absorption bands could be the photon–triggered reverse process, $Re^{III} \rightarrow Co^{III}$. If the spectroelectrochemical data is analyzed under the assumption that they are Re and Co–based MMCTs, the band at 12,500 cm^{-1} likely corresponds to Re^{III} and Co^{III}, while the one at 20,000 cm^{-1} involves Re^{III} and Co^{II}. In the CV, the processes at 0.05 V were assigned to $Co^{II/III}$ couples. Based on this assignment, a decrease in the Re^{III}–Co^{II} transitions should be observed as the Co^{II} ions within the cluster are oxidized to Co^{III}, concomitant with an increase in the intensity of the Re^{III}–Co^{III} absorption. This change is indeed observed in the data. If the direction of the transfer is labeled $Re^{III} \rightarrow Co^{III}$, then a decrease in the $Re^{III} \rightarrow Co^{III}$ MMCT should be seen as a +1.0 V potential is applied. In addition, the 0.762 V process was assigned to the $Re^{III/IV}$ couple. If that assignment is correct, then as Re^{IV} is produced a decrease in the $Re^{III} \rightarrow Co^{III}$ MMCT should occur, since Re^{IV} would have less electron density to transfer to the pendant Co^{III} ions. Furthermore, since Re^{IV} has a singly–occupied metal–centered orbital, the appearance of a relatively higher energy LMCT would be expected. Indeed, this is observed with the emergence

of the absorption at 23,000 cm^{-1}, although the assignment of this band as a LMCT is purely based on the above assumptions. The presence of an isosbestic point gives credence to the assignment of the 0.762 V process as $Re^{III/IV}$ because there is only one Re per cluster molecule.

My interest in the photophysical properties of **7** is spurred by the photomagnetic properties of several cyano–bridged extended framework and coordination cluster systems.[26,27] If the $Re^{III}\rightarrow Co^{III}$ MMCT state could be trapped via irradiation at low temperature, then the hypothesized $Co^{II}_4Re^{IV}$ state could be analyzed to probe for possible slow magnetic relaxation. The magnetic anisotropy associated with both Co^{II} and Re^{IV} ions, in conjunction with the expected $S = {}^{11}/_{2}$ spin ground state of the $Co^{II}_4Re^{IV}$ cluster, could give rise to a large spin–reversal barrier. Toward this end, solid-state reflectivity data were collected between 290 and 10 K (under white light irradiation of 0.05 mW/cm^2). With cooling, the spectra of **7** show an increase in the absolute reflectivity in the 10,000 − 25,000 cm^{-1} range (see Figure 2.S6). The compound is more reflecting (or less absorbing) at low temperature, with this effect being more important in the NIR (Near Infra-Red, 13,333 – 25,000 cm^{-1}) region. Upon heating, the absolute reflectivity decreases, and the compound recovers at 280 K the same spectrum observed before the thermal cycle. Photo-excitation properties of **7** were studied by cooling the sample to 5 K (under a very weak white light irradiation 0.05 mW/cm^2) followed by white light irradiation (6 mW/cm^2). Rapidly, a decrease in absolute reflectivity is observed above 12,500 cm^{-1} and after 12 minutes the spectrum remains unchanged (see Figure 2.S6). Upon heating, the photo-generated state decays smoothly, and the original spectrum is restored at room temperature, as observed in the thermal variation of $R_{10,000cm-1}$ (see Figure 2.S6). A similar behavior is obtained when the compound is irradiated at 5 K with a blue light of 21,277 cm^{-1} (6 mW/cm^2). This optical reflectivity study shows that **7** is thermochromic and photochromic using white and blue irradiation lights.

Magnetic measurements of an irradiated sample of **7** were performed at low temperatures with a variety of light sources. Although the reflectivity measurements suggest population of an excited state, a small photomagnetic effect at 10 K is observed as a decrease in $\chi_M T$ of about 1% when the compound is irradiated with blue light (21,277 cm^{-1}, 6 mW/cm^2). In line with the rapid saturation of the photoactivity observed in the reflectivity measurements, the very dark color of the crystals suggests that light cannot easily penetrate the material, thus highlighting the possibility that the photogenerated state is occurring mainly on the surface of the material.

2.4 Outlook and Conclusions

The foregoing results demonstrate the utility of the building unit $[Re(CN)_7]^{3-}$ in the preparation of new star-like clusters of formulae $[(PY5Me_2)_4M_4Re(CN)_7]^{n+}$ (M = Co, Ni, Cu). The formation of the Co_4Re cluster is accompanied by a one-electron transfer from cobalt to rhenium. In contrast, use of the electron-rich precursor complex $[(PY5Me_2)Ni]^{2+}$ in the cluster assembly forestalls a spontaneous reduction of the Re^{IV} ion and thus enables access to a redox-stable Ni_4Re cluster, which demonstrates slow magnetic relaxation at low temperature. Future efforts will focus on extending this synthetic strategy to star-like clusters bearing second– and third–row transition metals as the pendant metal centers, thereby providing a route to stronger magnetic anisotropy. In a parallel strategy, clusters featuring electron-rich $[(PY5Me_2)M]^{2+}$ units with unquenched orbital angular momentum will be targeted. Such efforts may strengthen the magnetic anisotropy and increase the redox stability of high-nuclearity clusters incorporating

$[Re(CN)_7]^{3-}$ will lead to the discovery of new single-molecule magnets with considerably larger relaxation barriers.

2.5. Acknowledgements

This work was supported by NSF Grant No. CHE-0617063 and the France-Berkeley Fund the University of Bordeaux, the CNRS, the ANR (NT09-469563, AC-MAGnets project), the Region Aquitaine and the GIS Advanced Materials in Aquitaine (COMET Project). I thank Drs. D. E. Freedman, T. D. Harris, D. M. Jenkins, and J. R. Long for considerable experimental assistance, insight, and help studying these compounds. I also thank Dr. A. T. Iavarone for being instrumental in the acquisition of high resolution ESI/MS data, and am grateful to Drs. Corine Mathonière and Rodolphe Clérac for performing photomagnetic measurements on the compounds. Dr. F. J. Hollander, Dr. A. DiPasquale, Dr. J. O'Brien, and Dr. D. M. D'Alessandro are also deserving of my thanks for insightful discussions and experimental assistance.

2.6. References, Notes, and Supplementary Information

(1) (*a*) Lis, T. *Acta Crystallogr. Sect. B* **1980**, *36*, 2042. (*b*) Sessoli, R.; Gatteschi, D.; Caneschi, A.; Novak, M. A. *Nature* **1993**, *365*, 141. (*c*) Sessoli, R. T.; Hui, L.; Schake, A. R.; Wang, S.; Vincent, J. B.; Folting, K.; Gatteschi, D.; Christou, G.; Hendrickson, D. N. *J. Am. Chem. Soc.* **1993**, *115*, 1804.

(2) (*a*) Garanin, D. A.; Chudnovsky, E. M. *Phys. Rev. B* **1997**, *56*, 11102. (*b*) Leuenberger, M. N.; Loss, D. *Nature* **2001**, *410*, 789. (*c*) Jo, M.-H.; Grose, J. E.; Liang, W.; Baheti, K.; Deshmukh, M. M.; Sokol, J. J.; Rumberger, E. M.; Hendrickson, D. N.; Long, J. R.; Park, H.; Ralph, D. C. *Nano Lett.* **2006**, *6*, 2014. (*d*) Ardavan, A.; Rival, O.; Morton, J. J. L.; Blundell, S. J.; Tyryshkin, A. M.; Timco, G. A.; Winpenny, R. E. P. *Phys. Rev. Lett.* **2007**, *98*, 057201. (*e*) Bogani, L.; Wernsdorfer, W. *Nature Mater.* **2008**, *7*, 884. (*f*) Stamp, P. C. E.; Gaita-Arino, A. *J. Mater. Chem.* **2009**, *19*, 1718.

(3) (*a*) Long, J. R. Molecular Cluster Magnets. In *Chemistry of Nanostructured Materials*; Yang, P., Ed.; World Scientific: Hong Kong, 2003; pp 291-315 and references therein. (*b*) Beltran, L. M. C.; Long, J. R. *Acc. Chem. Res.* **2005**, *38*, 325. (*c*) Shatruk, M.; Avendano, C.; Dunbar, K. in *Progress in Inorganic Chemistry*, ed. K. D. Karlin, John Wiley & Sons, Amsterdam, 2009, vol. 56, pp. 155 and references therein.

(4) Selected References: (*a*) Mallah, T.; Auberger, C.; Verdaguer, M.; and Veillet, P. *Chem. Commun.* **1995**, 61. (*b*) Parker, R. J.; Hockless, D. C. R.; Moubaraki, B.; Murray, K. S.; Spiccia, L. *Chem. Commun.* **1996**, 2789. (*c*) Zhong, Z. J.; Seino, H.; Mizobe, Y.; Hidai, M.; Fujishima, A.; Ohkoshi, S.-I.; Hashimoto, K. *J. Am. Chem. Soc.* **2000**, *122*, 2952. (*d*) Berlinguette, C. P.; Vaughn, D.; Cañada-Vilalta, C.; Galán-Mascarós, J. R.; Dunbar, K. R. *Angew. Chem., Int. Ed.* **2003**, *42*, 1523. (*e*) Marvaud, V.; Decroix, C.; Scuiller, A.; Guyard-Duhayon, C.; Vaissermann, J.; Gonnet, F.; Verdaguer, M. *Chem.−Eur. J.* **2003**, *9*, 1677. (*f*) Schelter, E. J.; Prosvirin, A. V.; Dunbar, K. R. *J. Am. Chem. Soc.* **2004**, *126*, 15004. (*g*) Wang, S.; Zou, J.-L.; Zhou, H.-C.; Choi, H. J.; Ke, Y.; Long, J. R.; You, X.-Z. *Angew.*

Chem., Int. Ed. **2004**, *43*, 5940. (*h*) Song, Y.; Zhang, P.; Ren, X.-M.; Shen, X.-F.; Li, Y.-Z.; You, X.-Z. *J. Am. Chem. Soc.* **2005**, *127*, 3708. (*i*) Li, D.; Parkin, S.; Wang, G.; Yee, G. T.; Prosvirin, A. V.; Holmes, S. M. *Inorg. Chem.* **2005**, *44*, 4903. (*j*) Ni, Z.-H.; Kou, H.-Z.; Zhang, L.-F.; Ge, C.; Cui, A.-L.; Wang, R.-J.; Li, Y.; Sato, O. *Angew. Chem., Int. Ed.* **2005**, *44*, 7742. (*k*) Wang, C.-F; Zuo, J.-L.; Bartlett, B. M.; Song, Y.; Long, J. R.; You, X.-Z. *J. Am. Chem. Soc.* **2006**, *128*, 7162. (*l*) Li, D.; Parkin, S.; Wang, G.; Yee, G. T.; Clérac, R.; Wernsdorfer, W.; Holmes, S. M. *J. Am. Chem. Soc.* **2006**, *128*, 4214. (*m*) Glaser, T.; Heidemeier, M.; Weyhermüller, T.; Hoffmann, R.-D.; Rupp, H.; Müller, P. *Angew. Chem., Int. Ed.* **2006**, *45*, 6033. (*n*) Lim, J. H.; Yoon, J. H.; Kim, H. C.; Hong, C. S. *Angew. Chem., Int. Ed.* **2006**, *45*, 7424. (*o*) Harris, T. D.; Long, J. R. *Chem. Commun.* **2007**, 1360. (*p*) Shatruk, M.; Dragulescu Andrasi, A.; Chambers, K. E.; Stoian, S. A.; Bominaar, E. L.; Achim, C.; Dunbar, K. R. *J. Am. Chem. Soc.* **2007**, *129*, 6104.

(5) (*a*) Weihe, H.; Güdel, H. *Comment. Inorg. Chem.* **2000**, *22*, 75. (*b*) Ruiz, E.; Rodríguez-Fortea, A.; Alvarez, S.; Verdaguer, M. *Chem. Eur. J.* **2005**, *11*, 2135. (*c*) Atanasov, M.; Comba, P.; Daul, C. *J. Phys. Chem. A* **2006**, *110*, 13332. (*d*) Rebilly, J.-N.; Mallah, T., Synthesis of Single–Molecule Magnets Using Metallocyanates. In *Single–Molecule Magnets and Related Phenomena*, 2006; pp 103–131.

(6) Bennett, M. V.; Long, J. R. *J. Am. Chem. Soc.* **2003**, *125*, 2394.

(7) Jorge, D.; Mendizabal, F.; Ramiro, A.-P. *J. Phys. Chem. A* **2006**, *110*, 1072.

(8) Freedman, D. E.; Jenkins, D. M.; Iavarone, A. T.; Long, J. R. *J. Am. Chem. Soc.* **2008**, *130*, 2884.

(9) Scholz, F.; Dostal, A. *Angew. Chem. Int. Ed.* **1996**, *34*, 2685.

(10) (*a*) Carlin, R. L. Magnetochemistry. Springer-Verlag: Berlin Heidelberg, 1986. (*b*) Kahn, O. Molecular Magnetism. John Wiley & Sons: New York, 1993. (*c*) Figgis, B. N.; Hitchman, M. A. Ligand Field Theory and Its Applications. Wiley-VCH: New York, 2000. (*d*) Lloret, F.; Julve, M.; Cano, J.; Ruiz-García, R.; Pardo, E. *Inorg. Chim. Acta.* **2008**, *361*, 3432.

(11) Harris, T. D.; Coulon, C.; Clérac, R.; Long, J. R. *J. Am. Chem. Soc.* **2011**, *133*, 123.

(12) Bechlars, B.; D'Alessandro, D. M.; Jenkins, D. M.; Iavarone, A. T.; Glover, S. D.; Kubiak, C. P.; Long, J. R. *Nat. Chem.,* **2010**, *2*, 362.

(13) *APEX2 v.2009*; Bruker Analytical X–Ray Systems, Inc: Madison, WI, 2009.

(14) Sheldrick, G. M. *SADABS, Version 2.03*; Bruker Analytical X–Ray Systems, Inc: Madison, WI, 2000.

(15) Sheldrick, G. M. *SHELXTL, Version 6.12*; Bruker Analytical X–Ray Systems, Inc: Madison, WI, 2000.

(16) Van der Sluis, P.; Spek, A. L. *Acta Crystallogr., Sect. A* **1990**, 46,194–201.

(17) (*a*) Wentworth, R. A. D.; Dahl, P. S.; Huffmann, C. J.; Gillum, W. O.; Streib, W. E.; Huffman, J. C. *Inorg. Chem.* **1982**, *21*, 3060. (*b*) Newkome, G. R.; Majestic, V. K.; Fronczek, F. R. *Inorg. Chim. Acta.* **1983**, *77*, L47. (*c*) Xu, H.; Song, Y.; Hou, H. *Inorg. Chim. Acta.* **2004**, *357*, 3541. (*d*) Barboiu, M.; Petit, E.; Vaughan, G. *Chem. Eur. J.* **2004**, *10*, 2263.

(18) (*a*) Drew, M. G. B.; Nelson, J.; Nelson, S. M. *J. Chem. Soc. Dalton Trans.* **1981**, *8*, 1691. (*b*) Xu, Z.; Thompson, L. K.; Black, D. A.; Ralph, C.; Miller, D. O.; Leech, M. A.; Howard, J. A. K. *J. Chem. Soc. Dalton Trans.* **2001**, *13*, 2042. (*c*) Park, H. W.; Sung, S.

M.; Min, K. S.; Bang, H.; Suh, M. P. *Eur. J. Inorg. Chem.* **2001**, *11*, 2857. (*d*) Park, K.-M.; Whang, D.; Lee, E.; Heo, J.; Kim, K. *Chem. Eur. J.* **2002**, *8*, 498.

(19) (*a*) Szalda, D. J.; Keene, F. R. *Inorg. Chem.* **1986**, *25*, 2795. (*b*) Cabort, A.; Michel, A.; Therrien, B.; Stoeckli-Evans, H.; Bernauer, K.; Suss-Fink, G.; Williams, A. F.; Stupka, G. *Inorg. Chim. Acta.* **2003**, *350*, 193. (*c*) Stupka, G.; Ludovic, G.; Bernardinelli, G.; Williams, A. F. *Dalton Trans* **2004**, *3*, 407. (*d*) Hausmann, J.; Brooker, S. *Chem. Commun.* **2004**, *13*, 1530.

(20) (*a*) Naumov, N. G.; Artemkina, S. B.; Virovets, A. V.; Fedorov, V. E. *J. Solid State Chem.* **2000**, *153*, 195. (*b*) Mironov, Y. V.; Fedorov, V. E.; Ijjaali, I.; Ibers, J. A. *Inorg. Chem.* **2001**, *40*, 6320. (*c*) Brylev, K. A.; Mironov, Y. V.; Naumov, N. G.; Fedorov, V. E.; Ibers, J. A. *Inorg. Chem.* **2004**, *43*, 4833.

(21) Herrera, J. M.; Bleuzen, A.; Dromzée, Y.; Julve, M.; Lloret, F.; Verdaguer, M. *Inorg. Chem.* **2003**, *42*, 7052.

(22) Schmitt, E. A. PhD. Thesis. University of Illinois at Urbana-Champaign, 1995.

(23) Shores, M. P.; Sokol, J. J.; Long, J. R. *J. Am. Chem. Soc.* **2002**, *124*, 2279.

(24) (*a*) Palii, A. V.; Ostrovsky, S. M.; Klokishner, S. I.; Tsukerblat, B. S.; Berlinguette, C. P.; Dunbar, K. R. *J. Am. Chem. Soc.* **2004**, *126*, 16860. (*b*) Bartlett, B. M.; Harris, T. D.; DeGroot, M. W.; Long, J. R. *Z. Anorg. Allg. Chem.* **2007**, *633*, 2380.

(25) (*a*) Robin, M.; Day, P. *Adv. Inorg. Chem. Radiochem.* **1967**, *10*, 247. (*b*) D'Alessandro, D.; Keene, F. *Chem. Soc. Rev.* **2006**, *35*, 424.

(26) (*a*) Macknight, F.; Haight, G. P. *Inorg Chem* **1973**, *12*, 3007. (*b*) Sato, O.; Iyoda, T.; Fujishima, A.; Hashimoto, K. *Science* **1996**, *272*, 704. (*c*) Verdaguer, M. *Science* **1996**, *272*, 698. (*d*) Sato, O.; Einage, Y.; Iyoda, T.; Fujishima, A.; Hashimoto, K. *J. Electrochem. Soc.* **1997**, *144*, 11. (*e*) Shimamoto, N.; Ohkoshi, S.-I.; Sato, O.; Hashimoto, K. *Inorg. Chem.* **2002**, *41*, 678. (*f*) Bleuzen, A.; Lomenech, C.; Escax, V.; Villain, F.; Varret, F.; Cartier dit Moulin, C.; Verdaguer, M. *J. Am. Chem. Soc.* **2000**, *122*, 6648. (*g*) Cartier dit Moulin, C.; Villain, F.; Bleuzen, A.; Arrio, M.-A.; Sainctavit, P.; Lomenech, C.; Excax, V.; Baudelet, F.; Dartyge, E.; Gallet, J. J.; Verdaguer, M. *J. Am. Chem. Soc.* **2000**, *122*, 6653. (*h*) Escax, V.; Bleuzen, A.; Cartier dit Moulin, C.; Villain, F.; Goujon, A.; Varret, F.; Verdaguer, M. *J. Am. Chem. Soc.* **2001**, *123*, 12536. (*i*) Ohkoshi, S.; Machida, N.; Zhong, Z. J.; Hashimoto, K. *Synth. Met.* **2001**, *122*, 523. (*j*) Rombaut, G.; Verelst, M.; Golhen, S.; Ouahab, L.; Mathonière, C.; Kahn, O. *Inorg. Chem.* **2001**, *40*, 1151. (*k*) Ohkoshi, S.-I.; Machida, N.; Abe, Y.; Zhong, Z. J.; Hashimoto, K. *Chem. Lett.* **2001**, 312. (*l*) Shimamoto, N.; Ohkoshi, S.; Sato, O.; Hashimoto, K. *Chem. Lett.* **2002**, *31*, 486. (*m*) Liu, H. W.; Matsuda, K.; Gu, Z. Z.; Takahashi, K.; Cui, A. L.; Nakajima, R.; Fujishima, A.; Sato, O. *Phys. Rev. Lett.* **2003**, *90*, 167403. (*n*) Gawali-Salunke, S.; Varret, F.; Maurin, I.; Enachescu, C.; Malarova, M.; Boukheddaden, K.; Codjovi, E.; Tokoro, H.; Ohkoshi, S.; Hashimoto, K. *J. Phys. Chem. B* **2005**, *109*, 8251. (*o*) Varret, F.; Boukheddaden, K.; Codjovi, E.; Maurin, I.; Tokoro, H.; Ohkoshi, S.-i.; Hashimoto, K. *Polyhedron* **2005**, *24*, 2857. (*p*) Ohkoshi, S.-I.; Ikeda, S.; Hozumi, T.; Kashiwagi, T.; Hashimoto, K. *J. Am. Chem. Soc.* **2006**, *128*, 5320. (*q*) Tokoro, H.; Matsuda, T.; Nuida, T.; Morimoto, Y.; Ohoyama, K.; Loutete–Dangui, E. D.; Boukheddaden, K.; Ohkoshi, S.-I. *Chem. Mater.* **2008**, *20*, 423. (*r*) Bleuzen, A.; Marvaud, V.; Mathonière, C.; Sieklucka, B.; Verdaguer, M. *Inorg. Chem.* **2009**, *48*, 3453.

(27) (*a*) Marvaud, V.; Decroix, C.; Scuiller, A.; Tuyéras, F.; Guyard-Duhayon, C.; Vaissermann, J.; Marrot, J.; Gonnet, F.; Verdaguer, M. *Chem. Eur. J.* **2003**, *9*, 1692. (*b*) Herrera, J.-M.; Marvaud, V.; Verdaguer, M.; Marrot, J.; Kalisz, M.; Mathonière, C. *Angew. Chem. Int. Ed.* **2004**, *43*, 5468. (*c*) Dei, A. *Angew. Chem. Int. Ed.* **2005**, *117*, 1184. (*d*) Mathonière, C.; Podgajny, R.; Guionneau, P.; Labrugère, C.; Sieklucka, B. *Chem. Mater.* **2005**, *17*, 442. (*e*) Sato, O.; Tao, J.; Zhang, Y.-Z. *Angew. Chem. Int. Ed.* **2007**, *46*, 2152. (*f*) Li, D.; Clérac, R.; Roubeau, O.; Harte, E.; Mathonière, C.; Le Bris, R.; Holmes, S. M. *J. Am. Chem. Soc.* **2008**, *130*, 252. (*g*) Tuyéras, F.; Scuiller, A.; Duhayon, C.; Hernandez-Molina, M.; Fabrizi de Biani, F.; Verdaguer, M.; Mallah, T.; Wernsdorfer, W.; Marvaud, V. *Inorg. Chim. Acta* **2008**, *361*, 3505. (*h*) Mathonière, C.; Kobayashi, H.; Le Bris, R.; Kaiba, A.; Bord, I. C. *Chimie* **2008**, *11*, 665.

Table 2.S1. Crystallographic Data[a] for $[(PY5Me_2)M(MeCN)](PF_6)_2$, where M = Co (**4**), Ni (**5**), and Cu (**6**), $[(PY5Me_2)_4M_4Re(CN)_7](PF_6)_5$, where M = Co (**7**) and Ni (**8**), and $[(PY5Me_2)_4Cu_4Re(CN)_7](PF_6)_4$ (**9**).

	4	**5**	**6**	**7**	**8**	**9**
formula	$C_{72}H_{75}Co_2F_{24}N_{15}OP_4$	$C_{72}H_{75}F_{24}N_{15}Ni_2OP_4$	$C_{62}H_{56}Cu_2F_{24}N_{13}P_4$	$C_{133}H_{100}Co_4F_{30}N_{27}P_5Re$	$C_{133}H_{100}F_{30}N_{30}Ni_4OP_5Re$	$C_{123}H_{100}Cu_4F_{24}N_{27}P_4Re$
fw	1864.19	1863.7	1712.17	3103.07	3299.37	2976.54
T, K	140	140	159	150	100	141
space group	$P\,2_1/c$	$P\,2_1/c$	$P\,1$	$C\,2/c$	$P\,-1$	$P\,-1$
Z	4	4	2	8	2	2
a, Å	22.419(2)	22.369(5)	11.407(1)	44.679(10)	12.029(1)	18.766(1)
b, Å	15.249(1)	15.229(3)	12.756(1)	18.870(4)	19.932(1)	19.334(1)
c, Å	24.564(2)	24.469(5)	13.182(1)	41.036(9)	32.048(1)	22.556(1)
α, deg	90	90	68.789(1)	90	80.202(3)	113.098(1)
β, deg	107.777(2)	107.777(2)	70.060(1)	107.277(3)	89.201(3)	97.219(1)
γ, deg	90	90	89.688(1)	90	73.901(3)	110.376(1)
V, Å^3	7997(1)	7946(3)	1665.7(2)	33036(13)	7267.2(6)	6722.5(6)
d_{calc}, g/cm^3	1.516	1.396	1.671	1.148	1.466	1.542
R_1 (wR_2), %[b]	5.74 (13.90)	5.72 (14.31)	3.53 (8.16)	10.22 (26.07)	6.28 (14.61)	8.15 (11.43)

[a]Obtained with graphite-monochromated Mo Kα (λ = 0.71073 Å) radiation for **4**, **5**, **6**, **7**, and **9**. Data for **8** were collected with graphite-monochromated Cu Kα (λ = 1.5405 Å) radiation. [b]$R_1 = \Sigma||F_o| - |F_c||/\Sigma|F_o|$, $wR_2 = \{\Sigma[w(F_o^2 - F_c^2)^2]/\Sigma[w(F_o^2)^2]\}^{1/2}$.

Table 2.S2. Selected mean interatomic distances (Å) and angles (°) for the structures of **4**, **5**, and **6**.

	4	**5**	**6**
$M - N_{py}$	2.130(12)	2.093(19)	2.07(5)
$M - N_{CN}$	2.130(6)	2.083(6)	2.52(1)
$C \equiv N$	1.167(9)	1.139(9)	1.16(1)
$M - N \equiv C$	179.1(7)	179.6(9)	170(1)
$N - M - N^a$	81(1)	82(1)	82(1)
$N - N - N^b$	98.88(2)	98.0(1)	98.1(2)

[a]These N atoms belong to pyridyl rings attached to the same methine carbon. [b]These N atoms belong to pyridyl rings attached to different methine carbons.

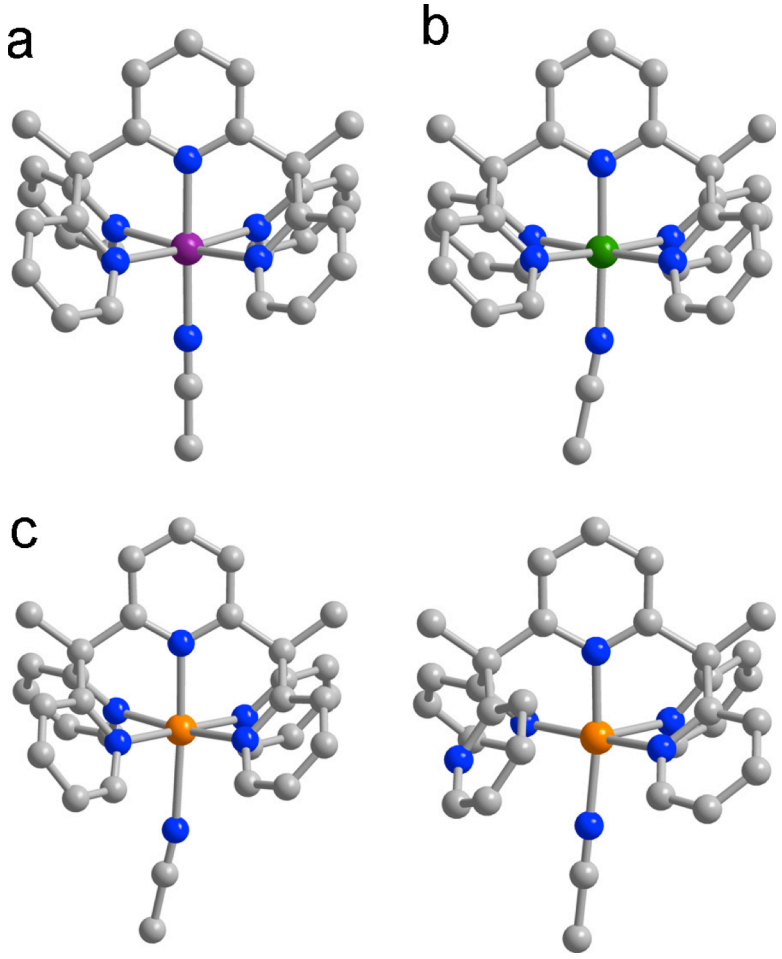


Figure 2.S1. **a.** Structure of $[(PY5Me_2)Co(MeCN)]^{2+}$. Cyan, blue, and gray spheres correspond to Co, N, and C atoms, respectively; hydrogen atoms are omitted for clarity. **b.** Structure of $[(PY5Me_2)Ni(MeCN)]^{2+}$. Green, blue, and gray spheres correspond to Ni, N, and C atoms, respectively; hydrogen atoms are omitted for clarity. **c.** Two isomers of $[(PY5Me_2)Cu(MeCN)]^{2+}$ in the crystal structure of **6**. Hydrogen atoms are omitted for clarity. Orange, blue, and gray spheres correspond to Cu, N, and C atoms respectively.

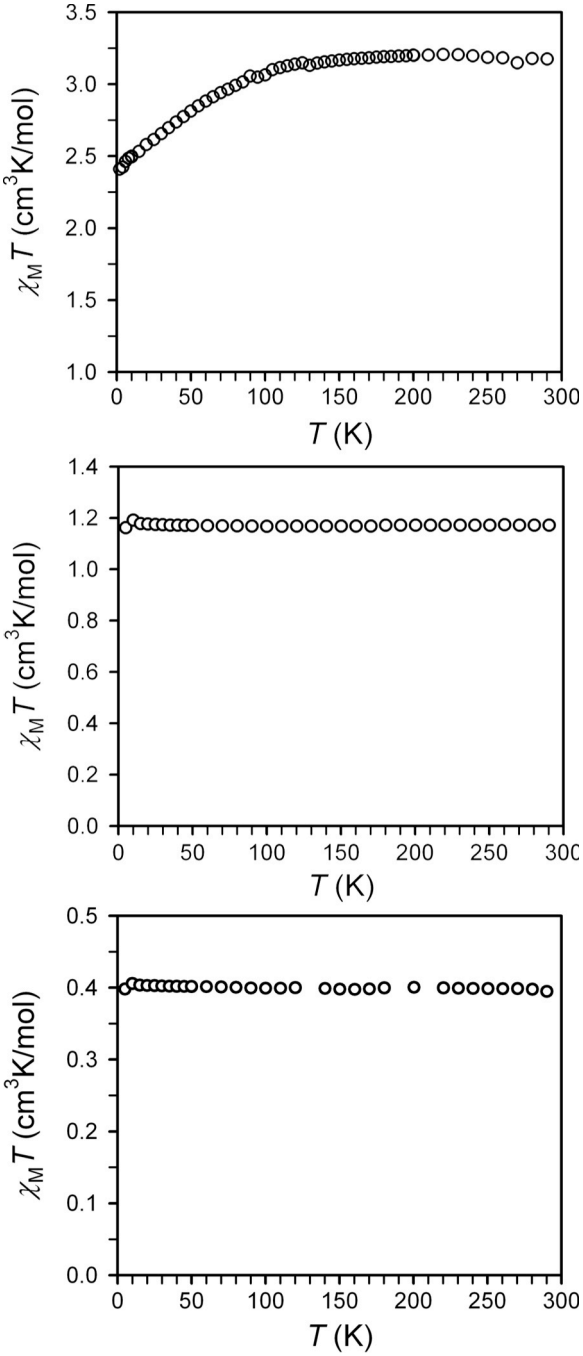


Figure 2.S2. Variable-temperature dc magnetic susceptibility data for **4** (top), **5** (middle), and **6** (bottom), collected on polycrystalline samples under an applied field of 1000 G.

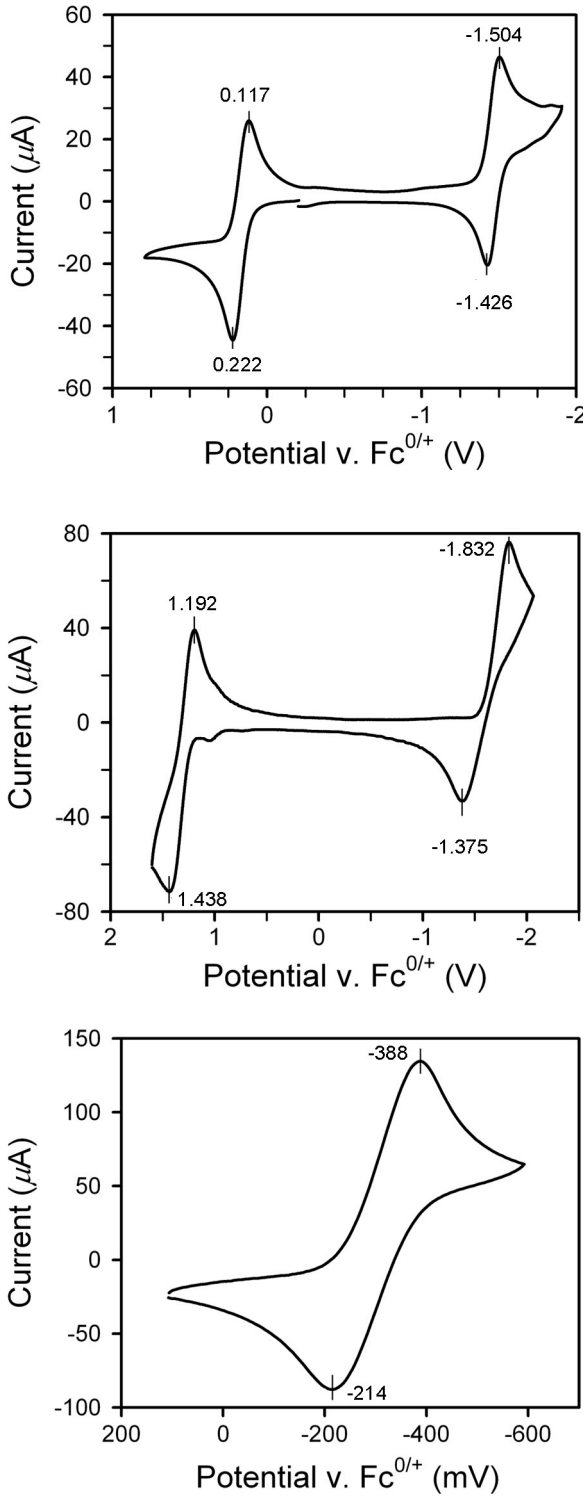


Figure 2.S3. Cyclic voltammograms of **4** (top), **5** (middle), and **6** (bottom) in acetonitrile. The measurement was performed using a platinum electrode and 0.1 M $(Bu_4N)PF_6$ supporting electrolyte.

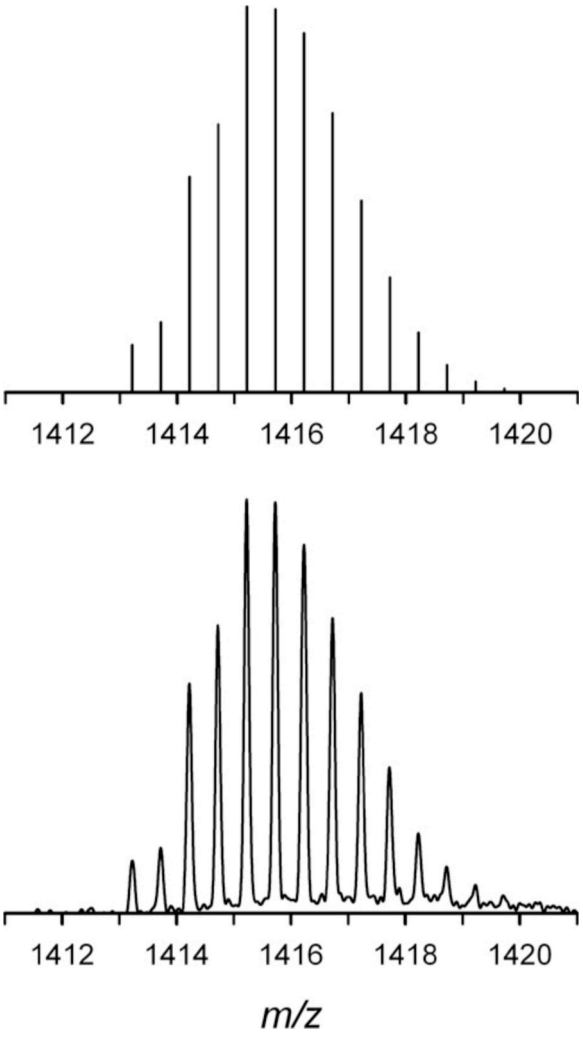


Figure 2.S4. Comparison of experimental data (bottom) and calculated isotopic distribution (top) for the ion $\{[(PY5Me)_2Cu^{II}_4Re^{IV}(CN)_7](PF_6)_3\}^{2+}$. The calculated distribution was obtained using the natural abundances of the relevant isotopes. Although the analyzed sample was prepared at low temperature, during the measurement it passes over an 80 °C heating block. As such, it is expected that the Re^{IV} containing species would be a minor component. This is indeed so, as the major ions observed in the measurement correspond to Re^{III} – containing clusters.

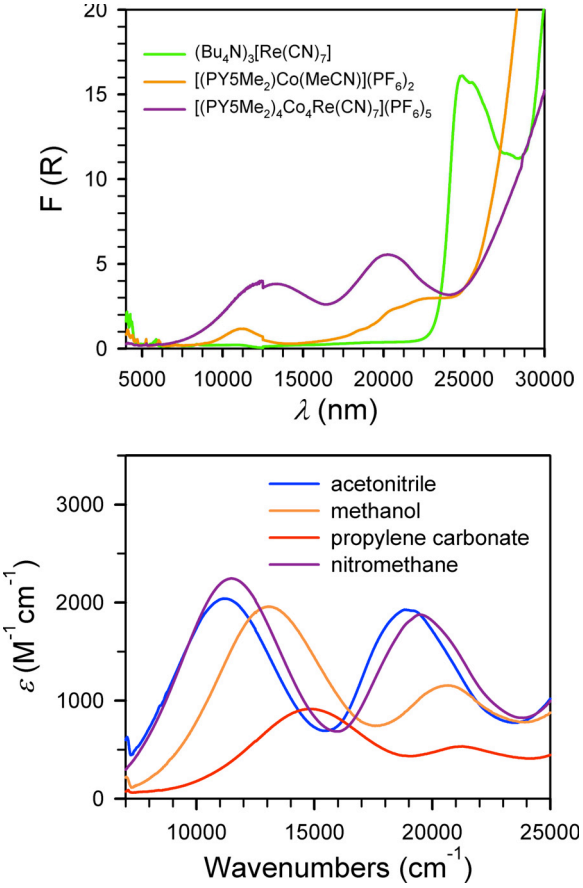


Figure 2.S5. Top: Solid state diffuse reflectance spectra of $(Bu_4N)_3[Re(CN)_7]$, **4**, and **7**. The y-axis is given as F(R), the Kubleka-Munk transform of the % Reflectance, for easier comparison to solution spectroscopic measurements. The values of F(R) for $[(PY5Me_2)Co(MeCN)](PF_6)_2$ have been multiplied by a factor of 10 for ease of view. Bottom: Solution UV-Vis spectra of **7** in solvents of different polarities.

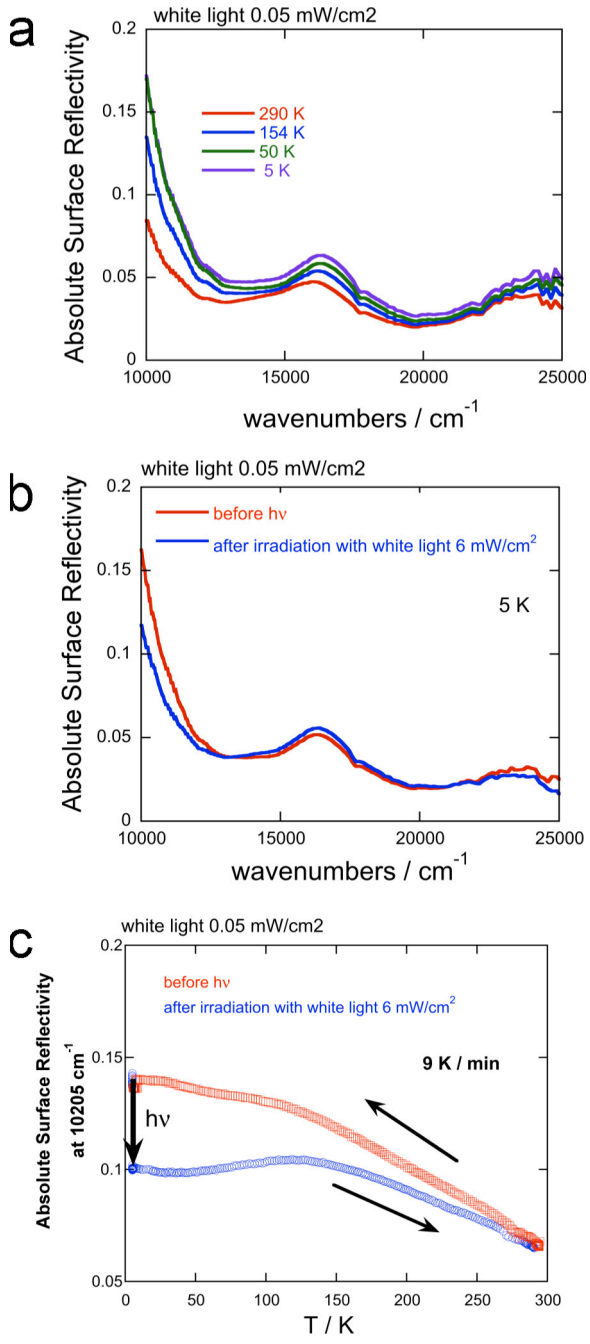


Figure 2.S6. **a.** Selected reflectivity spectra at different temperatures for **7** under white light irradiation (0.05 mW/cm^2). **b.** Absolute Surface Reflectivity spectra at 5 K before and after high power white light irradiation (6 mW/cm^2) for **7**. **c.** Absolute Surface Reflectivity at 10205 cm^{-1}, $R_{10205\ cm^{-1}}$, during cooling and heating modes (temperature sweep rate of 9 Kmin^{-1})

Chapter 3: Slow Magnetic Relaxation in a Pseudotetrahedral Cobalt(II) Complex with Easy-Plane Anisotropy

3.1. Introduction

Molecules that possess an axially bistable magnetic moment, referred to as single-molecule magnets, display slow magnetic relaxation upon removal of a magnetizing field, and have been suggested for applications in high-density information storage and quantum computing.[1] The recent observation of this effect in low-coordinate, high-spin iron(II) complexes[2] has prompted a new research effort geared toward developing mononuclear transition metal complexes as single-molecule magnets, since these species can exhibit significantly greater anisotropy than their multinuclear counterparts. Early observations of single-molecule magnet behavior in mononuclear complexes were restricted to the lanthanides,[3] where the spin-orbit coupling is great enough to compensate for any quenching effect from the ligand field. In contrast, for first-row transition metal complexes, the ligand field is usually much stronger than the spin-orbit coupling, such that first-order orbital angular momentum is largely quenched.[4] Here, however, a low coordination number can ensure a relatively weak ligand field, thereby maximizing the spin and spin-orbit coupling. Furthermore, variation of the ligand donor characteristics can then provide a means of tuning the magnetic anisotropy. Indeed, a variety of complexes of iron(II) with coordination numbers of four,[5] three,[6] and two[7] have been shown to possess a large axial zero-field splitting parameter, D, or even unquenched first-order orbital angular momentum.

For easy-axis ($D < 0$) integer-spin systems, resonant zero-field quantum tunnelling relaxation processes can be mediated by (i) dipolar interactions, (ii) hyperfine interactions, or (iii) transverse anisotropy (E).[8] In some instances, application of a small, static magnetic field can shut down such relaxation processes by removing the resonance through the Zeeman effect, thereby enabling the observation of slow magnetic relaxation via thermally activated mechanisms.[2,9] For example, field-induced slow relaxation has been observed for trigonal pyramidal iron(II) complexes, wherein the tunnelling between the $M_S = \pm 2$ levels was attributed to transverse anisotropy and/or dipolar interactions.[2ab] According to Kramers' theorem,[10] however, transverse anisotropy would not facilitate tunneling through mixing of the ground $\pm M_S$ levels for a non-integer spin system with $D < 0$. Thus, I began an investigation of low-coordinate $S = {}^3/_2$ cobalt(II) complexes with potentially large D values in an effort to find mononuclear transition metal complexes that display slow magnetic relaxation with no applied field.[11] In the course of this research, I unexpectedly discovered slow relaxation for a pseudotetrahedral cobalt(II) complex with easy-plane anisotropy ($D > 0$) under a dc field.

3.2. Experimental

3.2.1. Synthetic Materials and Methods. Unless otherwise noted, all manipulations were carried out at room temperature under an atmosphere of dinitrogen in a Vacuum Atmospheres glovebox or using Schlenk techniques. Acetonitrile (MeCN), diethylether (Et_2O), and

tetrahydrofuran (THF) were deoxygenated by sparging with dinitrogen and dried via a Vacuum atmospheres solvent purification system. $CoCl_2$ and $Na(CF_3SO_3)$ were purchased from Strem. Diatomaceous earth (Celite 545) was purchased from Fisher Scientific and dried by heating under vacuum. All other reagents were used as received. Literature procedures were used to prepare 1,1,1-tris[2*N*-(1,1,3,3-tetramethylguanidino)methyl]ethane (3G).[12] NMR spectra were recorded on Bruker DRX-500 spectrometer with Oxford Instruments 11.7 T magnet. Chemical shifts are reported in ppm and referenced to residual protiated solvent. Full-width at half maxima ($\Delta\nu_{1/2}$) are reported in Hz. IR spectra were recorded with a Bruker ALPHA FT-IR spectrometer fitted with a diamond ATR module. Elemental analyses were performed at the Microanalytical Facility at the University of California, Berkeley.

3.2.2. Synthesis of [(3G)CoCl](CF$_3$SO$_3$) (1). To a solution of 3G (560 mg, 1.36 mmol) in acetonitrile (3 mL) was added an acetonitrile solution (5 mL) of anhydrous $CoCl_2$ (176 mg, 1.36 mmol). The blue solution was stirred for 2 min, and then a solution of $Na(CF_3SO_3)$ (235 mg, 1.37 mmol) was added to the mixture. A suspension formed and the mixture was stirred for several hours. The resulting slurry was filtered through a bed of diatomaceous earth and the blue filtrate was concentrated to dryness under dynamic vacuum. The oily residue was dissolved in THF (5 mL) and the product was crystallized from this solution by vapor diffusion of Et_2O into the solution. The crystalline blue product was collected and dried under vacuum (650 mg, 0.99 mmol, 73% yield). Anal. Calcd. for $C_{21}H_{45}N_9CoClO_3F_3S$: C, 38.50; H, 6.92; N, 19.24 %. Found: C, 38.69; H, 7.14; N, 18.84 %. ^{1}H NMR (CD_3CN, 500 MHz, 20 ºC): 58.7 ($\Delta\nu_{1/2}$ = 650 Hz, N*Me*, 9H), 19.0 ($\Delta\nu_{1/2}$ = 130 Hz, N*Me*$_2$, 18H), 16.9 ($\Delta\nu_{1/2}$ = 440 Hz, N*Me*, 9H), –15.2 ($\Delta\nu_{1/2}$ = 40 Hz, C*Me*, 3H) ppm. FT-IR (ATR): 2896 (m), 1615 (m), 1532 (s), 1425 (m), 1397 (s), 1262 (CF_3SO_3, s), 1146 (CF_3SO_3, s), 1067 (CF_3SO_3, m), 1027 (CF_3SO_3, s), 921 (m), 780 (m), 635 (CF_3SO_3, s), 517 (CF_3SO_3, m) cm^{-1}.

3.2.3. HF-EPR Measurements. Single-crystal high-frequency EPR measurements were performed in a spectrometer that enabled in-situ rotation of the sample about a fixed axis; details can be found elsewhere.[13] The magnetic field was generated by a 36 T resistive magnet at the National High Magnetic Field Laboratory at FSU, Tallahassee. Variable frequency (300-450 GHz) and temperature measurements were conducted with the field aligned close to the molecular *z*-axis. Powder EPR measurements were carried out in a transmission type spectrometer based on a 17 T superconducting magnet at various frequencies in the range of 50-160 GHz.[14] The sample was finely ground and restrained with KBr in a Teflon container.

3.2.4. Magnetic Measurements. Magnetic data were collected using a Quantum Design MPMS-XL SQUID magnetometer. Measurements for **1** were obtained on finely ground microcrystalline powders (referred to as "solid samples" in the main manuscript) restrained in a frozen eicosane matrix within a polycarbonate capsule or as a butyronitrile solution sealed (under vacuum) in a quartz tube. All sample preparations were performed under an inert atmosphere and very quickly loaded into the SQUID to minimize any contact with air. Dc susceptibility measurements were collected in the temperature range 2-300 K under a dc field of 1000 Oe. Dc magnetization measurements were obtained in the temperature range 1.8-5 K under dc fields of 1, 2, 3, 4, 5, 6, and 7 T. Variable temperature, variable field magnetization data were fit with the program ANISOFIT 2.0.[15] In general, several different values of *E* could be obtained from fitting attempts and had little to no effect on the goodness-of-fit, depending only on the input values for

E. As such, only the maximum values of *E* are reported for fits to magnetization data. Ac susceptibility measurements were obtained in the temperature range 1.8 to 3.0 K under a 4 Oe ac field oscillating at frequencies of 1-1488 Hz, under an applied dc field of 1500 Oe. Dc magnetic susceptibility data were corrected for diamagnetic contributions from the sample holder and eicosane (or butyronitrile), as well as for the core diamagnetism of each sample (estimated using Pascal's constants). No differences in ac and dc susceptibility data were observed for crystals either dried *in vacuo* or moved immediately from the mother liquor to the sample holder with little time to dry.

3.2.5. X-ray Structure Determination. Data collection was performed on a single crystal coated with Paratone-N oil and mounted on Kaptan loops. During mounting, the crystals did not show any signs of desolvation, and the crystal was frozen under a stream of N_2 during measurements. Data were collected using a Bruker QUAZAR diffractometer equipped with a Bruker MICROSTAR X-ray source, APEX-II detector, and using Mo Ka (λ = 0.71073 Å) radiation. Raw data were integrated and corrected for Lorentz and polarization effects using Bruker APEX2 v. 2009.1.[16] Absorption corrections were applied using SADABS.[17] Space group assignments were determined by examination of systematic absences, *E*-statistics, and successive refinement of the structures. The crystal structure was solved by direct methods with the aid of successive difference Fourier maps in SHELXL.[18] The crystal did not show significant decay during data collection. Thermal parameters were refined anisotropically for all non-hydrogen atoms in the main body and the $CF_3SO_3^-$ counterion. Hydrogen atoms were placed in ideal positions and refined using a riding model for all structures. Full crystallographic details are given in Table 3.S1.

3.2.6. Electronic Absorption Spectroscopy. Solutions were prepared with butyronitrile that had been degassed by successive freeze pump thaw cycles and stored over activated sieves prior to use. Both solution and solid-state spectra were obtained on samples sealed under an inert atmosphere. Solution UV-vis-NIR absorption and diffuse reflectance spectra were collected over the range of 5000-30,000 cm^{-1} using a CARY5000 spectrophotometer interfaced to Varian WinUV software.

3.3. Results and Discussion

The compound $[(3G)CoCl](CF_3SO_3)$ (**1**; 3G = 1,1,1-tris[2*N*-(1,1,3,3-tetramethylguanidino)methyl]ethane)[12] was synthesized by addition of $Na(CF_3SO_3)$ to an acetonitrile solution of $CoCl_2$ and 3G. Diffusion of diethyl ether vapor into a THF solution of the isolated product subsequently afforded blue block-shaped crystals of **1** in 73% yield. X-ray analysis revealed the expected pseudotetrahedral coordination for the $[(3G)CoCl]^+$ complex, with three N donor atoms from the 3G ligand and an axial chloride ligand, as shown in Fig. 3.1. The complex deviates somewhat from local C_{3v} symmetry at the Co^{II} center, owing mainly to the chloride ligand being slightly displaced from the principal axis. With a shortest Co···Co separation of 8.593(1) Å, no close intermolecular exchange pathways are apparent in the structure.

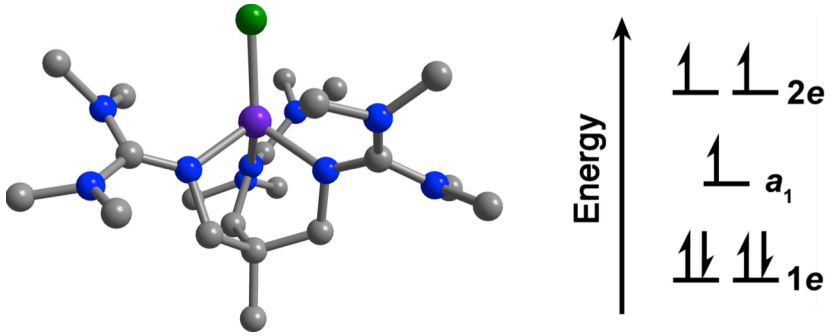


Figure 3.1. Left: Crystal structure of the pseudotetrahedral complex $[(3G)CoCl]^+$, as observed in **1**. Purple, green, blue, and gray spheres represent Co, Cl, N, and C atoms, respectively; H atoms are omitted for clarity. Selected interatomic distances (Å) and angles (deg): Co-N 1.993(1), 2.014(2), 2.024(1), Co-Cl 2.262(1), N-Co-N 96.14(6), 94.92(6), 94.27(6), N-Co-Cl 115.93(4), 120.50(4), 128.03(4). Right: Idealized d-orbital splitting diagram and electronic configuration for the complex, assuming C_{3v} symmetry.

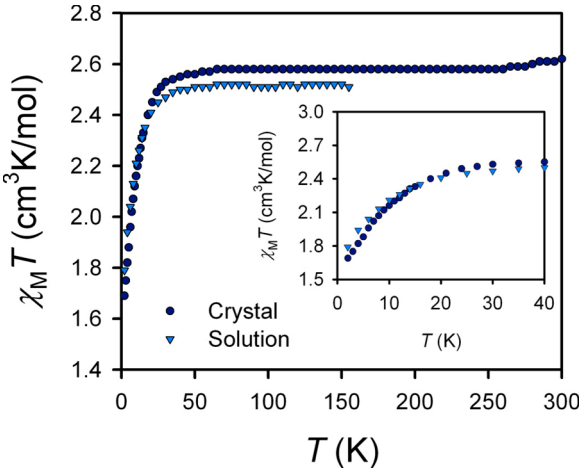


Figure 3.2. Variable temperature dc susceptibility data of microcrystalline (dark blue circles) and butyronitrile solution (light blue triangles) samples of **1**. Inset: Magnification of data collected at $T \leq 40$ K. Apparent differences in the low temperature $\chi_M T$ data could be due to the disruption of a very small long-range exchange interaction by the solution.

Dc magnetic susceptibility data were collected between 2 and 300 K for both crystalline powder and solution samples of **1** (see Fig. 3.2). At room temperature, $\chi_M T$ = 2.62 and 2.52 cm^3K/mol for the crystalline and solution samples, corresponding to an $S = {}^3/_2$ spin center with g = 2.36 and 2.15, respectively. For both samples, $\chi_M T$ begins to drop below 70 K, reaching respective values of 1.69 and 1.79 cm^3K/mol at 2 K. In the absence of any close Co···Co contacts, this downturn is likely attributable to the presence of magnetic anisotropy.

High-field, high-frequency EPR measurements were carried out on both powder and single crystal samples of **1** to obtain a definitive determination of the zero-field splitting parameters (see Figs. 3.3, 3.S1, 3.S2, and Appendix 2). The low-temperature powder data are typical for a system described by the zero-field Hamiltonian $H = D\hat{S}_z^2 + E(\hat{S}_x^2 - \hat{S}_y^2)$. Here, three components

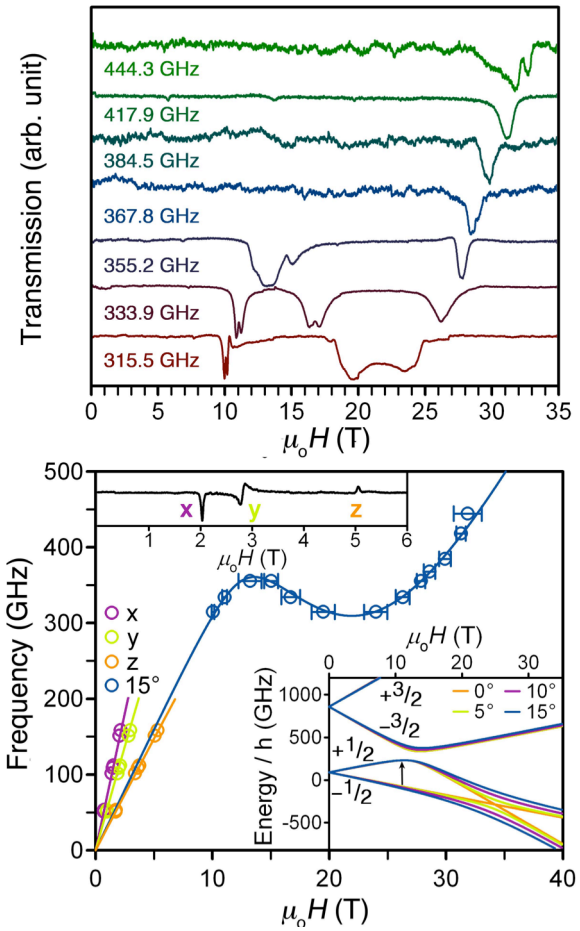


Figure 3.3. Top: Variable-frequency EPR spectra collected on a single crystal of **1** aligned 15° away from the *z*-axis at 4.2 K. The fine structure seen for some of the peaks is due either to weak disorder in the sample or an experimental artifact associated with the over-moded waveguide. Bottom: Peak positions as a function of frequency (f) from spectra collected on a powder sample of **1** at 5 K (f <200 GHz) and a single crystal at 4.2 K (f > 300 GHz) aligned 15° away from the parallel (z) direction. Solid lines are simulations of the frequency dependence of the peak positions employing the parameters given in the main text. Upper inset: Powder EPR spectrum recorded at 5 K and f = 151 GHz, showing x, y, and z transitions. Lower inset: Zeeman diagrams for various field misalignments; M_S levels are labelled and the arrow indicates the intra-Kramers doublet transition.

are observed, corresponding to transitions within the lowest $M_S = \pm^1/_2$ Kramers doublet, with the parallel component (effective Landé constant $g_{z,\mathrm{eff}}$ = 2.14) separated from the perpendicular components ($g_{x,\mathrm{eff}}$ = 5.28 and $g_{y,\mathrm{eff}}$ = 3.81), which are split due to a finite rhombic term.

The top panel of Fig. 3.3 shows the variable-frequency spectra collected at 4.2 K for a single crystal of **1** oriented *in situ* such that the field was close to the parallel (z) direction, while the bottom panel plots the resulting peak positions as blue circles. Most notable is the fact that three resonances are observed in the frequency range between 315 and 355 GHz. This observation can only be explained if $D > 0$ and the applied field is close to the parallel

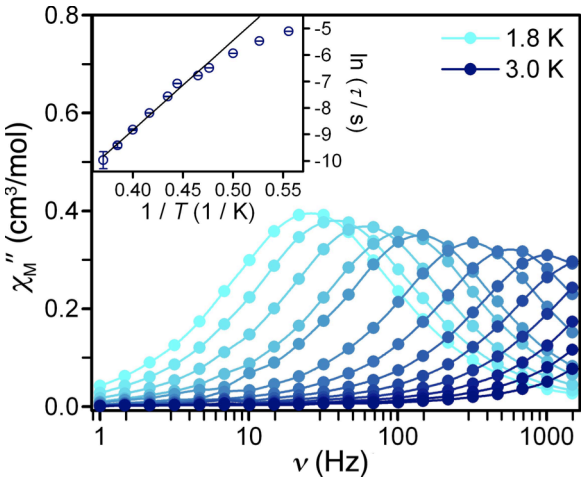


Figure 3.4. Variable-temperature ac magnetic susceptibility data obtained for **1** in a 1500-Oe dc field. Solid lines are guides for the eye. Inset: Arrhenius plot of relaxation time data (1σ error bars). The solid black line represents a fit to the linear region, giving $U_{\text{eff}} = 24$ cm^{-1} and $\tau_0 = 2 \times 10^{-10}$ s.

orientation; only a single resonance would be observed under all other physically relevant scenarios. The solid blue curve shows the best simulation of the data, as obtained for D = +12.7 cm^{-1}, E = 1.2 cm^{-1}, g_z = 2.17 and a field misalignment of 15°. Note that, even though the simulation included four parameters, the values obtained are quite robust (see Appendix 2). Moreover, the same parameterization (with $g_x = g_y = 2.30$) accounts perfectly for the powder data (see lower left portion of Fig. 3.2), and the D value is in reasonable agreement with the +11.4(1) cm^{-1} obtained by fitting magnetization data (see Fig. 3.S3).

Under zero applied dc field, no out-of-phase ac susceptibility (χ_M'') signal was observed for either the solid-state or solution sample at 2.0 K. Upon application of a 100-Oe dc field, however, a non-zero signal appeared for both phases (see Fig. 3.S4). For the crystalline sample, the peak maximum moves to lower frequencies until reaching a minimum at 65 Hz at 1500 Oe, staying relatively invariant to 4000 Oe. In contrast, the solution sample shows a high frequency shoulder that never develops into a full peak under applied dc fields of up to 1000 Oe. Cole-Cole plots were constructed from the molar in- and out-of-phase ac susceptibility data of the solid-state sample and fit to a generalized Debye model[19] to obtain values of the magnetic relaxation time for a given applied dc field (see Fig. 3.S5, top panel). With increasing field strength, the relaxation time increases to a maximum of 0.28 ms at 1500 Oe and then remains approximately constant up 4000 Oe (see Fig. 3.S5, bottom panel).

Variable-temperature ac frequency scans were performed on crystalline **1** to explore the thermal dependence of the magnetic relaxation time. As shown in Fig. 3.4, under a 1500-Oe dc field, a peak maximum is apparent from 1.8 to 2.6 K. Extraction of the magnetic relaxation times via fits to the Debye model were performed (see Fig. 3.S5, middle panel) and the subsequent data used to prepare the Arrhenius plot, depicted as the inset in Fig. 3.4. A fit to the linear portion of the data affords an effective relaxation barrier of $U_{\text{eff}} = 24$ cm^{-1} and $\tau_0 = 1.9 \times 10^{-10}$ s.

Under an applied field of 1500 Oe, any hyperfine and dipolar mediated relaxation processes are suppressed. In concert, the ground $M_S = \pm^1/_2$ levels are split by 0.12 cm^{-1} and direct relaxation between them is slow, possibly due to a lack of accessible phonon modes or inefficient

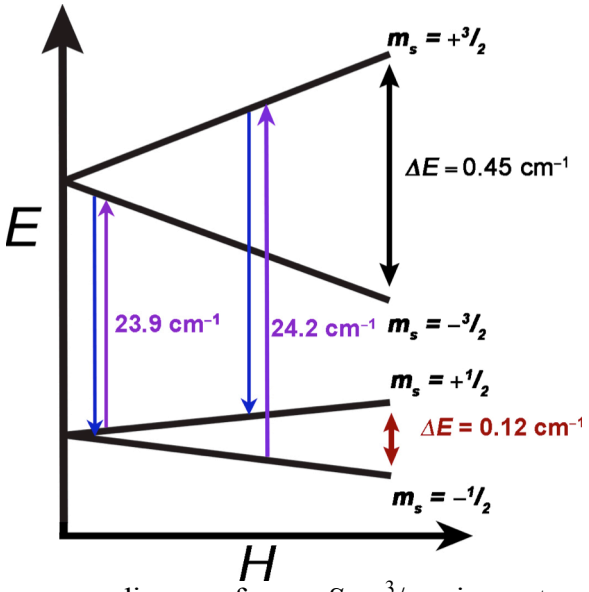


Figure 3.5. Zeeman energy diagram for an $S = {}^3/_2$ spin center with g, D, and E as determined by EPR. All energies correspond to $H = 1500$ Oe. Red arrows and energy indicate slow direct relaxation pathway. Purple arrows and labels indicate excitations utilized for Orbach relaxation pathways. Blue arrows indicate relaxations involved in the magnetic relaxation processes. Splitting of the m_s levels by the applied magnetic field is exaggerated for ease of depiction.

spin-phonon coupling. In addition, the transverse anisotropy mixes the $M_S = \pm{}^1/_2$ and $M_S = \pm{}^3/_2$ levels of opposite sign. The spin system thus follows a more efficient Orbach relaxation pathway through the excited $M_S = \pm{}^3/_2$ levels, leading to the observed barrier of 24 cm^{-1}, which is in close agreement with the $\pm{}^1/_2$ and $\pm{}^3/_2$ level separations calculated with the D values obtained from EPR and magnetization data (25 and 23 cm^{-1}, respectively). A graphical representation of the proposed relaxation mechanism is given in Fig. 3.5. A similar mechanism has been invoked recently for several polynuclear transition metal clusters, where relaxation has been proposed to occur through excited exchange coupled states.[20]

The faster relaxation rate of **1** in frozen solution can likely be attributed to a more efficient coupling between the spins and the phonon modes of the frozen glass compared to the crystal lattice. A substantial minimization of the D value via a distortion of the cobalt(II) coordination environment away from the crystal structure geometry is unlikely in view of the strong correlation of the spectral and magnetic data (see Figs 3.S2, 3.S3, 3.S6). The solution measurement also reveals that the phonon bottleneck is not due to poor contact with the thermal bath, as sometimes occurs for crystalline samples.[21] The value of τ_0 is in line with this idea, since it is much smaller than usual for a relaxation process involving a phonon bottleneck.

3.4 Outlook and Conclusions

The foregoing results demonstrate conclusively that typical single-molecule magnet behavior can be observed under an applied field for a mononuclear complex that has a positive axial zero-field splitting.[22] The direct relaxation between the $M_S = \pm{}^1/_2$ levels of the $S = {}^3/_2$

$[(3G)CoCl]^+$ complex in **1** is very slow, forcing the spin system to reach equilbrium through the higher-lying $M_S = \pm^3/_2$ levels via an Orbach mechanism. In such a situation, the thermal relaxation barrier, which corresponds to the energy difference between these levels, is identical to what would be expected if D were negative and of the same magnitude. In addition, the value of τ_0 obtained from the Arrhenius fit to the relaxation time data is within the usual range for single-molecule magnets with negative D. Thus, while higher-spin systems with negative D may potentially have a larger overall barrier, it is nonetheless of interest to look for slow relaxation in other complexes with large positive D values.

3.5. Acknowledgements

This research was supported by DoE/LBNL grant 403801 (synthesis) and NSF grants CHE-1111900 (magnetism) and DMR-0804408 (EPR). A portion of the work was performed at the National High Magnetic Field Laboratory, which is supported by the NSF (DMR-0654118) and the State of Florida. I am grateful to Drs. Nick Piro and Chris Chang for synthetic assistance as well as Drs. Junjie Liu and Stephen Hill for experimental assistance with HF-EPR. I thank also J. R. Long who served as a valuable resource throughout the performance of the work for this chapter.

3.6. References, Notes, and Supplementary Information

(1) Gatteschi, D.; Sessoli, R.; Villain, J. *Molecular Nanomagnets*, Oxford University Press: Oxford, 2006.

(2) (*a*) Freedman, D. E.; Harman, W. H.; Harris, T. D.; Long, G. J.; Chang, C. J.; Long, J. R. *J. Am. Chem. Soc.* **2010**, *132*, 1224. (*b*) Harman, W. H.; Harris, T. D.; Freedman, D. E.; Fong, H.; Chang, A.; Rinehart, J. D.; Ozarowski, A.; Sougrati, M. T.; Grandjean, F.; Long, G. J.; Long, J. R.; Chang, C. J. *J. Am. Chem. Soc.* **2010**, *132*, 18115. (*c*) Weismann, D.; Sun, Y.; Lan, Y.; Wolmershäuser, G.; Powell, A. K.; Sitzmann, H. D. *Chem. Eur. J.* **2011**, *17*, 4700. (*d*) Lin, P.-H.; Smythe, N. C.; Gorelsky, S. J.; Maguire, S.; Henson, N. J.; Korobkov, I., Scott, B. L, Gordon, J. C., Baker, R. T., Murugesu, M. *J. Am. Chem. Soc.* **2011**, *133*, 15806.

(3) (*a*) Ishikawa, N.; Sugita, M.; Ishikawa, T.; Koshihara, S.; Kaizu, Y. *J. Phys. Chem. B* **2004**, *108*, 11265. (*b*) Sorace, L.; Benelli, C.; Gatteschi, D. *Chem. Soc. Rev.* **2011**, *40*, 3092 and references therein.

(4) O. Kahn, *Molecular Magnetism*, John Wiley & Sons: New York, 1993; B. N. Figgis and M. A. Hitchman, *Ligand Field Theory and Its Applications*, John Wiley & Sons: New York, 2000.

(5) Popescu, C. V.; Mock, M. T.; Stoian, S. A.; Dougherty, W. G.; Yap, G. P. A.; Riordan, C. G. *Inorg. Chem.* **2009**, *48*, 8317.

(6) Andres, H.; Bominaar, E. L.; Smith, J. M.; Eckert, N. A.; Holland, P. L.; Münck, E. *J. Am. Chem. Soc.* **2002**, *124*, 3012.

(7) (*a*) Reiff, W. M.; Lapointe, A. M.; Witten, E. H. *J. Am. Chem. Soc.* ***2004***, *126*, 10206. (*b*) Reiff, W. M.; Schulz, C. E.; Whangbo, M.-H.; Seo, J. I.; Lee, Y. S.; Potratz, G. R.; Spicer, C. W.; Girolami, G. S. *J. Am. Chem. Soc.* **2009**, *131*, 404. (*c*) Merill, W. A.; Stich, T. A.; Brynda, M.; Yeagle, G. J.; Fettinger, J. C.; De Hont, R.; Reiff, W. M.; Schulz, C. E.; Britt, R. D.; Power, P. P. *J. Am. Chem. Soc.* **2009**, *131*, 12693.

(8) (*a*) Gatteschi, D.; Sessoli, R. *Angew. Chem. Int. Ed.* **2003**, *42*, 268. (*b*) Ishikawa, N.; Sugita, M.; Wernsdorfer, W. *J. Am. Chem. Soc.* **2005**, *127*, 3650. (*c*) Ishikawa, N.; Sugita, M.; Wernsdorfer, W. *Angew. Chem. Int. Ed.* **2005**, *44*, 2931.

(9) This means of supressing quantum relaxation processes has also been demonstrated for a number of f-element complexes: (*a*) Rinehart, J. D.; Long, J. R. *J. Am. Chem. Soc.* **2009**, *131*, 12558. (*b*) Rinehart, J. D.; Meihaus, K. R.; Long, J. R. *J. Am. Chem. Soc.* **2010**, *132*, 7572. (*c*) Meihaus, K. R.; Rinehart, J. D.; Long, J. R. *Inorg. Chem.* **2011**, *50*, 8484.

(10) N. M. Atherton, *Principles of Electron Spin Resonance*, Ellis Horwood Limited: Chichester, 1993.

(11) Very recently, two five-coordinate cobalt(II) complexes were reported to exhibit slow magnetic relaxation under an applied field: Jurca, T.; Farghal, A.; Lin, P.-H.; Korobkov, I.; Murugesu, M.; Richardson, D. S. *J. Am. Chem. Soc.* **2011**, *133*, 15814.

(12) Wittmann, H.; Schorm, A.; Sundemeyer, J. *Z. Anorg. Allg. Chem.* **2000**, *7*, 1583.

(13) Takahashi, S.; Hill, S. *Rev. Sci. Instrum.* **2005**, *76*, 023114.

(14) Hassan, A. K.; Pardi, L. A.; Krzystek, J.; Sienkiewicz, A.; Goy, P.; Rohrer, M.; Brunel, L. C. *J. Magn. Reson.* **2000**, *142*, 300.

(15) Shores, M. P.; Sokol, J. J.; Long, J. R. *J. Am. Chem. Soc.* **2002**, *124*, 2279.

(16) *APEX2*, v. 2009 ; Bruker Analytical X-Ray Systems, Inc: Madison, WI, 2009.

(17) Sheldrick, G. M. *SADABS,* Version 2.03; Bruker Analytical X-ray Systems, Inc: Madison, WI, 2000.

(18) Sheldrick, G. M., *SHELXTL*, Version 6.12; Bruker Analytical X-ray Systems, Inc: Madison, WI, 2000.

(19) (*a*) Cole, K. S.; Cole, R. H. *J. Chem. Phys.* **1941**, *9*, 341. (*b*) Böttcher, C. J. F. *Theory of Electric Polarisation*, Elsevier: New York, 1952. (*c*) Aubin, S. M. J.; Sun, Z. M.; Pardi, L.; Krzystek, J.; Folting, K.; Brunel, L. C.; Rheingold, A. L.; Christou, G.; Hendrickson, D. N. *Inorg. Chem.* **1999**, *38*, 5329.

(20) (*a*) Lampropoulos, C.; Hill, S.; Christou, G. *ChemPhysChem* **2009**, *10*, 2397. (*b*) Sanakis, Y.; Pissas, M.; Krzystek, J.; Telser, J.; Raptis, R. G. *Chem. Phys. Lett.* **2010**, *493*, 185. (*c*) Georgopoulou, A.; Sanakis, Y.; Boudalis, A. K. *Dalton Trans.* **2011**, *40*, 6371.

(21) Schenker, R.; Leuenberger, M. N.; Chaboussant, G.; Loss, D.; Gudel, H. U. *Phys. Rev. B* **2005**, *72*, 184403.

(22) Field-induced slow magnetic relaxation has previously been observed by Mössbauer spectroscopy for a mononuclear Fe^{III} complex with a positive *D*: Reiff, W. M.; Witten, E. H. *Polyhedron* **1984**, *3*, 443.

Table 3.S1. Crystallographic Data[a] for [(3G)CoCl](CF_3SO_3) (**1**).

Empirical formula	$C_{21}H_{45}ClCoF_3N_9O_3S$
Formula weight	655.11
T, K	100(2)
λ, Å	0.71073
Crystal system	Triclinic
Space group	$P\bar{1}$
a, Å	8.5546(3)
b, Å	13.9935(5)
c, Å	13.9935(5)
α, º	82.2440(10)
β, º	87.1460(10)
γ, º	72.3580(10)
V, Å^3	1529.76(9)
Z	2
$\rho_{calculated}$, g/cm^3	1.422
μ, mm^{-1}	0.774
F_{000}	690
Crystal dimensions	0.32 x 0.19 x 0.10 mm^3
θ range	2.50 to 28.90 º
Index ranges	$-10 \le h \le 11$
	$-17 \le k \le 18$
	$-17 \le l \le 18$
Reflections collected	30253
Independent reflections	6563 [R_{int} = 0.0287]
Completeness to θ = 28.90	99.50%
Data / restraints / parameters	6563 / 0 / 354
Goodness-of-fit on F^2	1.026
Final R indices [$I > 2\sigma(I)$][b]	R_1 = 0.0310, wR_2 = 0.0816
R indices (all data)	R_1 = 0.0345, wR_2 = 0.0840
Largest diff. peak and hole	0.470 and −0.378 eÅ^3

[a]Obtained with Mo Kα (λ = 0.71073 Å) radiation monochromated by QUAZAR multilayer mirrors. [b]$R_1 = \Sigma||F_o| - |F_c||/\Sigma|F_o|$, $wR_2 = \{\Sigma[w(F_o^2 - F_c^2)^2]/\Sigma[w(F_o^2)^2]\}^{1/2}$.

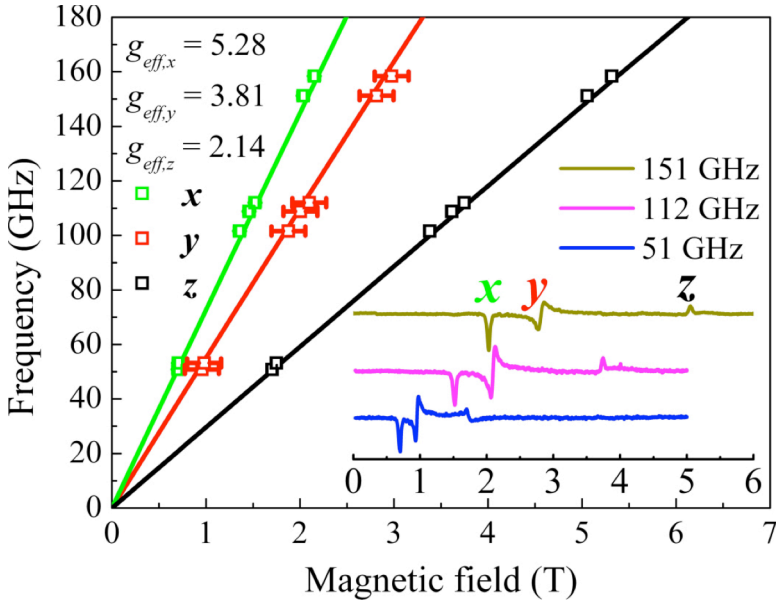


Figure 3.S1. Frequency dependence of the high-frequency EPR peak positions deduced from studies of a powder sample of **1** at 5 K. Representative spectra recorded in first-derivate mode are displayed in the inset (see ref. [2] for details of the measurement technique). Three branches of resonance are observed, corresponding to the three components of the Landé *g*-tensor (field parallel to *x*, *y* and *z*). The solid lines are simulations of these three branches employing the optimum parameters given in the main text. The presence of a lone high-field component ($g_{z,eff}$ = 2.14), well separated from two low-field components ($g_{y,eff}$ = 3.81 and $g_{x,eff}$ = 5.28), is indicative of easy-plane type anisotropy. It is also noteworthy that the parallel (*z*) component is weaker than expected, suggesting a possible reorientation of the microcrystallites in the powder under the application of the magnetic field. Such an effect would tend to weaken the parallel (*z*) component in the case of an easy-plane ($D > 0$) anisotropy. Finally, the splitting between the two low-field components ($g_{y,eff}$ and $g_{x,eff}$) is due to the non-negligible rhombic *E* term.

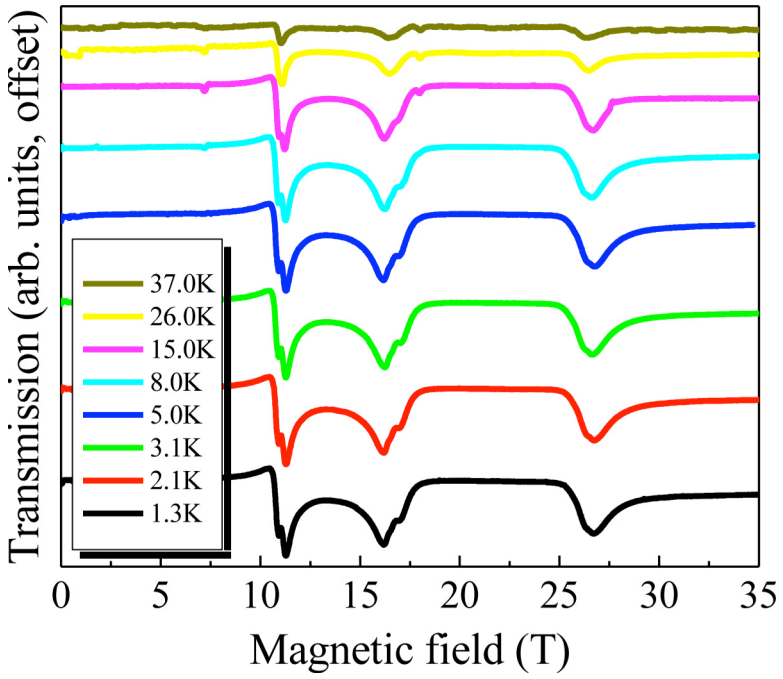


Figure 3.S2. Temperature dependence of the 333.9 GHz spectra displayed in Fig. 2. These measurements demonstrate that all three resonances strengthen and persist to the lowest temperature (k_BT << inter-Kramers separation). Consequently, all three excitations must occur within the ground state doublet.

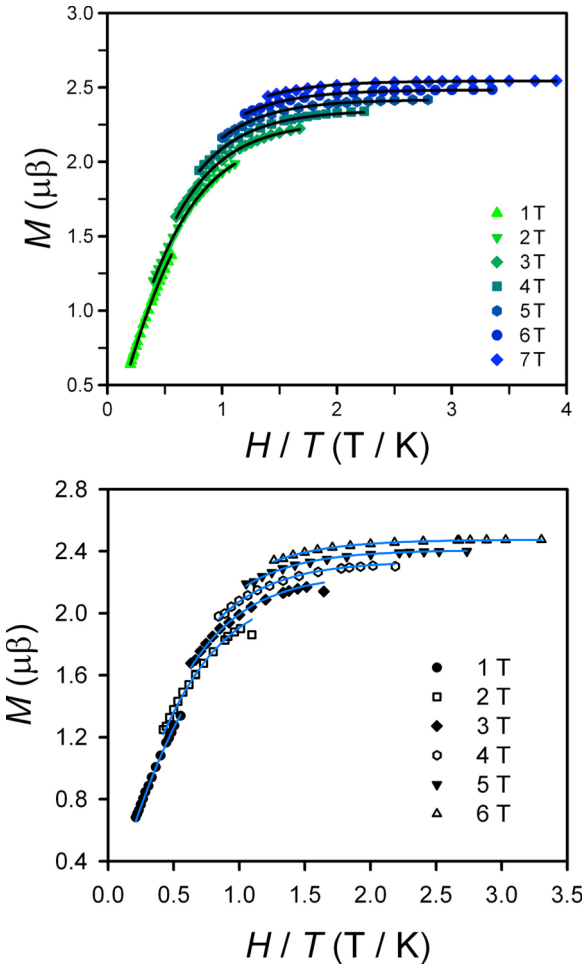


Figure 3.S3. Top: Magnetization data collected on microcrystalline **1** at various dc fields. Black lines correspond to best fits obtained with ANISOFIT 2.0, yielding $D = +11.3$ cm^{-1}, $|E| \leq 0.8$ cm^{-1}, and $g = 2.32$. Bottom: Variable temperature, variable field magnetization data collected on a solution sample of 1. Solid blue lines indicate the best fit to the data via ANISOFIT: $D = +11.5$ cm^{-1}, $|E| \leq 1.9$ cm^{-1}, $g_{iso} = 2.15$.

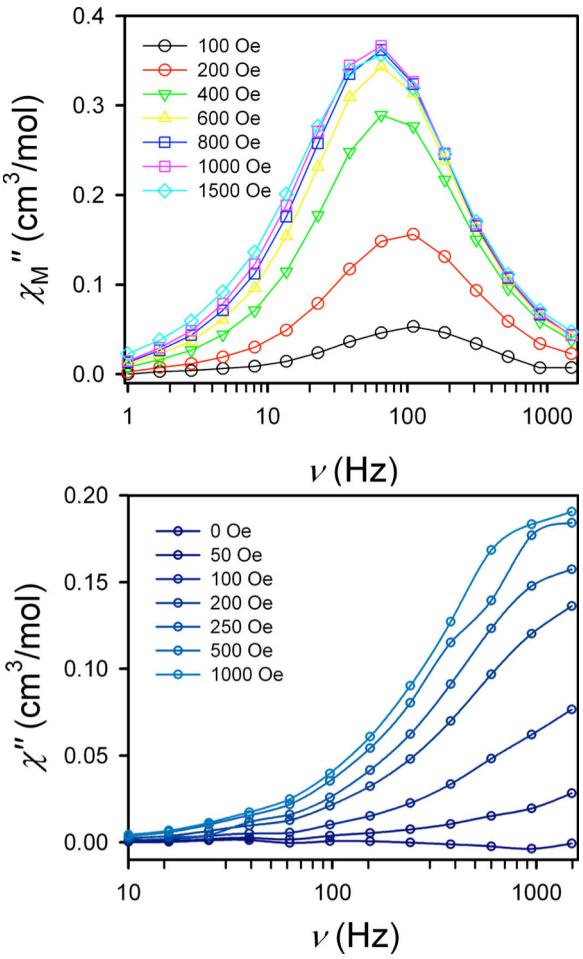


Figure 3.S4. Top: Frequency dependence of χ_M'' for a polycrystalline sample of **1** at 2 K under various applied dc field strengths. Data are shown only to the plateau in τ for clarity (see Fig. S10). Lines are guides for the eye. Bottom: Frequency dependence of χ_M'' under various applied dc field strengths for a butyronitrile solution of **1** at 2 K. Solid lines are guides for the eye. Lack of defined maxima precluded accurate determination of the field dependence of τ for **1** in solution.

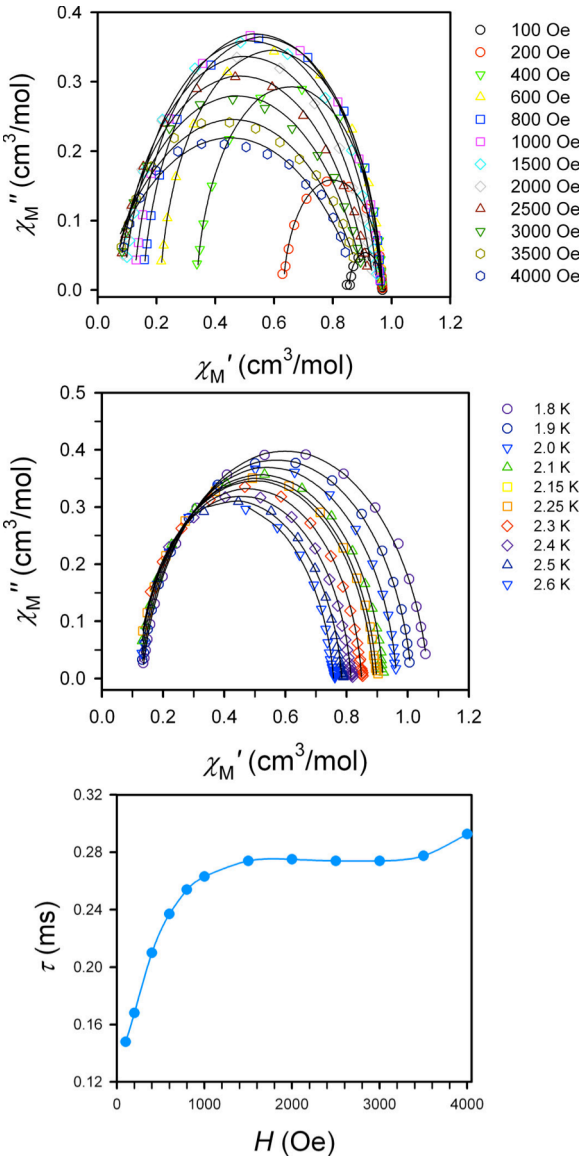


Figure 3.S5. Top: Cole-Cole plot for determining field dependence of the magnetic relaxation time of **1**. Black lines indicate fits via a generalized Debye model, as described in the main text. Middle: Cole-Cole plot used to determine the temperature dependence of the magnetic relaxation time, τ. Black lines represent best fits to a generalized Debye model, as discussed in the main body of the communication. Bottom: Field dependence of the magnetic relaxation time, τ, of a microcrystalline sample of **1** at 2 K.

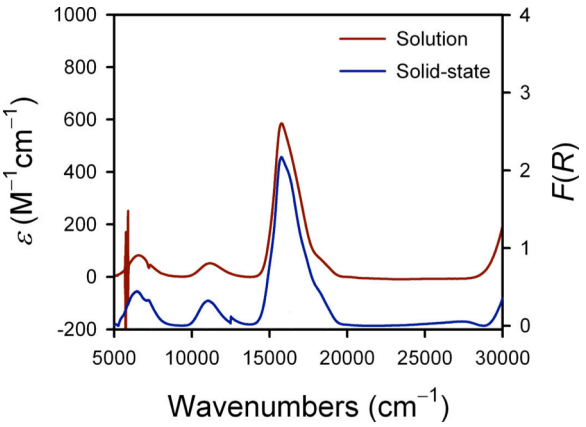


Figure 3.S6. Solution UV-Vis (red) and solid-state diffuse reflectance (blue) data obtained on **1**. Diffuse reflectance data are reported in terms of $F(R)$, the Kubelka-Munk transform of the % reflectance, for easier comparison to the solution data. The similarity spectral data of the solution and solid states eliminates a large structural distortion away from the crystal structure geometry as the source of the enhancement of the relaxation rate, as discussed in the main body of the report.

Chapter 4: Slow Magnetic Relaxation at Zero Field in the Tetrahedral Complex $[Co(SPh)_4]^{2-}$

4.1. Introduction

Molecules possessing an easy-axis ($D < 0$) anisotropy can display slow relaxation of the magnetic moment upon removal of a polarizing field. If the timescale of the relaxation exceeds that of computation, such single-molecule magnets could potentially find applications in high-density information storage or quantum computing.[1] The first molecule shown to exhibit magnetic bistability, $Mn_{12}O_{12}(O_2CMe)_{16}(H_2O)_4$, has a magnetic relaxation time of 2 months at 2 K.[2] Since this discovery, chemists have sought new, synthetically-tunable systems wherein the relaxation barrier might be systematically increased. In 2003, slow magnetic relaxation was observed in lanthanide complexes,[3] while more recently this behavior has also been reported for simple mononuclear complexes of actinides[4] and first-row transition metals.[5] Significantly, the ability to enhance the relaxation barrier by manipulating the ligand field has now been demonstrated for a series of trigonal pyramidal iron(II) complexes with $S = 2$ ground states.[5b] To date, however, all such mononuclear transition metal-based single-molecule magnets require application of a dc field to disrupt fast quantum tunneling relaxation processes.

Quantum tunneling of the magnetization stems from the mixing of $\pm M_S$ levels via hyperfine interactions, dipolar interactions, or transverse zero-field splitting (E).[6] The latter two possibilities can potentially be avoided by ensuring a large separation between molecules, and by utilizing a non-integer spin system, for which Kramers' theorem predicts that mixing of the ground $\pm M_S$ levels by E is forbidden.[7] Herein, the $S = {}^3/_2$ complex $[Co(SPh)_4]^{2-}$ is demonstrated to display slow magnetic relaxation in the absence of an applied magnetic field.

The compound $(Ph_4P)_2[Co(SPh)_4]$ (**1**)[8] was identified as a likely candidate for exhibiting slow magnetic relaxation in zero field, owing to its well-established ground state properties. In contrast to other mononuclear cobalt(II) systems probed for single-molecule magnet behavior, where the sign of D is either undetermined[5e] or positive,[9] extensive single-crystal EPR spectroscopy and susceptibility experiments,[10] as well as computations,[11] have shown **1** to possess a large, negative D value of -70 cm^{-1} and a relatively low rhombicity ($E/D < 0.09$). The large magnetic anisotropy of this system can be understood qualitatively by considering the electronic configuration and splitting of the d-orbitals, as shown in Figure 4.1. Calculations employing the angular overlap model indicate the close energetic proximity of the filled $3d_{x2-y2}$ orbital and the singly-occupied $3d_{xy}$ orbital.[10b] This near degeneracy results in a low-lying electronic excited state that can couple to the ground electronic state through spin-orbit coupling to afford a large zero-field splitting.

4.2. Experimental

4.2.1. Synthetic Methods and Dilution Characterization. Preparation of $(Ph_4P)_2[Co(SPh)_4]$ (**1**) and $(Ph_4P)_2[Zn(SPh)_4]$ were performed according the method of Dance.[12] Preparation of a sample possessing a 1:10 Co:Zn molar dilution (**2**) was done via co-preparation starting with a

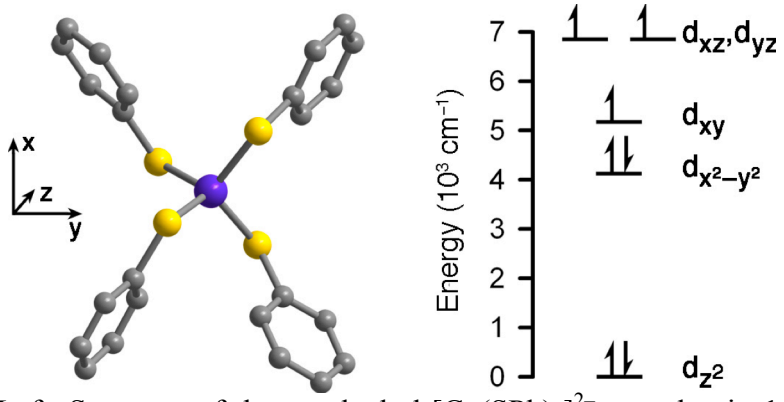


Figure 4.1. Left: Structure of the tetrahedral $[Co(SPh)_4]^{2-}$ complex in **1**,[8b] as viewed approximately along the *z*-axis. Purple, yellow, and gray spheres represent Co, S, and C atoms, respectively; H atoms are omitted for clarity. The molecule is somewhat elongated along *z*, so as to give approximate D_{2d} symmetry at the Co^{II} center. Selected interatomic distances (Å) and angles (deg): Co-S 2.316(4)-2.342(4), S-Co-S 95.6(2), 97.0(2), 113.5(2), 114.8(2), 116.1(2), 121.3(2), mean Co-S-C 110(2).[8b] Right: Electronic configuration and d-orbital energy level splitting for the molecule, with energies derived using the angular overlap model.[10b]

1:10 stoichiometry of $Co(NO_3)_2$•$6(H_2O)$ and $Zn(NO_3)_2$•$6(H_2O)$. Successful co-crystallization was confirmed by three methods. First, powder x-ray diffraction patterns were collected on pure **1** and **2** (see Fig 3.S1). Favorable comparison between that of pure **1** and **2**, as well as successful identification of the unit cells for both samples suggested successful dilution. Unfortunately, the similarity of the unit cells of **1** (a = 17.583(4) Å, b = 13.794(3) Å, c = 24.941(6) Å, $Pca2_1$) and **2** (a = 17.499(6) Å, b = 13.735(2) Å, c = 24.810(5) Å, $Pca2_1$) precluded accurate evaluation of sample composition by unit cell comparison.[13] At 2 K, the variable field magnetization data of pure **1** and **2** were compared. With a known sample mass, adjustment of the Co:Zn ratio in the sample was performed until the value of the saturation magnetization at 7 T was equivalent between the two samples. This technique suggested an effective Co:Zn ratio of 1:8. The third technique involved UV-Vis spectroscopy and has been previously employed[14] to determine the extent of dilution for EPR studies on **1**. The color of pure **1** is a dark green, while **2** is lime green. Although this alone suggests good dilution (as opposed to a collection of dark green and colorless crystals), a more quantitative measure of the Co:Zn ratio was obtained via solution UV-Vis measurements. Several standard solutions of **1** were prepared to develop a simple Beer's law calibration curve. Three solutions of the diluted sample were prepared and the corresponding measured absorbances, in addition to the known mass of the solid used to create the solutions, were used to calculate the concentrations. Utilizing two separate peaks (a MLCT at 23000 cm^{-1} and a *d-d* transition at 7500 cm^{-1}), the dilution is estimated at a ratio of 1 Co(II) to 10(2) Zn(II) ions. A picture of the two samples, as prepared for a SQUID measurement, is shown in Figure 3.S1. The color of the crystals is another good indication of successful dilution, since crystals of **2** are lime green, as opposed to a mixture of dark green and colorless crystals, which would correspond to $(Ph_4P)_2[Co(SPh)_4]$ and $(Ph_4P)_2[Zn(SPh)_4]$.

4.2.2. Magnetic Measurements. Magnetic data were collected using a Quantum Design MPMS-XL SQUID magnetometer. Measurements on **1** and **2** were obtained with finely ground microcrystalline powders restrained in a frozen eicosane matrix within a sealed quartz tube. Dc susceptibility measurements were collected in the temperature range 2-300 K under a dc field of

1000 Oe. Dc magnetization measurements were obtained in the temperature range 1.8-5 K under dc fields of 1, 2, 3, 4, 5, 6, and 7 T. Variable temperature, variable field magnetization data were fit with the program ANISOFIT 2.0.[15] In the course of fitting the magnetization data, an additional, good fit of $g_{iso} = 2.89$, $D = -114$ cm^{-1}, $|E| = 19$ cm^{-1} was obtained. The inability of the program to obtain a fit closer to the values obtained via EPR ($D = -70$ cm^{-1}, $|E| = 6$ cm^{-1}) could be from the assumption that g is isotropic. For systems with a large D, g should be very anisotropic. Ac susceptibility measurements were obtained in the temperature range 1.7 to 7.0 K under a 4 Oe ac field oscillating at frequencies of 0.06-1488 Hz, under applied dc fields from 0 to 1000 Oe. Dc magnetic susceptibility data were corrected for diamagnetic contributions from the sample holder and eicosane, as well as for the core diamagnetism of each sample (estimated using Pascal's constants).[16]

4.2.3. Powder X-ray Diffraction. Powder X-ray diffraction (PXRD) data for **1** and **2** were collected using a Bruker D8-Advance θ–2θ diffractometer in reflectance Bragg-Brentano geometry employing Ni filtered Cu K$\alpha_{1,2}$ lines focused radiation (1.54059 Å, 1.54439 Å) at 1600 W (40 kV, 40 mA) power and equipped with a Na(Tl) scintillation detector fitted at 0.2 mm radiation entrance slit. Samples were packed in air-free capillaries and mounted on a goniometer for measurement. The best counting statistics were achieved by collecting samples using a 0.02° 2θ step scan from 5° to 50° with exposure time of 1 s per step. All measurements were performed at room temperature and atmospheric pressure. A standard peak search, followed by indexing via the Single Value Decomposition approach,[17] as implemented in TOPAS-Academic,[18] allowed the determination of approximate unit cell parameters.

4.2.4. UV-Vis Spectroscopy. UV-Vis-NIR solution spectra were collected using a CARY 5000 spectrophotometer interfaced with Varian WinUV software. Solutions were prepared with deoxygenated, anhydrous acetonitrile and sealed in airfree quartz cuvettes for measurement.

4.3. Results and Discussion

Dc magnetic susceptibility data collected for **1** reveal the hallmarks of a significant magnetic anisotropy (see Fig. 4.S2). At 300 K, $\chi_M T = 3.11$ cm^{3}K/mol, consistent with an $S = {}^3/_2$ complex with $g = 2.57$. This value of $\chi_M T$ remains relatively constant down to 80 K, where it begins to decrease, reaching 2.46 cm^{3}K/mol at 2 K. Variable-temperature magnetization data were collected between 2 and 5 K at selected applied fields to extract a D value for comparison with the results obtained previously from EPR spectra. Employing ANISOFIT 2.0,[19] the best fit to the data afforded $D = -74$ cm^{-1} and $|E| \leq 0.01$ cm^{-1}. While the D value is comparable to that observed by EPR spectroscopy, albeit only crudely-determined, the E value is lower by at least two orders of magnitude.

As depicted in Fig. 4.2, ac magnetic susceptibility data collected in the absence of an applied dc field display a temperature-dependent peak in the out-of-phase ac susceptibility (χ_M'') indicative of a slowly relaxing magnetic moment. From 1.8 to 2.5 K, the peak appears at 28 Hz and decreases in height with increasing temperature. At temperatures above 2.5 K, the peak begins to shift to higher frequencies, until at 7 K it reaches the frequency limit of the instrument. Thus, compound **1** represents the first example of a mononuclear transition metal complex that behaves as a single-molecule magnet without requiring an applied field to suppress quantum relaxation processes.

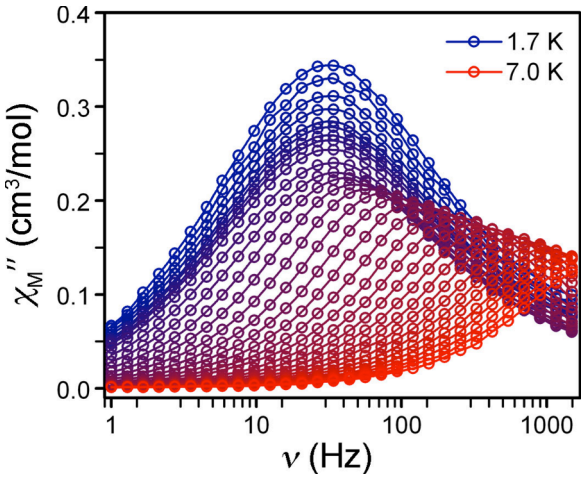


Figure 4.2. Frequency dependence of the molar out-of-phase ac susceptibility (χ_M'') of **1** collected at temperature intervals of 0.1 K between 1.7 and 2.4 K and 0.2 K between 2.4 and 7.0 K with no applied dc field. Solid lines are guides for the eye.

Application of a small dc field at 2 K does, however, dramatically alter the profile of the χ_M'' frequency scan, as shown in Figure 4.3. Here, the peak observed at 28 Hz under zero field rapidly diminishes while a much lower-frequency peak simultaneously intensifies. This change continues until 1 kOe, at which point the high-frequency peak has completely disappeared. The low-frequency peak is strongly temperature-dependent over the entire temperature region probed (see Figure 4.S3), and above 5 K it begins to overlay with the peak obtained in zero field. Overall, this nearly isosbestic behavior nicely illustrates the change in the relaxation mechanism from quantum tunneling to thermal activation, as discussed below.

To elucidate the role of intermolecular interactions in the magnetic relaxation of **1**, a magnetically dilute sample was prepared by cocrystallization with the isostructural compound $(Ph_4P)_2[Zn(SPh)_4]$[8a,b] to yield $(Ph_4P)_2[Co_{0.09}Zn_{0.91}(SPh)_4]$ (**2**). The relaxation dynamics of this diluted phase at zero field are slow and display strong temperature dependence from 1.7 to 7.0 K (see Figure 4.S3). Importantly, the peaks approximately overlay those of pure **1** under an applied field. Application of a static dc field to **2** also slows the magnetization dynamics (see Figure 4.S3), but in a much less dramatic fashion. Here, a single low-frequency peak shifts slightly from 1.8 Hz at 0 Oe to 0.2 Hz at 800 Oe instead of generating a second peak at a much different frequency.

The temperature dependence of the magnetic relaxation time, τ, provides valuable information about the magnetic relaxation processes that occur in **1** and **2**. Cole-Cole plots were generated from the ac magnetic susceptibility data, and a generalized Debye model[20] was used to extract relaxation times (see Figures 4.S4 and 4.S5). The results were employed in constructing the Arrhenius plots shown at the bottom of Figure 4.3. For compound **1**, τ is temperature-independent between 1.8 and 2.5 K, a common observation for relaxation processes that are associated with quantum tunneling of the magnetization. In contrast, above 2.5 K, τ becomes temperature-dependent, eventually approximating the Arrhenius behavior associated with a thermally activated regime. In contrast, upon application of a dc field of 1 kOe, τ shows a strong temperature dependence at all temperatures. The relaxation times for **2** almost perfectly overlay those obtained for **1** under a 1 kOe dc field, and do not display the dramatic field dependence

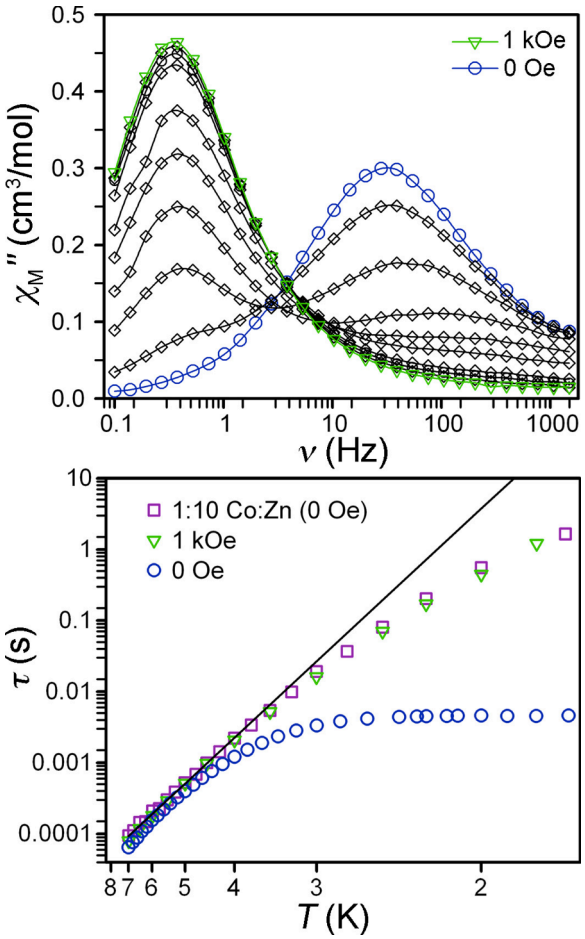


Figure 4.3. Top: Molar out-of-phase susceptibility (χ_M'') collected on pure **1** at 2 K under applied dc fields from 0 to 1 kOe in 100 Oe increments. Solid lines are guides for the eye. Bottom: Arrhenius plots of relaxation times of **1** as a pure substance under 0 and 1 kOe, and diluted in a matrix of $(Ph_4P)_2[Zn(SPh)_4]$ under 0 Oe. The black line corresponds to a linear fit to the highest-temperature data of the diluted sample, as described in the main text.

associated with **1**. Here, τ shifts from 0.55 s at 0 Oe to only 1.01 s at 600 Oe (see Figure 4.S3). Linear fits to the relaxation times observed between 5 and 7 K for **1** under 0 and 1 kOe, as well as for **2**, yield the following average values for the spin reversal barrier and attempt time for the tetrahedral $[Co(SPh)_4]^{2-}$ complex in this structure: $U_{eff} = 21(1)$ cm^{-1} and $\tau_o = 1.0(3) \times 10^{-6}$ s. We note that the latter value is slightly larger than the range typically observed for single-molecule magnets. The observation of slow magnetic relaxation for the diluted compound **2** confirms that the slow magnetic relaxation is intrinsic to the individual $[Co(SPh)_4]^{2-}$ molecules, and is not associated with phonon bottleneck effects or polymolecular relaxation processes.[21]

In light of the large, negative D values obtained from magnetization and EPR data, which predict a relaxation barrier of at least 140 cm^{-1}, the much small value of U_{eff} is somewhat surprising. Were this barrier achieved, magnetic hysteresis loops for **1** and **2**, which are closed at the lowest temperatures reachable with the magnetometer (see Figure 4.S6), would likely be

open at low temperatures. The temperature-independent region of the Arrhenius plot for **1** in a zero applied dc field indicates that quantum relaxation processes are operational, and these could be hindering the observation of the full barrier, as also evidenced by the large τ_0. The dilution experiments, however, show that the barrier height is unchanged after mitigating the intermolecular interactions. The source of the small U_{eff} must therefore be a different mediator for quantum tunneling or something else entirely. Inspection of the bistable ground state wavefunctions of an $S = {}^3/_2$ system with a negative D and non-zero E reveals that the $|M_S = \pm{}^3/_2>$ wavefunctions contain a small but non-negligible contribution from the $M_S = \pm{}^1/_2$ levels.[22] Although E does not directly mix the $M_S = \pm{}^3/_2$ levels, the mixing of the ground and excited levels could perhaps be at the root of the observation of a U_{eff} value much less than $2D$.

4.4. Outlook and Conclusions

The foregoing results constitute the first instance of slow magnetic relaxation for a mononuclear transition metal complex without the requirement of a static applied dc field, as directly probed via ac magnetic susceptibility measurements. Importantly, dilution of the $[Co(SPh)_4]^{2-}$ complex within an isostructural diamagnetic matrix was shown to eliminate quantum tunneling relaxation processes, indicating that they occur via intermolecular dipolar interactions. Future efforts will study the effects of varying the geometry and ligand field of this complex on the single-molecule magnet behavior through changes in the countercation and thiolate ligands, as well as the exploration of other low-coordinate complexes with non-integer spin and a large axial anisotropy.

4.5. Acknowledgements

This research was supported by NSF grant CHE-1111900. I thank Tyco Electronics for fellowship support, and Dr. T. D. Harris and Dr. D. E. Freedman for helpful discussions, as well as Dr. M. E. Fasulo for an initial supply of benzenethiol.

4.6. References, Notes, and Supplementary Information

(1) (*a*) Leuenberger, M. N.; Loss, D. *Nature* **2001**, *410*, 789. (*b*) Gatteschi, D.; Sessoli, R.; Villain, J. *Molecular Nanomagnets*, Oxford University Press: Oxford, 2006.

(2) (*a*) Sessoli, R.; Hui, L.; Schake, A. R.; Wang, S.; Vincent, J. B.; Folting, J.; Gatteschi, D.; Christou, G.; Hendrickson, D. N. *J. Am. Chem. Soc.* **1993**, *115*, 1804. (*b*) Sessoli, R.; Gatteschi, D.; Caneschi, A.; Novak, M. A. *Nature* **1993**, *365*, 141.

(3) (*a*) Ishikawa, N.; Sugita, M.: Ishikawa, T.; Koshihara, S.-Y.; Kaizu, S. *J. Am. Chem. Soc.* **2003**, *125*, 8694. (*b*) Ishikawa, N.; Sugita, M.; Ishikawa, T.; Koshihara, S.; Kaizu, S. *J. Phys. Chem. B.* **2004**, *108*, 11265. (*c*) AlDamen, M. A.; Clemente-Juan, J. M.; Coronado,

E.; Martí-Gastaldo, C.; Gaita-Ariño, A. *J. Am. Chem. Soc.* **2008**, *130*, 8874. (*d*) AlDamen, M. A.; Cardona-Serra, S.; Clemente-Juan, J. M.; Coronado, E.; Gaita-Ariño, A.; Martí-Gastaldo, C.; Luis, F.; Montero, O. *Inorg. Chem.* **2009**, *48*, 3467.

(4) (*a*) Rinehart, J. D.; Long, J. R. *J. Am. Chem. Soc.* **2009**, *131*, 12558. (*b*) Rinehart, J. D.; Meihaus, K. R.; Long, J. R. *J. Am. Chem. Soc.* **2010**, *132*, 7572. (*c*) Magnani, N.; Apostolidis, C.; Morgenstern, A.; Colineau, E.; Griveau, J.-C.; Bolvin, H.; Walter, O.; Caciuffo, R. *Angew. Chem. Int. Ed.* **2011**, *50*, 1696. (*d*) Antunes, M. A.; Pereira, L. C. J.; Santos, I. C.; Mazzanti, M.; Marçalo, J.; Almeida, M. *Inorg. Chem.* **2011**, *50*, 9915.

(5) (*a*) Freedman, D. E.; Harman, W. H.; Harris, T. D.; Long, G. J.; Chang, C. J.; Long, J. R. *J. Am. Chem. Soc.* **2010**, *132*, 1224. (*b*) Harman, W. H.; Harris, T. D.; Freedman, D. E.; Fong, H.; Chang, A.; Rinehart, J. D.; Ozarowski, A.; Sougrati, M. T.; Grandjean, F.; Long, G. J.; Long, J. R.; Chang, C. J. *J. Am. Chem. Soc.* **2010**, *132*, 18115. (*c*) Weismann, D.; Sun, Y.; Lan, Y.; Wolmershäuser, G.; Powell, A. K.; Sitzmann, H. *Chem. Eur. J.* **2011**, *17*, 4700. (*d*) Lin, P.-H.; Smythe, N. C.; Gorelsky, S. I.; Maguire, S.; Henson, N. J.; Korobkov, I.; Scott, B. L.; Gordon, J. C.; Baker, R. T.; Murugesu, M. *J. Am. Chem. Soc.* **2011**, *133*, 15806. (*e*) Jurca, T.; Farghal, A.; Lin, P.-H.; Korobkov, I.; Murugesu, M.; Richeson, D. S. *J. Am. Chem. Soc.* **2011**, *133*, 15814.

(6) Gatteschi, D.; Sessoli, R. *Angew. Chem. Int. Ed.* **2003**, *42*, 268.

(7) Kramers, H. A. *Proc. R. Acad. Sci. Amsterdam* **1930**, *33*, 959.

(8) (*a*) Holah, D. G.; Coucouvanis, D. *J. Am. Chem. Soc.* **1975**, *97*, 6917. (*b*) Swenson, D.; Baenziger, N. C.; Coucouvanis, D. *J. Am. Chem. Soc.* **1978**, *100*, 1932. (*c*) Dance, I. G. *J. Am. Chem. Soc.* **1979**, *101*, 6264.

(9) Zadrozny, J. M.; Liu, J.; Piro, N. A.; Chang, C. J.; Hill, S.; Long, J. R. *Chem. Commun.* **2012**, *48*, 3927.

(10) (*a*) Fukui, K.; Ohya-Nishiguchi, H.; Hirota, N. *Bull. Chem. Soc. Jpn.* **1991**, *64*, 1205. (*b*) Fukui, K.; Kojima, N.; Ohya-Nishiguchi, H.; Hirota, N. *Inorg. Chem.* **1992**, *31*, 1338. (*c*) Fukui, K.; Masuda, H.; Ohya-Nishiguchi, H.; Kamada, H. *Inorg. Chim. Acta.* **1995**, *238*, 73.

(11) Maganas, D.; Sottini, S.; Kyritsis, P.; Groene, E. J. J.; Neese, F. *Inorg. Chem.* **2011***, 50*, 8741.

(12) Dance, I. G. *J. Am. Chem. Soc.* **1979**, *101*, 6264.

(13) Swenson, D.; Baenziger, N. C.; Coucouvanis, D. *J. Am. Chem. Soc.* **1978**, *100*, 1932.

(14) Fukui, K.; Kojima, N.; Ohya-Nishiguchi, H.; Hirota, N. *Inorg. Chem.*, **1992**, *31*, 1338.

(15) Shores, M. P.; Sokol, J. J.; Long, J. R. *J. Am. Chem. Soc.* **2002**, *124*, 2279.

(16) Though these constants are well established in a variety of references, the following has an exceptional collection of almost all useful values for the necessary calculations: Bain, G. A.; Berry, J. F. *J. Chem. Educ.* **2008**, *85*, 532.

(17) Coelho, A. *Appl. Cryst.* **2003**, *36*, 86.

(18) Coelho, A. *TOPAS-Academic*, Version 4.1, Coelho Software, Brisbane, **2007**.

(19) Shores, M. P.; Sokol, J. J.; Long, J. R. *J. Am. Chem. Soc.* **2002**, *124*, 2279.

(20) (*a*) Cole, K. S.; Cole, R. H. *J. Chem. Phys.* **1941**, *9*, 341. (*b*) Böttcher, C. J. F. *Theory of Electric Polarisation*, Elsevier: New York, 1952. (*c*) Aubin, S. M. J.; Sun, Z. M.; Pardi, L.; Krzystek, J.; Folting, K.; Brunel, L. C.; Rheingold, A. L.; Christou, G.; Hendrickson, D. N. *Inorg. Chem.* **1999**, *38*, 5329.

(21) (*a*) Schenker, R.; Leuenberger, M. N.; Chaboussant, G.; Loss, D.; Güdel, H. U. *Phys. Rev. B.* **2005**, *72*, 184403. (*b*) Lopez, N.; Prosvirin, A. V.; Zhao, H.; Wernsdorfer, W.; Dunbar, K. R. *Chem. Eur. J.* **2009**, *15*, 11390. (*c*) Meihaus, K. R.; Rinehart, J. D.; Long, J. R. *Inorg. Chem.* **2011**, *50*, 8484.
(22) Atherton, N. M. *Principles of Electron Spin Resonance*, Ellis Horwood Limited: Chichester, 1993.

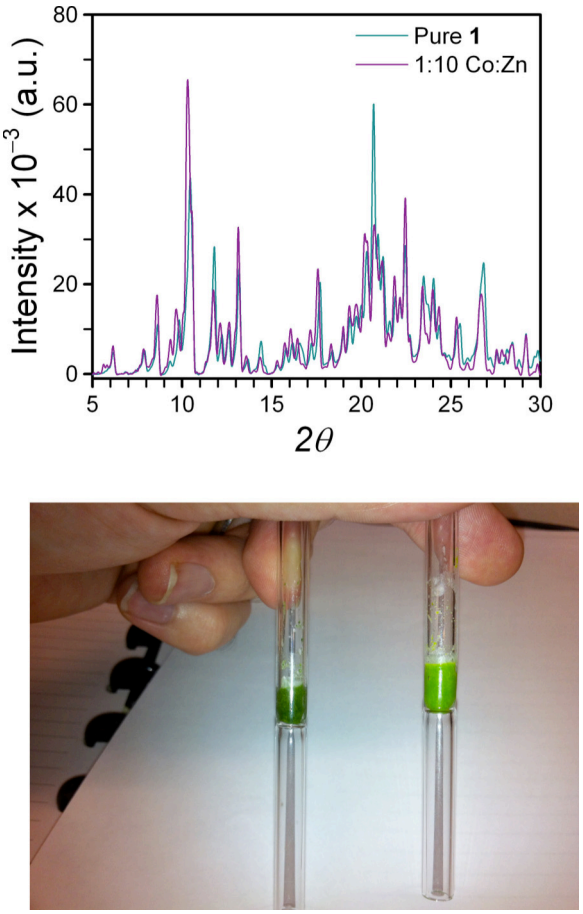


Figure 4.S1. Top: X-ray diffraction patterns collected on powder samples of pure **1** and the diluted compound. Bottom: Photograph of the thesis author holding pure **1** (left) and the diluted compound **2** (right), as prepared for SQUID magnetometry experiments. Note the limegreen color of **2** in contrast to the dark green color of pure **1**.

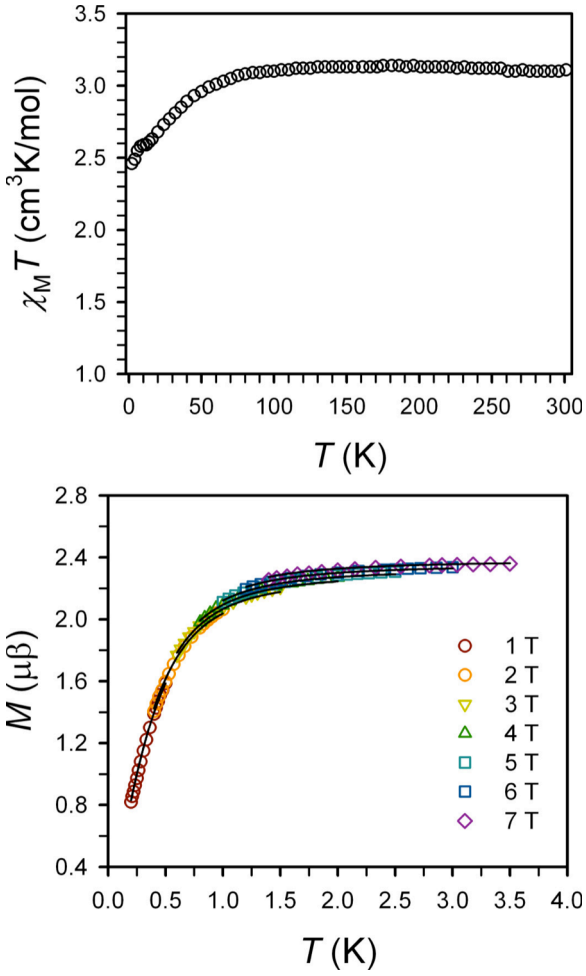


Figure 4.S2. Top: Variable-temperature dc susceptibility data under an applied dc field of 1000 Oe of a pure polycrystalline sample of **1** restrained under eicosane. Bottom: Variable-temperature, variable-field dc magnetization data collected on a polycrystalline sample of **1** restrained under eicosane. Fields of 1 to 7 T were used at temperatures from 2 to 5 K. Solid black lines indicate the best fits with the program ANISOFIT 2.0 yielding the spin-hamiltonian parameters $g = 2.91$, $D = -74\ \text{cm}^{-1}$, and $|E| = 0.01\ \text{cm}^{-1}$, as discussed in the main body of the report.

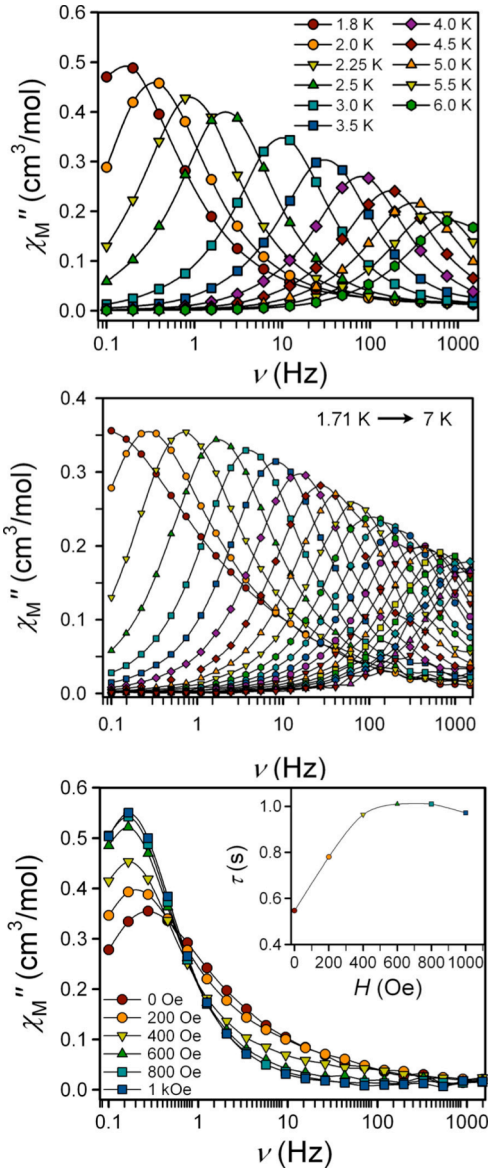


Figure 4.S3. Top: Frequency dependence of χ_M'' as a function of temperature of **1** under a static 1000 Oe applied dc field. Solid lines are a guide for the eye. Middle: Frequency dependence of χ_M'' as a function of temperature of **2** under zero applied dc field. Solid lines are guides for the eye. Bottom: Frequency dependence of χ_M'' as a function of applied field of **2** at 2 K. Inset: Field dependence of τ for **2**. Black lines for the main plot and the inset are guides for the eye.

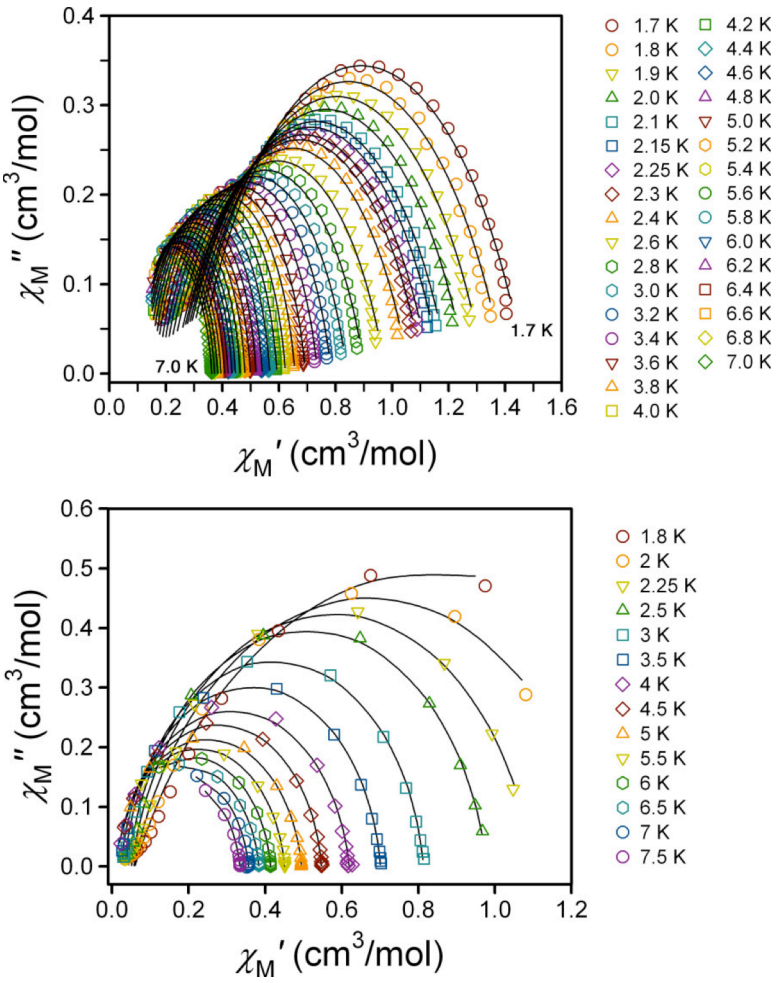


Figure 4.S4. Top: Cole-cole plots fit for the determination of the temperature dependence of τ for pure **1** under zero dc applied field. Black lines are the result of fits to a generalized Debye model as described in the main text. Bottom: Cole-Cole plots fit for the determination of the temperature dependence of τ for pure **1** under 1000 Oe dc applied field. Black lines are the result of fits to a generalized Debye model as described in the main text.

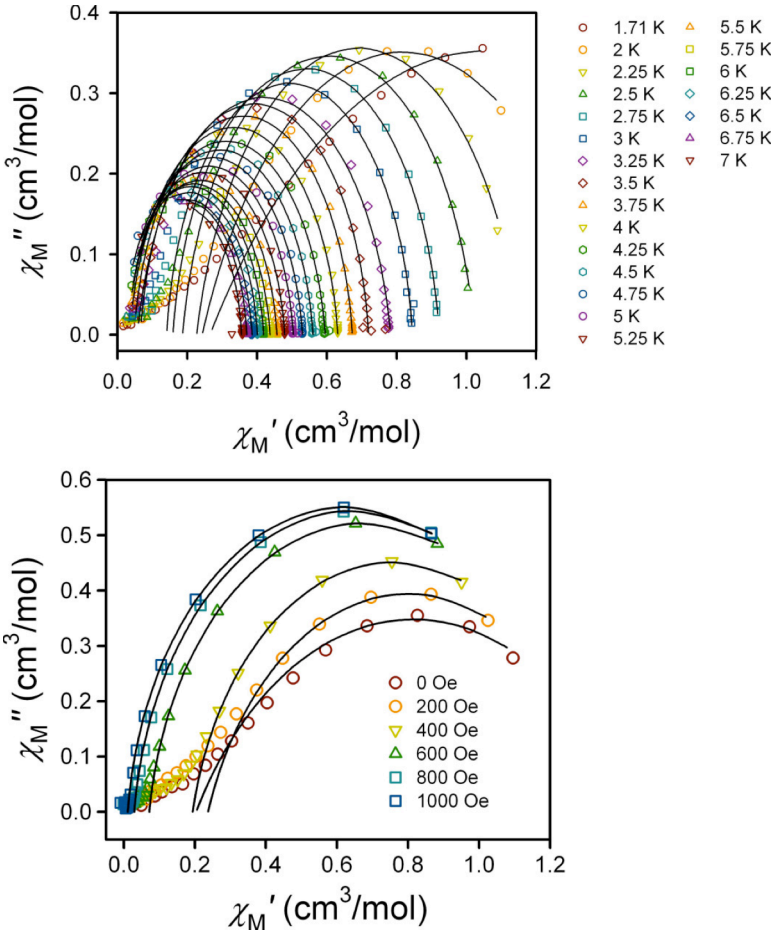


Figure 4.S5. Top: Cole-Cole plots fit for the determination of the temperature dependence of τ for **2**. Black lines are the result of fits to a generalized Debye model as described in the main text. Bottom: Cole-Cole plots of the variable-field ac susceptibility of **2**. Black lines are fits according to the general Debye model.

Chapter 5: Slow Magnetic Relaxation in the Tetrahedral Cobalt(II) Complexes $[Co(EPh)_4]^{2-}$ (E = O, S, Se)

5.1. Introduction

Mononuclear lanthanide complexes have been known for a decade to display single-molecule magnet behavior as a result of highly axial magnetic moments.[1,2,3,4] In such systems, the characteristic strong spin-orbit couplings of the constituent lanthanide ions work in concert with unquenched orbital angular momenta to produce magnetic moments that prefer to align up or down relative to a molecular axis. Implicit in this property is an energy barrier for inversion of the magnetic moment between the two orientations. If the barrier is appropriately large, slow magnetic relaxation and even magnetic hysteresis of a molecular nature can be observed. This property of single-molecule magnets has elicited proposals for applications as information storage media[5] or qubits for quantum computing.[6,7,8]

Three years ago, slow magnetic relaxation was observed for a series of trigonal pyramidal complexes of iron(II),[9,10] extending the field of single-molecule magnet research to mononuclear transition metal complexes. In these complexes, the coordination geometries enforced by the picketed tris(pyrrolyl-a-methyl)amine (tpa^R) ligands were found to give rise to large, negative values for the axial zero-field splitting parameters, D, and large spin reversal barriers, U_{eff}. For example, the complex $[(tpa^{tBu})Fe]^-$ was found to exhibit D = -48 cm^{-1} and U_{eff} = 65 cm^{-1}.[10] Further studies[11,12,13,14] have since revealed slow magnetic relaxation for iron(II) in a variety of other coordination environments, most notably two-coordinate linear geometries, for which U_{eff} values as large as 181 cm^{-1} can arise as a result of unquenched orbital angular momentum.[11] Importantly, however, in all of these cases, the observation of magnetic blocking on a time-scale accessible with a conventional ac magnetic susceptibility experiment (< 1500 Hz) requires the application of a bias dc magnetic field to disrupt ground-state tunneling between the ground $\pm M_S$ (or $\pm M_J$) levels.

The direct observation of slow magnetic relaxation for a mononuclear transition metal complex without a requisite bias dc field was achieved for the first time in the tetraphenylphosphonium salt of the tetrahedral cobalt(II) complex $[Co(SPh)_4]^{2-}$.[15] Prior characterization of this species[16,17,18] via EPR spectroscopy and magnetic susceptometry revealed a substantial, negative zero-field splitting ($D \approx -70$ cm^{-1}). In accordance with Kramers' theorem,[19] ground state magnetization tunneling between the $M_S = \pm^3/_2$ sublevels is weakened due to the half-integer spin, and consequently this complex displays slow relaxation of the magnetization with U_{eff} = 21(1) cm^{-1} in zero applied dc field. Independently, a trigonal bipyramidal $S = {}^3/_2$ iron(III) complex was also discovered to demonstrate slow magnetic relaxation without an applied dc field at low temperature.[20]

The magnitude of the relaxation barrier observed for $[Co(SPh)_4]^{2-}$ is modest when compared to many of the aforementioned mononuclear single-molecule magnets, but could potentially be increased through manipulation of the ligand field. Previous studies of other pseudotetrahedral cobalt(II) complexes with four S-donor ligands revealed a strong dependence of D on the relative arrangements of the donor atoms within the coordination sphere of the cobalt(II) center[16,21,22] In particular, these studies showed that a distortion away from ideal T_d symmetry via a tetragonal

elongation enforces a large, negative *D* value. Zero-field splitting is a second order effect, and thus within the tetragonally-elongated coordination geometry, *D* will hypothetically be enhanced for weak-field ligands, as such ligands may lower the d-d excitation energies responsible for the magnitude of *D*. Further, the relation between *D* and *U* for an $S = {}^3/_2$ complex, $U = 2D$, suggests that the observed spin reversal barriers will increase linearly with an increase in *D*. Herein, we report the preparation and structural, magnetic, and spectral characterization of a series of homoleptic cobalt(II) complexes of phenylchalcogenide ligands: $(Ph_4P)_2[Co(OPh)_4]\cdot CH_3CN$ (**1**), $(Ph_4P)K[Co(OPh)_4]$ (**2**), $(Ph_4P)_2[Co(SPh)_4]$ (**3**),[23,24,25] and $(Ph_4P)_2[Co(SePh)_4]$ (**4**).[26] We demonstrate that the increasing softness of the heavier phenylchalcogenide ligands leads to larger *D* values among **1-4**, but that this does not necessarily afford larger U_{eff} values.

5.2. Experimental

5.2.1. Synthetic Procedures. All manipulations were performed in an inert atmosphere box under N_2. Acetonitrile (MeCN), diethylether (Et_2O), and tetrahydrofuran (THF) were dried using a commercial solvent purification system designed by JC Meyer Solvent Systems. The compounds KOPh,[27] KSPh,[28] and KSePh,[29] were prepared employing previously reported methods. Anhydrous $CoCl_2$, CoI_2, ZnI_2, and $(Ph_4P)Br$ were purchased from Aldrich and used as received. Diatomaceous earth (Celite® 545) was dried under vacuum prior to use.

$(Ph_4P)_2[Co(OPh)_4]\cdot CH_3CN$ (1). A solution of $(Ph_4P)Br$ (0.45 g, 1.1 mmol) in 4 mL of MeCN was added to a slurry of KOPh (0.14 g, 1.1 mmol) in 2 mL of MeCN with vigorous stirring to afford a yellow solution and a white precipitate. The yellow solution was filtered through diatomaceous earth. A solution of $CoCl_2$ (16 mg, 0.12 mmol) in 2 mL of MeCN was added to the filtrate, stirred briefly, and allowed to stand overnight. Dark blue, block-shaped crystals suitable for x-ray analysis formed from this solution, accompanied by a white precipitate. The large blue triangular-block-shaped crystals were separated from the mixture mechanically, washed with 2 mL of MeCN, and briefly dried in the atmosphere of the glovebox to yield 64 mg (46%) of product. IR (neat): 3053 (m), 3019 (w), 1921 (w), 1841 (w), 1580 (vs), 1560 (w), 1474 (vs), 1468 (vs), 1299 (vs), 1277 (w), 1190 (m), 1158 (m), 1105 (vs), 1088 (w), 1026 (w), 985 (s), 870 (m), 848 (m), 829 (m), 756 (vs), 720 (vs), 685 (vs), 617 (m), 569 (s), and 522 (vs) cm^{-1}. Anal. Calcd. for $C_{70}H_{60}CoO_4P_2\cdot CH_3CN$: C, 77.21; H, 5.52; N, 1.22 %. Found: C, 77.28; H, 5.34; N, 1.36 %.

$K(Ph_4P)[Co(OPh)_4]$ (2). A solution of $(Ph_4P)Br$ (0.41 g, 0.97 mmol) in 2 mL of MeCN was added to a slurry of KOPh (0.13 g, 0.98 mmol) in 2 mL of MeCN with vigorous stirring to afford a yellow solution and a white precipitate. The yellow solution was filtered through diatomaceous earth. A solution of CoI_2 (60 mg, 0.19 mmol) in 2 mL of MeCN was added to the filtrate, stirred briefly, and allowed to stand overnight to afford purple, block-shaped crystals suitable for x-ray analysis. The crystals were collected via filtration, washed with 1 mL of MeCN, and dried briefly to yield 80 mg (40 %) of product. IR (neat): 3082 (m), 3066 (m), 3048 (m), 3014 (m), 2982 (m), 1584 (vs), 1560 (m), 1475 (vs), 1436 (s), 1337 (m), 1316 (m), 1290 (vs), 1266 (w), 1186 (m), 1165 (s), 1146 (m), 1107 (vs), 1069 (m), 1020 (m), 996 (w), 986 (vs), 932 (m), 865 (s), 841 (s), 826 (s), 756 (vs), 722 (vs), 689 (vs), 620 (s), 563 (s), 527 (m), and 518 (vs) cm^{-1}. Anal. Calcd. for $C_{48}H_{40}CoKO_4P$: C, 71.19; H, 4.98; N, 0.00 %. Found: C, 70.91; H, 5.18; N, 0.02 %.

$(Ph_4P)_2[Co(SPh)_4]$ (3). This compound was prepared by an alternative method to the reported procedure.25 A solution of $(Ph_4P)Br$ (0.37 g, 0.87 mmol) in 2 mL of MeCN was added with stirring to a slurry of KSPh (0.13 g, 0.88 mmol) in 2 mL of MeCN, affording a yellow-

orange solution and a white precipitate. The solution was filtered through diatomaceous earth, and a solution of $CoCl_2$ (16 mg, 0.12 mmol) in 2 mL of MeCN was added to the filtrate to afford a dark green solution. This solution was stirred briefly, then allowed to sit undisturbed for 24 h to yield 0.11 g (76%) of product as large green, block-shaped crystals of product with a unit cell matching that previously reported.[16] IR (neat): 3054 (w), 3039 (w), 3001 (w), 2984 (w), 1569 (vs), 1469 (vs), 1436 (vs), 1342 (w), 1319 (m), 1264 (w), 1188 (m), 1162 (m), 1105 (vs), 1079 (vs), 1020 (s0, 994 (s), 899 (m), 849 (m), 745 (vs), 719 (vs), 688 (vs), 631 (w), 522 (vs), 479 (s), and 416 (m) cm^{-1}. Anal. Calcd. for $C_{72}H_{60}CoP_2S_4$: C, 73.64; H, 5.15; N, 0.00 %. Found: C, 73.64; H, 5.30; N, 0.02 %.

$(Ph_4P)_2[Co(SePh)_4]$ (4). This compound was prepared by an alternative method to the reported procedure.[26] A solution of $(Ph_4P)Br$ (0.86 g, 2.1 mmol) in 5 mL of MeCN was added with stirring to a slurry of KSePh (0.40 g, 2.0 mmol) in 2 mL of THF, forming a deep orange solution and a white precipitate. The solution was filtered, and the white solid was washed with an additional 3 mL of MeCN. A solution of $CoCl_2$ (68 mg, 0.54 mmol) in 2 mL of MeCN, was added to the filtrate, forming a blue, then green solution and a brown precipitate. This mixture was filtered to collect the brown precipitate, which was then washed with 2 × 3 mL aliquots of MeCN. The solid was then redissolved in 100 mL of MeCN, and diffusion of Et_2O vapor into the resulting solution produced 0.52 g (70%) of dark brown, block-shaped crystals suitable for x-ray analysis. IR (neat): 3056 (m), 3035 (m), 1583 (s), 1568 (vs), 1482 (s), 1467 (vs), 1433 (vs), 1340 (m), 1314 (vs), 1264 (w), 1183 (m), 1164 (m), 1104 (vs), 1063 (s), 1019 (s), 995 (s), 933 (m), 899 (m), 847 (m), 756 (vs), 740 (vs), 719 (vs), 687 (vs), 661 (vs), 615 (s), 522 (vs), and 467 (s) cm^{-1}. Anal. Calcd. for $C_{72}H_{60}CoP_2Se_4$: C, 63.49; H, 4.44; N, 0.00 %. Found: C, 63.47; H, 4.63; N, 0.00 %.

$K(Ph_4P)[Co_{0.06}Zn_{0.94}(OPh)_4]$ (5). A solution of $(Ph_4P)Br$ (0.69 g, 1.6 mmol) in 2 mL of MeCN was added to a slurry of KOPh (0.22 g, 1.7 mmol) in 2 mL of MeCN with vigorous stirring to afford a yellow solution and a white precipitate. The yellow solution was filtered through diatomaceous earth. A solution of CoI_2 (9 mg, 0.03 mmol) and ZnI_2 (94 mg, 0.29 mmol) in 2 mL of MeCN was added to the filtrate, stirred briefly, and allowed to stand overnight to afford light-purple, block-shaped crystals. The crystals were collected via filtration, washed with 1 mL of MeCN, and dried briefly to yield 0.5 g of product with the same unit cell as **2**. Successful dilution, and the relative transition metal ion composition, was confirmed by the consistent unit cell, magnetization, and solution UV-Vis data, as was done previously for **3** [15] to yield a ratio of 1 cobalt to 17(2) zinc ions. The transition metal composition listed for **5** is taken from the magnetization data.

5.2.2. Magnetic Measurements. Polycrystalline samples were loaded into quartz tubes and coated with eicosane in a glove box. To avoid possible desolvation in **1**, which contains cocrystallized MeCN in the crystal structure, the crystals were removed from mother liquor immediately prior to placement in the sample quartz tubes. The quartz tubes were then fixed to a sealable hose-adapter, evacuated briefly with a Schlenk line outside of the glove box, frozen in liquid N_2, and flame sealed. Samples were measured from 2 to 300 K at dc fields ranging from 0 to 7 T with a Quantum Design MPMS-XL SQUID magnetometer. Dc susceptibility and magnetization data were fit or simulated, respectively, with the Van Vleck equation for an $S = {}^3/_2$ system with axial zero-field splitting using Excel®. Ac magnetic susceptibility data measurements were performed using a 4-Oe switching field. Ac magnetic relaxation data were fitted using formulae describing χ' and χ'' in terms of frequency, constant temperature susceptibility (χ_T), adiabatic susceptibility (χ_S), relaxation time (τ), and a variable to represent a

distribution of relaxation times (α).[30] All data were corrected for diamagnetic contributions from the eicosane restraint, sample holder, and the compound itself (estimated with Pascal's constants[31]). The errors in all fitted magnetic parameters were determined from a nonlinear least-squares analysis using the program SolverAid.[32]

5.2.3. X-ray Data Collection, Structure Solution, and Refinement. Data collections were performed on single crystals coated in paratone oil and mounted on Kaptan loops under a freezing stream of N_2. Data were collected using a Bruker QUAZAR diffractometer (**1**, **4**) equipped with a Bruker MICROSTAR x-ray source of Mo Kα (λ = 0.71073 Å) radiation and a APEX-II detector, or a Bruker MICROSTAR-H diffractometer (**2**) equipped with a Microfocus rotating anode x-ray source of Cu Kα (λ = 1.54178 Å) radiation and a APEX-II detector. Raw data were integrated and corrected for Lorentz and polarization effects using Bruker Apex2 v. 2009.1.[33] Absorption corrections were applied using SADABS.[34] The space group was determined by examination of systematic absences, E-statistics, and successive refinement of the structure. The crystal structures were solved with SIR-97[35] and further refined with SHELXTL[36] operated with the WIN-GX interface.[37] The crystals did not show significant decay during data collection. Thermal parameters were refined anisotropically for all non-hydrogen atoms or ions in **1**, **2**, and **4**. Hydrogen atoms were placed in ideal positions and refined using a riding model for all structures. Twinning in **1** required application of the twin law [0 0 1 0 1 0 –1 0 0] and yielded a final BASF of 0.245. Full crystallographic tables for **1**, **2**, and **4** can be found in Tables 5.S1, 5.S2, and 5.S3.

5.2.4. Ligand Field Theory Analysis. Ligand field theory (LFT) analyses of the electronic structure of the cobalt(II) complexes in **1-4** were performed with two approaches. The first approach used a crystal-field parameterization described by Ballhausen,[38] while the second approach employed the angular overlap model (AOM)[39] originally due to Schäffer. Two programs were used for the computations resulting from these two approaches. Ligfield, written by J. Bendix[40] (University of Copenhagen, Denmark) and DDN, available from J. Telser, were chosen because both programs use the complete d^7 weak-field basis set including interelectron repulsions (Racah parameters *B* and *C*), spin-orbit coupling (SOC), and either crystal-field (for DDN, the parameters *Dq*, *Ds*, and *Dt*,[38]) or AOM ligand-field bonding parameters ($\varepsilon(\sigma)$, $\varepsilon(\pi)$).[39,41] DDN allowed input of single-electron d orbital energies, while Ligfield allowed the identification of the orbital occupancy and spin progeny of a given energy level (eigenstate). The two programs gave identical results when directly compared. An additional version of DDN, DDNFIT, was used to fit the experimental electronic absorption band positions to single-electron d orbital energy values calculated by iteration of Racah and either crystal-field (first approach) or AOM bonding parameters (second approach). Assignments were made as discussed in the manuscript (see also Appendix A.3.) and input into DDNFIT, along with the transition energies, for fitting. Definitive values of Racah parameters for free d-block ions are given by Brorson and Schäffer[42] and those of SOC constants by Bendix, Brorson, and Schäffer.[40] Free-ion Racah and SOC parameters (in cm^{-1}) for Co(II) are B = 988.6 cm^{-1}, C = 4214 cm^{-1} (C/B = 4.26) and ζ = 533 cm^{-1}, respectively.

5.2.5 Other Physical Measurements. UV-vis-NIR diffuse reflectance spectroscopy over the range of 4,000-20,000 cm^{-1} was performed on pulverized microcrystalline samples using a CARY 5000 spectrophotometer interfaced to Varian WinUV software. Elemental (C, H, and N) analyses were performed at the Microanalytical Laboratory of the University of California, Berkeley.

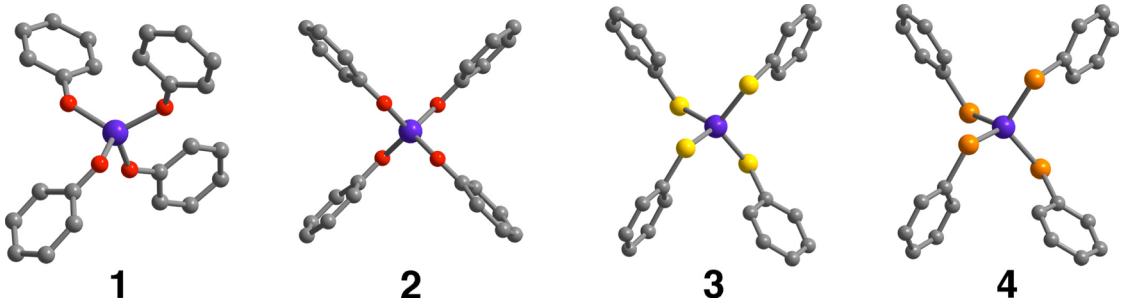


Figure 5.1. Observed structures of the $[Co(EPh)_4]^{2-}$ complexes in **1**-**4**. The molecules are viewed approximately down the S_4 molecular axis for **2**-**4**, but perpendicular to the S_4 axis for **1**. Counterions and hydrogen atoms have been omitted for clarity. Purple, orange, yellow, red, and gray spheres represent cobalt, selenium, sulfur, oxygen, and carbon atoms, respectively.

5.3. Results and Discussion

5.3.1. Syntheses and Structures. Preparations of **1**-**4** proceeded via the addition of acetonitrile solutions of $CoCl_2$ (**1**, **3**, **4**) or CoI_2 (**2**) to acetonitrile solutions containing excess amounts of the Ph_4P^+ salts of the respective phenylchalcogenide ligands. Upon work-up, high-quality crystals of **1**-**4** were obtained, allowing for the determination of the crystal structures of **1**, **2**, and **4** by single-crystal x-ray diffraction analysis.

All compounds possess pseudotetrahedral environments around the cobalt(II) centers with tetragonal distortions to give exactly or approximately D_{2d} symmetry (see Fig. 5.1). For **1**, a tetragonal compression of the cobalt(II) coordination sphere is observed, and the local CoO_4 symmetry is D_{2d}. The overall molecular symmetry for $[Co(OPh)_4]^{2-}$ in **1**, however, is actually lower than D_{2d} due to significant twisting of the phenyl rings about the Co–O bonds, which leads to C_1 molecular symmetry. In **2**-**4**, tetragonal elongations are instead observed in the cobalt(II) coordination spheres, but local symmetries of the cobalt(II) ions are D_{2d}, as in **1**. Of note here is that the K^+ cation in the structure of **2** appears to enforce the tetragonal elongation via $K^+\cdots O$ interactions along the *c* axis of the crystal (see Fig. 5.2). For **2**, the molecular symmetry assignment of D_{2d} for $[Co(OPh)_4]^{2-}$ is exact because the molecule resides on a crystallographic site of D_{2d} symmetry. In **3** and **4**, this same assignment is in contrast only approximate due to slight variations in the positions of the phenyl rings, though these variations are significantly less pronounced than in **1**. Selected interatomic bond distances and angles are reported in Table 5.1. The average Co–O distances for **1** and **2** (1.963(8) and 1.962(2) Å respectively) are longer than calculated using the sum of ionic radii (Co–O: 1.93 Å),[43] possibly indicating relatively more ionic Co–E interactions than for **3** and **4**, where the average Co–S and Co–Se bond distances, 2.323(8) and 2.432(6) Å, respectively, are shorter than those predicted by the sums of their respective ionic radii (2.42 Å and 2.56 Å).

Surprisingly, the crystal structures of the homoleptic $[Co(OPh)_4]^{2-}$ complexes in **1** and **2** represent the first crystallographic characterization of this moiety as a mononuclear species. The first published preparations of $Li_2Co(OPh)_4{\cdot}4THF$, $Na_2Co(OPh)_4{\cdot}5THF$ and $K_2Co(OPh)_4{\cdot}0.75$ THF were reported in 1991, but the lack of structural characterization left in doubt whether the authors truly obtained isolated $[Co(OPh)_4]^{2-}$ moieties.[44] Some thirteen years later, it was questioned whether these mononuclear complexes were really even isolable, due to the tendency of the phenoxy oxygen to bridge cobalt(II) ions[45] and produce multinuclear structures.[46] Preparations of the related mononuclear complexes $[Co(OAr')_4]^{2-}$ and $[Co(OAr^F)_4]^{2-}$ (OAr′ =

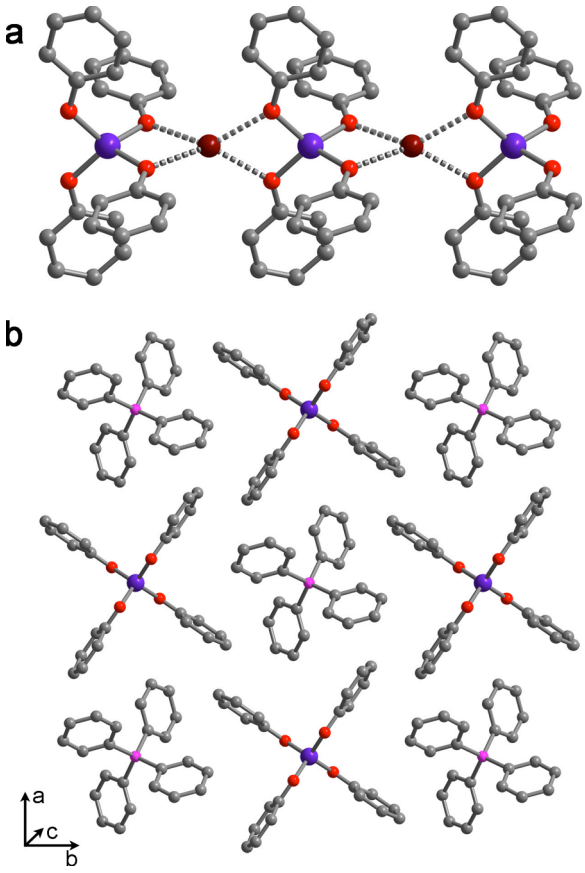


Figure 5.2. Packing arrangement of $[Co(OPh)_4]^{2-}$ moieties in **2**. **a.** Chain-like extended structure observed in **2**. The molecules are viewed along the crystallographic *a* axis, which is perpendicular to the coincident molecular S_4 and crystallographic *c* axes. Hydrogen atoms and Ph_4P^+ counterions are omitted. Purple, dark red, light red, and gray spheres represent cobalt, potassium, oxygen, and carbon atoms, respectively. **b.** Packing arrangement of chains and Ph_4P^+ counterions, as viewed along the crystallographic *c* axis. Crystallographic axes are denoted. Note that the chains are aligned parallel.

3,5-bis(trifluoromethyl)phenoxide; OAr^F = pentafluorophenoxide) were reported and their accessibility was attributed to the strongly electron-withdrawing substituents on the phenoxide ligands, which were argued to reduce the electron density around the phenoxide oxygen and prevent the formation of multinuclear assemblies.[45] The observation that in solution, low ratios of free PhS^- ligand to Co^{2+} ion favor multinuclear species rather than mononuclear $[Co(SPh)_4]^{2-}$ complexes[25] inspired the syntheses employed here with large ligand:cobalt molar ratios. The resulting compounds therefore suggest that the difficulties in isolating mononuclear $[Co(OPh)_4]^{2-}$ and related species can be circumvented by adjusting the reaction conditions.

5.3.2. Magnetic Properties. Investigation of the magnetic properties of **1-4** first proceeded via the analysis of variable-temperature dc magnetic susceptibility data (see Figure 5.3). At 300 K, the values of $\chi_M T$ for **1-4** are 2.18, 3.67, 3.11, and 2.99 cm^3K/mol, respectively, and are significantly greater than the expected value of 1.875 cm^3K/mol for an isotropic $S = {}^3/_2$ center. With decreasing temperature, $\chi_M T$ stays relatively constant down to 100 K, when $\chi_M T$ begins to

Table 5.1. Selected interatomic distances (Å) and angles (°) for **1**-**4**.

	1	**2**	**3**[b]	**4**
Co–E	1.957(3)	1.962(2)	2.326(4)	2.436(1)
	1.957(3)	-	2.342(4)	2.429(1)
	1.967(3)	-	2.316(4)	2.425(1)
	1.970(3)	-	2.328(4)	2.437(1)
E–Co–E	111.4(2)	94.3(1)	95.6(2)	97.74(3)
	122.9(2)	-	97.0(2)	94.25(3)
	104.1(2)	117.5(1)	121.3(2)	116.89(3)
	106.9(2)	-	116.1(2)	114.95(3)
	104.4(2)	-	114.8(2)	113.55(3)
	105.9(2)	-	113.5(2)	120.96(3)
Co–E–C[c]	128(4)	125(1)	110(2)	108(2)
Co···Co[d]	12.10(1)	6.99(1)	10.46(1)	10.68(1)

[a]D_{2d} site symmetry at Co(II) ion in this structure. [b]Taken from [25]. [c]Average value. [d]Shortest Co···Co distance.

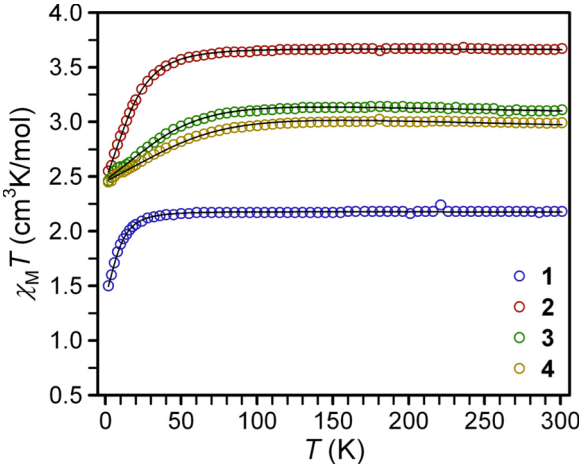


Figure 5.3. Variable temperature dc magnetic susceptibility data for **1**-**4**. Data were collected on microcrystalline samples of **1**-**4** under a static 1000 Oe applied magnetic field. Black lines represent the best fits to the hamiltonian $\hat{H} = D\hat{S}_z^2 + \mu_B g\boldsymbol{S}\cdot\boldsymbol{H}$, as decribed in the main body of the report.

drop, ultimately reaching 1.50, 2.55, 2.46, and 2.45 cm^{3}K/mol at 2 K for **1**-**4**, respectively. For a system with one spin center, the temperature dependence of the $\chi_M T$ plot reflects the fluctuating populations of the M_S levels for the spin ground state. Anisotropic spins possess energy separations between their M_S levels that are often within an order of magnitude of $k_B T$ (k_B = Boltzmann constant), leading to a temperature dependence. Thus, the temperature dependent $\chi_M T$ values for **1**-**4** likely highlight the presence of an appreciable magnetic anisotropy.

To quantitate the axial zero-field splitting parameter D, the variable-temperature $\chi_M T$ data were fit to the following two-term Hamiltonian for a perfect powder of randomly oriented magnetic moments: $\hat{H} = D\hat{S}_z^2 + m_B g\boldsymbol{S}\cdot\boldsymbol{H}$. Here, D is the zero-field splitting, μ_B is the Bohr magneton, g is the Landé g-factor, $\hat{S}_z$ the spin operator, $\boldsymbol{S}$ the spin, and $\boldsymbol{H}$ the magnetic field. Our

Table 5.2. Spin Hamiltonian and Orbach relaxation parameters for **1**-**4.**

	g_z	$g_{x,y}$	D (cm^{-1})	U_{eff} (cm^{-1})	τ_0 (s)
1[a]	2.222(9)	2.118(6)	–11.1(3)	21(1)	$7(1) \times 10^{-10}$
2[b]	2.958(3)	2.701(2)	–23.8(2)	-	-
3	2.960(3)	2.285(4)	–62(1)	21(1)	$1.0(3) \times 10^{-6}$[c]
4	2.953(3)	2.165(5)	–83(1)	19(1)	$3(1) \times 10^{-6}$
5[d]	-	-	-	34.0(5)	$1.0(1) \times 10^{-9}$

[a]Ac data obtained under 1400 Oe applied dc field. [b]Determination of U_{eff} and τ_0 ruled out by nonlinearity of Arrhenius plot. [c]Erroneously reported as $1.0(3) \times 10^{-7}$ s in ref 15. [d]Diamagnetic dilution of composition $(Ph_4P)K[Co_{0.06}Zn_{0.94}(OPh)_4]$.

model employs only these axial D and g-tensors ($g_z \neq g_x = g_y$), and ignores any transverse anisotropy (E) (see Appendix A.3). The best fits produced g_z, g_x, g_y, and D values for **1-4** as given in Table 5.2 (see also Figure 5.3). The resulting D values show a marked dependence upon both the donor atom of the ligand, as well as the coordination environment. For $[Co(OPh)_4]^{2-}$ in **1**, the best fits afford $D = -11.1(3)$ cm^{-1}, indicating a $2D = 22.2$ cm^{-1} splitting between the ground $M_S = \pm^3/_2$ levels and the excited $M_S = \pm^1/_2$ levels. In contrast, for the more symmetric complex in **2**, a D value of –23.8(2) cm^{-1} was obtained. For the $[Co(EPh)_4]^{2-}$ complexes in **3** and **4**, with softer ligand donor atoms (E = S, Se, respectively), a substantial increase in the magnitude of D is apparent, with the best fits revealing $D = -62(1)$ and $-83(1)$ cm^{-1}, respectively. These values suggest very large splittings between the $\pm^3/_2$ and $\pm^1/_2$ M_S levels, and therefore predict substantial energy barriers of 124 and 166 cm^{-1} for spin inversion from $M_S = +^3/_2$ to $-^3/_2$ and vice versa. We note that the D value obtained here is slightly lower in magnitude than those determined before. [15-18] The discrepancy may originate from the difficulty that ANISOFIT[47] has with spin systems possessing highly anisotropic g-tensors. Good agreement was observed between the isofield lines in the experimental magnetization data for **3** and simulations performed with the spin Hamiltonian parameters obtained from fitting the $\chi_M T$ plot (see Figure 5.S1).

Ac magnetic susceptibility measurements were conducted to check for the slow magnetic relaxation predicted by the derived negative D values of the $S = {}^3/_2$ centers in **1-4** (see Figs. 5.S2-S5 and Chapter 4). For **1**, no slow magnetic relaxation is observed from 1 to 1500 Hz at 2 K under zero applied field, as evidenced by a featureless plot of the out-of-phase susceptibility (χ_M'') versus applied ac field frequency (see Figure 5.S2). Upon an application of a small dc field, however, a peak emerges for **1** that moves to lower frequency with increasing field, eventually plateauing at 65 Hz under a 1400 Oe dc field. In contrast, **2-4** exhibit slow magnetic relaxation at 2 K under zero applied field, with χ_M'' peak maxima observed at 267, 28, and 3 Hz, respectively (see Figures 5.S3-5.S5 and Chapter 4).

The ac field frequency at which peak maxima occur provides the magnetic relaxation time via the fitting of the variable-frequency ac susceptibility data to a Debye model[30] (see Figs. 5.S7 and 5.S8). Further, the temperature dependence of the resulting relaxation times, when used to construct Arrhenius plots (see Figure 5.4), allows for the determination of the magnitudes of the spin-reversal barriers giving rise to the slow magnetic relaxation. Here, a linear regime in the Arrhenius plot corresponds to a temperature range where the spin system relaxes via an Orbach process,[48] whereas other relaxation processes, such as Raman and direct processes, produce

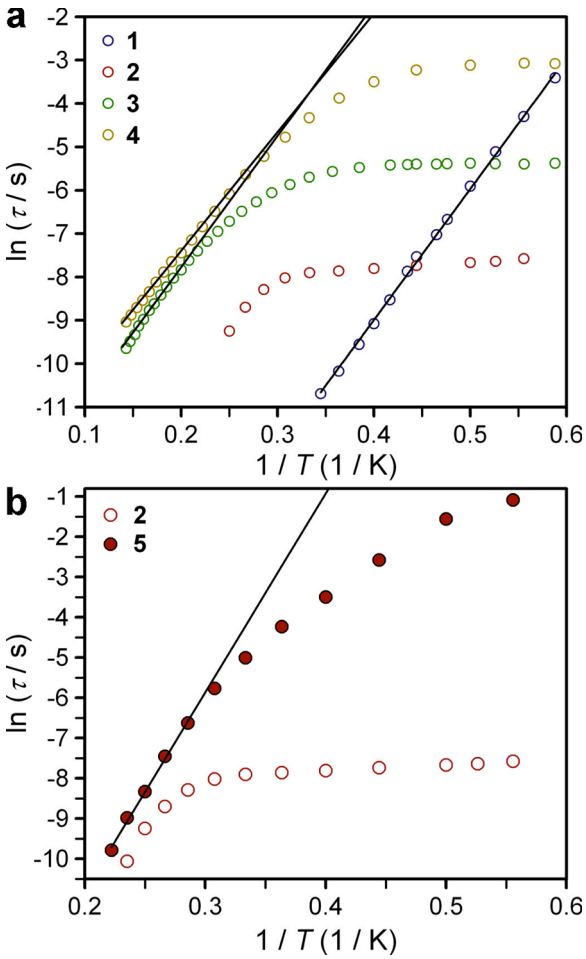


Figure 5.4. Arrhenius plots of the natural log of the relaxation time, τ, versus the inverse temperature. **a.** Data for **1**-**4**: relaxation time data for **2**-**4** were collected under zero applied dc field; data for **1** were collected under a 1400 Oe applied dc field. Black lines represent fits to Orbach relaxation processes, as described in the main body of the report. **b.** Data for **2** and the 1:18 Co:Zn diluted compound, **5**, both collected under zero applied dc field, with Arrhenius fit applied to 5 highest-temperature data points.

curvature in the plot.[48] Further, when relaxation via quantum tunneling is operative, temperature independent regimes are observed in the Arrhenius plots, as the absorption or emission of phonons is not required. These latter relaxation mechanisms are predominantly encouraged by nuclear spin, intermolecular dipolar interactions, and transverse anisotropy.[49] For compound **1**, a linear regime is observed in the Arrhenius plot over the entire temperature range of investigation at H_{dc} = 1400 Oe, corresponding to dominant Orbach relaxation with U_{eff} = 21 cm^{-1} and $\tau_0 = 7 \times 10^{-10}$ s. In contrast, **2** and **4** display both temperature-dependent and temperature-independent regimes for τ, as also previously observed for **3** (Chapter 4). For **2**, however, τ appears to become strongly temperature dependent only after the peak has moved to a frequency above the range of our instrument. In contrast, for **4**, the peak is temperature dependent within the frequency range accessible by the magnetometer, yielding U_{eff} = 19(1) cm^{-1} and $\tau_0 = 3(1) \times 10^{-6}$ s.

The temperature independent regimes of the data collected for **2** and **4** are likely attributable to dipolar interactions between adjacent cobalt centers, as was discovered for **3**. Of note here is

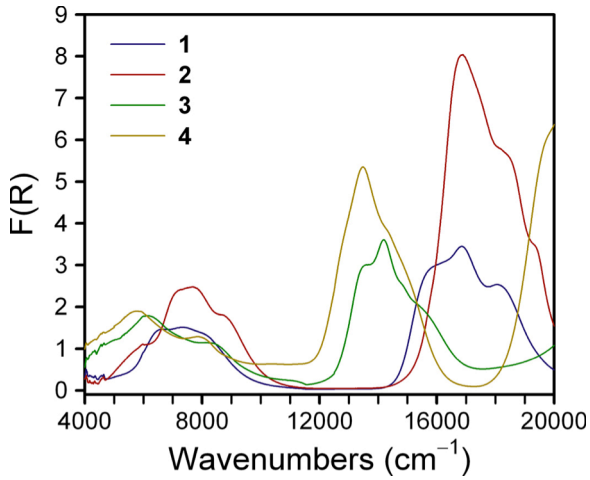


Figure 5.5. Solid-state diffuse reflectance spectrum for pulverized crystals of **1**-**4.** Data were collected at 298 K and 2 cm^{-1} resolution. The absorption intensity is given in terms of the Kubelka-Munk transform of the % reflectance data

that the relaxation times for the temperature independent regimes of **2**-**4** follow the trend in the nearest Co···Co contacts determined for the crystalline phase (see Table 5.1). Additionally, the dipolar interactions appear to be strong enough in **2** that an estimation of the magnitude of U_{eff} from the high temperature regime of the Arrhenius plot is unfeasible. To achieve a better estimation of U_{eff} for this system, $(Ph_4P)K[Co_{0.06}Zn_{0.94}(OPh)_4]$ (**5**) was prepared by performing the synthesis of **2** starting from a 1:10 mixture of CoI_2 and ZnI_2 in a manner similar to that accomplished for **3** as detailed in Chapter 4. This magnetically dilute sample was then subjected to ac susceptibility measurements (see Figs. 5.S6, 5.S8). The Arrhenius plot derived from the χ_M'' data for **5** is comparatively temperature dependent over the entire temperature range of investigation (see Figure 5.4b). At the highest temperatures, a linear fit to the Arrhenius plot affords U_{eff} = 34.0(5) cm^{-1} and $\tau_0 = 1.0(1) \times 10^{-9}$ s. Furthermore, the remnant curvature of the Arrhenius plot for **5** indicates relaxation processes other than the Orbach process are operative, even upon dilution of the complex, as was also observed for $(Ph_4P)_2[Co_{0.09}Zn_{0.91}(SPh)_4]$.

5.3.3. Solid-State Electronic Absorption Spectra. To facilitate a ligand field theory analysis, UV-Vis-NIR diffuse reflectance spectra were collected at room temperature on pulverized crystals of **1**-**4** in the energy range 4000 to 20,000 cm^{-1} (see Figure 5.5). There are two main features of each spectrum. Some relatively weak absorption bands appear below 6000 cm^{-1} and three stronger, overlaid bands are found from 10,000 to 20,000 cm^{-1} (see also Table 5.S4 and Appendix A.3). Based on the previous work of Fukui *et al.*[16-18] these peaks result from d-d excitations. Thus, the general decrease in the energies of the transitions from **1** and **2** to **3** to **4**, suggests a decreasing ligand-field strength in the order of $PhO^- > PhS^- > PhSe^-$. Notably, despite having the same CoO_4 chromophore, the spectra for **1** and **2** are significantly different. The spectrum of **2** appears to be blue-shifted relative to that of **1** by ~300 cm^{-1}, except at the lowest edge of the set of peaks at ~6,000 cm^{-1}. The contrast in the spectra for **1** and **2** is likely due to the two distinct types of tetragonal distortion in the structures of these complexes. A more quantitative analysis of the spectra is given in the following section to account for such distortions.

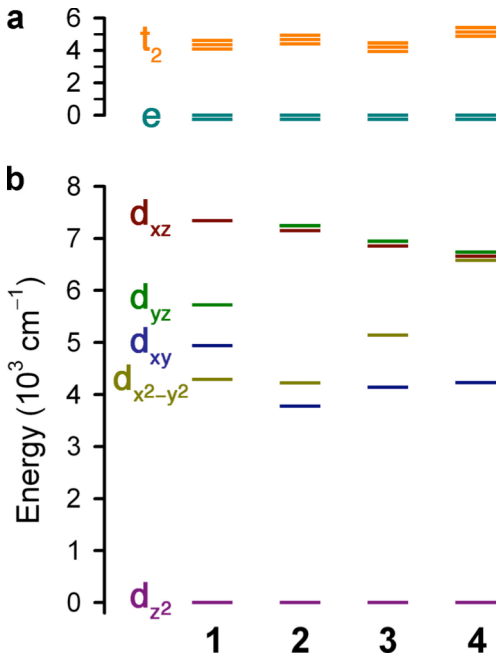


Figure 5.6. Relative energy diagrams for the 3d orbitals of the $[Co(EPh)_4]^{2-}$ complexes in **1-4**, as extracted from diffuse reflectance data. **a.** Splitting of the 3d-orbitals for **1**-**4** assuming a simple T_d symmetry model. **b.** Relative energies of the 3d orbitals assuming a reduced symmetry. Orbitals for **1** were determined from C_{2v} symmetry, while those for **2** were from D_{2d} symmetry and incorporating an estimated $^4A_2 \rightarrow {}^4T_2$ transition; orbitals for **3** correspond to those obtained by Fukui *et al.*[17] Energies for **4** were determined in D_{2d} symmetry and incorporating an estimated $^4A_2 \rightarrow {}^4T_2$ transition. For **2**, **3**, and **4**, the d_{xz} and d_{yz} orbitals are degenerate, but depicted separately for ease of viewing.

5.3.4. Ligand Field Analysis of Solid State Absorption Spectra. The analyses of the spectra begin within an idealized T_d symmetry reference frame. The d^7 cobalt(II) center in T_d symmetry gives a ^4A ground state and $^4T_2$, $^4T_1(^4F)$, and $^4T_1(^4P)$ excited states, listed in order of increasing energy, which can produce three strong absorptions in the UV-vis-NIR spectra. In order to perform an analysis of the transitions of **1**, **2**, and **4**, the observed transitions were assigned assuming idealized T_d symmetry and input along with transition energies to DDNFIT (see Appendix A.3. for details). Approximate values of $10Dq$ obtained for **1**-**4** via this method are –4350, –4656, –4200, and –5130 cm^{-1}, respectively, leading to the T_d d-orbital splittings depicted in Fig. 6a. Further, the Racah B parameters obtained from the best fits to the spectra for **1**-**4** are 763.3, 768.9, 590, and 408 cm^{-1}, respectively, suggesting considerable Co–E covalency on account of the deviations from the free cobalt(II) ion value of B (956 cm^{-1}, ref. 42). Indeed, the trend also appears to follow the increasing softness of the PhE^- ligands, suggesting more Co–E covalency in **3** and **4** than **1** and **2**. The presence of the K^+ cation in the structure of **2** possibly engenders a more ionic Co–O interaction than **1** and thus a slightly larger B value. The analysis of the $10Dq$ values here would benefit from the accuracy afforded by knowledge of the energy of the $^4A_2 \rightarrow {}^4T_2$ transition, which was not observed (see Appendix A.3 for more details regarding transition assignments). Note that tetragonal distortions of the coordination geometries of the cobalt(II) centers are observed in the crystal structures of these complexes. Such distortions

necessitated the exploration of lower symmetry models for more realistic insight into the electronic structures of **1**-**4**.

The structures of **1**-**4** undergo tetragonal distortions such that the local symmetries around the cobalt(II) centers are lowered from T_d to D_{2d}, or possibly even C_{2v}. Such a symmetry lowering splits the T_d d-d excitations into multiple transitions, yielding the heavily-featured peaks observed in Figure 5.5. Given the overall similarities among the diffuse reflectance spectra, the transitions observed for **1**, **2**, and **4** were assigned in accord with the interpretation by Fukui *et al.* of the single-crystal UV-vis absorption data obtained for **3**.[17] Two separate geometric models, assuming D_{2d} and C_{2v} symmetry, respectively, were applied to determine spectral assignments for the fitting (see Appendix A.3 for details). Observed absorption energies, their assignments, and calculated values from DDNFIT are listed in Table 5.S4. The fitted d-orbital splittings giving rise to the calculated excitation energies for **1**-**4** are listed in Table 5.S5, while selected results are depicted in Figure 5.6.

For **1**-**4**, all models found the d_{z2} orbitals to be lowest in energy. The next lowest energy orbitals tended to be the d_{xy} and d_{x2-y2} orbitals, with d_{xz} and d_{yz} orbitals at higher energy. In particular, the energies of the d_{xy} and d_{x2-y2} orbitals are very sensitive to the assignment and energy of the $^4A_2 \rightarrow {}^4T_2$ transition, which may not be observed in Figure 5.5. The fitted energies of the two sets of (d_{xy}, d_{x2-y2}) and (d_{xz}, d_{yz}) orbitals may be split depending upon the use of D_{2d} or C_{2v} symmetry, with the D_{2d} symmetry model tending to produce the best fits, but with unrealistic degeneracies of the (d_{xy}, d_{x2-y2}) orbitals. Degeneracies of the (d_{xz}, d_{yz}) orbitals also result, but these are reasonable within an idealized D_{2d} symmetry, as closely approximated by **3** and **4** and crystallographically exact for **2**. The averaged B values for **1**-**4** are 786(2), 841(12), 584(1) and 508(30) cm^{-1}, respectively, and follow the same trend observed for the simple T_d model. The current values, however, suggest a much stronger influence for the K^+ ion in the Co–E interactions in **2** as compared to **1**.

Application of the angular overlap model (AOM) to the interpretation of the above spectra was also performed, as this allowed the incorporation of the crystal structures in the analyses of the ligand fields in **1**-**4**. We applied two separate bonding models with metrical parameters determined from the crystal structures. Each model assumed that the AOM parameters ($e(\sigma)$, $e(\pi)$) were equal for all four phenylchalcogenide ligands; a more detailed discussion of the models employed is given in Appendix A.3. These parameters, once defined, were then adjusted to fit the diffuse reflectance and polarized absorption spectra.[17] The results are summarized in Table 5.S6. These fits, like those from DDNFIT, would benefit from definitive observations of the $^4A_2 \rightarrow {}^4T_2$ transitions. Note, however, that the Racah B parameters obtained by AOM follow those obtained from the model using single electron d-orbitals. Here, values averaged over the two models utilized are $B \approx 770$ cm^{-1} for **1**, 550 cm^{-1} for **3**, and 480 cm^{-1} for **4**. For **1**-**4**, fits utilizing σ-only Co–E interactions were of significantly lower quality than those incorporating π-interactions, as dramatically demonstrated in **2**, for which a successful fit of the transitions was impossible using the σ-only model.

5.3.5. Impact of Electronic Structure on Anisotropy and Magnetization Dynamics. The magnetic anisotropy of a given spin center without any first-order orbital angular momentum is determined by a second-order interaction between the electronic ground state and excited states with anisotropy.[50] This interaction is chiefly responsible for whether or not the sign of D is positive or negative.[51] The magnitude of D is determined by two factors: it is inversely proportional to the energy separation between the electronic ground state and the anisotropic excited states contributing to D, and it is proportional to the square of the effective spin-orbit

coupling constant, ζ, for the spin center. The earlier-highlighted ambiguity regarding the $^4A_2 \rightarrow {}^4T_2$ transition precluded definitive determination of the energies of the d orbitals and of the excited states involved in the generation of the magnetic anisotropy for **1**-**4**. In principle, the expected weaker ligand-fields induced by the diffuse PhS^- and $PhSe^-$ ligands should ensure lower energy d-d excitations compared to **1** and **2**, and this is indeed evidenced by the diffuse reflectance data.

The results of our analyses of the d-orbital splittings for **1**-**4**, though approximate, consistently suggest (d_{x2-y2}, d_{xy}) orbitals that are lower in energy than the (d_{xz}, d_{yz}) orbitals. Thus, it stands to reason that the lowest electronic excited state is likely an excitation between the nondegenerate d_{x2-y2} and d_{xy} orbitals. This excitation, which connects two orbitals linked by the $\hat{l}_z$ operator, would interact strictly with the $\hat{S}_z$ spin components of the $S = {}^3/_2$ moment and generate a negative contribution to the axial anisotropy.[51,52] Thus, weaker field ligands can be envisioned to ensure a lower energy splitting of the d_{x2-y2} and d_{xy} orbitals, and produce lower-energy excited states, which would result in the increasing trend of $|D|$ for **2**-**4**. That this correlation is not observed with our fitted parameters is likely attributable to the lack of direct observation of the lowest energy transition, which is crucial for the definitive evaluation of the relative energies of the d_{xy} and d_{x2-y2} orbitals. However, the trend in D values for **1**-**4** follows the B parameters obtained, highlighting the importance of soft donor-atom ligands in the design of molecules with large magnetic anisotropies. Highly covalent systems may also potentially increase the anisotropy via a spin-orbit coupling enhancement mechanism from heavy diamagnetic ligand donor atoms, as has been observed in the past for chromium(III) complexes[53] and investigated on theoretical grounds for pseudotetrahedral complexes of nickel(II).[54] The factors that affect the magnetic anisotropy of the cobalt(II) center in **1**-**4** are not limited to the influences of the ligand-field strength and/or donor atom spin-orbit coupling constants. As demonstrated by the difference in the anisotropies of **1** and **2**, as well as previous studies of the anisotropies of the Me_4N^+, Et_4N^+, and Ph_4P^+ salts of $[Co(SPh)_4]^{2-}$,[18] the geometric arrangement of the ligands is very important for generating the appropriate d-orbital splitting necessary for large, negative D values.

The differing low-temperature zero-field magnetization dynamics for **1** and **2** could be attributed to two factors. The first difference, which would explain why **1** requires an applied field for slow magnetic relaxation to be observed, is that D is in fact positive for **1** but negative for **2**. In this case, the slow magnetic relaxation process for **1** under nonzero dc field could be an Orbach process made favorable by a bottlenecked direct relaxation process, as is suggested for the $D > 0$ complex $[(3G)CoCl]^+$ in Chapter 3.[55] The second difference between **1** and **2** of import to the generation of slow magnetic relaxation is the relatively lower-symmetry ligand field around the cobalt(II) center of **1** compared to **2**, which may open pathways for ground state magnetic tunneling at zero dc field that are not present for the rigorously D_{2d}-symmetric $[Co(OPh)_4]^{2-}$ complex in **2**.

The ac magnetic susceptibility data for compounds **1**-**4** revealed a surprising independence of U_{eff} on D. Here, the relatively large τ_0 values for **3** and **4** suggest that pure thermal relaxation may not be observed in the temperature ranges of our investigations. If this is true, then the magnitudes of U_{eff} determined for **3** and **4** may in fact be lower estimates of the true values.

5.4 Outlook and Conclusions

Slow magnetic relaxation at zero field has been demonstrated in the series of cobalt(II) complexes of the phenylchalcogenato ligands PhE^- (E = O, S, Se). Zero-field splittings in **1**-**4**, determined by the fitting of variable-temperature magnetic susceptibility data, appear to be highly sensitive to the donor atoms of the ligand, as exemplified by significant increase in *D* along the nearly isostructural series of **2**, **3**, and **4**. Inspection of the electronic absorption spectra and d-orbital splittings highlight the importance of soft ligands in generating weak ligand fields with significant covalency (those with small *Dq* and small *B*) and thus larger zero-field splitting parameters. However, the arrangement of the ligands around the metal ion is also clearly influential, as underlined by the differences in the magnetic properties of **1** and **2**. The arrangements are also important to the low temperature magnetization dynamics, as **2** displays slow magnetic relaxation at zero field while **1** requires a modest applied field to observe a peak in the out-of-phase ac susceptibility. Further, the magnitudes of the relaxation barriers for **1**-**4** do not appear to follow the trend in *D* values, implying that there may be other factors that influence the low temperature magnetization dynamics. As suggested by the relatively large t_0 values for **3** and **4**, the magnetic relaxation in **3** and **4** may not approach a completely thermally activated relaxation over the temperature range of our investigations, a possibility that we are currently studying. Also of particular interest is the role of vibronic coupling in reducing the magnitude of the effective barrier, as has been suggested for iron(II) complexes with both trigonal pyramidal and linear geometries.[11,12,56] Notably, the large magnetic anisotropies observed in the present complexes suggest that large barriers may also be obtained in single-chain magnets or even multinuclear single-molecule magnets incorporating exchange-coupled D_{2d} cobalt(II) ions.

5.5. Acknowledgements

This research was supported by NSF grant CHE-1111900. I thank Professor J. Telser for fruitful discussions and performing the ligand field theory analysis of the diffuse reflectance data. I am also grateful to Professor J. R. Long for assistance throughout the study.

5.6. References and Notes

(1) Ishikawa N.; Sugita, M.; Ishikawa, T.; Koshihara, S.-Y.; Kaizu, Y. *J. Am. Chem. Soc.* **2003**, *125*, 8694.
(2) Ishikawa, N. *Struct. Bond.* **2010**, *135*, 211.
(3) Rinehart, J. D.; Long, J. R. *Chem. Sci.* **2011**, *2*, 2078.
(4) Luzon, J.; Sessoli, R. *Dalton. Trans.* **2012**, *41*, 13556.
(5) Mannini, M.; Pineider, F.; Sainctavit, P.; Danieli, C.; Otero, E.; Sciancalepore, C.; Talarico, A. M.; Arrio, M.-A.; Cornia, A.; Gatteschi, D.; Sessoli, R. *Nat. Mater.* **2009**, *8*, 194.
(6) Leuenberger, M. N.; Loss, D. *Nature* **2001**, *410*, 789.

(7) Ardavan, A.; Rival, O.; Morton, J. J. L.; Blundell, S. J.; Tyryshkin, A. M.; Timco, G. A.; Winpenny, R. E. P. *Phys. Rev. Lett.* **2007**, *98*, 057201.
(8) Stamp, P. C. E.; Gaita-Ariño, A. *J. Mater. Chem.* **2009**, *19*, 1718.
(9) Freedman, D. E.; Harman, W. H.; Harris, T. D.; Long, G. J.; Chang, C. J.; Long, J. R. *J. Am. Chem. Soc.* **2010**, *132*, 1224.
(10) Harman, W. H.; Harris, T. D.; Freedman, D. E.; Fong, H.; Chang, A.; Rinehart, J. D.; Ozarowski, A.; Sougrati, M. T.; Grandjean, F.; Long, G. J.; Long, J. R.; Chang, C. J. *J. Am. Chem. Soc.* **2010**, *132*, 18115.
(11) Zadrozny, J. M.; Atanasov, M.; Bryan, A. M.; Lin, C.-Y.; Rekken, B. D.; Power, P. P.; Neese, F.; Long, J. R. *Chem. Sci.* **2013**, *4*, 125.
(12) Atanasov, M.; Zadrozny, J. M.; Long, J. R.; Neese, F. *Chem. Sci.* **2013**, *4*, 139.
(13) Lin, P.-H.; Smythe, N. C.; Gorelsky, S. I.; Maguire, S.; Henson, N. J.; Korobkov, I.; Scott, B. L.; Gordon, J. C.; Baker, R. T.; Murugesu, M. *J. Am. Chem. Soc.* **2011**, *133*, 15806.
(14) Weismann, D.; Sun, Y.; Lan, Y.; Wolmershauser, G.; Powell, A. K.; Sitzmann, H.; *Chem.-Eur. J.* **2011**, *17*, 4700.
(15) Zadrozny, J. M.; Long, J. R. *J. Am. Chem. Soc.* **2011**, *133*, 20732.
(16) Fukui, K.; Ohya-Nishiguchi, H.; Hirota, N. *Bull. Chem. Soc. Jpn.* **1991**, *64*, 1205.
(17) Fukui, K.; Kojima, N.; Ohya-Nishiguchi, H.; Hirota, N. *Inorg. Chem.* **1992**, *31*, 1338.
(18) Fukui, K.; Masuda, H.; Ohya-Nishiguchi, H.; Kamada, H. *Inorg. Chim. Acta.* **1995**, *238*, 73.
(19) Kramers, H. A. *Proc. R. Acad. Sci. Amsterdam* **1930**, *33*, 959.
(20) Mossin, S.; Tran, B. L.; Adikari, D.; Pink. M.; Heinemann, F. W.; Sutter, J.; Szilagyi, R. K.; Meyer, K.; Mindiola, D. J. *J. Am. Chem. Soc.* **2012**, *134*, 13651.
(21) Maganas, D.; Milikisyants, S.; Rijnbeek, J. M. A.; Sottini, S.; Levesanos, N.; Kyritsis, P.; Groenen, E. J. J. *Inorg. Chem.* **2010**, *49*, 595.
(22) Maganas, D.; Sottini, S.; Kyritsis, P.; Groene, E. J. J.; Neese, F. *Inorg. Chem.* **2011***, 50*, 8741.
(23) Holah, D. G.; Coucouvanis, D. *J. Am. Chem. Soc.* **1975**, *97*, 6917.
(24) Swenson, D.; Baenziger, N. C.; Coucouvanis, D. *J. Am. Chem. Soc.* **1978**, *100*, 1932.
(25) Dance, I. G. *J. Am. Chem. Soc.* **1979**, *101*, 6264.
(26) McConnachie, J. M.; Ibers, J. A. *Inorg. Chem.* **1991**, *308*, 1771.
(27) Hatano, M.; Takagi, E.; Ishihara, K. *Org. Lett.* **2008**, *9*, 4527.
(28) Baumgarner, C. D.; Malen, A. H.; Pastor, S. D.; NabiRahni, M. A. *Helv. Chim. Acta.* **1992**, *75*, 480.
(29) Dowd, P.; Kennedy, P. *Synthetic Commun.* **1981**, *11*, 935.
(30) Cole, K. S.; Cole, R. H. *J. Chem. Phys.* **1941**, *9*, 341.
(31) Bain, G. A.; Berry, J. F. *J. Chem. Educ.* **2008**, *85*, 532.
(32) de Levie, R. SolverAid (Version 7) [Microsoft Excel Macro], 2007.
(33) APEX2, v. 2009 ; Bruker Analytical X-Ray Systems, Inc: Madison, WI, 2009.
(34) Sheldrick, G. M. SADABS, Version 2.03; Bruker Analytical X-Ray Systems, Inc.: Madison, WI, 2000.
(35) Altomare, A.; Burla, M. C.; Camalli, M.; Cascarano, G. L.; Giacovazzo, C.; Guagliardi, A.; Moliterni, A. G. G.; Polidori, G.; Spagna, R. *J. Appl. Cryst.* **1999**, *32*, 115.

(36) Sheldrick, G. M. SHELXTL, Version 6.12; Bruker Analytical X-ray Systems, Inc.: Madison, WI, 2000
(37) Farrugia, L. J. *J. Appl. Cryst.* **1999**, *32*, 837.
(38) Ballhausen, C. J. Introduction to Ligand Field Theory, McGraw-Hill, New York, 1962.
(39) Schäffer, C. E. *Struct. Bonding* **1968**, *5*, 68.
(40) Bendix, J.; Brorson, M.; Schäffer, C. E. *Inorg. Chem.* **1993**, *32*, 2838.
(41) Figgis, B. N.; Hitchman, M. A. Ligand Field Theory and its Applications, John Wiley & Sons, New York, 2000.
(42) Brorson, M.; Schäffer, C. E. *Inorg. Chem.* **1988**, *27*, 2522.
(43) Shannon, R. D. *Acta Crystallogr.* **1976**, *A32*, 751.
(44) Ibrahim, A. I.; Gaube, W.; Kalies, W.; Witt, B.; *J. Prakt. Chem.* **1991**, *333*, 397.
(45) Buzzeo, M. C.; Iqbal, A. H.; Long, C. M.; Millar, D.; Patel, S.; Pellow, M. A.; Saddoughi, S. A.; Smenton, A. L.; Turner, J. F. C.; Wadhawan, J. D.; Compton, R. G.; Golen, J. A.; Rheingold, A. L.; Doerrer, L. H. *Inorg. Chem.* **2004**, *43*, 7709.
(46) Bradley, D. C.; Mehrotra, R. C.; Rothwell, I. P.; Singh A., Alkoxo and Aryloxo Derivatives of Metals, Academic Press, New York, 2001.
(47) Shores, M. P.; Sokol, J. J.; Long, J. R. *J. Am. Chem. Soc.* **2002**, *124*, 2279.
(48) Carlin, R. L. Magnetochemistry, Springer, New York, 1986.
(49) Gatteschi, D.; Sessoli, R. *Angew. Chem. Int. Ed.* **2003**, *42*, 268.
(50) McGarvey, B. R.; Telser, J. *Inorg. Chem.* **2012**, *51*, 6000.
(51) Dai, D.; Xiang, H.; Whangbo, M.-H. *J. Comput. Chem.* **2008**, *29*, 2187.
(52) Ruamps, R.; Batchelor, L. J.; Maurice, R.; Gogoi, N.; Jiménez-Lozano, P.; Guihéry, N.; de Graaf, C.; Barra, A.-L.; Sutter, J.-P.; Mallah, T. *Chem.-Eur. J.* **2013**, *19*, 950.
(53) Karunadasa, H. I.; Arquero, K. D.; Berben, L. A.; Long, J. R. *Inorg. Chem*. **2010**, *49*, 4738.
(54) Ye, S.; Neese, F. *J. Chem. Theory Comput.* **2012**, *8*, 2344.
(55) Zadrozny, J. M.; Liu, J.; Piro, N. A.; Chang, C. J.; Hill, S.; Long, J. R. *Chem. Commun.* **2012**, *48*, 3927.
(56) Atanasov, M.; Ganyushin, D.; Pantazis, D. A.; Sivalingam, K. ; Neese, F. *Inorg. Chem.* **2011**, *50*, 7460.

Table 5.S1. Crystal data for structure refinement of **1**.

Empirical Formula	$C_{76}H_{66}CoN_2O_4P_2$
Formula weight	1192.18 g/mol
Temperature	100(2) K
Wavelength	0.71069 Å
Crystal System	Monoclinic
Space Group	$P2_1$
Unit Cell Dimensions	a = 13.015(1) Å, α = 90.00°
	b = 17.876(1) Å, β = 90.187(3)°
	c = 13.132(1) Å, γ = 90.00°
Volume	3055.3(3) Å^3
Z	2
Density (calculated)	1.300 Mg/m^3
Absorption coefficient	0.388 mm^{-1}
F_{000}	1250
Crystal color	Blue
Crystal size	0.10 × 0.10 × 0.05 mm^3
θ range	1.55 to 25.40°
Index ranges	$-14 \le h \le 13$
	$-21 \le k \le 21$
	$-15 \le l \le 15$
Reflections collected	39754
Independent reflections	9843 [R_{int} = 0.0417]
Completeness to θ = 25.40°	93.4 %
Absorption correction	Multi-scan
Maximum and minimum transmission	0.6496 and 0.7452
Refinement method	Full-matrix least-squares on F^2
Data / restraints / parameters	9843 / 1 / 770
Goodness-of-fit on F^{2a}	1.078
Final R indices [I > 2σ(I) = 9843 data]^b	R_1 = 3.88 %, wR_2 = 8.62 %
R indices (all data, 0.80 Å)	R_1 = 4.46 %, wR_2 = 9.16 %
Largest diff. peak and hole	0.645 and –0.675 e.Å^{-3}

[a] GooF = $[\Sigma[w(F_o^2-F_c^2)^2] / (n-p)]^{1/2}$ where n is the number of reflections and p is the total number of parameters refined. [b] $R_1 = \Sigma||F_o|-|F_c|| / \Sigma|F_o|$; $wR_2 = [\Sigma[w(F_o^2-F_c^2)^2] / \Sigma[w(F_o^2)^2]]^{1/2}$

Table 5.S2. Crystal data for structure refinement of **2**.

Empirical Formula	$C_{48}H_{40}CoKO_4P$
Formula weight	809.80 g/mol
Temperature	100(2) K
Wavelength	1.54178 Å
Crystal System	Tetragonal
Space Group	*I*–4
Unit Cell Dimensions	a = 17.446(2) Å, $\alpha = 90^\circ$
	b = 17.446(2) Å, $\beta = 90^\circ$
	c = 6.9858(6) Å, $\gamma = 90^\circ$
Volume	2126.2(3) Å^3
Z	2
Density (calculated)	1.265 Mg/m^3
Absorption coefficient	4.726 mm^{-1}
F_{000}	842
Crystal color	Blue
Crystal size	0.30 × 0.13 × 0.13 mm^3
θ range	3.58 to 68.28°
Index ranges	$-19 \le h \le 21$
	$-20 \le k \le 18$
	$-8 \le l \le 8$
Reflections collected	4825
Independent reflections	1569 [R_{int} = 0.0314]
Completeness to $\theta = 26.06^\circ$	96.9 %
Absorption correction	Multi-scan
Maximum and minimum transmission	0.502 and 0.541
Refinement method	Full-matrix least-squares on F^2
Data / restraints / parameters	1569/ 0 / 124
Goodness-of-fit on F^{2a}	1.056
Final R indices [I > 2σ(I) = 1569 data]^b	R_1 = 3.32 %, wR_2 = 8.45 %
R indices (all data, 0.80 Å)	R_1 = 3.34 %, wR_2 = 8.45 %
Largest diff. peak and hole	0.351 and –0.214 e.Å^{-3}

[a] GooF = $[\Sigma[w(F_o^2-F_c^2)^2] / (n-p)]^{1/2}$ where n is the number of reflections and p is the total number of parameters refined. [b] $R_1 = \Sigma||F_o|-|F_c|| / \Sigma|F_o|$; $wR_2 = [\Sigma[w(F_o^2-F_c^2)^2] / \Sigma[w(F_o^2)^2]]^{1/2}$

Table 5.S3. Crystal data for structure refinement of **4**.

Empirical Formula	$C_{72}H_{60}CoP_2Se_4$
Formula weight	1361.91 g/mol
Temperature	100(2) K
Wavelength	0.71069 Å
Crystal System	Orthorhombic
Space Group	$Pca2_1$
Unit Cell Dimensions	a = 17.561(1) Å, α = 90°
	b = 13.801(1) Å, β = 90°
	c = 24.716(1) Å, γ = 90°
Volume	5990.2(5) Å^3
Z	4
Density (calculated)	1.510 Mg/m^3
Absorption coefficient	2.814 mm^{-1}
F_{000}	2740
Crystal color	brown
Crystal size	0.12 × 0.10 × 0.05 mm^3
θ range	1.48 to 25.34°
Index ranges	$-21 \le h \le 21$
	$-14 \le k \le 16$
	$-29 \le l \le 27$
Reflections collected	75335
Independent reflections	10776 [R_{int} = 0.0521]
Completeness to θ = 26.06°	99.9 %
Absorption correction	Multi-scan
Maximum and minimum transmission	0.946 and 0.849
Refinement method	Full-matrix least-squares on F^2
Data / restraints / parameters	10776 / 1 / 712
Goodness-of-fit on F^{2a}	1.058
Final R indices [I > 2σ(I) = 10776	R_1 = 3.91 %, wR_2 = 8.03 %
R indices (all data, 0.80 Å)	R_1 = 5.49 %, wR_2 = 8.57 %
Largest diff. peak and hole	1.961 and –1.241 e.Å^{-3}

[a] GooF = $[\Sigma[w(F_o^2-F_c^2)^2] / (n-p)]^{1/2}$ where n is the number of reflections and p is the total number of parameters refined. [b] $R_1 = \Sigma||F_o|-|F_c|| / \Sigma|F_o|$; $wR_2 = [\Sigma[w(F_o^2-F_c^2)^2] / \Sigma[w(F_o^2)^2]]^{1/2}$

Table 5.S4. Observed and calculated electronic absorption data (in cm^{-1}) for **1**-**4** with labels corresponding to T_d, D_{2d}, and C_{2v} symmetries.[a]

	1	**2**[c]	**3**[d]	**4**
T_d[b]				
$^4A_2 \rightarrow {}^4T_2$	- (4350)	5500 (4656, *4910*)	-	5500 (4740; *5130*)
$^4A_2 \rightarrow {}^4T_1(^4F)$	7500 (7500)	8000 (8000, *8390*)	-	7800 (7800; *8190*)
$^4A_2 \rightarrow {}^4T_1(^4P)$	17000 (17000)	17500 (17500, *17480*)	-	13400 (13400, *13300*)
D_{2d}				
$^4B_1 \rightarrow {}^4B_2$ (z)	- (0)	- (0, *440*)	~1000[f] (980, *80*)	- (2530, *0*)
$^4B_1 \rightarrow {}^4E$ (x, y)	- (4490)	5720 (4680, *5440*)	4850 (4920, *4930*)	5510 (4640, *5510*)
$^4B_1 \rightarrow {}^4A_2$ (z)	7890 (7860)	8350 (8270, *8580*)	8400[e] (8200, *8220*)	- (8420, *8370*)
$^4B_1 \rightarrow {}^4E$ (x, y)	6670 (6900)	7020 (7290, *7380*)	7100[e] (7350, *7340*)	7780 (7780,*7800*)
	7100 (6900)	7470 (7290, *7380*)	- (7350, *7340*)	
$^4B_1 \rightarrow {}^4A_2$ (z)	17760 (17750)	19120 (19080, *18580*)	15350[e] (15230, *15250*)	15170 (15170, *15060*)
$^4B_1 \rightarrow {}^4E$ (x, y)	15950 (16320)	16720 (17480, *17720*)	13850[e] (13990, *13980*)	12770 (13600, 13640*)*
	16670 (16320)	18020 (17480, *17720*)	- (13990, *13980*)	13370 (13600, 13640*)*
				14310 (13600, 13640*)*
C_{2v}				
$^4A_2 \rightarrow {}^4A_1$ (z)	- (650)	- (0, *1600*)	~1000[f] (980, *80)*	- (*1580*)
$^4A_2 \rightarrow {}^4B_1, {}^4B_2$ (x, y)	- (4620)	- (3220, *3480*)	4290 (4140, *4210*)	5510 (*5510, 5770*)
	- (4750)	5720 (4880, *5600*)	5130 (5200, *5110*)	
$^4A_2 \rightarrow {}^4A_2$ (z)	7890 (7760)	8350 (8080, *8110*)	8400 (8180, *8160*)	- (*8820*)
$^4A_2 \rightarrow {}^4B_2, {}^4B_1$ (x, y)	6670 (6870)	7020 (7230, *7370*)	6600 (7340, *7290*)	7780 (*7770*)
	7100 (7050)	7470 (7590, *7440*)	7600 (7360, *7460*)	- (*7740)*
$^4A_2 \rightarrow {}^4A_2$ (z)	17760 (17700)	19120 (19040, *18920*)	15350 (15260, *15210*)	15170 (*14900*)
$^4A_2 \rightarrow {}^4B_2, {}^4B_1$ (x, y)	15950 (15990)	16720 (16890, *17140*)	13850 (13780, *13650*)	12770 (*13060*)
	16670 (16700)	18020 (18120, *18020*)	- (14100, *14390*)	13370 (*13060*)
				14310 (*14530*)

[a]Values rounded to nearest 10 cm^{-1}. Calculated values in parentheses. Dashes indicate unobserved transitions. Transitions for D_{2d} and C_{2v} symmetries are grouped into three sets corresponding to the three T_d transitions to which they are respectively associated. [b]Barycenters of transitions are estimated. Calculated values for **1** and **2** were obtained with a crystal field model and values of B = 763.3 cm^{-1} and $10Dq$ = –4350 cm^{-1} for **1** and B = 768.9 cm^{-1} and $10Dq$ = –4656 cm^{-1}. [c]T_d calculated values in italics include the $^4A_2 \rightarrow {}^4T_2$ transition estimated from the magnetic parameters and the best fit used B = 743 cm^{-1} and $10Dq$ = –4910 cm^{-1}. [d]The availability of single-crystal absorption data from ref. 6 allowed immediate analyses at the more realistic D_{2d} and C_{2v} symmetries. [e]Taken from ref. 6; see Table S4 for comparison with diffuse-reflectance spectra. Calculated values are from this work; see Table S4 for further comparison. [f]Estimated from magnetic parameters (g, D), not spectroscopically observed.

Table 5.S5. Energies of the 3d-orbitals as determined by fitting the diffuse reflectance spectra for **1**-**4**.

	1[a]		**2**[b]			
	D_{2d}	C_{2v}	D_{2d}		C_{2v}	
B	788	784	852	828	850	833
$E(d_{xz})$	6900	7340	7290	7150	8800	7940
$E(d_{yz})$	6900	5720	7290	7150	5550	5000
$E(d_{xy})$	4800	4290	5210	4220	5330	5560
$E(d_{x2-y2})$	4800	4940	5210	3780	5330	3970
$E(d_{z2})$	0	0	0	0	0	0

	3[c]		**4**	
	D_{2d}[d]	C_{2v}	D_{2d}[e]	C_{2v}[f]
B	583.5 (583.5)	582.1(585.1)	529 (521)	(474)
$E(d_{xz})$	6850 (7300)	7580 (7810)	6654 (7800)	(5580)
$E(d_{yz})$	6850 (7300)	6180 (6000)	6654 (7800)	(8360)
$E(d_{xy})$	5000 (4590)	5310 (4220)	6580 (4270)	(1870)
$E(d_{x2-y2})$	4020 (4510)	4360 (5000)	4230 (4270)	(3450)
$E(d_{z2})$	0	0	0	0

[a]Fits made ignoring $^4A_2 \rightarrow {}^4T_2(x,y)$ transition. [b]The left columns under axial and rhombic ignore $^4A_2 \rightarrow {}^4T_2(x,y)$ transition. The right columns incorporate the $^4A_2 \rightarrow {}^4T_2(x,y)$ transitions in the fits and correspond to D_{2d} and C_{2v} symmetries, respectively. [c]Values in parentheses ignore the 1000 cm^{-1} $^4A_2 \rightarrow {}^4T_2(z)$ transition. [d]3d-orbital energies (in cm^{-1}) determined by Fukui et al.: $E(d_{z2}) = 0$; $E(d_{x2-y2}) = 4140$; $E(d_{xy}) = 5140$; $E(d_{xz}, d_{yz}) = 6850$. [e]Values in parentheses include 1000 cm^{-1} $^4A_2 \rightarrow {}^4T_2(z)$ transition. [f]Unable to obtain reasonable fit by ignoring $^4A_2 \rightarrow {}^4T_2(z)$ transition.

Table 5.S6. Electronic absorption data and AOM fits for $[Co(EPh)_4]^{2-}$ (values in cm^{-1}).[a]

Complex	Experimental[f]	σ-bonding only	σ- and π-bonding
1, $(Ph_4P)_2[Co(OPh)_4]$ [b]	---	3460	3090
	5720	3920	3680
	5720	4860	4180
	6670	6300	6510
	7100	6920	7190
	7890	8380	7920
	15 960	16 400	15 830
	16 670	16 960	16 770
	17 760	17 020	17 800
2, $K(Ph_4P)[Co(OPh)_4]$ [c]	---	not successful	1370
	---		2400
	5720		6320
	7020		6320
	7470		8020
	8350		8020
	16 720		17 500
	18 200		17 500
	19 120		18 980
3, $(Ph_4P)_2[Co(SPh)_4]$ [d]	~1000 [g]	3860	4150
	4290	3990	4400
	5130	5580	4550
	6600	7300	7540
	7600	7360	7840
	8400	7870	8090
	13 400	14 500	13 790
	14 300	14 630	13 970
	15 350	14 770	15 270
4, $(Ph_4P)_2[Co(SePh)_4]$ [e]	---	4640	4530
	5510	4690	4590
	5510	5640	5760
	7000	8030	8050
	7780	8180	8080
	7780	8240	8260
	13 070	13 940	13 900
	14 310	13 990	14 040
	15 170	14 050	14 090

[a] All values are rounded to the nearest 10 cm^{-1}. [b] θ = 53.40° (O1, O2), 118.57° (O3, O4); idealized ϕ = 0° (S1), 180° (S2), 90° (S3), 270° (S4). σ-bonding only: B = 768, ε_σ = 3175 ; σ- and π-bonding: B = 775, ε_σ = 3850, $\varepsilon_{\pi\text{-}S}$ = 995 ($\varepsilon_{\pi\text{-}C} \equiv 0$). [c] θ = 33.68°, 146.32° (all O atoms symmetry equivalent); idealized ϕ = 0°, 180°, 90°, 270°. σ-bonding only gave no reasonable parameters; σ- and π-bonding: B = 402, ε_σ = 7880, $\varepsilon_{\pi\text{-}S}$ = 2650 ($\varepsilon_{\pi\text{-}C} \equiv 0$). B is unreasonably small for this fit and the bonding parameters too large. Fitting with $\varepsilon_{\pi\text{-}C} \neq 0$, $\varepsilon_{\pi\text{-}S} \equiv 0$ also did not converge. [d] θ = 59.80° (S1, S2), 121.86° (S3, S4); idealized ϕ = 0° (S1), 180° (S2), 90° (S3), 270° (S4). σ-bonding only: B = 580, ε_σ = 3450; σ- and π-bonding: B = 523, ε_σ = 4520, $\varepsilon_{\pi\text{-}S}$ = 1080 ($\varepsilon_{\pi\text{-}C} \equiv 0$). Use of cylindrical π-bonding gave unreasonably large parameters for both σ- and π-bonding, while fits with $\varepsilon_{\pi\text{-}S} \equiv 0$, $\varepsilon_{\pi\text{-}C} \neq 0$, gave π-acceptor behavior for the S-donors, which is also unreasonable. [e] θ = 57.48° (S1, S2), 123.22° (S3, S4); idealized ϕ = 0° (S1), 180° (S2), 90° (S3), 270° (S4). σ-bonding only: B = 478, ε_σ = 3780; σ- and π-bonding: B = 483, ε_σ = 3690, $\varepsilon_{\pi\text{-}S}$ = –90 ($\varepsilon_{\pi\text{-}C} \equiv 0$). This π-bonding is not significant. [f] For assignments, see Table 3. [g] Estimated based on magnetic data; not observed directly.

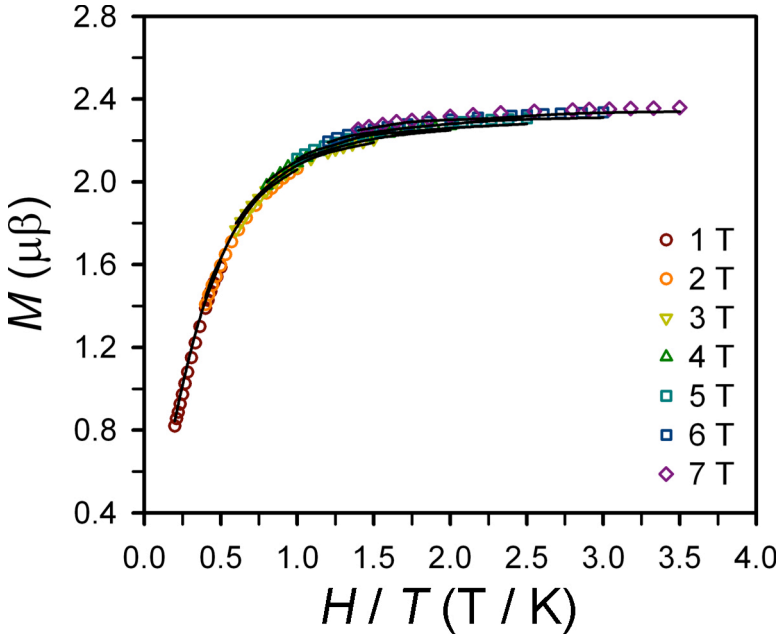


Figure 5.S1. Reduced magnetization data collected on **3**. Experimental data taken from ref. 15. Black lines are simulations with $D = -62$ cm^{-1}, $g_z = 2.96$, $g_{x,y} = 2.285$.

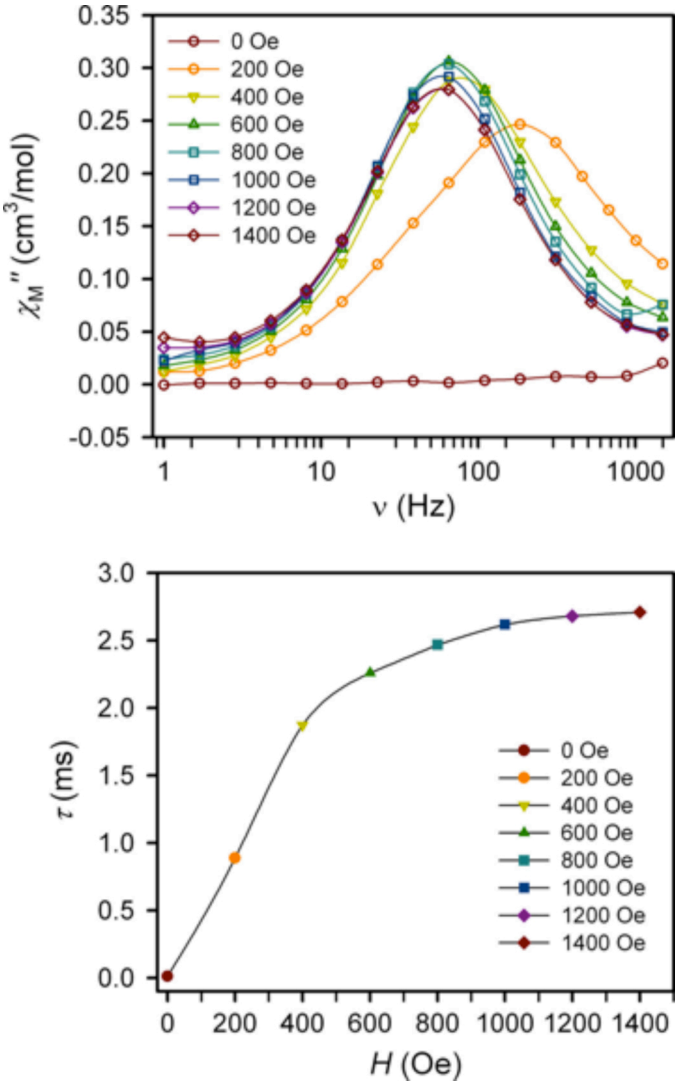


Figure 5.S2. Variable-field variable-frequency out-of phase ac susceptibility data for **1** (top) and field dependendence of τ (bottom). Solid colored and black lines are guides for the eye.

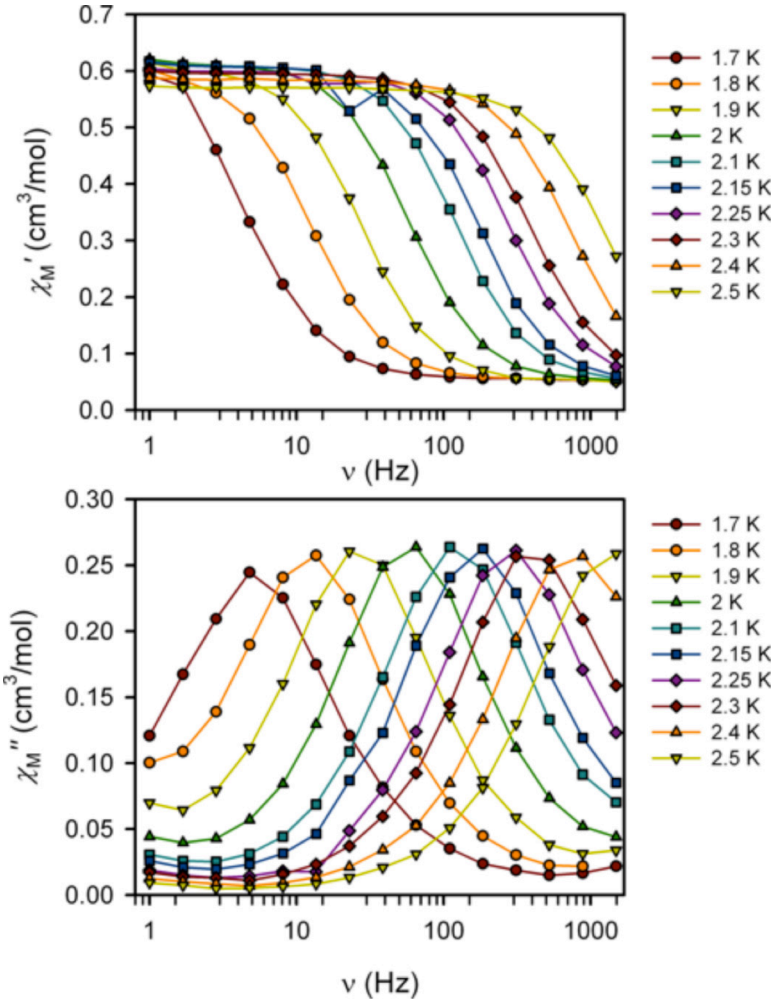


Figure 5.S3. In-phase and out-of phase ac susceptibility data for **1** under 1400 Oe field. Solid colored lines are guides for the eye.

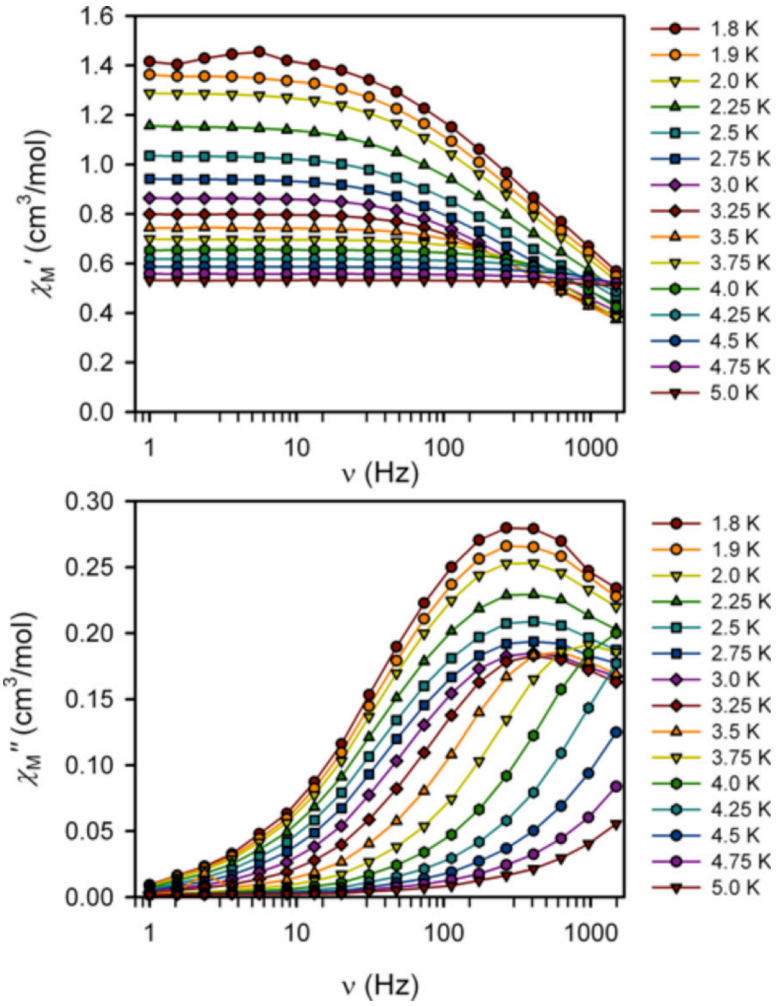


Figure 5.S4. In-phase (top) and out-of phase (bottom) ac susceptibility data for **2** under zero dc field. Solid colored lines are guides for the eye.

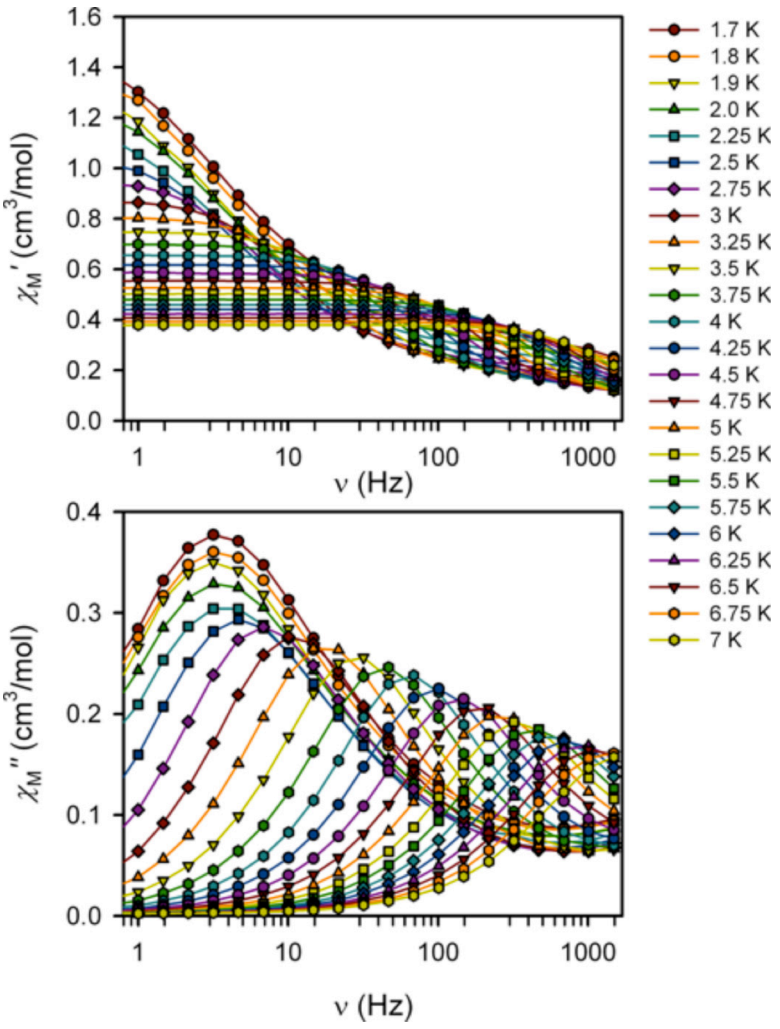


Figure 5.S5. In-phase (top) and out-of phase (bottom) ac susceptibility data for **4** under zero dc field. Solid colored lines are guides for the eye.

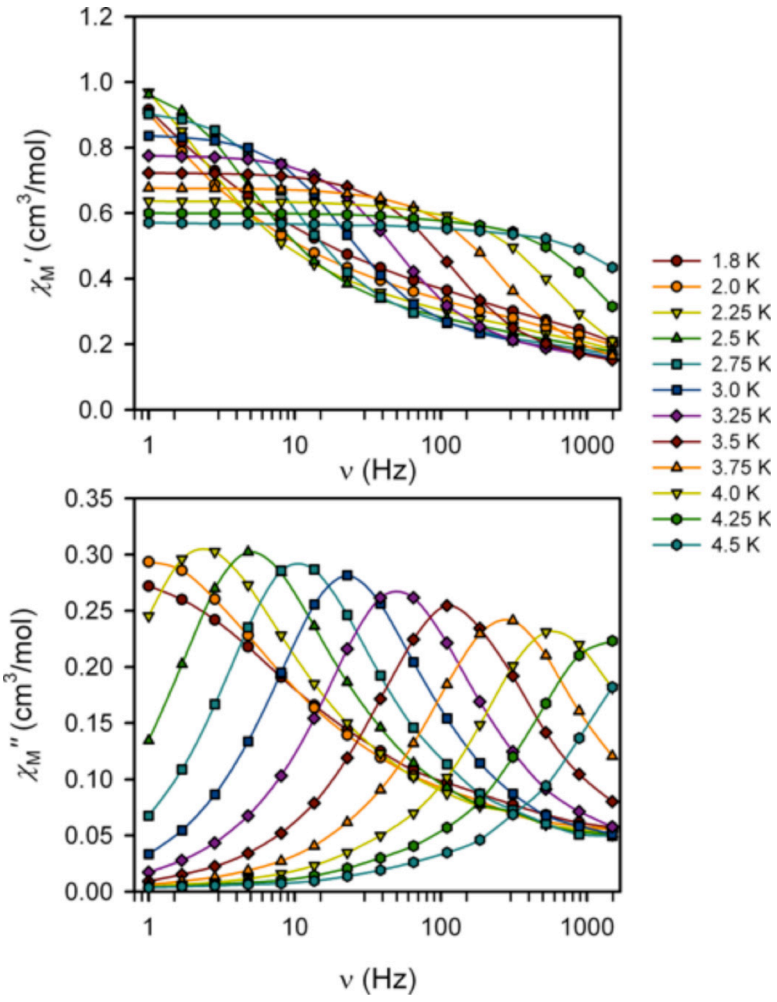


Figure 5.S6. In-phase (top) and out-of phase (bottom) ac susceptibility data for **5** under zero dc field. Solid colored lines are guides for the eye.

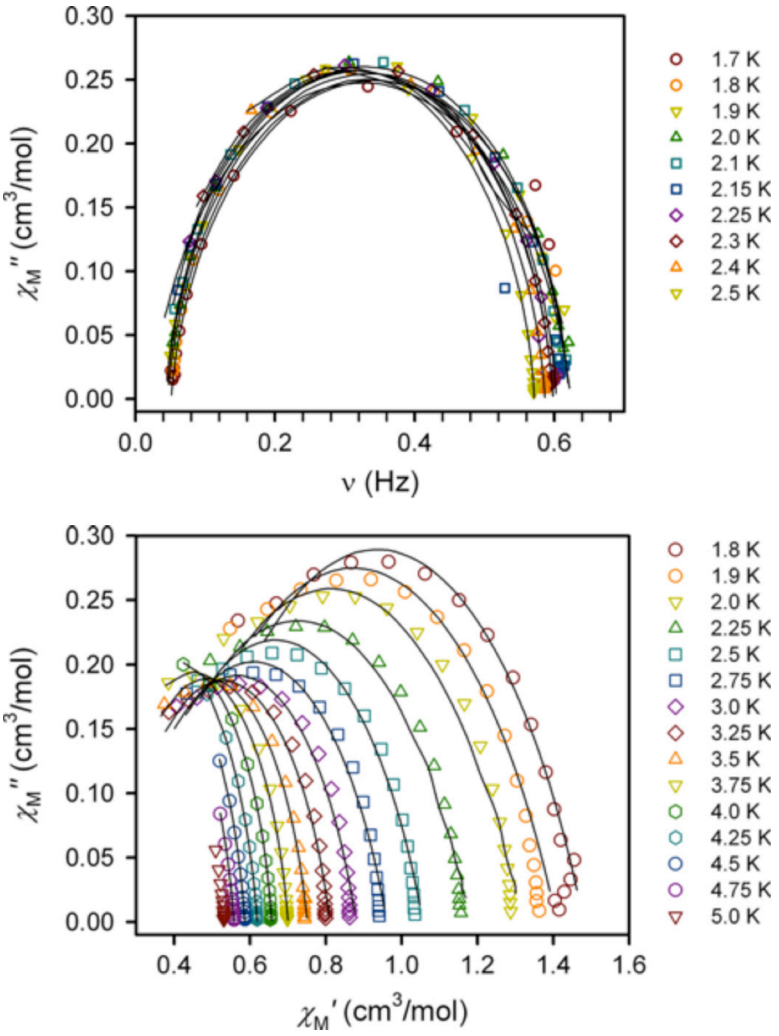


Figure 5.S7. Cole-cole plots used for the determination of the temperature dependence of the magnetic relaxation times for **1** (top) and **2** (bottom). Solid lines are best fits to a Debye model, as described in the main text.

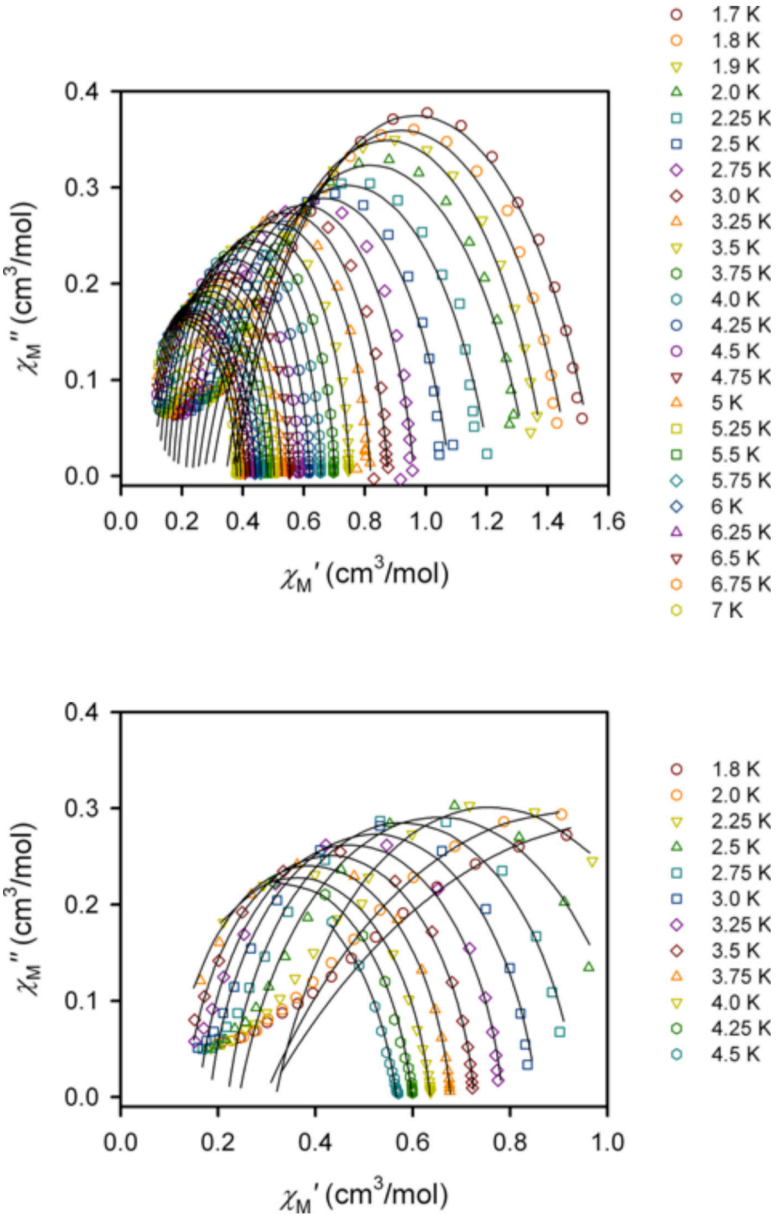


Figure 5.S8. Cole-cole plots used for the determination of the temperature dependence of the magnetic relaxation time for **4** (top) and **5** (bottom). Solid lines are best fits to a generalized Debye model, as discussed in the text.

Chapter 6: Slow Magnetization Dynamics in a Series of Two-Coordinate Iron(II) Complexes

7.1. Introduction

In the presence of axial magnetic anisotropy (D), the M_S levels of a system with total spin S will split under zero magnetic field according to the Hamiltonian $\hat{H} = D\hat{S}_z^2$. If D is negative, the two $\pm M_S$ levels of maximal projection along the z-axis are degenerate and form a bistable ground state. Reversing the moment by converting $-M_S$ to $+M_S$ then requires traversal of a spin-inversion barrier, $U = S^2|D|$ (or $U = (S^2 - {}^1/_4)|D|$ for non-integer S), where the system passes through the $M_S = 0$ (or $M_S = \pm {}^1/_2$ for non-integer S) levels at the height of the barrier. The existence of this energy barrier can lead to the slow relaxation of the magnetic moment at low temperatures upon removal from a polarizing dc field. An important manifestation of this barrier is a magnetic hysteresis that is molecular in origin, as first observed for the compound $Mn_{12}O_{12}(CH_3CO_2)_{16}(H_2O)_4$.[1]

Molecules exhibiting such behavior are known as single-molecule magnets, and have been invoked as possible media for high-density information storage,[2] quantum computing,[3] and magnetic refrigeration.[4] A significant effort has therefore been dedicated to the preparation and study of new systems in search of a better understanding of the various phenomena that influence single-molecule magnet behavior. These studies have led to the discovery of slow magnetic relaxation in a variety of polynuclear coordination clusters[5] as well as in mononuclear lanthanide,[6] actinide,[7] and, most recently, transition metal complexes.[8] Synthetic efforts have occurred in tandem with theoretical studies, with the latter showing the magnitude of D to decrease with increasing S, implying that the overarching goal of the discovery a single-molecule magnet with a large U should not be pursued solely in terms of maximizing S.[9]

Mononuclear transition metal complexes provide a fertile new platform for research in the field. Experimental techniques for characterizing their electronic structures are well established,[10] and ligand field theory provides chemists with an intuitive framework for tuning the electronic properties by ligand and/or metal ion variation.[11]

Several classes of first-row transition metal complexes lend themselves to bearing large magnetic anisotropies. Octahedral complexes of cobalt(II) have long been known[12] to display significant magnetic anisotropy as result of the orbital angular momentum of the $t_{2g}^5e_g^2$ electron configuration. This behavior extends to complexes with lower coordination numbers, for which the 3d orbital energy splittings are reduced. For example, iron(II) complexes of coordination numbers 4 and 3 have been characterized as having the magnetic signatures of orbital angular momentum.[13] Furthermore, recent studies on the trigonal pyramidal iron(II) complexes $[(tpa^R)Fe]^-$ have presented the ability to systematically enhance the magnetic anisotropy of the $S = 2$ center via increasing the electron donating abilities of the tris(pyrrolyl-α-methyl)amine ligand.[8a,b] Together, these observations suggest that the common principles of molecular inorganic chemistry can be utilized in the search for and design of systems with large magnetic relaxation barriers.

In our study of mononuclear transition metal single-molecule magnets, we have deliberately targeted complexes with low-coordination numbers. Here, the low coordination number supports

the preparation, via appropriate ligand choice, of local coordination geometries with one principal axis of rotation of order greater than 2. This will engender orbital degeneracies that, when coupled with the appropriate number of d-electrons, produce orbital angular momentum conducive to a large magnetic anisotropy.

Although many are known,[14] paramagnetic two-coordinate transition metal complexes have yet to be evaluated in detail as potential single-molecule magnets. Of particular interest are complexes displaying a rigorously linear L–M–L geometry with local $D_{\infty h}$ symmetry at the metal center. Here, the ligand field splits the energies of the d-orbitals as (d_{xy}, d_{x2-y2}) < (d_{xz}, d_{yz}) < d_{z2}, with the (d_{xz}, d_{yz}), and d_{z2} orbital energies being destabilized by π and σ-metal-ligand interactions, respectively. In contrast, the (d_{xy},d_{x2-y2}) orbitals have d symmetry with respect to the axial ligands and are thus not engaged in bonding. Consequently, for a d^6 metal center, such as iron(II), we can expect a large first-order contribution to the orbital angular momentum that will not be quenched through a Jahn-Teller distortion.[15] There are many two-coordinate complexes of iron(II) known,[16] some with rigorously linear L–M–L geometries.[16e,f,j,k,l,m] Importantly, magnetic and spectroscopic measurements on a select few have revealed the signatures of large magnetic anisotropies.[16g,j,m]

Herein, we report the first detailed characterization of the magnetization dynamics for a series of homoleptic, two-coordinate iron(II) complexes of varying ligand-field donor strength, which indeed behave as single-molecule magnets. In particular, we explore the direct current (dc) and alternating current (ac) susceptibility and magnetization data for the six iron(II) complexes depicted in Figure 6.1, each featuring two sterically encumbering ligands. All compounds display slow magnetic relaxation under an applied field, and the trends observed in relaxation behavior are explored using first-principles calculations within the context of ligand field theory.

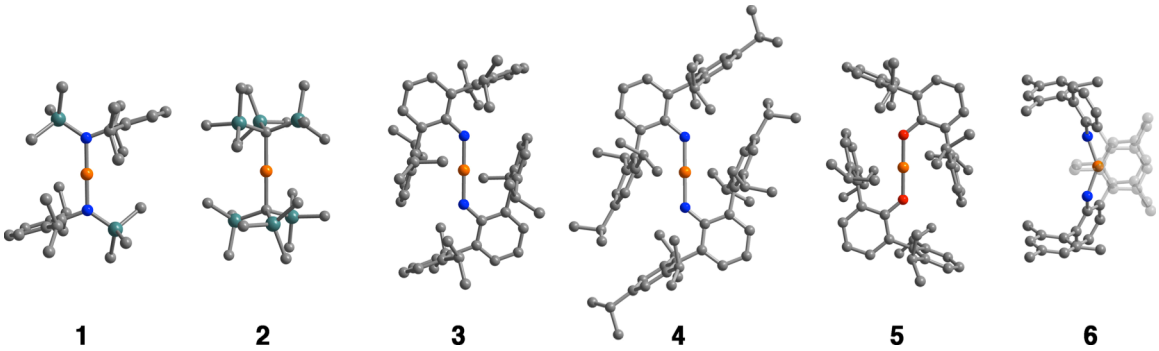


Figure 6.1. Structures of the two-coordinate iron(II) complexes analyzed in this study: Fe[N(SiMe$_3$)(Dipp)]$_2$ (Dipp = C$_6$H$_3$-2,6-Pr$^i_2$) (**1**), Fe[C(SiMe$_3$)$_3$]$_2$ (**2**),[16e,f] Fe[N(H)Ar']$_2$ (Ar' = C$_6$H$_3$-2,6-(C$_6$H$_3$-2,6-Pr$^i_2$)$_2$) (**3**), Fe[N(H)Ar*]$_2$ (Ar* = C$_6$H$_3$-2,6-(C$_6$H$_2$-2,4,6-Pr$^i_3$)$_2$) (**4**),[16m] Fe(OAr')$_2$ (**5**),[16l] and Fe[N(H)Ar$^{\#}$]$_2$ (Ar$^{\#}$ = C$_6$H$_3$-2,6-(C$_6$H$_2$-2,4,6-Me$_3$)$_2$) (**6**).[16m] Orange, cyan, red, blue, and gray spheres represent Fe, Si, O, N, and C atoms, respectively; H atoms have been omitted for clarity.

6.2. Experimental

6.2.1. Synthetic Procedures. All manipulations were performed with the use of modified Schlenk techniques or in a Vacuum Atmospheres glove box under N_2 or Ar. Solvents were dried and collected using a Grubbs-type solvent purification system[17] (Glass Contour) and degassed by using the freeze-pump-thaw method. Unless otherwise stated, all materials were obtained from commercial sources and used as received. The compound $[Fe(N(SiMe_3)_2)_2]_2$ was prepared by a modified literature procedure[18] from 'activated,' anhydrous $FeCl_2$, which was obtained from finely powdered $FeCl_2 \cdot 4H_2O$ by following a similar dehydration procedure as previously reported for $MnCl_2$.[19] The compounds LiN(SiMe$_3$)(Dipp), LiN(H)Ar*, LiN(H)Ar′, LiN(H)Ar$^{\#}$ and HOAr′ were prepared according to literature procedures,[16m,20] as was Fe[C(SiMe$_3$)$_3$]$_2$ (**2**).[16f]

Synthesis of Fe[N(SiMe$_3$)(Dipp)]$_2$ (1). To a slurry of $FeCl_2$ (0.70 g, 5.6 mmol) in ca. 10 mL of diethyl ether was added a solution of LiN(SiMe$_3$)(Dipp) (3.0 g, 12 mmol) in 50 mL of diethyl ether at 0 °C. The dark brown reaction mixture was allowed to warm to room temperature and stirred for 18 h. All volatile materials were removed *in vacuo* and the residue was extracted with hexanes. This extract was filtered via a cannula and the dark brown filtrate was concentrated and refrigerated at –18 °C overnight to afford large, brown crystals of **1** (1.8 g, 58 %). M.p.: 209-211 °C. UV-Vis (hexane): λ_{max} (ε_M, $M^{-1}cm^{-1}$) 344 (6200) nm. IR (Nujol): ν_{Fe-N}, 400 cm^{-1}. Anal. Calcd. for $C_{30}H_{52}FeN_2Si_2$: C, 65.19; H, 9.48; N, 5.07. Found: C, 66.01; H, 9.25; N, 4.95.

Synthesis of Fe[N(H)Ar′]$_2$ (3). To a slurry of $FeCl_2$ (0.12 g, 0.96 mmol in 10 mL of diethyl ether) at 0 °C was added a slurry of LiN(H)Ar′ (0.81 g, 1.9 mmol in 60 mL of diethyl ether) dropwise over 30 min. The resultant pale orange slurry was allowed to warm to room temperature and stirred for 3 days, during which time the solution darkened to red. All volatile components were removed *in vacuo* and the residue was extracted with hexanes (70 mL) and filtered via cannula. The solution was concentrated to ca. 40 mL and stored at –18 °C for 2 days to produce x-ray quality orange-red crystals of **3** (0.31 g, 36%). M.p.: 196-198 °C. ^{1}H NMR (600 MHz, C_6D_6, 298 K): δ 7.31 (br, s, *p*-C_6H_3-2,6-Pr$^i_2$), 7.22 (br, s, *m*-C_6H_3-2,6-Pr$^i_2$), 6.99 (br, s, *m*-C_6H_3-2,6-Pr$^i_2$), 6.83 (br, s, p-C_6H_3-2,6-Pr$^i_2$), 2.95 (br, S, -C*H*Me$_2$), 2.88 (br, s, N-H), and 1.17 (br, d, CHC*H*$_3$) ppm. UV-Vis (hexanes): λ_{max} (ε_M, $M^{-1}cm^{-1}$) 449 (1190), 424 (1240), 323 (3200), and 298 (9400) nm. IR (Nujol): ν_{N-H} 3345 and ν_{Fe-N} 385 cm^{-1}. Anal. Calcd. for $C_{60}H_{76}FeN_2$: C, 81.79; H, 8.69; N, 3.18. Found: C, 82.64; H, 8.86; N, 2.90.

Synthesis of Fe[N(H)Ar*]$_2$ (4). This compound was prepared by an alternative route to a reported procedure.[16m] To a slurry of $FeCl_2$ (0.25 g, 2.0 mmol) in 10 mL of diethyl ether at 0 °C was added a solution of LiN(H)Ar* (2.0 g, 4.0 mmol in 45 mL of diethyl ether) slowly over 20 min. The resultant red solution was stirred at 0 °C for 30 min then allowed to warm to room temperature and stirred for a further 3 days. All volatile components were removed *in vacuo* and the residue was extracted with hexanes (80 mL) and filtered via cannula. The solution was concentrated to ca. 30 mL and stored at –18 °C for 3 days to produce red crystals of **4** (0.86 g, 41%). Compound identity was confirmed via single-crystal x-ray analysis.

Synthesis of Fe(OAr′)$_2$ (5). This compound was prepared by an alternative route to the reported procedure.[16l] Solid $[Fe(N(SiMe_3)_2)_2]_2$ (1.1 g, 1.5 mmol) was dissolved in diethyl ether (ca. 20 mL) with rapid stirring. This solution was cooled to –78 ºC, and a solution of HOAr′ (2.5 g, 6.0 mmol) in diethyl ether (ca. 30 mL) was added dropwise via cannula to afford a green solution that slowly turned brown after several days of stirring. Diethyl ether was removed under reduced pressure and the resulting brown solid was extracted with 40 mL of hexanes. The extract was filtered through diatomaceous earth (Celite 545) and concentrated to ca. 15 mL under

reduced pressure. This solution yielded yellow crystals of **5** (0.60 g, 23%) after storage overnight at –18 ºC. The identity of the compound was confirmed by UV-Vis spectroscopy, x-ray crystallography, and elemental analysis.

Synthesis of Fe[N(H)Ar$^{\#}$]$_2$ (6). This compound was prepared by an alternative route to the reported procedure.[16m] The reagent $H_2NAr^{\#}$ (3.8 g, 12 mmol) was treated with a 2.5 M solution of *n*-BuLi (5 mL, 13 mmol) in hexanes to generate a solution of $LiN(H)Ar^{\#}$, which was then added dropwise to a slurry of $FeCl_2$ (0.76 g, 6.0 mmol) in ca. 20 mL of diethyl ether chilled to 0 °C. The solution was allowed to warm to room temperature and allowed to stir for 3 days, becoming dark red in the process. All volatile components were removed *in vacuo* and the orange residue was extracted with 40 mL of hot toluene and filtered through diatomaceous earth using a filter stick. The solution was concentrated to ca. 30 mL and stored at ca. –18 °C for 3 days to produce red crystals of **6** (3.2 g, 79%). This yield represents a significant improvement over the previously reported transamination method (39%).[16m] Compound identity was confirmed by single crystal x-ray analysis.

6.2.2. Magnetic Measurements. Magnetic susceptibility data were collected using a Quantum Design MPMS-XL SQUID magnetometer. Measurements for all compounds were performed on finely ground microcrystalline powders restrained in a frozen eicosane matrix within a vacuum-sealed fused silica tube. Loading of the powders into the fused silica tube was performed under an inert atmosphere. Dc susceptibility measurements were collected in the temperature range 2-300 K under a dc field of 1 kOe. Dc magnetization data were obtained in the temperature range 1.8-5 K under dc fields of 1, 2, 3, 4, 5, 6, and 7 T. Ac susceptibility measurements were obtained in a variety of temperature ranges under a 4 Oe ac field oscillating at frequencies of 0.06-1488 Hz, under applied dc fields from 0 to 5 kOe. Dc magnetic susceptibility data were corrected for diamagnetic contributions from the sample holder and eicosane, as well as for the core diamagnetism of each sample (estimated using Pascal's constants).[21]

6.2.3. Single-Crystal X-ray Diffraction. Crystals suitable for x-ray diffraction were covered in a thin layer of hydrocarbon oil and mounted on a glass fiber attached to a copper pin and placed under an N_2 cold stream. Data for **1** and **3** were collected at 90 K on a Bruker SMART 1000 diffractometer and Bruker APEX diffractometer equipped with a Bruker APEX-II CCD using Mo Kα radiation (λ = 0.71073 Å), respectively. Absorption corrections were applied using SADABS.[22] Crystal structures were solved by direct methods and refined by full-matrix least-squares procedures in SHELXTL.[23] All non-H atoms were refined anisotropically, while all H-atoms were placed at calculated positions and refined using a riding model. The data obtained for **3** were best modelled assuming a partial occupancy of the Fe atom in and cocrystallization with the protonated ligand H_2NAr'. Cocrystallization was verified by infrared spectroscopy, which indicated a slight presence of free-amine N-H stretches. Full crystallographic tables for **1** and **3** are presented in the Supporting Information (see Tables 6.S1 and 6.S2).

6.2.4. All Other Physical Measurements. ^{1}H NMR data were obtained on a Varian Inova 600 MHz spectrometer. All ^{1}H NMR spectra are referenced to an external standard of tetramethylsilane (d = 0). IR spectra were recorded as Nujol mulls between KBR plates on a Perkin Elmer 1430 spectrophotometer. UV-Vis spectra were recorded on dilute hexane solutions in 3.5 mL quartz cuvettes using a HR2000 CG-UVNIR spectrometer with Ocean Optics DH2000 light source. Melting points were measured on samples sealed under N_2 in glass capillaries with a Mel-Temp II apparatus and are uncorrected. Combustion analyses were performed by Columbia Analytical Services.

6.2.5. Computational Details. Electronic multiplets and their magnetic sublevels are highly sensitive probes to small structural variations governed by their surroundings in the crystalline phase.[24] Thus, a complete theoretical account of all of the subtle influences of small distortions that occur due to crystal packing is not feasible. For this reason, ground- and excited-state energies and wave functions were calculated using geometries obtained directly from the x-ray crystal structures (see Figure 6.1). Since positions of hydrogen atoms from such data are subject to large error-bars their coordinates have been optimized using DFT by freezing out the non-hydrogen atoms core and allowing H-atom relaxation only. The Complete-Active-Space Self-Consistent-Field (CASSCF) module of ORCA (to account for static correlation) together with N-Electron Valence Perturbation Theory (NEVPT2)[25,26] (to account for dynamic correlation) were used to perform the calculations, in a manner detailed elsewhere.[24*b*]

Non-truncated complexes **1-6** were used throughout in the calculations. It is worth emphasizing that this is essential to obtain realistic results. For the correlated calculations, basis sets of TZVP quality alongside with the corresponding auxiliary sets (TZVP/C) were used.[26] In this set of calculations, only the metal d-orbitals were included in the active space.

Spin-orbit coupling (SOC) was taken into account using quasi-degenerate perturbation theory.[27] In a ^{5}E orbitally degenerate ground state SOC occurs in first order of perturbation theory, but generally to second order for orbitally non-degenerate states with $S > {}^1/_2$. This leads to mixing of states which differ in their spin by $\Delta S = \pm 1, 0$. Through this mixing, SOC reintroduces some orbital angular momentum into the electronic ground state that is otherwise quenched through low-symmetry. In a first step, non-relativistic multireference CASSCF wave functions in the form given by eq 1 are calculated within the Born-Oppenheimer (BO) approximation; the upper indices *SS* stand for a many-particle wavefunction (configuration state function, CSF) with a spin quantum number S and spin projection quantum number $M_S = S$.

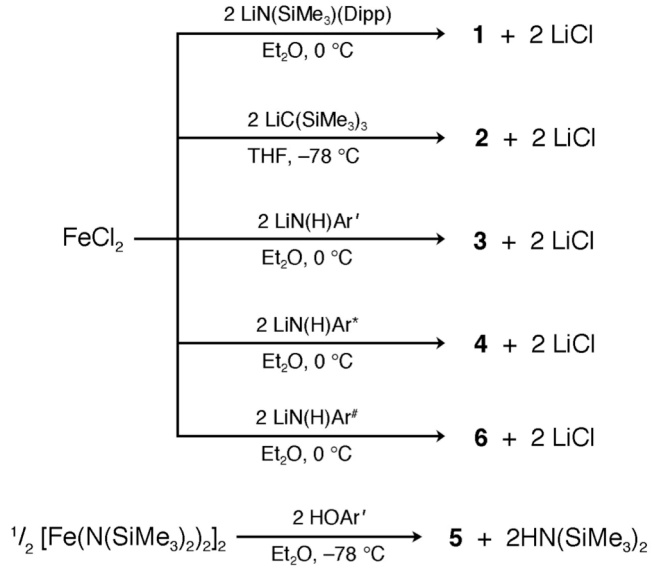
$$\left|\Psi_I^{SS}\right\rangle = \sum_{\mu} C_{\mu I} \left|\Phi_{\mu}^{SS}\right\rangle \qquad (1)$$

SOC lifts the $(2S + 1)$ degeneracy of the total spin S $\hat{H}_{\mathrm{BO}}$ eigenfunctions. Thus, the basis for the SOC treatment are the $|\Psi_I^{SS}\rangle$ states, in which I extends to all states calculated in the first step of the procedure and $M_S = -S, \ldots, +S$ labels all members of a given term. Matrix elements of SOC over the $|\Psi_I^{SMs}\rangle$ basis functions are easily generated making use of the Wigner-Eckart theorem, since all $(2S + 1)$ term components share the same spatial part of the wavefunction.[28] In this way, the SOC and Zeeman interactions are accounted for accurately. Specifically, the Zeeman interaction can be accounted for by diagonalization of the matrix representation of $\hat{H} = \hat{H}_{\mathrm{BO}} + \hat{H}_{\mathrm{SOC}} + \hat{H}_{\mathrm{z}}$ in the $|\Psi_I^{SMs}\rangle$ basis (eq 2).

$$\begin{aligned}\left\langle \Psi_I^{SM_s} \left| \hat{H}_{BO} + \hat{H}_{SOC} + \hat{H}_Z \right| \Psi_J^{S'M'_{M_s}} \right\rangle &= \delta_{IJ}\delta_{SS'}\delta_{M_sM_s'} E_I^S + \\ &+ \left\langle \Psi_I^{SM_s} \left| \hat{H}_{SOC} + \hat{H}_Z \right| \Psi_J^{S'M'_{M_s}} \right\rangle \end{aligned} \qquad (2)$$

The complete manifold of 5 quintet and 45 triplet states were included in the calculations and SOC was accounted for by the mean field (SOMF) Hamiltonian.[29] Evaluation of the matrix elements of the orbital momentum operators between the $|\Psi_I^{SMs}\rangle$ basis functions was done in terms of one-electron matrix elements within the MO basis. This procedure carries us beyond the perturbative regime and accounts for strong SOC effects to all orders. Test calculations also included the 50 singlet states but did not change the results. Similar to the procedures followed in

Scheme 6.1. Synthetic routes to **1-6.**



the closely related CASSCF/CASPT2 methodology with inclusion of SOC,[30] matrix elements were calculated using the state averaged CASSCF wavefunctions and NEVPT2 corrections were only included in the diagonal of the QDPT matrix.

6.3. Results and Discussion

6.3.1. Syntheses and Structures. With the exception of **5**, all compounds were synthesized via simple salt elimination reactions, as shown in Scheme 6.1. The standard procedure involved slow addition of a either an ether or THF solution of a freshly prepared lithium salt of $LiN(C_6H_3$-2,6-$Pr^i_2)(SiMe_3)$, $LiC(SiMe_3)_3$, or $LiN(H)Ar^{\prime,*,\#}$ to one of freshly dehydrated $FeCl_2$ that was chilled to –78 or 0 °C. In the cases of **1**, **2**, and **4**, the color change of the reaction mixture was immediate, whereas the less bulky aryl amide (as used in the synthesis of **3**) darkened upon slow warming to room temperature.

The syntheses of **3**, **4**, and **6** presented here differ from the previously published transamination method, which treated $[Fe(N(SiMe_3)_2)_2]_2$ with 2 equiv of the respective primary amine.[16*m*] In light of the recent publication of the cobalt(II) and nickel(II) analogues of **4** and **6**, which were obtained via salt elimination in good yields,[31] compounds **3**, **4** and **6** were synthesized analogously, with yields nearly double those of the transamination results.

Complex **5** was synthesized through the reaction of $[Fe(N(SiMe_3)_2)_2]_2$ with two equivalents of the respective bulky phenol ligand. Here, an ether solution of the ligand was added slowly to an ether solution of $[Fe(N(SiMe_3)_2)_2]_2$ at –78 °C, and upon warming to room temperature, the resulting solution slowly changed from green to brown after several days of stirring. Overall, the process is similar to the transamination approach used to prepare **4** and **6** in previous studies. This route differs from the previously reported synthetic route to **5**, accomplished via O_2 insertion into the Fe–C bonds of the diaryl complex $Fe(Ar')_2$.[16*l*]

All solutions were stirred for ca. 3 days to ensure completeness of the reaction, and, upon workup, the products were obtained as crystals and characterized by single-crystal x-ray analysis. The structures of **1-6** are illustrated in Figure 6.1, and some important interatomic distances and angles are listed in Table 6.1. For compounds **1-5**, the Fe atom resides on a crystallographic

Table 6.1. Selected mean interatomic distances and angles and space groups for compounds **1**-**6**.

	1[b]	**2**	**3**[b]	**4**	**5**	**6**
Fe–L (Å)	1.853(1)	2.045(5)	1.893(1)	1.902(1)	1.947(1)	1.911(3)
L–Fe–L (°)	180[a]	180[a]	180[a]	180[a]	180[a]	140.9(2)
Fe···Fe (Å)	8.823(2)	8.925(4)	10.894(2)	11.696(1)	11.156(1)	9.297(2)
space group	*P*–1	*C*2/*c*	$P2_1/n$	$P2_1/n$	$P2_1/n$	*P*–1

[a]Denotes zero error because the Fe atom lies on a special position. [b]Full crystal tables can be found at the end of this chapter.

inversion center, resulting in strictly linear L–Fe–L moieties. Compound **6**, in contrast, exhibits a bent coordination geometry, with an N–Fe–N angle of 140.9(2)° and local C_{2v} symmetry at the Fe atom.

As observed in the crystal structures, Fe–N and Fe–O distances are in general shorter than those found for iron(II) complexes with higher coordination numbers. While this could indicate greater Fe–L covalency for the lower coordinate species, there are no ionic radii for 2-coordinate metal ions published,[32] so a strict comparison of bond distances to the sums of ionic radii is not possible. Covalent radii for Fe, N, C, and O have been reported as 1.16, 0.71, 0.75, and 0.63 Å, respectively,[33] which provide Fe–N, Fe–C, and Fe–O distances of 1.87, 1.91, and 1.79 Å, respectively. The numbers compare reasonably well with the observed distances, although the differences from the calculated values hint at the influence of steric repulsion in determining the Fe–L bond distances in this class of compounds. The Fe–N distances in **1**, **3**, **4**, and **6** (1.8532(13), 1.8937(18), 1.9017(14), and 1.911(3) Å, respectively) are comparable to those reported for $Fe[N(SiMe_2Ph)_2]_2$ (1.903(7) Å), $Fe[N(SiMePh_2)_2]_2$ (1.917(2) Å), $Fe[N(C_6H_2\text{-}2,4,6\text{-}Me_3)B(C_6H_2\text{-}2,4,6\text{-}Me_3)_2]_2$ (1.938(2) Å) and $Fe[N(t\text{-}Bu)_2]_2$ (1.879(2) Å).[16a,b,c,j] Complex **1** has an unusually short Fe–N bond, while, **2**, which possesses significant steric bulk adjacent to the metal center, displays a Fe–C distance of 2.045(5) Å — much greater than the simple difference in size between N and C atoms. In addition, it should be noted that the origin of the planar $Fe[N((C_{ipso})(Si))]_2$ array of C_{2h} symmetry in **1** may be due to a combination of packing and Fe–N π-bonding effects.

In the crystalline state, the metal atoms are well separated from one another in all of the structures, with the closest Fe···Fe separation being 8.823(4) Å, as observed in **1** (see Table 6.1). None of the structures exhibit hydrogen bonding contacts that would encourage significant long-range magnetic interactions. Interactions between the π-clouds of the aromatic ligands are other possible mediators of long-range magnetic coupling, and such interactions presumably require close contacts between the carbon atoms of co-facial aromatic moieties. Only the structures of **1**, **4**, and **6** suggest any possible π interactions of this type. While portions of the ligands of **1** and **4** have the necessary alignment for π-stacking, the rings are rather well separated with minimum C···C distances of 4.766(11) and 5.696(2) Å, respectively. In contrast, portions of the ligands of complex **6** do possess the necessary alignment together with a relatively short C···C contact of 3.203(6) Å.

Thermal ellipsoid plots from the structures of **1-5** feature significant anisotropic displacement parameters perpendicular to the L–Fe–L axis (See Fig 6.S1). Dynamic vibronic behavior could explain this observation, as a result of Renner-Teller coupling. This possibility was further explored in a complementary manuscript.[15] Another possible explanation is that **1-5** are slightly bent and disorder about the special position gives the illusion of a linear structure accompanied

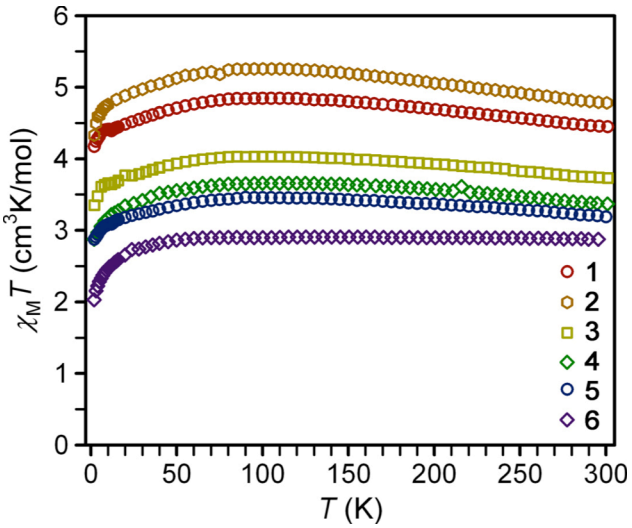


Figure 6.2. Variable temperature magnetic susceptibility data collected on restrained microcrystalline samples of **1-6** under an applied dc field of 1 kOe. The expected spin-only value of $\chi_M T$ for $S = 2$ is 3.0 cm^{3}K/mol.

by vibronic activity. Differention between these two cases would be possible by variable temperature diffraction experiments, which are beyond the scope of this chapter, thus, the references to the thermal ellipsoids are, at this point, speculative. Of note, however, is that **6**, which is not situated on a position of inversion symmetry, also shows thermal ellipsoids of the necessary orientation to suggest vibronic activity.

6.3.2. Static Magnetic Properties. Variable-temperature dc magnetic susceptibility data for compounds **1-6** indicate high-spin ($S = 2$) iron(II) centers with varying magnitudes of magnetic anisotropy (see Figure 6.2). Landé g-values were extracted from the values of $\chi_M T$ at room temperature, and provide a more quantitative measure of the magnetic anisotropy by the magnitude of their deviation from the isotropic value of $g = 2.0023$. As listed in Table 6.2, the values obtained range from 2.53 to 1.96 and follow the order: **2** > **1** > **3** > **4** > **5** > **6**. Notably, the g-values observed for linear complexes **1-5** are in general greater than the isotropic value, while **6**, which possesses a bent L–Fe–L angle, has a g-value slightly below 2.0023.

As the temperature is lowered, compounds **1-5** exhibit an increase in the $\chi_M T$ value, reaching a maximum near 100 K. After this maximum, there is a gradual decrease in $\chi_M T$ as the temperature is lowered, eventually reaching a minimum at 2 K. The extent of the increase in $\chi_M T$ at the maximum relative to the 300 K value is largest for **1** and **2**, but somewhat less pronounced in **3-5**. In contrast, complex **6** displays a relatively constant $\chi_M T$ value at higher temperatures. In the absence of magnetic anisotropy or exchange coupling, the magnetic moment of a transition metal ion will display Curie behavior, with $\chi_M T$ remaining invariant with temperature at a magnitude corresponding to the Curie constant. Alternatively, systems that possess magnetic anisotropy can be expected to display some temperature dependence for $\chi_M T$ which reflects the changing Boltzmann populations of their respective low-lying magnetic states.[34] The rise in $\chi_M T$ as the temperature decreases from 300 to 100 K thus also likely mirrors the presence of magnetic anisotropy. The low temperature maxima, however, are atypical for a $\chi_M T$ plot of a complex with spin-only magnetic anisotropy (D), where a monotonic decrease in $\chi_M T$ with decreasing T is instead the common observation.[12] Contrastingly to **1-5**, the data for complex **6** do not show such

Table 6.2. Summary of parameters obtained from dc magnetic susceptibility data for compounds **1**-**6**.

compound	g^a	$R\sigma^b$	M_{sat} (μ_B)^c
1	2.44	0.029	3.00
2	2.53	0.027	3.24
3	2.23	0.013	2.74
4	2.13	0.062	2.14
5	2.06	0.005	2.06
6^c	1.96	0.135	1.93

[a]Determined from $\chi_M T$ at 300 K. [b]Degree of non-superimposability; see Supporting Information for details regarding this parameter. [c]Saturation magnetization, as determined from magnetization data collected at 1.8 K and 7 T.

a rise, likely due to quenching of the magnetic anisotropy by the bent N–Fe–N angle. At the lowest temperatures, all plots display a monotonic decrease in $\chi_M T$. Such a decrease is perhaps also attributable to magnetic anisotropy, but could also be due to long-range antiferromagnetic interactions between molecules (possibly via π-π interactions in **1**, **4**, and **6**) and/or magnetic saturation (the Zeeman effect) at the very lowest temperatures.

Low-temperature magnetization data for **1**-**6** reveal saturation at M_{sat} = 3.00, 3.24, 2.74, 2.14, 2.06, and 1.93 μ_B, respectively (see Figures 6.S2 and 6.S3). These values are much lower than the 4 μ_B that would be expected for a spin-only $S = 2$ center. Such differences are typical for a measurement of randomly-oriented highly-anisotropic species. Previous magnetization studies[16g,m] of **2**, **4**, and **6** afforded higher values of M_{sat} (5.82, 4.79, and 3.40 μ_B, respectively) than observed here. Differing sample restraints, as well as the observation of O_2 contamination in the previous measurements, may be influencing the absolute magnitudes of these values, but the general trend observed, as well as the shapes of the $\chi_M T$ plots for **2** and **4**, are at least consistent with the results reported here.

The field and temperature dependence of low-temperature magnetization data can be fit to quantify the axial (D) and transverse (E) magnetic anisotropies of a compound. To probe these values, variable-temperature magnetization data were collected for **1**-**6** at applied dc fields of 1, 2, 3, 4, 5, 6, and 7 T (see Figures 6.S2 and 6.S3). In general, isotropic systems will produce a set of variable-temperature magnetization data at one field (termed an isofield line) that will be superimposable with the Brillouin function[12] for a given S and g. Further, isofield lines collected at different fields for an isotropic system will all be superimposable upon the same Brillouin function when plotted versus H/T. In contrast, anisotropic moments can produce isofield lines that are non-superimposable with a single Brillouin-like curve. Complexes **1**-**4** and **6** all produce non-superimposable isofield lines consistent with the latter case, confirming dominant magnetic anisotropy. Complex **5**, in contrast, produces isofield lines that are superimposable to a single line, although not to the Brillouin curve (see Appendix 4). The degree to which the magnetization were superimposable to a Brillouin like curve was quantified by the index R_σ, which represents an error with respect to the derived curve (further details are again provided in Appendix 4). Complexes **1**-**4** and **6** display R_σ values greater than 0.13, signaling non-superimposability, while **5** has a smaller R_σ of 0.005, indicating a high degree of superimposability of the isofield lines. This parameter does not follow any apparent trend across the series of complexes. Complex **5**, which is a linear molecule and should be expected to be highly anisotropic, produces isofield lines that seem to suggest isotropic behavior. In contrast, **6**,

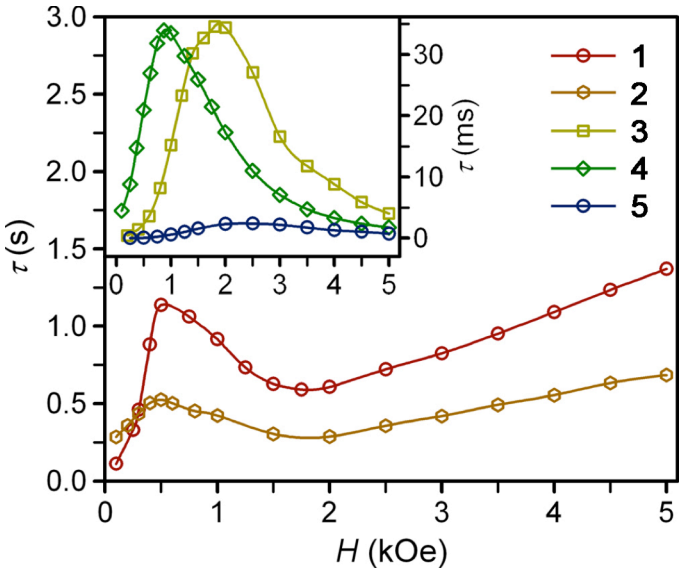


Figure 6.3. Field dependence of the magnetic relaxation time, τ, at 2 K for restrained microcrystalline samples of **1**-**5**.

which is bent and expected to be approximately isotropic, instead shows a large R_σ, suggesting the presence of significant magnetic anisotropy.

In an attempt to quantify the magnetic anisotropy of complexes **1**-**6**, ANISOFIT 2.0[35] was used to try and fit the magnetization data employing a Hamiltonian incorporating the axial (D) and transverse anisotropy (E) of an $S = 2$ center:

$$\hat{H} = D\hat{S}_z^2 + E(\hat{S}_x^2 - \hat{S}_y^2) + g_{iso}\mu_B \boldsymbol{S}\cdot\boldsymbol{H} \qquad (3)$$

No acceptable fits were possible with this model for the entire series of compounds. Here, an untenable assumption of the model Hamiltonian is probably the cause. A description of the system with D and E assumes that the ground magnetic states are characterized as spin-only and that any anisotropy is due to the interaction between the ground spin-only state and unpopulated excited states. For a rigorously linear L–Fe–L angle, however, the ground state is expected to display a significant unquenched orbital component to its magnetization. Upon bending, this orbital component is expected to be quenched, making it somewhat surprising that the data obtained for **6** could not be fit using equation 3. The second assumption made by the model Hamiltonian is that g is isotropic. Linear iron(II) complexes have been shown both experimentally and theoretically to possess highly anisotropic g-tensors as result of their orbital moments.[16m,36]

Taken together, the results from the $\chi_M T$ and magnetization data indicate that the two-coordinate iron(II) complexes **1**-**6** all have highly anisotropic magnetic moments. The inability to fit the magnetization data, as well as the shapes of the $\chi_M T$ plots, further suggest that the magnetic anisotropies of these compounds cannot be attributed to spin-only phenomena.

6.3.3. Dynamic Magnetic Properties. Ac magnetic susceptibility measurements were performed for complexes **1**-**6** to probe the low-temperature magnetic relaxation behavior of the highly anisotropic magnetic moments. Within the frequency range 0.1–1500 Hz, all of the compounds were found to display fast magnetic relaxation under zero applied dc field. This is likely attributable to ground state magnetic tunneling, as usually observed for mononuclear iron(II) systems.[8a-d] We note, however, that slow magnetic relaxation has been previously

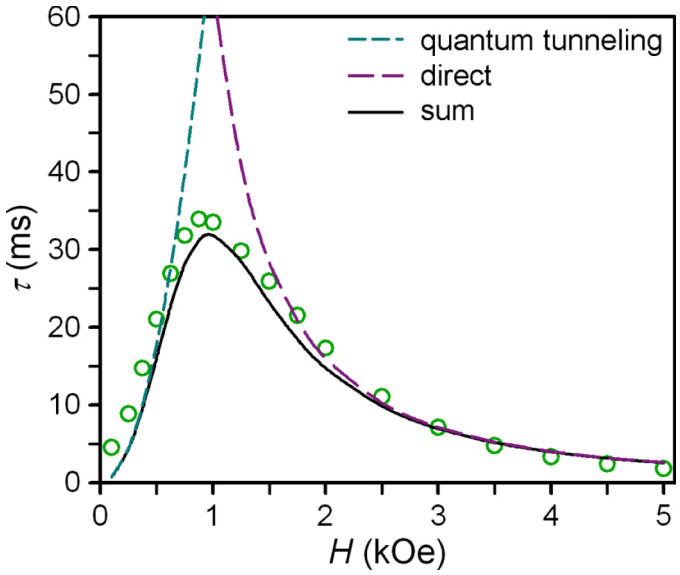


Figure 6.4. Field dependence of the magnetic relaxation time, τ, at 2 K for a restrained microcrystalline sample of **4**. The dashed cyan and purple lines correspond to the contributions to the relaxation time from the zero-field tunneling and direct relaxation processes, as discussed in the text. The solid black line corresponds to the weighted sum of the two processes.

observed for compound **2** under zero applied dc field using Mössbauer spectroscopy,[16g] which probes relaxation on a much faster time scale. For all complexes, application of a small dc field slows the magnetic relaxation sufficiently to afford a nonzero signal in the out-of-phase ac susceptibility (χ_M'') (see Figures 6.3, 6.4, and 6.S4-6.S6). For complexes **1**-**5**, well-resolved peaks appear in the plots of χ_M'' versus ac field switching frequency, with maxima that shift in frequency with applied dc field strength. In contrast, only tails of peaks at high frequency are apparent for **6** under an applied dc field, and the magnetic relaxation never slowed enough for the peak maxima to fall within the frequency range of our magnetometer. Fits of the frequency dependence of the in-phase (χ_M') and out-of-phase (χ_M'') ac susceptibility to a generalized Debye model[37] were performed to determine the dc field dependence of the magnetic relaxation time (τ) for the complexes (see Figures 6.3, 6.4, and 6.S4-6.S6). For each compound, τ increases from H = 0 Oe to a maximum value at some field strength denoted $H_{\tau,max}$ (see Table 6.3). At dc fields greater than this value, the relaxation time begins to decrease again. For **1** and **2**, τ begins to increase again when H_{dc} is roughly 1 kOe greater than $H_{\tau,max}$. The τ values observed for complexes **3**, **4**, and **5**, however, continue to decrease at these higher dc field strengths.

At zero applied dc field, fast spin-reversal between the $\pm M_S$ levels occurs via resonant quantum-mechanical tunneling processes, which can be mediated by transverse anisotropy (E), dipolar interactions, or nuclear hyperfine coupling, any of which can serve to mix the ground $\pm M_S$ levels.[38] Upon application of a dc magnetic field, however, the degeneracy of the ground $\pm M_S$ levels is split, reducing the degree of mixing and mitigating the quantum tunnelling process. Slow magnetic relaxation is therefore induced, as the moments now have to traverse a thermal activation barrier in order to reverse direction. At higher fields, however, magnetic relaxation can become fast again by the emergence of a separate spin-reversal pathway, the direct relaxation process,[39] which can occur between the non-degenerate $\pm M_S$ levels, provided the corresponding energy of the transition can be released as a phonon. Quantum tunnelling and direct moment

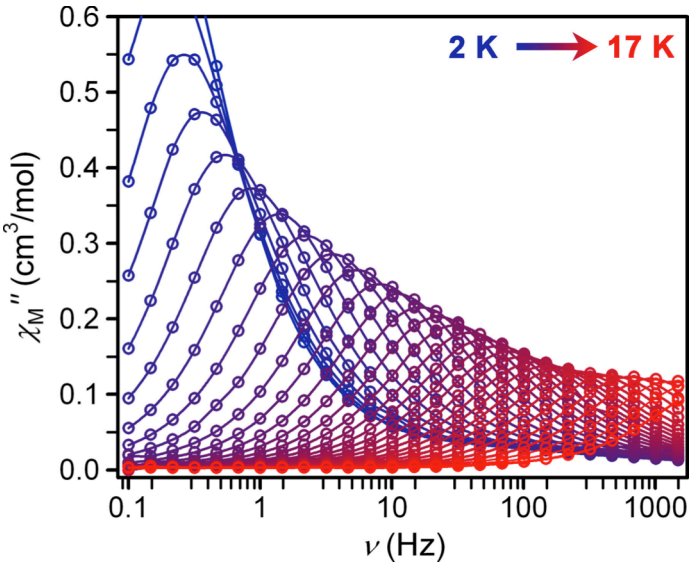


Figure 6.5. Frequency dependence of χ_M'' for **1** as a function of temperature under a 500 Oe dc field from 2 to 17 K in 0.5 K intervals.

reversal processes, which allow the spin to flip without traversing the energy barrier, display different dependences upon the strength of the applied dc field. Equation 4 was employed to model the field dependence of τ for **1**-**5**, in a manner analogous to that previously utilized for a polynuclear single-molecule magnet.[40] In this expression, the first term represents the direct process, while the second corresponds to the zero-field tunnelling process. The competition between these two spin reversal pathways gives rise to the maxima displayed in Figures 6.3 and 6.4.

The maxima in Figure 6.3 suggest two field-dependent regimes for the slow magnetic relaxation: lower dc field, where resonant quantum tunnelling is suppressed and therefore moment reversal becomes slow, and higher dc field, where direct relaxation becomes dominant and spin reversal again becomes rapid (see Figures 6.4 and 6.S6). Approximate fits to the data for compounds **3**-**5** can be obtained using equation 4, yielding values for A, B_1, and B_2, as enumerated in Table 6.3.

$$\tau^{-1} = AH^2T + \frac{B_1}{1 + B_2H^2} \qquad (4)$$

In contrast, the τ versus H plots for **1** and **2** are complicated by the rise in τ with H values greater than 2 kOe, which cannot be modelled using equation 4. The origin of this behavior at higher fields remains unknown. In many mononuclear single-molecule magnet species, the relaxation barrier corresponds to the first excitation up the M_S or M_J spectrum. After this initial excitation, tunnelling occurs through the barrier, such that the magnetization dynamics of mononuclear complexes do not elucidate the full height of the barrier. It is possible that at higher fields, this tunnelling via the excited states could be shut down for **1** and **2**, leading to an increase in τ. It is unknown, however, why this same effect would not occur for **3**-**5**. At a basic level, the fluctuation of $H_{\tau,max}$, B_1, and B_2 across the series represents the increasing degree of mixing of

Table 6.3. Summary ac magnetic data collected for compounds **1**-**5**.

	1	**2**	**3**	**4**	**5**
$H_{\tau,max}$ (Oe)	500	500	1800	875	2500
τ (s) at 2 K[a]	1.14	0.52	0.035	0.034	0.002
AH^2 ($s^{-1}K^{-1}$)[b,c]	0.12	0.265	9.04	6.00	122.5
B_1 (s^{-1})[b]	40.02	3.35	8.92×10^{12}	220	4.89×10^{12}
B_2 (T^{-2})[b]	22933	570	1.72×10^{13}	1560	3.94×10^{11}
C ($s^{-1}K^{-5}$)[d]	0.003	0.005	0.011	0.473	0.152
τ_0 (s)[d]	1×10^{-11}	4×10^{-9}	5×10^{-9}	4×10^{-8}[e]	3×10^{-7}
U_{eff} (cm^{-1})	181	146	109	104	43

[a]Obtained at $H_{dc} = H_{\tau,max}$. [b]Determined from fitting the H-dependence of τ for **1**-**5**. [c]Calculated with $H = H_{\tau,max}$, where $H_{\tau,max}$ is in units of Teslas. [d]Parameters for Raman exponent $n = 5$. [e]Parameters for Raman exponent $n = 4$; C is in units of $s^{-1}K^{-4}$.

the ground $\pm M_S$ levels from **1** to **5**, which in turn leads to an increasing degree of significance for the zero-field quantum tunnelling process.

The temperature dependence of the relaxation time provides an invaluable experimental probe of the processes responsible for spin reversal in a magnetic system. The magnetic relaxation times for **1**-**6** were therefore evaluated by measuring the frequency dependences of χ_M' and χ_M'' over a range of temperatures (see Figures 6.5, 6.S7, and 6.S8). These data were then used to construct the Arrhenius plots in Figure 6.6. For **1**-**5**, the magnetic relaxation times are approximately temperature-independent at very low temperatures and then become increasingly temperature dependent above 5 K. An absence of temperature dependence for τ suggests that the spin reversal occurs due to a quantum tunneling process that does not require the input or release of energy to proceed. Temperature dependence of τ, however, signifies that the spin reversal process requires the exchange of energy with lattice vibrations. In particular, an exponential temperature-dependence indicates that absorption of phonons is promoting the moments of the complexes from the ground state to the height of the energy barrier. This "over-barrier" spin reversal pathway (Orbach relaxation[41]) will produce a linear plot of $\ln(\tau)$ versus $1/T$, where the slope corresponds to the effective spin reversal barrier, U_{eff}, and the y-intercept yields the inverse of the attempt relaxation time, τ_0^{-1}. In contrast, when τ is proportional to T or T^n, "through-barrier" direct ($n = 1$) and Raman ($n \geq 4$) spin reversal processes[39,41] are presumed operative. Unlike an Orbach relaxation process, these latter two processes produce curvature in an Arrhenius plot. Thus, in Figure 6.6 we see evidence of significant direct and Raman spin-reversal processes. To quantitatively compare the respective influences of the above three relaxation processes, the temperature-dependent relaxation time profiles of **1**-**5** were fit as a sum of the contributions of the quantum tunneling, direct, Orbach, and Raman relaxation mechanisms. The expression used to model the data in Figure 6.6, for example, is given as equation 5.

$$\tau^{-1} = AH^2T + \frac{B_1}{1 + B_2H^2} + CT^n + \tau_0^{-1}\exp\left(-U_{eff}/kT\right) \qquad (5)$$

In view of the many unknowns in equation 5, we sought to avoid possibly meaningless fits as result of overparameterization. The field-dependent τ data for **1**-**5**, which were successfully

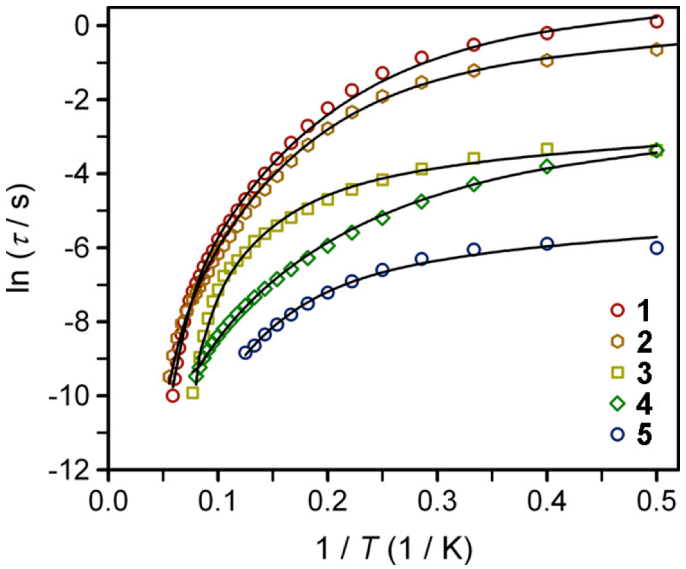


Figure 6.6. Arrhenius plots of the temperature dependences of τ for compounds **1**-**5**. Black lines represent fits to multiple relaxation processes, as discussed in the text.

modeled using equation 4, were relatively insensitive to the inclusion of the Orbach and Raman terms in equation 5. In contrast, inclusion of the Orbach and Raman processes in modeling the temperature dependence of τ proved essential for describing the relaxation behavior at the lowest temperatures. Thus, the values of A, B_1, and B_2 were taken from fits to the data presented in Figure 6.3, and were then used in modeling the Arrhenius plots. Values of C, τ_0 and U_{eff} were then obtained from the best fit of the Arrhenius plots (see Table 6.3). In the course of fitting attempts, we noticed that the Raman exponent, n, best fit **1**, **2**, **3**, and **5** with the value of 5, as expected for integer-spin systems with low-lying excited states,[41c] while $n = 4$ afforded a much better fit for compound **4**. In line with the decreasing relaxation times at 2 K from **1** to **5**, the value of U_{eff} decreases across the series. The contributions of the direct and Raman processes also increase from **1** to **5**, as evidenced by increasing magnitudes of A and C. The physical significance of the coefficients A and C is not easily intuited, as both values depend on variables such as the crystal density, the speed of sound in the solid, and the strength of the interaction of the spin system with the phonons.[41a,b] At a most basic level, the increase in A and C across **1** to **5** is a reflection of an increasing prevalence of a through-barrier spin-reversal mechanism under the applied fields, and is also manifest in the drop in τ at 2 K from **1** to **5**. Significantly, the U_{eff} values of as high as 181 cm^{-1} obtained for **1**-**4** are the largest yet observed for mononuclear iron(II) complexes, with the previous record corresponding to 100 cm^{-1} for $[(C_5Me_5)Fe(2,6\text{-}Pr^i_2\text{-}C_6H_3)]$.[8c] We further note that the values of τ_0 obtained are in the typical range observed for single-molecule magnets.

6.3.4. Ligand Field Description of $D_{\infty h}$ Iron(II) Complexes. In the absence of intermolecular interactions, slow magnetic relaxation in mononuclear complexes is governed by the lowest energy magnetic states that stem from their respective electronic configurations. To better understand the magnetic relaxation in these complexes, we therefore explored the electronic structures **1**-**6** by computational methods. Under a local $D_{\infty h}$ ligand field, the d orbital energies split into δ_g (d_{xy}, d_{x2-y2}), π_g (d_{xz}, d_{yz}), and σ_g^+ (d_{z2}) sets. The characters of these sets with respect to the ligand orbitals are non-bonding, π-antibonding, and σ-antibonding, respectively. Hence, they are listed in order of increasing energy if the ligand is capable of π- and σ-donation.

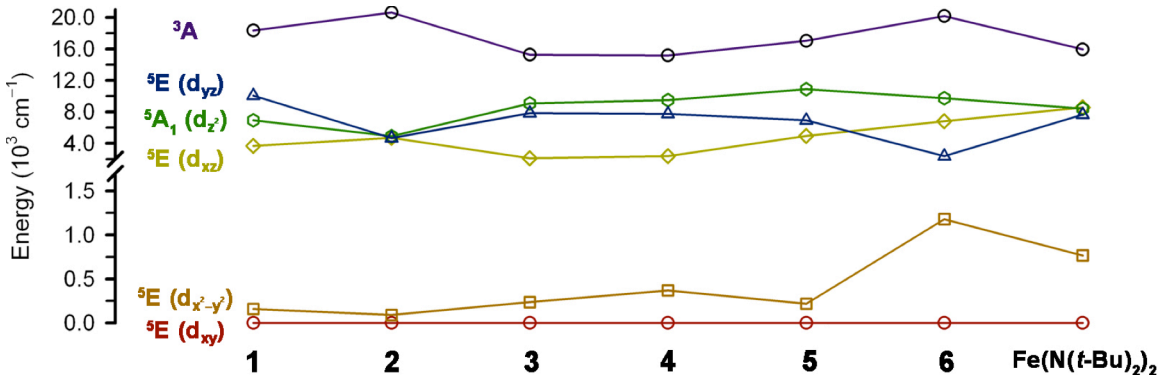


Figure 6.7. Calculated quintet energy states of **1**-**6** and Fe(N(*t*-Bu)$_2$)$_2$ with structures taken from X-ray diffraction data. The symmetry labels correspond to D_3 point group notation. As discussed in the text, the energies of the depicted quintet states can be mapped to d-orbital energies. The orbitals corresponding to each quintet state are labeled in parentheses.

The ordering of the π_g and σ_g^+ energies can invert if there is prominent s-d mixing for the metal orbitals. In either case, the pair of δ_g orbitals remains lowest in energy and non-bonding. A high-spin d^6 ion in this coordination environment is therefore expected to have a large magnetic anisotropy as result of the triply occupied δ_g set and the resulting first-order contribution to the orbital angular momentum.

For a d^6 ion in $D_{\infty h}$ geometry, the $(\delta_g)^3(\pi_g)^2(\sigma_g^+)^1$ electronic configuration yields a ground $^5\Delta$ state characterized by an unquenched orbital angular momentum with $M_L = 2$. One-electron excitations from the δ_g to the π_g and σ_g^+ orbitals, respectively, generate the electronic configurations responsible for the $^5\Pi$ and $^5\Sigma^+$ excited states. The $^5\Pi$ state possesses orbital angular momentum ($M_L = 1$), while the $^5\Sigma^+$ state does not. Spin-orbit coupling serves to split the $^5\Delta$ ground state into spin-orbit coupled M_J sublevels with energies dictated by the strength of the spin-orbit coupling constant of the iron(II) center ($\zeta \approx 400$ cm^{-1} for the free Fe^{2+} ion).[10-12] This splitting of the M_J energies is similar to the divergence of the energies of M_S sublevels under the action of a negative D, whereby the $\pm M_J$ sublevels with maximal projection along the z-axis constitute a bistable ground state. In this case the magnitude of the spin reversal barrier, U, is governed by ζ, and the calculated value is $U = 2\zeta$. Given the fact that ζ is much greater than even the largest reported D values,[42,43,44] a simple ligand field description of compounds **1**-**5** predicts that they should have very large spin reversal barriers on the order of 800 cm^{-1}.

The foregoing description of the electronic structure has been successfully applied to the interpretation of the UV-vis absorption spectra of metal dihalide complexes in the gas phase,[45] where the MX_2 geometries are purported to be linear on the basis of a variety of spectroscopic evidence.[46] Here, the lone pairs of the chloride ions are related by symmetry and interact indistinguishably with the d orbitals of the metal ion, providing ideal $D_{\infty h}$ symmetry. We took this model as a starting point for assessing the ligand fields of the linear iron(II) complexes and, ultimately, for understanding the origins of the slow magnetic relaxation.

6.3.5. Ligand Field Description of Linear Iron(II) Complexes with Lower-Symmetry Ligand Fields. For the linear complexes investigated here, we hypothesized that the varying orientations of the lone pairs of the ligand donor atoms could disrupt the rigorous axial symmetry of the L–Fe–L moiety, leading to an asymmetry in the x and y directions (the z direction here is defined as the L–Fe–L axis). This lower-symmetry ligand field could relax the symmetry-

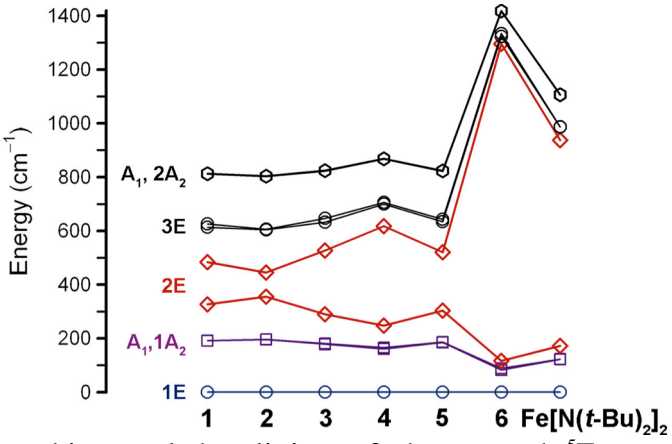


Figure 6.8. Spin-orbit coupled splitting of the ground ^{5}E state, calculated for complexes **1**-**6** and Fe[N(*t*-Bu)$_2$]$_2$. Symmetry labels are according to D_3 notations. Energies are given as numerical values in the following paper.[15]

required nonbonding character of the δ_g (d_{xy}, d_{x2-y2}) orbitals by allowing mixing between the (d_{xy}, d_{x2-y2}) orbitals and the d_{xz}, d_{yz}, and d_{z2} orbitals. The d_{xy} and d_{x2-y2} orbitals resulting from this interaction could have enough d_{xz}, d_{yz}, or d_{z2} character such that their respective interactions with the asymmetric ligand field would split the (d_{xy}, d_{x2-y2}) orbital degeneracy and quench the associated orbital angular momentum.

First-principles computational techniques were utilized to study the effect of the xy-asymmetry on the low-energy electronic structures of complexes **1**-**5**. Calculations were also performed on **6** to study the effect of the bent L–Fe–L angle, and on another known linear two-coordinate Fe(II) complex, Fe(N(*t*-Bu)$_2$)$_2$,[16j] for comparison. Monoconfigurational DFT methods were avoided owing to the orbital degeneracy of the ^{5}D ground state of the linear, 3d^6 Fe^{II} center. Instead, CASSCF and NEVPT2 methods were employed with the ORCA electronic structure package.[26]

The 3d^6 configurations of the Fe^{II} centers in complexes **1**-**6** and Fe(N(*t*-Bu)$_2$)$_2$ each give rise to 5 quintet states with NEVPT energies, computed using the crystal structure geometries, as depicted in Figure 6.7. Further details on these calculations can be found in the subsequent paper.[15] For the present system, the five lowest energy states are mapped onto d-orbital energies, provided one takes the ground d_{xy} orbital as an energy reference point. Thus, the energies given in Figure 6.7 represent not only the splitting of the multi-electron states in the lower-symmetry ligand field, but also that of the d orbitals. In the following discussion, we refer to the state labels primarily, but also list the orbital labels, as done in Figure 6.7.

The ground states of all complexes are S = 2 quintet (hereafter given in D_3 symmetry notation, as would apply to complex **2**) states with energies that are 15200-20600 cm^{-1} lower than the first ^{3}A excited states. Fe–L σ- and π-interactions, resulting from the non-rigorous $D_{\infty h}$ symmetry, split the degeneracy of the ^{5}E(d_{xy}) and ^{5}E(d_{x2-y2}) states. The splitting is just 90 cm^{-1} for **2**, and increases to 235 cm^{-1} for **3** and 369 cm^{-1} for **4**, and becomes as large as 1188 cm^{-1} for the bent complex **6**. The splittings of 158 and 218 cm^{-1} for complexes **1** and **5**, respectively, are intermediate between those of **2** and **3**, such that a monotonic increase across the series is not observed. Interestingly, the splitting of 766 cm^{-1} for the ^{5}E(d_{xy}) and ^{5}E(d_{x2-y2}) states in Fe(N(*t*-Bu)$_2$)$_2$ is large compared to that of the other linear compounds, and second only to the bent complex **6**. Also of note is that the ^{5}A(d_{z2}) state is in the same energy range as the ^{5}E(d_{xz}) and

$^5E(d_{yz})$ states.

As depicted in Figure 6.8, spin-orbit coupling splits the $^5E(d_{xy})$ ground state into five pairs of spin-orbit coupled magnetic sublevels, corresponding to different linear combinations of the spin and orbital angular momenta. The asymmetric ligand field in turn splits these pairs. However, for all complexes included in this study, such splitting of the spin-orbit coupled states by asymmetric π-interactions is negligible, except for the 2E state ($M_S = 0$, $M_L = 2$), shown in red in Figure 6.8, which is highly sensitive to the low symmetry of the ligand field. Complexes **1** and **2** display the smallest splitting of the 2E state, and this splitting increases across the series, becoming very large for **6** and $Fe(N(t\text{-}Bu)_2)_2$. Additionally, in moving across the series, the energy separation between the ground 1E sublevels (blue in Figure 6.8) and the first excited $\{1A_1, 1A_2\}$ sublevels (purple in Figure 6.8) decreases from 191 cm^{-1} for **1** to 122 cm^{-1} for **6.**

The *ab initio* results are readily interpreted starting from the $D_{\infty h}$ electronic structure and considering the xy-asymmetry and the spin-orbit coupling as perturbations on the ligand field states. In contrast to ideal $D_{\infty h}$ symmetry, we see in Figure 6.7 that the non-rigorous axial symmetry imposed by the lone pairs of the ligand donor atoms of **1**-**5** and $Fe(N(t\text{-}Bu)_2)_2$ relaxes the non-bonding character of the δ_g (d_{xy}, d_{x2-y2}) orbitals, causing them to split in energy. This is expected to quench the orbital angular momentum of the compounds. This would in turn minimize the magnetic anisotropy, promoting faster magnetic relaxation times. A dramatic example of this effect occurs in **6**, where the bent L–Fe–L angle strongly splits the δ_g orbitals, and as result **6** displays the fastest magnetic relaxation times of the series at low temperature. We emphasize again that the $^5A(d_{z2})$ state ($^5\Sigma^+$ in $D_{\infty h}$ notation) is comparable in energy to the $^5E(d_{xz})$ and $^5E(d_{yz})$ states ($^5\Pi$ in $D_{\infty h}$ notation). This is a direct manifestation of s-d mixing which serves to weaken the antibonding character of the Fe^{II} $3d_{z2}$ orbital. This could, in part, contribute to the relatively short Fe–N bond distances observed in the crystal structures of **1**-**5** compared with higher-coordination number complexes, where in the latter case electrons occupy strongly antibonding orbitals. Note also that such a shortening of the Fe–L bond distances is expected on account of the decrease in iron(II) ionic radius as a function of coordination number.[32]

In comparison with the spin-orbit coupling, the influence of the ligand field asymmetry is relatively weak. Here, by virtue of a suitably weak ligand field, the electronic structures of these 3d transition metal complexes are similar to those observed for many lanthanide and 5d transition metal complexes, where the spin-orbit coupling is comparable with or stronger than the influence of the ligand field.

6.3.6. Correlation of *Ab Initio* Results with Relaxation Dynamics. The magnetic properties of mononuclear transition metal complexes are by and large dictated by the relative energy spacings of the lowest lying magnetic sublevels in addition to the angular momenta associated with each of these sublevels. As the surrounding ligand field strongly influences the energies and spins of the sublevels of a transition metal complex, it is expected that the ligands, through their electron donating/withdrawing abilities and/or their spatial arrangement, are predominantly responsible for the magnetic properties of the complex. In both the experimental[8a,b] and theoretical[24a,b] studies of the magnetic properties of the $[(tpa^R)Fe]^-$ series of complexes, the magnetic anisotropies and spin reversal barriers were found to correlate to the lewis basicity of the tpa^R ligand. This same observation is not present here, where the magnetic behaviors do not appear to follow a trend based on the ligand-field strength of the donor atoms. For example, **3** and **4**, which should have nearly identical ligand field strengths, exhibit different relaxation behaviors, and the *ab initio* results indicate a significant difference in the relative energy spacings of their low lying magnetic sublevels. Additionally, **3** and **5**, which are the same

except for their respective NH and O donor moieties, possess similar splitting in Fig. 6.8, yet their respective relaxation behaviors are very different. Rigorous axial symmetry about the iron could be envisioned to enhance the slow magnetic relaxation, but **2**, which has relatively high D_{3d} molecular symmetry, is not a better single-molecule magnet than **1**, which is of lower C_I symmetry. Furthermore, the computational results indicate that there is not a large energetic difference in the spin-orbit coupled sublevels between **1** and **2**, which seems to downplay the importance of symmetry in dictating the magnetic relaxation properties for these compounds, if only the spacings of the sublevels present in Figure 6.8 are directing the low temperature magnetization dynamics. We note, however, that **2** shows slow magnetic relaxation at zero field in the Mössbauer spectrum, while **4**, **6**, and $Fe(N(t\text{-}Bu)_2)_2$ only do so under modest applied dc fields, suggesting that symmetry may have greater influence on the magnetization dynamics at zero applied dc field.

The spin reversal barriers of mononuclear systems often appear to correlate to the energy requirement for excitation to the first excited M_S or M_J sublevel.[6a,g,j,8b,47] In the present series of complexes, therefore, the *ab initio* results predict U_{eff} values corresponding to the excitation from the 1E ground state to the $\{A_1, {}^1A_2\}$ set of states depicted in Figure 6.8. Complex **1** does not deviate far from the predicted behavior, and possesses a U_{eff} (181 cm^{-1}) in reasonable agreement with the energy separation between its ground and first-excited spin-orbit coupled state (191 cm^{-1}). Across the series, this separation appears to decrease, thus, if dominant Orbach spin reversal invoking the first excited spin-orbit coupled state were observed for all compounds, one would expect the observed U_{eff} values to follow the trend **1** > **2** > **5** > **3** > **4** > **6**. While U_{eff} indeed decreases across the series in qualitative agreement with the *ab initio* results, it does so at a quicker pace than the gap between the 1E and $\{A_1, {}^1A_2\}$ states. Thus, factors other than simply the 1E to $\{A_1, {}^1A_2\}$ energy gap are influencing the barrier magnitude involved in the Orbach process.

One such factor could be the dynamic vibrational activity of the iron(II) coordination sphere in the crystalline state. A bent L–Fe–L angle strongly influences the energies of the magnetic sublevels as demonstrated in the *ab initio* results, where a bent L–Fe–L angle yields the largest splitting of the d_{xy} and d_{x2-y2} orbitals and hence the strongest quenching of the orbital angular momentum. If dynamic activity were occurring, its subtle effects could easily be overlooked, given that the L–Fe–L angles are linear as depicted in the crystal structures. A preliminary inspection of the thermal ellipsoids of **1**-**5** suggests that dynamic movement in the crystalline state may be present. As shown in Figure 6.S1, all structures feature thermal ellipsoids for the Fe atom with significant anisotropic displacement oriented away from the L–Fe–L axis, suggestive of dynamic bending vibrations. As evidenced by complex **6**, which in this context represents a snapshot of a complex with a high degree of distortion, a bent L–Fe–L angle is accompanied by fast magnetic relaxation.

Given the U_{eff} predictions from the *ab initio* computations (191, 196, 178, 161, 185, and 82 cm^{-1} for **1**-**6** respectively) one may expect Arrhenius plots of **1**-**5** to be indicative of dominant Orbach relaxation and very large spin reversal barriers. Hypothetically, such behavior would be expected at zero applied dc field, in the absence of the zero-field tunneling process and possible vibronic influences. An applied dc field, however, is required to observe slow magnetic relaxation for all complexes, and, as evidenced by our analysis, while the applied field disrupts the tunnelling process, it also enhances the direct process. Thus, all compounds produce highly curved Arrhenius plots from the influence of spin reversal relaxation pathways other than the Orbach process. Over most of the temperatures of the measurements (< 20 K, kT = 13.9 cm^{-1}),

phonons of the necessary energy for excitation to the first excited M_J sublevels are likely very scarce. Thus, spin reversal by thermally activated relaxation mechanisms (Orbach) can be expected to be less favorable than the field-induced direct relaxation processes, as well as multi-phonon relaxation processes (Raman), neither of which require relatively high-energy phonons for spin-reversal. The foregoing argument implies that there may be a limit to the energy separation between the ground and first excited M_J levels if one is to observe Orbach relaxation behavior under applied dc fields. If the separation is above this limit, faster relaxation mechanisms take over since the first excitation requires much more energy than is available from phonons. This is a key observation, because many efforts to produce mononuclear transition metal single-molecule magnets with larger barriers have been guided by the belief that increasing the energy of the first excitation would necessarily result in larger magnetic relaxation barriers.

The direct and Raman relaxation processes, which may be interfering with the observation of the Orbach process under an applied field, are highly dependent upon the interactions between the spins and the vibrational structure of the lattice. Such interactions are mediated by the coupling between the orbital moment of the iron(II) center and the phonons, as evidenced by the calculations and magnetic data. Our results also indicate that the coupling of the orbital moment to the iron(II) spin is strong. By invoking a transitive relationship, this means that the moments of the studied molecules are strongly coupled to the phonon system. Thus, the influence of the spin-orbit coupling on the slow magnetic relaxation under an applied dc field is bilateral. On one hand, the spin-orbit coupling overrides the deleterious quenching effects of the ligand field, resulting in sustained magnetic anisotropy, despite the deviation of the ligand field from rigorous $D_{\infty h}$ symmetry. Adversely, the spin-orbit coupling bolsters the coupling of the spins to the lattice phonons and promotes other faster magnetic relaxation processes. Ultimately, this means that the same effect responsible for generating the large magnetic anisotropy is also facilitating fast magnetic relaxation under an applied field.

6.4 Outlook and Conclusions

Taken together, the foregoing results demonstrate how two-coordinate iron(II) complexes can provide a fruitful platform for the study of slow magnetic relaxation in highly anisotropic systems. Direct- and alternating-current magnetic susceptibility measurements confirmed the existence of substantial magnetic anisotropy, with the latter indicating very slow relaxation times for **1-5** at low temperature. Importantly, the field and temperature dependences of the magnetic relaxation times were modelled to yield U_{eff} values ranging from 181 cm^{-1} for **1** to 43 cm^{-1} for **5**. Partial quenching of the magnetic anisotropy across the series of compounds can be attributed to non-axial symmetry of the L–Fe–L moieties, though this quenching is mostly cancelled due to the relative strength of the orbital angular momentum compared to the ligand field. The inability to observe a strong temperature dependence for the relaxation time, indicative of dominant Orbach relaxation, across the series has been attributed to either far more efficient direct and Raman relaxation processes, or the influence of vibronic coupling. This ambiguity highlights the need for more detailed studies into the relaxation processes of mononuclear systems and the various factors that influence them. A study of this nature is presented as a complement to this work.[15]

6.5. Acknowledgements

This research was funded by the National Science Foundation through grant CHE-1111900 and CHE-0948417. I thank Tyco Electronics for fellowship support during this study. I thank Aimee M. Bryan, Chun-Yi Lin, Dr. Brian Rekken, and Prof. Philip P. Power for preparing compounds **1** and **4**-**6** for this study as well as helpful suggestions for repeating the synthesis of **2**. I also am grateful to Dr. Mihail Atanasov and Professor Frank Neese for lending their computational expertise to the analyses of the ligand fields of these compounds. I thank Drs. Anne M. Lapointe and Meg E. Fasulo as well as Erik Hosler for fruitful discussions. I am grateful to Professor J. R. Long for assistance and support throughout the study.

6.6. References, Notes, and Supplementary Information

(1) (*a*) Sessoli, R.; Hui, L.; Schake, A. R.; Wang, S.; Vincent, J. B.; Folting, K.; Gatteschi, D.; Christou, G.; Hendrickson, D. N. *J. Am. Chem. Soc.* **1993**, *115*, 1804. (*b*) Sessoli, R.; Gatteschi, D.; Caneschi, A.; Novak, M. A. *Nature* **1993**, *365*, 141. (*c*) Gatteschi, D.; Sessoli, R.; Villain, J. *Molecular Nanomagnets*; Oxford University Press: Oxford, 2006.

(2) Mannini, M.; Pineider, F.; Sainctavit, P.; Danieli, C.; Otero, E.; Sciancalepore, C.; Talarico, A. M.; Arrio, M.-A.; Cornia, A.; Gatteschi, D.; Sessoli, R. *Nat. Mater.* **2009**, *8*, 194.

(3) (*a*) Leuenberger, M. N.; Loss, D. *Nature* **2001**, *410*, 789. (*b*) Ardavan, A.; Rival, O.; Morton, J. J. L.; Blundell, S. J.; Tyryshkin, A. M.; Timco, G. A.; Winpenny, R. E. P. *Phys. Rev. Lett.* **2007**, *98*, 057201. (*c*) Stamp, P. C. E.; Gaita-Ariño, A. *J. Mater. Chem.* **2009**, *19*, 1718.

(4) Torres, F.; Hernández, J. M.; Bohigas, X.; Tejada, J. *J. Appl. Phys. Lett.* **2000**, *77*, 3248.

(5) (*a*) Tang, J.; Hewitt, I.; Madhu, N. T.; Chastanet, G.; Wernsdorfer, W.; Anson, C. E.; Benelli, C.; Sessoli, R.; Powell, A. K. *Angew. Chem. Int. Ed.* **2006**, *45*, 1729 (*b*) Accorsi, S.; Barra, A. L.; Caneschi, A.; Chastanet, G.; Cornia, A.; Fabretti, A. C.; Gatteschi, D.; Mortalò, C.; Olivieri, E.; Parenti, F.; Rosa, P.; Sessoli, R.; Sorace, L.; Wernsdorfer, W. and Zobbi, L. *J. Am. Chem. Soc.* **2006**, *128*, 4742. (*c*) Wang, C.-F.; Zuo, J.-L.; Bartlett, B. M.; Song, Y.; Long, J. R.; You, X.-Z. *J. Am. Chem. Soc.* **2006**, *128*, 7162. (*d*) Martínez-Lillo, J.; Armentano, D.; De Munno, G.; Wernsdorfer, W.; Julve, M.; Lloret, F.; Faus, J. *J. Am. Chem. Soc.* **2006**, *128*, 14218. (*e*) Yang, C.-I.; Wernsdorfer, W.; Lee, G.-H.; Tsai, H.-L. *J. Am. Chem. Soc.* **2007**, *129*, 456. (*f*) Milios, C. J.; Vinslava, A.; Wood, P. A.; Parsons, S.; Wernsdorfer, W.; Christou, G.; Perlepes, S. P.; Brechin, E. K. *J. Am. Chem. Soc.* **2007**, *129*, 8. (*g*) Milios, C. J.; Vinslava, A.; Wernsdorfer, W.; Moggach, S.; Parsons, S.; Perlepes, S. P.; Christou, G.; Brechin, E. K. *J. Am. Chem. Soc.* **2007**, *129*, 2754. (*h*) Schelter, E. J.; Karadas, F.; Avendano, C.; Prosvirin, A. V.; Wernsdorfer, W.; Dunbar, K. R. *J. Am. Chem. Soc.* **2007**, *129*, 8139. (*i*) Freedman, D. E.; Jenkins, D. M.; Iavarone, A. T.; Long, J. R. *J. Am. Chem. Soc.* **2008**, *130*, 2884. (*j*) Yoshihara, D.; Karasawa, S.; Koga,

N. *J. Am. Chem. Soc.* **2008**, *130*, 10460. (*k*) Lin, P.-H.; Burchell, T. J.; Clérac, R.; Murugesu, M. *Angew. Chem. Int. Ed.* **2008**, *47*, 8848. (*l*) Lin, P.-H.; Burchell, T. J.; Ungur, L.; Chibotaru, L. F.; Wernsdorfer, W.; Murugesu, M. *Angew. Chem. Int. Ed.* **2009**, *48*, 9489. (*m*) Zadrozny, J. M.; Freedman, D. E.; Jenkins, D. M.; Harris, T. D.; Iavarone, A. T.; Mathionière, C.; Clérac, R.; Long, J. R. *Inorg. Chem.* **2010**, *49*, 8886. (*n*) Karasawa, S.; Koga, N. *Inorg. Chem.* **2011**, *50*, 5186. (*o*) Rinehart, J. D.; Fang, M.; Evans, W. J.; Long, J. R. *Nat. Chem.* **2011**, *3*, 538. (*p*) Rinehart, J. D.; Fang, M.; Evans, W. J.; Long, J. R. *J. Am. Chem. Soc.* **2011**, *133*, 14236.

(6) (*a*) Ishikawa, N.; Sugita, M.; Ishikawa, T.; Koshihara, S.-Y.; Kaizu, S. *J. Am. Chem. Soc.* **2003**, *125*, 8694. (*b*) Ishikawa, N.; Sugita, M.; Ishikawa, T.; Koshihara, S.; Kaizu, S. *J. Phys. Chem. B* **2004**, *108*, 11265. (*c*) Ishikawa, N.; Sugita, M.; Wernsdorfer, W. *J. Am. Chem. Soc.* **2005**, *127*, 3650. (*d*) AlDamen, M. A.; Cardona-Serra, S.; Clemente-Juan, J.-M.; Coronado, E.; Gaita-Ariño, A. *J. Am. Chem. Soc.* **2008**, *130*, 8874. (*e*) AlDamen, M. A.; Cardona-Serra, S.; Clemente-Juan, J.-M.; Coronado, E.; Gaita-Ariño, A.; Martí-Gastaldo, C.; F. Luis, and O. Montero, *Inorg. Chem.* **2009**, *48*, 3467. (*f*) Jiang, S.-D.; Wang, B.-W.; Su, G.; Wang, Z.-M.; Gao, S. *Angew. Chem. Int. Ed.* **2010**, *49*, 7448. (*g*) Jiang, S.-D.; Wang, B.-W.; Sun, H.-L.; Wang, Z.-M.; Gao, S. *J. Am. Chem. Soc.* **2011**, *133*, 4730. (*h*) Jeletic, M.; Lin, P.-H.; Le Roy, J. J.; Korobkov, I.; Gorelsky, S. I.; Murugesu, M. *J. Am. Chem. Soc.* **2011**, *133*, 19286. (*i*) Feltham, H. L. C.; Lan, Y.; Klöwer, F.; Ungur, L.; Chibotaru, L. F.; Powell, A. K.; Brooker, S. *Chem. Eur. J.* **2011**, *17*, 4362. (*j*) Cucinotta, G.; Perfetti, M.; Luzon, J.; Etienne, M.; Car, P.-E.; Caneschi, A.; Calvez, G.; Bernot, K.; Sessoli, R. *Angew. Chem. Int. Ed.* **2012**, *51*, 1606.

(7) (*a*) Rinehart, J. D.; Long, J. R. *J. Am. Chem. Soc.* **2009**, *131*, 12558. (*b*) Rinehart, J. D.; Meihaus, K. R.; Long, J. R. *J. Am. Chem. Soc.* **2010**, *132*, 7572. (*c*) Magnani, N.; Apostolidis, C.; Morgenstern, A.; Colineau, E.; Griveau, J.-C.; Bolvin, H.; Walter, O.; Caciuffo, R. *Angew. Chem., Int. Ed.* **2011**, *50*, 1696. (*d*) Antunes, M. A.; Pereira, L. C. J.; Santos, I. C.; Mazzanti, M.; Marçalo, J.; Almedia, M. *Inorg. Chem.* **2011**, *50*, 9915.

(8) (*a*) Freedman, D. E.; Harman, W. H.; Harris, T. D.; Long, G. J.; Chang, C. J.; Long, J. R. *J. Am. Chem. Soc.* **2010**, *132*, 1224. (*b*) Harman, W. H.; Harris, T. D.; Freedman, D. E.; Fong, H.; Chang, A.; Rinehart, J. D.; Ozarowksi, A.; Sougrati, M. T.; Grandjean, F.; Long, G. J.; Long, J. R.; Chang, C. J. *J. Am. Chem. Soc.* **2010**, *132*, 18115. (*c*) Weismann, D.; Sun, Y.; Lan, Y.; Wolmershäuser, G.; Powell, A. K.; Sitzmann, H. *Chem.-Eur J.* **2011**, *17*, 4700. (*d*) Lin, P.-H.; Smythe, N. C.; Gorelsky, S. L.; Maguire, S.; Henson, N. J.; Korobkov, I.; Scott, B. L.; Gordon, J. C.; Baker, R. T.; Murugesu, M. *J. Am. Chem. Soc.* **2011**, *133*, 15806. (*e*) Jurca, T.; Farghal, A.; Lin, P.-H.; Korobkov, I.; Murugesu, M.; Richeson, D. S. *J. Am. Chem. Soc.* **2011**, *133*, 15814. (*f*) Zadrozny J. M.; Long, J. R. *J. Am. Chem. Soc.* **2011**, *133*, 20732.

(9) (*a*) Neese, F.; Solomon, E. I. *Inorg. Chem.* **1998**, *37*, 6568. (b) Waldmann, O. *Inorg. Chem.* **2007**, *46*, 10035. (*c*) Neese, F.; Pantazis, D. A.; *Faraday Discuss.* **2011**, *148*, 229.

(10) Drago, R. S. *Physical Methods For Chemists*; Surfside Scientific Publishers: Gainesville, 1992.

(11) Figgis, B. N.; Hitchman, M. A. *Ligand Field Theory and Its Applications*; John Wiley & Sons: New York, 2000.

(12) Kahn, O. *Molecular Magnetism*; John Wiley & Sons: New York, 1993;

(13) (*a*) Andres, H.; Bominaar, E. L.; Smith, J. M.; Eckert, N. A.; Holland, P. L.; Münck, E. *J. Am. Chem. Soc.* **2002**, *124*, 3012. (*b*) Popescu, C. V.; Mock, M. T.; Stoian, S. A.; Dougherty, W. G.; Yap, G. P. A.; Riordan, C. G. *Inorg. Chem.* **2009**, *48*, 8317.
(14) Power, P. P. *Chem. Rev.* **2012**, *112*, 3482 and references therein.
(15) The orbital angular momentum can be highly influenced by subtle, dynamic distortions of the L–Fe–L moiety. Such distortions may be minor enough that they would not appear via a bent L-Fe-L angle in the crystal structure. These influences are explored in full in the following manuscript: Atanasov, M.; Zadrozny, J. M.; Long, J. R.; Neese, F. *Chem. Sci*. **2013**, *4*, 139.
(16) (*a*) Bartlett, R. A.; Power, P. P. *J. Am. Chem. Soc.* **1987**, *109*, 7563. (*b*) Chen, H.; Bartlett, R. A.; Dias, H. V. R.; Olmstead, M. M.; Power, P. P. *J. Am. Chem. Soc.* **1989**, *111*, 4338. (*c*) Chen, H.; Bartlett, R. A.; Olmstead, M. M.; Power, P. P.; Shoner, S. C. *J. Am. Chem. Soc.* **1990**, *112*, 1048. (*d*) Müller, H.; Seidel, W.; Görls, H. *Angew. Chem. Int. Ed.* **1995**, *34*, 325. (*e*) Viefhaus, T.; Schwarz, W.; Hübler, K.; Locke, K.; Weidlein, J. *Z. Anorg. Allg. Chem.* **2001**, *627*, 715. (*f*) LaPointe, A. M. *Inorg. Chim. Acta.* **2003**, *345*, 359. (*g*) Reiff, W. M.; LaPointe, A. M.; Witten, E. *J. Am. Chem. Soc.* **2004**, *126*, 10206. (*h*) Nguyen, T.; Panda, A.; Olmstead, M. M.; Richards, A. F.; Stender, M.; Brynda, M.; Power, P. P. *J. Am. Chem. Soc.* **2005**, *127*, 8545. (*i*) Au-Yeung, H. Y.; Lam, C. H.; Lam, C.-K.; Wong, W.-Y.; Lee, H. K. *Inorg. Chem.* **2007**, *46*, 7695. (*j*) Reiff, W. M.; Schulz, C. E.; Whangbo, M.-H.; Seo, J. I.; Lee, Y. S.; Potratz, G. R.; Spicer, C. W.; Girolami, G. S. *J. Am. Chem. Soc.* **2009**, *131*, 404. (*k*) Ashley, A. E.; Cowley, A. R.; Green, J. C.; Johnston, D. R.; Watkin, D. J.; Kays, D. L. *Eur. J. Inorg. Chem.* **2009**, 2547. (*l*) C. Ni and P. P. Power, *Chem Commun.* **2009**, 5543. (*m*) Merrill, W. A.; Stich, T. A.; Brynda, M.; Yeagle, G. J.; Fettinger, J. C.; De Hont, R.; Reiff, W. M.; Schulz, C. E.; Britt, R. D.; Power, P. P. *J. Am. Chem. Soc.* **2009**, *131*, 12693. (*n*) Lei, H.; Guo, J.-D.; Fettinger, J. C.; Nagase, S.; Power, P. P. *J. Am. Chem. Soc.* **2010**, *132*, 17399.
(17) Pangborn, A. B.; Giardello, M. A.; Grubbs, R. H.; Rosen, K. R.; Timmens, F. J. *Organometallics* **1996**, *15*, 518.
(18) Andersen, R. A.; Faegiri Jr., K.; Green, J. C.; Haaland, A.; Lappert, M. F.; Leung, W.; Rypdal, K. *Inorg. Chem.* **1988**, *27*, 1782.
(19) Horvath, B.; Möseler, R.; Horvath, E. G. *Z. Anorg. Allg. Chem.* **1979**, *450*, 165.
(20**)** (*a*) Chao, Y. W.; Wexler, P. A.; Wigley, D. E. *Inorg. Chem.* **1989**, *28*, 3860. (*b*) Kennepohl, D. K.; Brooker, S.; Sheldrick, G. M.; Roesky, H. W. *Chem. Ber.* **1991**, *124*, 2223. (*c*) Li, J.; Song, H.; Cui, C.; Cheng, J.-P. *Inorg. Chem.* **2008**, *47*, 3468.
(21) Though these constants are located in a variety of references, the following is an exceptional collection of almost all necessary values for the calculations: Bain, G. A.; Berry, J. F. *J. Chem. Educ.* **2008**, *85*, 532.
(22) Sheldrick, G. SADABS, Madison, WI, 1996.
(23) SHELXTL PC v. 5.1; Siemens Analytical X-ray Instruments Inc., Madison, WI, 1994.
(24) (*a*) Cremades, E.; Ruiz, E. *Inorg. Chem.* **2011**, *50*, 4016. (*b*) Atanasov, M.; Ganyushin, D.; Pantazis, D. A.; Sivalingam, K.; Neese, F. *Inorg. Chem.* **2011**, *50*, 7640. (*c*) Maganas, D.; Sottini, S.; Kyritsis, P.; Groenen, E. J. J.; Neese, F. *Inorg. Chem.* **2011**, *50*, 8741.
(25) (*a*) Angeli, C.; Cimiraglia, R.; Malrieu, J.-P. *Chem. Phys. Lett.* **2001**, *350*, 297. (*b*) Angeli, C.; Cimiraglia, R.; Evangelisti, S.; Leininger, T.; Malrieu, J.-P. *J. Chem. Phys.* **2001**, *114*,

10252. (*c*) Angeli, C.; Cimiraglia, R.; Malrieu, J.-P. *J. Chem. Phys.* **2002**, *117*, 9138. (*d*) Angeli, C.; Bories, B.; Cavallini, A.; Cimiraglia, R. *J. Chem. Phys.* **2006**, *124*, 054108.
(26) Neese, F.; Wennmohs, F. *ORCA*; version 2.8; An ab initio, DFT, and semiempirical SCF-MO package with contributions from U. Becker, D. Ganyushin, A. Hansen, D. G. Liakos, C. Kollmar, S. Kossman, T. Petrenko, C. Reimann, C. Riplinger, K. Sivalingam, E. Valeev, B. Wezisla; Lehrstuhl fur theoretische Chemie: Bonn, Germany, 2010.
(27) Neese, F. *J. Chem. Phys.* **2005**, *122*, 34107.
(28) McWeeny, R. *Methods of Molecular Quantum Mechanics*; Academic Press: London, 1992.
(29) Ganyushin, D.; Neese, F. *J. Chem. Phys.* **2006**, *125*, 024103.
(30) Roos, B. O.; Malmqvist, P.-Å. *Phys. Chem. Chem. Phys.* **2004**, *6,* 2919.
(31) Bryan, A. M.; Merrill, W. A.; Reiff, W. M.; Fettinger, J. C.; Power, P. P. *Inorg. Chem.* **2012**, *51*, 3366.
(32) Shannon, R. D. *Acta. Cryst.* **1976**, *A32*, 751.
(33) Pyykkö, P.; Atsumi, M. *Chem. Eur. J.* **2009**, *15*, 186.
(34) Kotani, M. *J. Phys. Soc. Jpn.* **1949**, *4*, 293.
(35) Shores, M. P.; Sokol, J. J.; Long, J. R. *J. Am. Chem. Soc.* **2002**, *124*, 2279.
(36) Dai, D.; Whangbo, M.-H. *Inorg. Chem.* **2005**, *44*, 4407.
(37) (*a*) Cole, K. S.; Cole, R. H. *J. Chem. Phys.* **1941**, *9*, 341. (*b*) Böttcher, C. J. F. *Theory of Electric Polarisation*; Elsevier: New York, 1952. (*c*) Aubin, S. M. J.; Sun, Z. M.; Pardi, L.; Krzystek, J.; Folting, K.; Brunel, L. C.; Rheingold, A. L.; Christou, G.; Hendrickson, D. N. *Inorg. Chem.* **1999**, *38*, 5329.
(38) Gatteschi, D.; Sessoli, R. *Angew. Chem. Int. Ed.* **2003**, *42*, 268.
(39) Carlin, R. *Magnetochemistry*; Spinger-Verlag: Berlin, 1986.
(40) Fort, A.; Rettori, A.; Villain, J.; Gatteschi, D.; Sessoli, R. *Phys. Rev. Lett.* **1998**, *80*, 612.
(41) (*a*) Orbach, R. *Proc. R. Soc. Lond. A* **1961**, *264*, 458. (*b*) Orbach, R. *Proc. R. Soc. Lond. A* **1961**, *264*, 485. (*c*) Walker, M. B. *Can. J. Phys.* **1968**, *46*, 1347.
(42) $D = -70$ cm^{-1}, $(Ph_4P)_2[Co(SPh)_4]$: (*a*) Fukui, K.; Ohya-Nishiguchi, H.; Hirota, N. *Bull. Chem. Soc. Jpn.* **1991**, *64*, 1205. (*b*) Fukui, K.; Kojima, N.; Ohya-Nishiguchi, H.; Hirota, N. *Inorg. Chem.* **1992**, *31*, 1338. (*c*) Fukui, K.; Masuda, H.; Ohya-Nishiguchi, H.; Kamada, H. *Inorg. Chim. Acta.* **1995**, *238*, 73.
(43) $|D| = 76$ cm^{-1}, $[(^{H}L)_2Fe_6(NCMe)_6](PF_6)_3$: Zhao, Q.; Harris, T. D.; Betley, T. A. *J. Am. Chem. Soc.* **2011**, *133*, 8293.
(44) $D \approx 70$ cm^{-1}, Mixed-valence di-Ruthenium tetracarboxylate complexes: (*a*) Telser, J.; Drago, R. S. *Inorg. Chem.* **1984**, *23*, 3114. (*b*) Telser, J.; Drago, R. S. *Inorg. Chem.* **1985**, *24*, 4765. (*c*) Cukiernik, F. D.; Giroud-Godquin, A. M.; Maldivi, P.; Marchon, J. C. *Inorg. Chim. Acta.* **1994**, *215*, 203. (*d*) Handa, M.; Sayama, Y.; Mikuriya, M.; Nukada, R.; Hiromitsu, L.; Kasuga, K. *Bull. Chem. Soc. Jpn.* **1998**, *71*, 119. (*e*) Jimenez-Apraricio, R.; Urbanos, F. A.; Arrieta, J. M. *Inorg. Chem.* **2001**, *40*, 613. (*f*) Vos, T. E.; Liao, Y.; Shum, W. W.; Her, J.-H.; Stephens, P. W.; Reiff, W. M.; Miller, J. S. *J. Am. Chem. Soc.* **2004**, *126*, 11630.
(45) (*a*) Hougen, J. T.; Leroi, G. E.; James, T. C. *J. Chem. Phys.* **1960**, *34*, 1670. (*b*) DeKock, C. W.; Gruen, D. M. *J. Chem. Phys.* **1966**, *44*, 4387.
(46) Hargittai, M. *Chem. Rev.* **2000**, *100*, 2233 and references therein.
(47) Zadrozny, J. M.; Liu, J.; Piro, N. A.; Chang, C. J.; Hill, S.; Long, J. R. *Chem. Commun.*

2012, *112*, 3927.

Table 6.S1. Crystal data for structure refinement of **1**.

Empirical formula	$C_{30}H_{52}FeN_2Si_2$
Formula weight	552.77
T, K	95(1)
λ, Å	0.7107
Crystal system	Triclinic
Space group	P–1
Habit	Block
Color	Brown
a, Å	8.8101(5)
b, Å	9.1759(5)
c, Å	11.1624(6)
α, °	102.4670(10)
β, °	92.5030(10)
γ, °	113.9320(10)
V, Å^3	796.59(8)
Z	1
ρ_{calc}, g/cm^3	1.152
μ, mm^{-1}	0.568
F_{000}	300
Crystal dimensions	0.368 × 0.367 × 0.358 mm^3
2θ range, °	3.78 – 55.02
Index ranges	-10 <= h <= 11
	-11 <= k <= 11
	-14 <= l <= 14
Reflections collected	8827
Independent reflections	3654 [R_{int} = 0.0140]
Completeness to 2θ = 55.02	99.6 %
Data / restraints / parameters	3654 / 167 / 0
Goodness-of-fit on F^2	1.002
Final R indices [I > 2σ(I)][b]	R_1 = 0.0345, wR_2 = 0.1035
R indices (all data)	R_1 = 0.0376, wR_2 = 0.1065
Largest diff. peak and hole	0.484 and -0.535 eÅ^3

[a]Obtained with graphite-monochromated Mo Kα (λ = 0.7107 Å) radiation. [b]$R_1 = \Sigma||F_o||F_c||/|F_o|$, $wR_2 = \{\Sigma[w(F_o^2 - F_c^2)^2]/\Sigma[w(F_o^2)^2]\}^{1/2}$.

Table 6.S2. Crystal data for structure refinement of **3**.

Empirical formula	$C_{60}H_{76}Fe_{0.93}N_2$[c]
Formula weight	877.17
T, K	90(2)
λ, Å	0.7107
Crystal system	Monoclinic
Space group	$P2_1/n$
Habit	Block
Color	Red-orange
a, Å	10.8937(18)
b, Å	20.234(3)
c, Å	11.2231(19)
α, °	90
β, °	90.829(3)
γ, °	90
V, Å^3	2473.5(7)
Z	2
ρ_{calc}, g/cm^3	1.178
μ, mm^{-1}	0.325
F_{000}	948
Crystal dimensions	0.25 × 0.17 × 0.14 mm^3
2θ range, °	4.02 – 50.70
Index ranges	-13 <= h <= 13
	-24 <= k <= 24
	-13 < =l < =13
Reflections collected	27437
Independent reflections	4534 [R_{int} = 0.0416]
Completeness to 2θ = 50.70	100.0 %
Data / restraints / parameters	4534 / 0 / 298
Goodness-of-fit on F^2	1.031
Final R indices [I > 2σ(I)][b]	R_1 = 0.0338, wR_2 = 0.0800
R indices (all data)	R_1 = 0.0449, wR_2 = 0.0857
Largest diff. peak and hole	0.359 and -0.212 eÅ^3

[a]Obtained with graphite-monochromated Mo Kα (λ = 0.7107 Å) radiation. [b]$R_1 = \Sigma||F_o||F_c||/|F_o|$, $wR_2 = \{\Sigma[w(F_o^2 - F_c^2)^2]/\Sigma[w(F_o^2)^2]\}^{1/2}$.

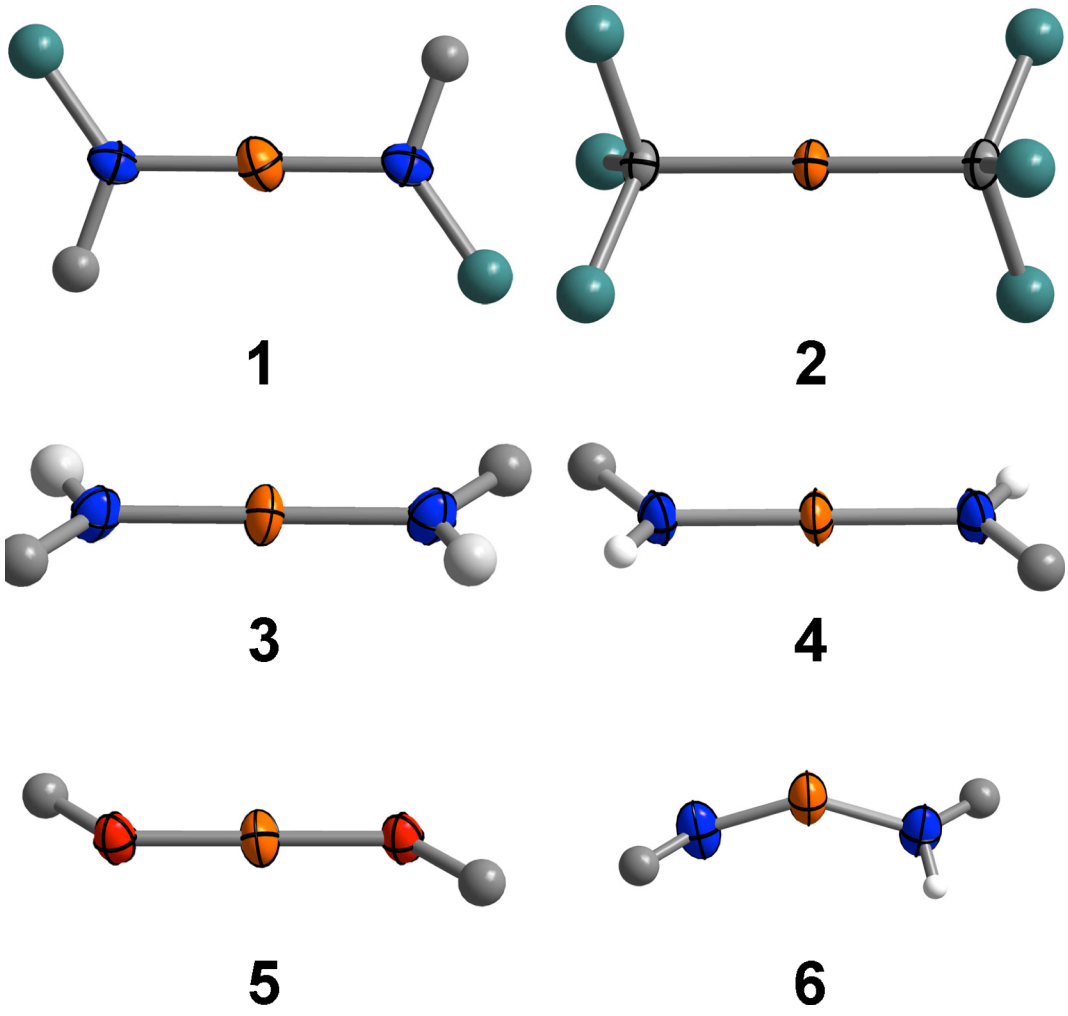


Figure 6.S1. Probability ellipsoids of the L-Fe-L moieties for complexes **1-6,** depicted at the 80% level. Only the thermal parameters of the Fe ions and their immediate neighbors are depicted. Orange, blue, red, and gray ellipsoids correspond to Fe, N, O, and C atoms, respectively. Cyan, gray, and white spheres correspond to Si, C, and H atoms, respectively. Next-nearest structure around the donor atoms is given to assist in comparison of the principal axes of the ellipsoids with the overall molecular geometry.

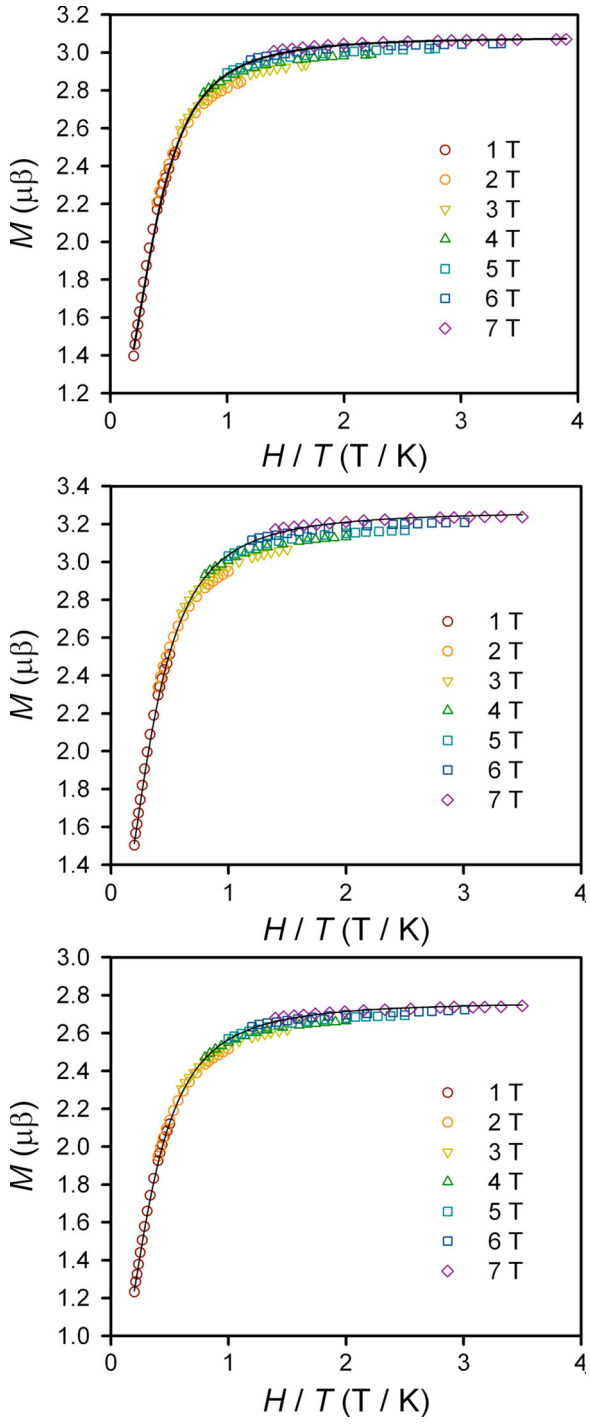


Figure 6.S2. Variable field, variable temperature magnetization data collected on **1** (top), **2** (middle), and **3** (bottom) from 1 to 7 T at temperatures from 1.8 to 5 K. The black line represents the master equations used to determine the superimposability index, as discussed in the main text and Appendix 4.

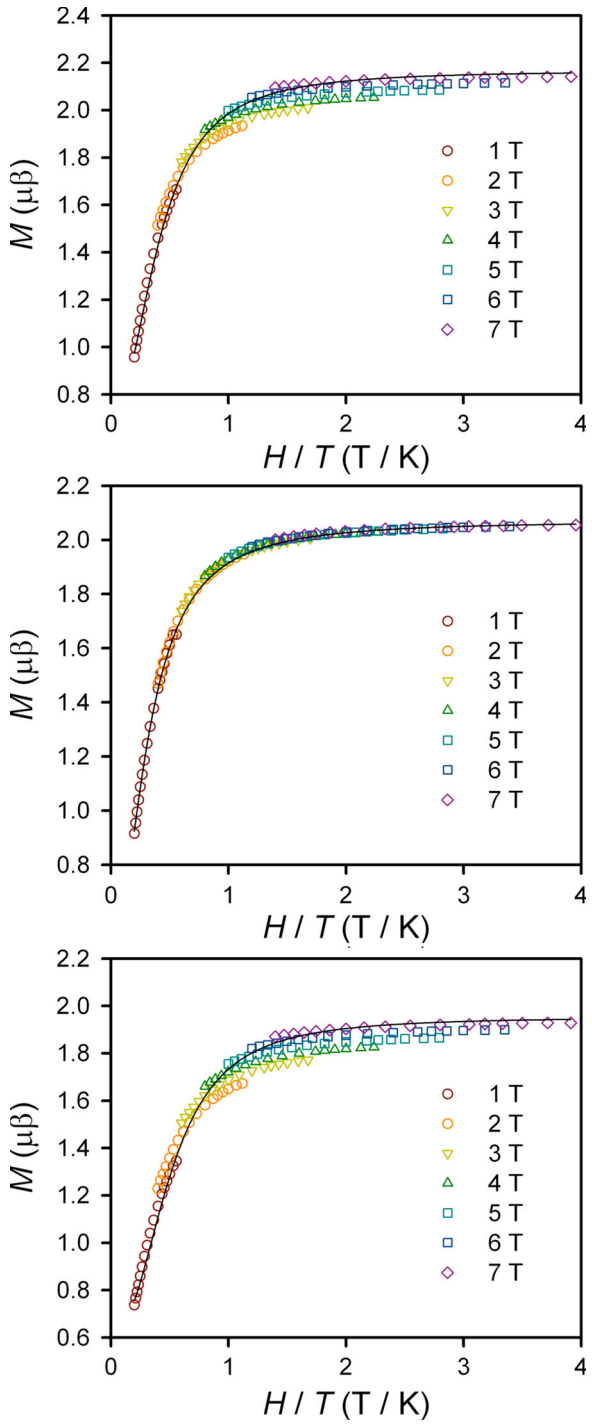


Figure 6.S3. Variable field, variable temperature magnetization data collected on **4** (top), **5** (middle), and **6** (bottom) from 1 to 7 T at temperatures from 1.8 to 5 K. The black line represents the master equations used to determine the superimposability index, as discussed in the main text and Appendix 4.

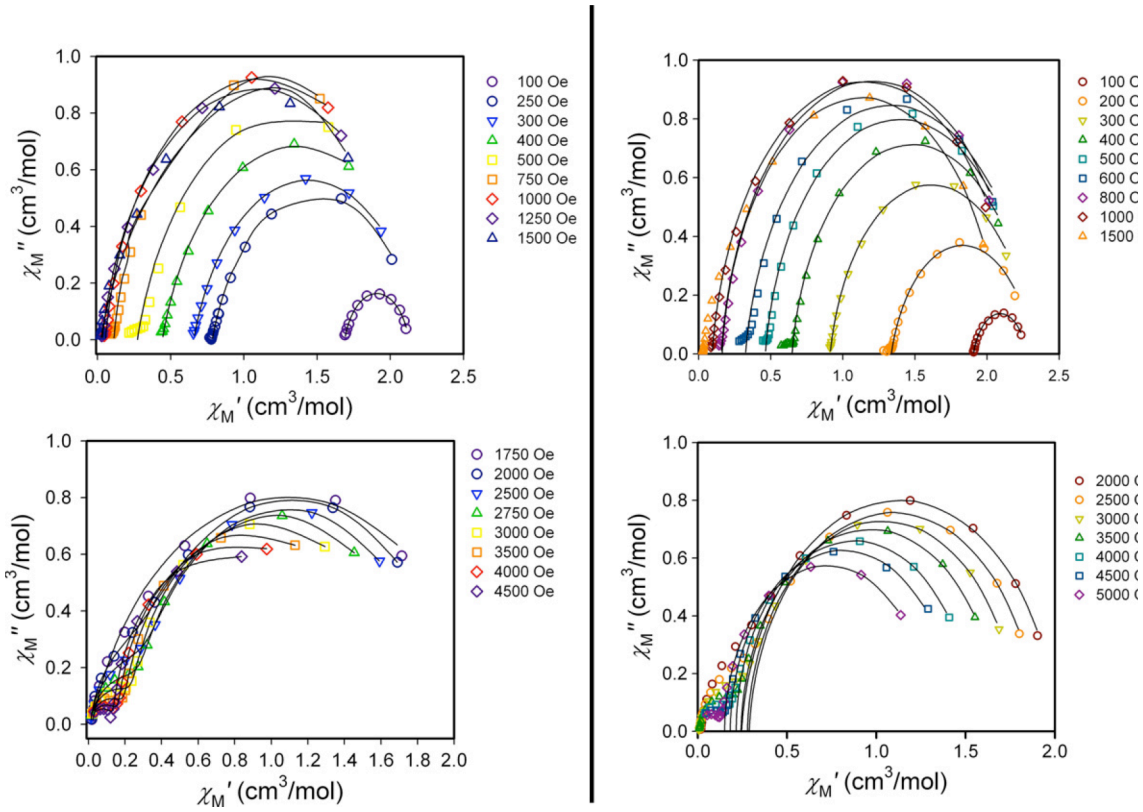


Figure 6.S4. Cole-cole plots fit for the determination of the field dependence of τ for **1** (left) and **2** (right) at 2 K. Black lines are the result of fits to a generalized Debye model as described in the main text.

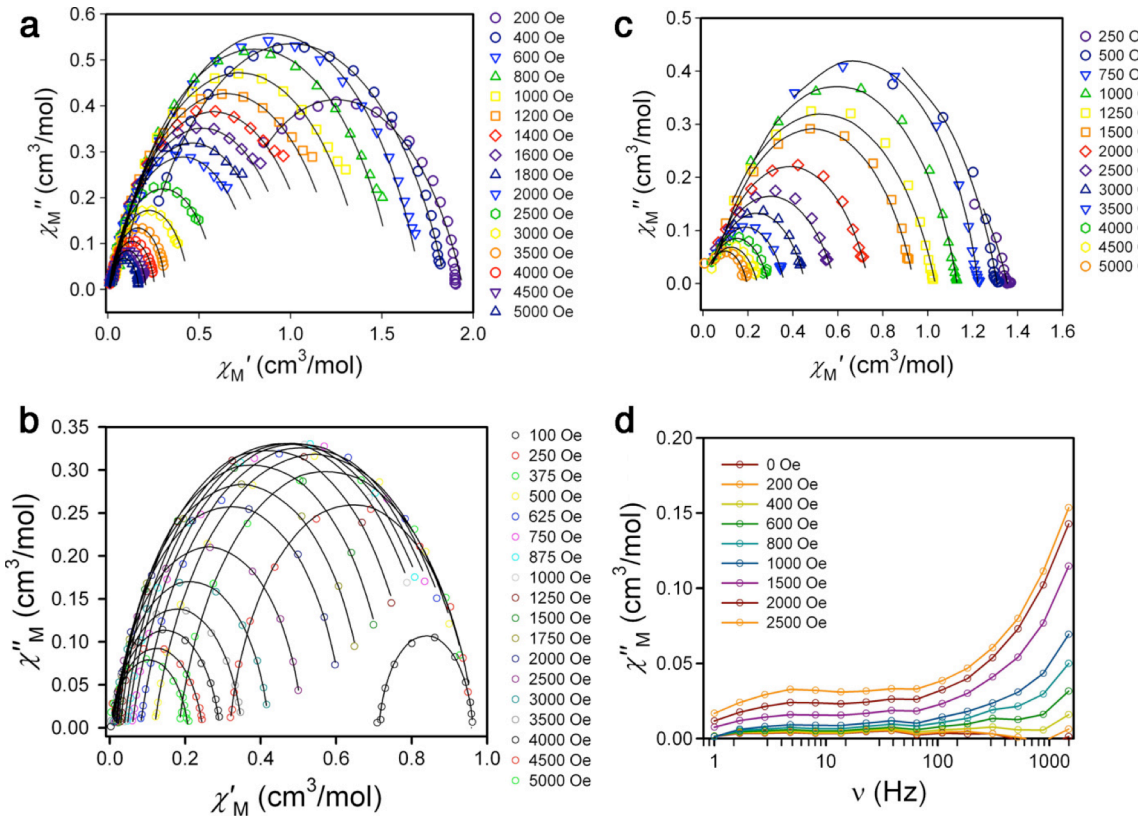


Figure 6.S5. Cole-cole plots fit for the determination of the field dependence of τ for **3** (**a**), **4** (**b**), and **5 (c)** at 2 K. Black lines are the result of fits to a generalized Debye model as described in the main text. **d**. Frequency dependence of the out-of-phase susceptibility of **6** as a function of applied field at 2K. Solid lines are guides for the eye.

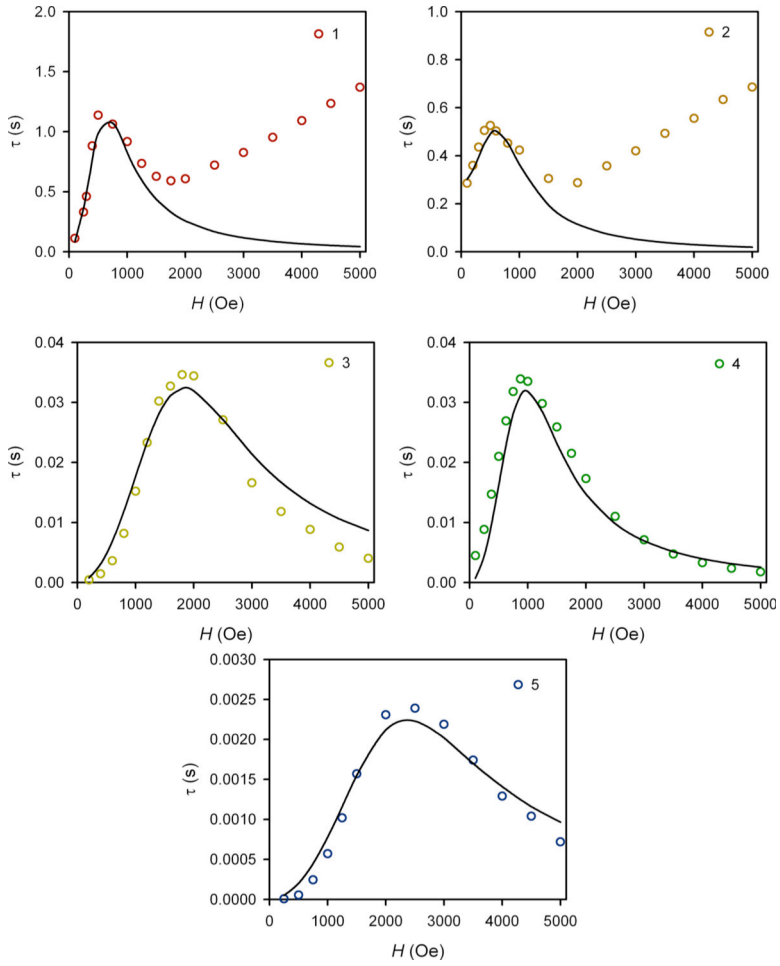


Figure 6.S6. Field dependence of τ for **1-5** at 2 K. Black lines represent fits as discussed in the main body of the report.

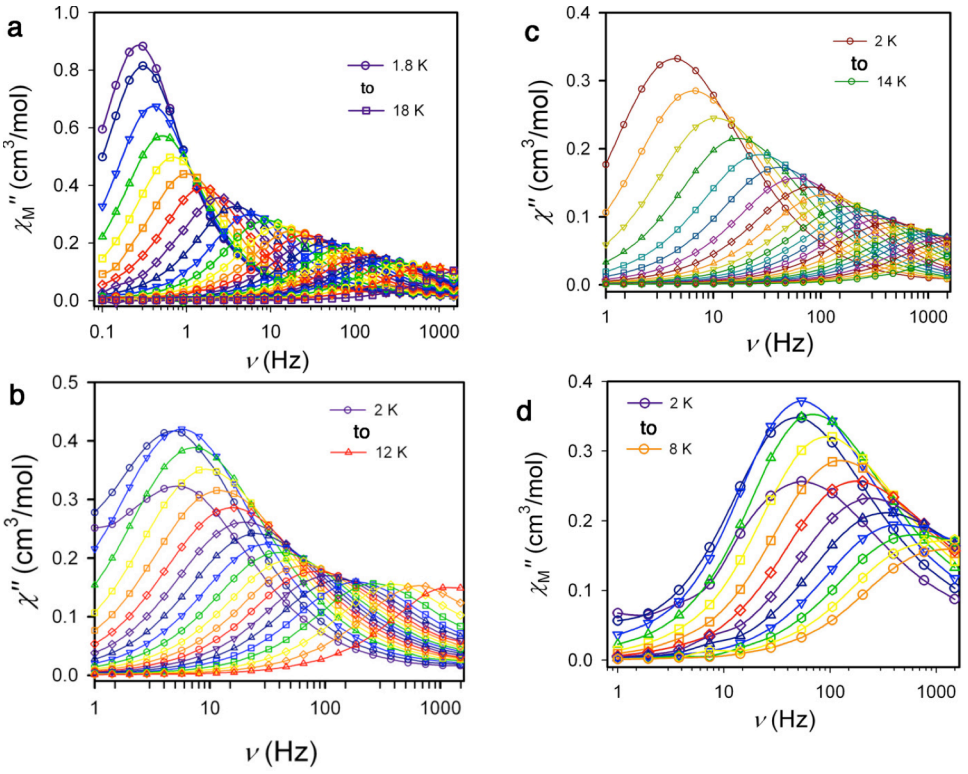


Figure 6.S7. Frequency dependence of the out-of-phase susceptibility for **2**-**5**. **a**. Data collected for **2** under an applied dc field of 500 Oe. **b**. Data collected for **3** under an applied dc field of 875 Oe. **c**. Data collected for **4** under an applied dc field of 875 Oe. **d**. Data collected for **5** under an applied dc field of 2500 Oe.

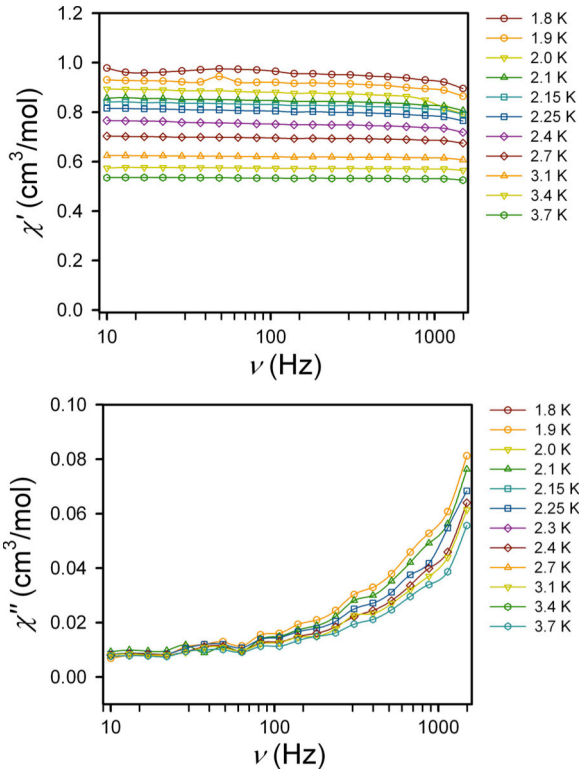


Figure 6.S8. Frequency dependence of the in-phase (top) and out-of-phase (bottom) susceptibilities of **6** as a function of temperature. Data were collected under an applied dc field of 1000 Oe.

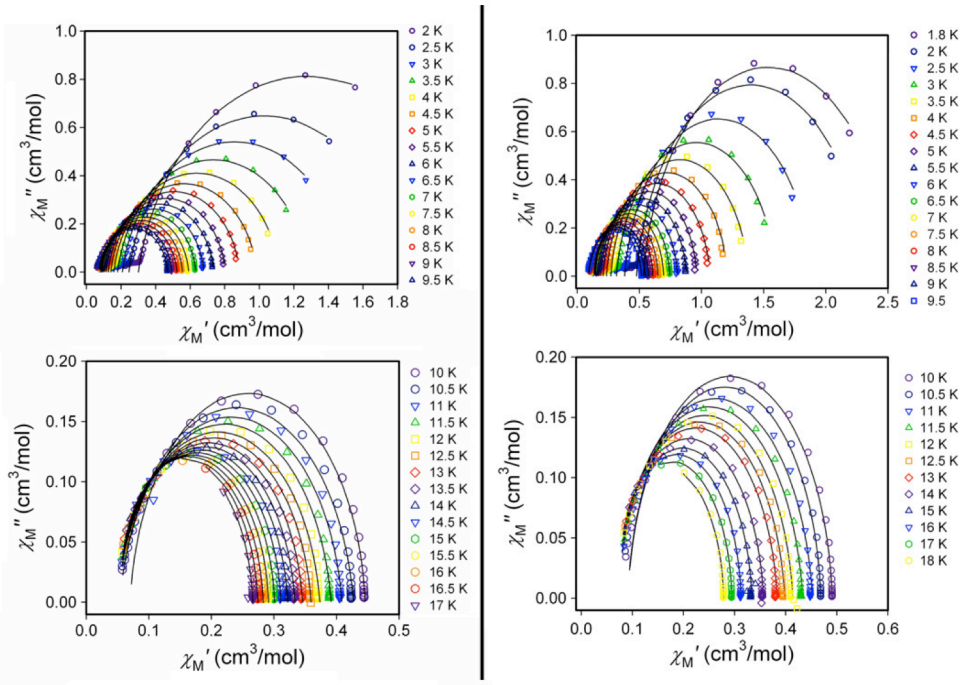


Figure 6.S9. Cole-cole plots of the frequency dependence of χ_M' and χ_M'' used to evaluate the temperature dependence of τ for **1** (left) and **2** (right).

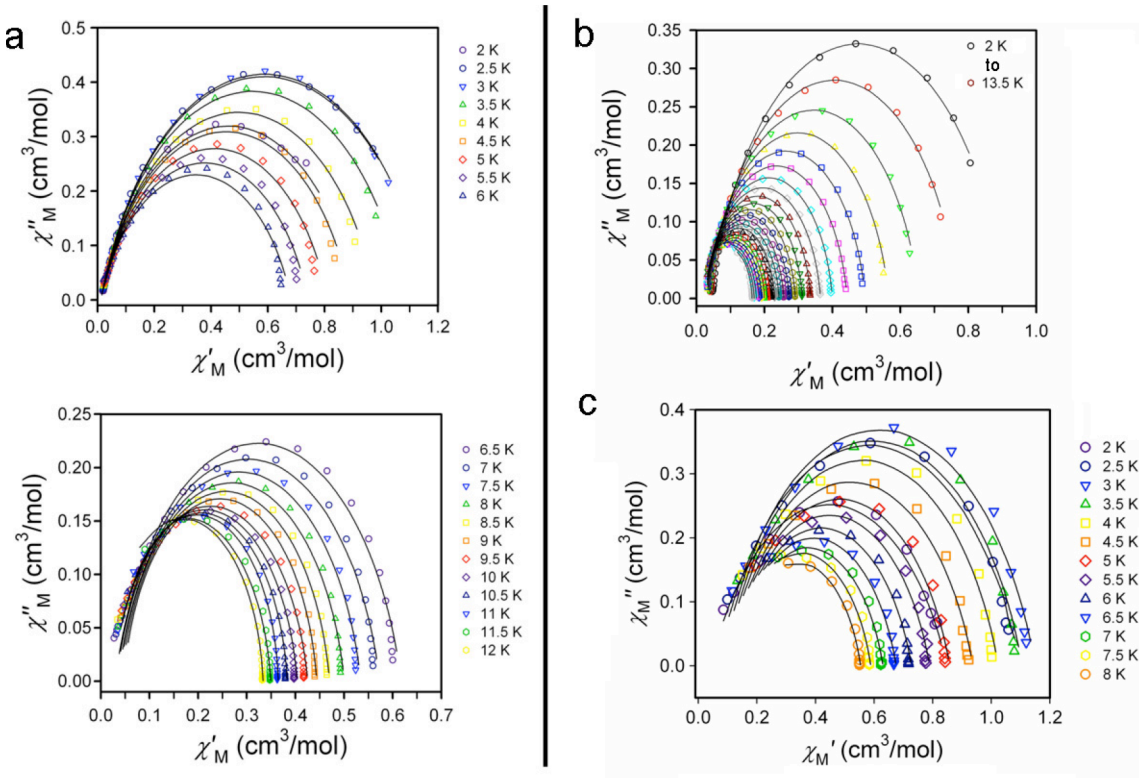


Figure 6.S10. Cole-cole plots of the frequency dependence of χ_M' and χ_M'' used to evaluate the temperature dependence of τ for **3** (left, **a**), **4** (right top, **b**) and **5** (right bottom, **c**).

Chapter 7: Magnetic Blocking in a Linear Iron(I) Complex

7.1. Introduction

Nearly a decade ago, the mononuclear lanthanide complexes $[LnPc_2]^-$ (H_2Pc = phthalocyanine; Ln = Tb, Dy) were discovered to possess directionally bistable magnetic moments.[1] In these molecules, the spin and orbital angular momenta couple strongly to generate inherent directionality for the molecular magnetic moments (see Chapter 1). As a result of these highly anisotropic spin-orbit coupled ground states, and the relaxation barriers imposed by the axial ligand fields,[2] the magnetic moments of these molecules reorient only slowly upon removal from a magnetizing field. When the relaxation time is sufficiently long, molecular magnetic hysteresis is observed, similar to that of classical magnets, but here due to the moment of a single metal ion.[3] Significantly, the effective relaxation barriers for such species, determined by spectral and/or magnetic susceptibility measurements, can be as high as U_{eff} = 641 cm^{-1},[2,4,5,6] surpassing by an order of magnitude that obtained for the original single-molecule magnet, $Mn_{12}O_{12}(O_2CCH_3)_{16}(H_2O)_4$,[7,8] and other transition metal-containing clusters.[9,10] Thus, f-element complexes seemingly present the best opportunities for attaining the high relaxation barriers required for potential applications of single-molecule magnets in information storage,[11] quantum computation,[12,13,14] and spintronics.[15]

The investigation of the magnetic anisotropies of transition metal-based systems is of renewed interest as part of a larger general effort to find magnetic alternatives to the f-block elements. However, compared to lanthanides and actinides, mononuclear complexes of transition metals appear to be poorly-suited for achieving high relaxation barriers, owing to their smaller magnetic moments and, at least for first-row transition metal ions, lower spin-orbit coupling constants. In addition, the larger ligand field splitting energies of the transition metal d orbitals can be expected to suppress the orbital contributions to the magnetism required for developing magnetic anisotropy. In one manifestation of this effect, first-order orbital angular momentum can be quenched as the result of a Jahn-Teller distortion.[16] In another, the second-order contribution to the magnetic anisotropy (i.e., zero-field splitting) is diminished, owing to the large energy separation between ground and excited electronic states, which reduces the degree of mixing. Importantly, these ligand field effects can be substantially overcome by enforcing a low coordination number at the transition metal center, which causes the d orbitals to fall within a narrow energy range, similar to the situation found for the 4f orbitals of a lanthanide complex. Indeed, four-coordinate trigonal pyramidal complexes of iron(II) with an $S = 2$ ground state have been shown to behave as single-molecule magnets with thermal relaxation barriers as high as 65 cm^{-1}.[17,18] In these and a number of other mononuclear transition metal complexes,[19,20,21,22] however, the observation of slow magnetic relaxation requires a dc field bias to suppress fast magnetization reversal via quantum tunneling. Alternatively, tunneling of the magnetic moment due to mixing of the ground $\pm M_S$ levels will be minimized in half-integer spin systems, as posited by Kramers.[23] Thus, such systems should not require a dc field bias to display slow magnetic relaxation. As initial examples, the $S = {}^3/_2$ complexes in $(Ph_4P)_2[Co(SPh)_4]$ and $(PNP)FeCl_2$ (PNP^- = N[2-$P(CHMe_2)_2$-4-methylphenyl]$_2$ anion) have recently been shown to

behave as single-molecule magnets in the absence of an applied dc field, exhibiting U_{eff} = 21(1) and 34(2) cm^{-1}, respectively.[24,25]

A linear two-coordinate geometry presents perhaps the best opportunity for mitigating ligand field effects in transition metal complexes and creating a large anisotropy barrier.[26] Here, a high-spin d^6 electron configuration can be expected to provide unquenched orbital angular momentum, which maximizes the magnitude of the magnetic moment, while the ligands define an axis for its preferential alignment. Recently, we and others have studied linear, two-coordinate complexes of iron(II), which possess $S = 2$ ground states under the influence of an unquenched orbital angular momentum.[27,28,29,30,31] These investigations revealed that very large spin reversal barriers, as high as 181 cm^{-1}, could be observed by ac magnetic susceptibility measurements, albeit only in the presence of an applied dc field. To determine if such large barriers could be attained in the absence of an applied field, again taking advantage of Kramers' theorem, we chose to investigate the magnetic properties of two-coordinate complexes with $S = {}^3/_2$ ground states. Here, we report the first two-coordinate complex of iron(I), $[Fe(C(SiMe_3)_3)_2]^-$, which indeed possesses a highly anisotropic $S = {}^3/_2$ spin state, resulting in a record high barrier for magnetic relaxation in a transition metal complex under zero applied field.

7.2. Experimental

7.2.1. Synthetic Procedures. All manipulations were performed in an inert atmosphere box under N_2. Tetrahydrofuran (THF), and hexanes were dried using a commercial solvent purification system designed by JC Meyer Solvent Systems. Diisopropylether (iPr_2O) was dried over Na/benzophenone and degassed via successive freeze pump thaw cycles prior to use. 4,7,13,16,21,24-hexaoxa-1,10-diazabicyclo[8.8.8]hexacosane (2.2.2-cryptand, abbreviated also as crypt-222) was purchased from TCI America and used as received. KC_8 was prepared according to literature methods.[32] $Fe(C(SiMe_3)_3)_2$ was prepared according to the literature method and sublimed prior to use in synthesis and analysis by Mössbauer spectroscopy.[33]

[K(crypt-222)][Fe(C(SiMe$_3$)$_3$)$_2$] (1). A solution of $Fe(C(SiMe_3)_3)_2$ (0.10 g, 0.19 mmol) in 2 mL of THF was added to a slurry of KC_8 (26 mg, 0.19 mmol) in 2 mL of THF. Upon stirring vigorously for 2 h, the solution changed from a deep red to a bright yellow-orange color. The solution was filtered through diatomaceous earth (Celite® 545), and 2.2.2-cryptand (74 mg, 0.20 mmol) was added. The solvent was removed under reduced pressure to afford a crude product, which was washed with 10 mL of hexanes to remove unreacted $Fe(C(SiMe_3)_3)_2$, dried under nitrogen flow, and dissolved in 100 mL of iPr_2O. Hexanes were layered on top of the solution, leading to the formation of bright yellow-green block-shaped crystals of **1** (65 mg, 49%). ESI/MS (*m*/*z*): $[M]^-$ calcd. for $C_{20}H_{54}FeSi_6$, 518.219. Found: 518.217. UV-vis (2-MeTHF); λ_{max} (ε_M, $M^{-1}cm^{-1}$) 845 (1456), 723 (3270), 596 (1023), and 417 (7040) nm. IR (Nujol): 2942(m), 2922(w), 2885(m), 2814(w), 1477(m), 1459(m), 1445(m), 1354(s), 1296(s), 1259(w), 1241(vs), 1230(w), 1174(w), 1133(s), 1103(vs), 1078(s), 1058(w), 1029(w), 950(s), 932(s), 865(vs), 824(vs), 770(s), 754(m), 665(s), 644(vs), 606(s), 591(s), 566(w), and 523(m) cm^{-1}. Anal. Calcd. for $C_{38}H_{90}N_2FeKO_6Si_6$: C, 48.84; H, 9.71; N, 3.00 %. Found: C, 48.80, H 9.39, N 2.96 %.

7.2.2. Magnetic Measurements. All manipulations of the samples in preparation for analysis were performed with Teflon-coated spatulae. Polycrystalline samples were loaded into a quartz tube, and coated in eicosane with a glove box. The quartz tubes were fixed to a sealable hose-adapter, evacuated with a Schlenk line outside of the glove box, frozen in liquid N_2, then flame

sealed. Solution measurements were prepared similarly, omitting the eicosane step. The bright yellow color of all samples was retained throughout the sealing process, and once flame sealed in tubes, the samples are stable indefinitely. Samples were measured from 2 to 300 K at dc fields ranging from 0 to 7 T with a Quantum Design MPMS-XL SQUID magnetometer. All data were corrected for diamagnetic contributions from the eicosane restraint, sample holder, and the compound itself estimated with Pascal's constants. Hysteresis loops collected at 100 K confirmed the absence of ferromagnetic impurities.

7.2.3. X-ray Data Collection, Structure Solution, and Refinement. Data collection was performed on a single crystal of **1** coated in paratone oil and mounted on Kaptan loops under a freezing stream of N_2. During mounting, crystals of **1** did not show any signs of desolvation. Data were collected using a Bruker QUAZAR diffractometer equipped with a Bruker MICROSTAR X-ray source of Mo Kα (λ = 0.71073 Å) radiation, and a APEX-II detector. Raw data were integrated and corrected for Lorentz and polarization effects using Bruker Apex2 v. 2009.1.[34] Absorption corrections were applied using SADABS.[35] The space group was determined by examination of systematic absences, E-statistics, and successive refinement of the structure. The crystal structure was solved with SIR-97[36] and further refined with SHELXL[37] operated with the WIN-GX interface.[38] The crystal did not show significant decay during data collection. Thermal parameters were refined anisotropically for all non-hydrogen atoms or ions in **1** except for those atoms which were modeled as disordered. Hydrogen atoms were placed in ideal positions and refined using a riding model for all structures. Significant disorder of the $[(\text{crypt-222})\text{K}]^+$ counterion in the structure required modeling, but ultimately gave rise to several level B alerts from checkcif. Significant changes to our disorder model did not alter the geometry of the $[\text{Fe}(\text{C}(\text{SiMe}_3)_3)_2]^-$ moiety. Full crystallographic details are located in Table 7.S1.

7.2.4 All Other Physical Measurements. UV-vis-NIR spectroscopy over the range of 5000-30,000 cm^{-1} was performed using a CARY 5000 spectrophotometer interfaced to Varian WinUV software. Solutions were prepared under a N_2 atmosphere and sealed prior to measurement. Molar absorptivities were determined via three-point fittings to Beers' law. Cyclic voltammograms were obtained with a Bioanalytical Systems CV-50W Voltammograph, a platinum wire counter electrode, a silver sire reference electrode, and a glassy carbon working electrode. Analyte solutions were prepared with 0.1 M solutions of $(\text{Bu}_4\text{N})\text{PF}_6$ in difluorobenzene. Ferrocene was used as an internal standard and all potentials reported here are referenced to the $[\text{Cp}_2\text{Fe}]^{+/0}$ couple. Mössbauer spectra were collected on freshly recrystallized **1** at 295 K with a constant acceleration spectrometer that utilized a rhodium matrix cobalt-57 source and was calibrated at 295 K with 27 μm α-iron foil. The absorber contained 65 mg/cm^2 of powder. The sample was prepared in an N_2-filled glovebox and inserted into the cryostat under dry helium. Mass spectra were acquired in negative ion mode using a quadrupole time-of-flight (Q-Tof) mass spectrometer equipped with a Z-spray electrospray ionization (ESI) source (Q-Tof Premier, Waters, Milford, MA) at the QB3/Chemistry Mass Spectrometry Facility at UC Berkeley. Elemental (C, H, and N) analysis was performed at the Microanalytical Laboratory of the University of California, Berkeley.

7.2.5. Computation Details. Multireference calculations (CASSCF and NEVPT2) of the energy levels of $[\text{Fe}(\text{C}(\text{SiMe}_3)_3)_2]^-$ were computed based on the X-ray geometry using def2-TZVP basis set and corresponding auxiliary functions def2-TZVP/C and the resolution of the identity option. The full manifold of electronic multiplets spanned by the nominal $3d^7$ configuration of iron(I) in the complex have been computed using state averaging over the 10 quartets ($S = {}^3/_2$) and the 40 doublet ($S = {}^1/_2$) states. Sample state-specific calculations did not

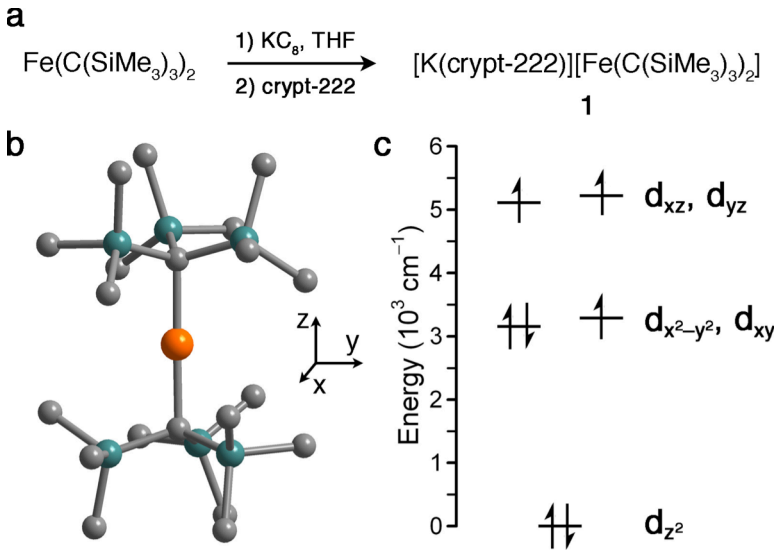


Figure 7.1. Preparation, structure, and d-orbital splitting of the linear iron(I) complex $[Fe(C(SiMe_3)_3)_2]^-$. **a.** General reaction scheme for the synthesis of **1**. **b**. Structure of the $[Fe(C(SiMe_3)_3)_2]^-$ anion, as observed in the crystal structure of **1**. Orange, cyan, and gray spheres represent Fe, Si, and C, respectively; H atoms are omitted for clarity. Selected interatomic distances (Å) and angles (˚) for **1**: Fe–C = 2.062(4), 2.058(4); Fe•••Fe = 9.211(3); C–Fe–C = 179.2(2). **c**. Energies of the 3d-orbitals extracted from an *ab-initio* computational analysis of $[Fe(C(SiMe_3)_3)_2]^-$.

yield results which differed much from the adopted computational protocol. Such calculations sometimes suffer from a lack of convergence at the CASSCF level. CASSCF wavefunctions were rotated and purified following the implementation by K. Sivalingam available in the current version of ORCA[39] The *ab-initio* based ligand field method utilized here has been described in detail previously.[40,41]

7.3. Results and Discussion

7.3.1. Syntheses and Structures. The viability of reducing the linear two-coordinate complex $Fe(C(SiMe_3)_3)_2$ by one electron was first recognized upon measuring its cyclic voltammogram in difluorobenzene (see Fig. 7.S1). Here, a reversible reduction event corresponding to the $[Fe(C(SiMe_3)_3)_2]^{0/1-}$ couple is apparent at $E_{1/2}$ = –1.82 V versus the $[FeCp_2]^{1+/0}$ (Cp^- = cyclopentadienyl anion) couple with a peak-to-peak separation of 78 mV. In view of this result, KC_8 was employed to reduce the complex, which, upon addition of 2.2.2-cryptand (crypt-222), enabled isolation of the yellow-green compound [K(crypt-222)][$Fe(C(SiMe_3)_3)_2$] (**1**). X-ray diffraction analysis of a single crystal of **1** revealed the linear two-coordinate structure of $[Fe(C(SiMe_3)_3)_2]^-$, as depicted in Fig. 7.1. Here, the C–Fe–C angle of 179.2(2)° is almost perfectly linear, placing **1** among a small family of homoleptic two-coordinate metal(I) complexes of the $[C(SiMe_3)_3]^-$ ligand.[42-45] Notably, the $SiMe_3$ groups are nearly eclipsed, in contrast to the structure of $Fe(C(SiMe_3)_3)_2$ in which they are staggered.[46] The

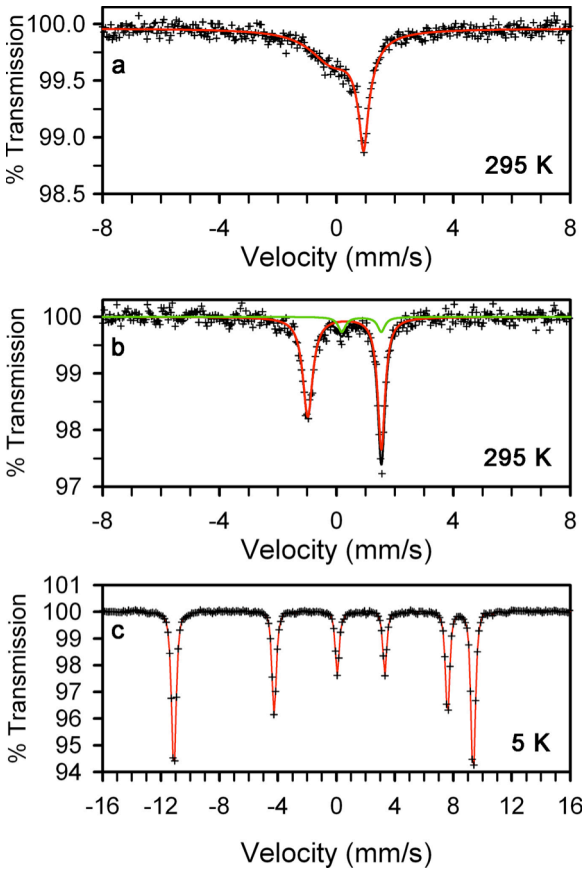


Figure 7.2. **a**. Data collected on $Fe(C(SiMe_3)_3)_2$ at 295 K. The black line corresponds to a fit giving $\delta = 0.39(1)$ mm/s, $\Delta E_Q = -1.08(1)$ mm/s, $H_{int} = 152$ T, and $\tau = 1.13(1) \times 10^{-10}$ s. **b.** Data collected on **1** at 295 K. The black line represents the sum of two fitted components. The major component, red, corresponds to **1**, while the second component, green, corresponds to a minor unidentified, oxidized impurity. The red component is a result of a fit with a relaxation profile calculated for a fixed experimental linewidth of 0.314 mm/s and with $\delta = 0.278(4)$ mm/s, $\Delta E_Q = -2.520(7)$ mm/s, $H_{int} = 63.97(1)$ T, $\tau = 5.1(6) \times 10^{-11}$ s, and 90.0(5) % area. **c.** Data collected on **1** at 5 K. The red line corresponds to a fit with $\delta = 0.410(2)$ mm/s, $\Delta E_Q = -2.557(5)$ mm/s, $H_{int} = 63.97(1)$ T, and $\Gamma = 0.314(2)$ mm/s.

Fe–C distances of 2.058(4) and 2.062(4) Å are only marginally longer than the distance of 2.051(1) Å in $Fe(C(SiMe_3)_3)_2$.[46]

7.3.2. Mössbauer Analysis. Compound **1** was characterized by ^{57}Fe Mössbauer spectroscopy, a technique that is highly sensitive to the oxidation state and chemical environment of the iron center (see Appendix A.5 for additional interpretive details). While the structures of the linear complexes in $Fe(C(SiMe_3)_3)_2$ and **1** are very similar, different Mössbauer parameters are observed for the two compounds, in agreement with a change in the oxidation state of the iron upon reaction with KC_8. The spectrum of $Fe(C(SiMe_3)_3)_2$ at 295 K consists of a quadrupole doublet broadened by paramagnetic relaxation and characterized by an isomer shift of $\delta = 0.39(1)$ mm/s, a quadrupole splitting of $\Delta E_Q = -1.08(1)$ mm/s, and an internal hyperfine field of $H_{int} = 152$ T (see Fig. 7.2).[27] For **1** an asymmetric quadrupole doublet is also observed at 295 K,

indicating the onset of slow paramagnetic relaxation on the Mössbauer timescale. At 5 K, the spectrum is a sharp sextet, and a fit yields H_{int} = 63.97(1) T. To account for the paramagnetic relaxation, the 295 K spectrum was fit with a relaxation profile with H_{int} = 63.97(1) T, yielding δ = 0.278(4) mm/s, ΔE_Q = –2.520(7) mm/s, and a relaxation time $\tau = 5.1(6) \times 10^{-11}$ s. These parameters are consistent with a change in oxidation state for the two-coordinate iron(I) ion and furthermore mirror similar trends observed in three-[47,48] and four-coordinate[49] iron(II/I) systems.

7.3.3. *Ab-Initio* Analysis. A ligand-field analysis of the results of *ab initio* calculations performed on **1** following methods described previously[31] provided the d-orbital splitting depicted in Fig. 1c (see also Table 7.S2 and Appendix A.5). The calculations demonstrate that the combination of a low coordination number and low oxidation state generates a very weak ligand field. This situation has important consequences for the electronic structure and magnetic properties of **1**: (i) a very strong 4s-3d_{z2} mixing is induced and (ii) an almost unquenched orbital momentum arises. Together, these two features are likely the origin of the relatively low *d* and large H_{int} observed in the Mössbauer spectra. Spin-orbit coupling (SOC) leads to a splitting of the ^{4}E ground state of **1** into four doublets that are best characterized by the quantum number M_J, where *J* refers to the total angular momentum of the system. In order of increasing energy, these doublets correspond to the quantum numbers $M_J = \pm^7/_2, \pm^5/_2, \pm^3/_2$, and $\pm^1/_2$ (see table 7.S2). The energy spacings between these doublets are approximately $^2/_3\ \zeta$, where ζ is the effective spin-orbit coupling constant (ζ = 361 cm^{-1} for a free iron(I) ion).

7.3.4. Static and Dynamic Magntic Properties. The variable-temperature dc magnetic susceptibility data for **1** collected under a 1 kOe applied dc field reveal non-Curie law behavior, consistent with a highly anisotropic magnetic moment (see Fig. 7.3). At 300 K, $\chi_M T$ = 3.39 cm^{3}K/mol, lower than the 4.80 cm^{3}K/mol observed for Fe(C(SiMe$_3$)$_3$)$_2$, yet significantly higher than the value of 1.875 cm^{3}K/mol expected for an isotropic $S = ^3/_2$ metal center. As the temperature is lowered, $\chi_M T$ increases to a maximum of 3.64 cm^{3}K/mol at 125 K, and then gradually decreases to 3.21 cm^{3}K/mol at 5.5 K before precipitously dropping to 0.18 cm^{3}K/mol at 2 K. The $\chi_M T$ data above 5.5 K are typical for transition metal complexes with first-order orbital angular momenta. Further, there is close agreement between the experimental data and the simulations on the basis of the electronic structure results (see Figs. 7.3, 7.S1).[30,31]

The large energy splittings of the M_J sublevels obtained from the *ab initio* calculations indicate that [Fe(C(SiMe$_3$)$_3$)$_2$]$^-$ should behave as a single-molecule magnet with a substantial energy barrier. As a direct probe of the relaxation dynamics, ac magnetic susceptibility measurements were performed on a microcrystalline sample of **1**. Variable-frequency, variable-temperature in-phase (χ_M') and out-of-phase (χ_M'') ac magnetic susceptibility data were collected under a 4 Oe ac field at frequencies (χ) of 0.1 to 1488 Hz from 9 to 29 K at zero applied dc field. As shown in Fig. 7.4, the maximum in the χ_M'' versus ν plot shifts to higher frequencies with increasing temperature until it moves beyond the high-frequency limit of the instrument at 29 K. At a given temperature, the ν at which a maximum occurs in χ_M'' corresponds to $\nu = (2\pi\tau)^{-1}$, where τ is the magnetic relaxation time. Thermally-activated spin-reversal[50] yields an exponential dependence of τ upon temperature: $\tau = \tau_0 \exp(U_{eff}/k_B T)$, where τ_0 is the attempt time, U_{eff} is the effective spin reversal barrier, and k_B is the Boltzmann constant. The resulting Arrhenius plot for **1** reveals a linear set of data from 20 to 29 K, indicating dominant spin relaxation via an Orbach mechanism (see Fig. 7.4). A linear fit to this regime yields U_{eff} = 226(4) cm^{-1} (325(6) K) and $\tau_0 = 1.3(3) \times 10^{-9}$ s. The former value is the largest relaxation barrier yet reported for single-molecule magnets containing either one (181 cm^{-1})[30] or multiple transition-

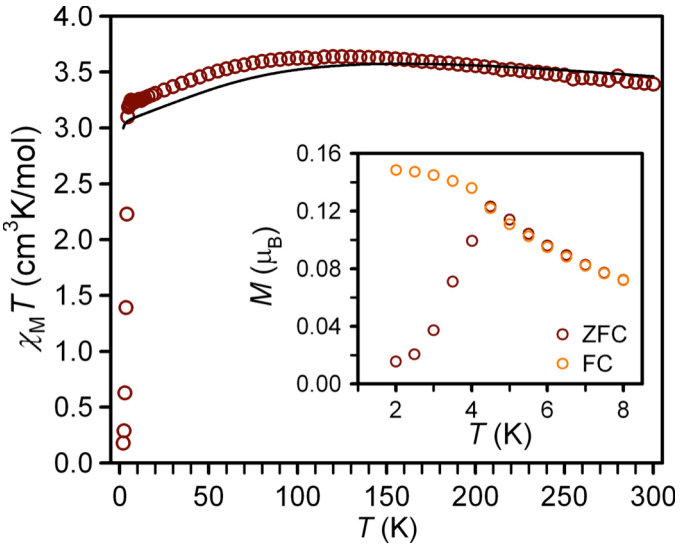


Figure 7.3. Variable-temperature molar magnetic susceptibility times temperature ($\chi_M T$) and field-cooled vs. zero-field cooled magnetization data**.** Data for a microcrystalline sample of **1** were collected under a 1 kOe applied dc field at temperatures from 2 to 300 K. The black line corresponds to a simulated set of susceptibility data utilizing the electronic structure determined computationally, as described in the main text. Inset: Low-temperature magnetization data highlighting a divergence at 4.5 K, indicative of magnetic blocking, which arises when the sample is cooled under a 1 kOe applied dc field (FC) compared to cooling under zero dc field (ZFC).

metal centers (67 cm^{-1}),[10] while τ_0 is within the range of 10^{-7} to 10^{-10} s expected for a molecular species.[3] Note that the value of U_{eff} is close to the calculated energy gap of 210 cm^{-1} between the the ground $M_J = {}^7/_2$ pair and the first excited doublet $M_J = {}^5/_2$, suggesting that the magnetic relaxation proceeds via this latter state. Below 20 K, τ deviates from an exponential temperature dependence, indicating the emergence of tunneling relaxation processes that short-cut the energy barrier.

A nearly discontinuous decrease in $\chi_M T$ at low temperature, as apparent in Fig. 7.3, can signify the blocking of the magnetic moments by a spin reversal barrier. In such a case, a difference will be apparent in magnetic susceptibility data collected upon cooling the sample with or without an applied dc field. Indeed, such a difference is observed for **1** below 4.5 K (see inset to Fig 7.3), indicating that the magnetic moments of **1** at these low temperatures are blocked from reorientation upon application of a 1 kOe dc field. This result further suggests that magnetic hysteresis should be apparent at these temperatures. Consistently, hysteresis is observed for $H \neq 0$ Oe, as demonstrated by variable-field magnetization data collected for a microcrystalline sample of **1** from 1.8 to 6.5 K under applied fields of up to 2 T (see Fig. 7.5). At zero field, however, the hysteresis loops collected at an average sweep rate of 50 Oe/s suddenly close, giving a waist-restricted shape. This feature is due to the presence of tunneling pathways for the magnetic relaxation, which, as indicated by the relaxation times obtained from the ac susceptibility data (see Fig. 7.4), can occur at zero field on a time-scale faster than the magnetic measurement.

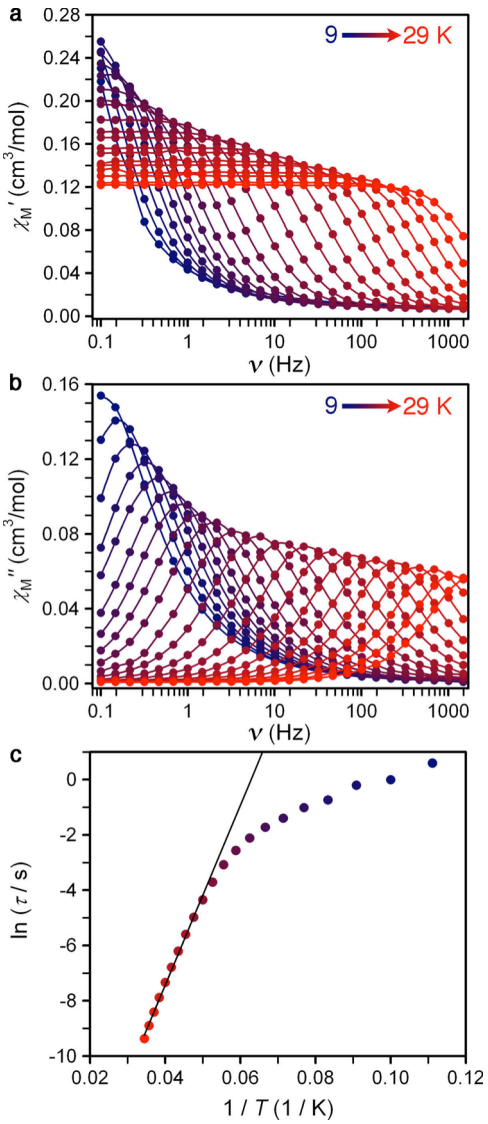


Figure 7.4. Dynamic magnetic data for **1.** Variable-temperature, variable-frequency in-phase (χ_M', **a**) and out-of-phase (χ_M'', **b**) components of the ac magnetic susceptibility data collected for **1** under zero applied dc field from 9 to 29 K. For a given temperature, a peak in χ_M'' indicates an energy barrier with respect to spin reversal. **c**. Arrhenius plot of the natural log of the relaxation time, τ, versus the inverse temperature. Standard deviations of the relaxation times were determined from a nonlinear least squares analysis using the program SolverAid (de Levie, R. *SolverAid (Version 7)* [Microsoft Excel Macro] (2007)); however, error bars are omitted as they are within the radius of the symbols. The black line corresponds to a fit of the data in the range 20-29 K to the Arrhenius expression $\tau = \tau_0 \exp(U_{eff}/k_B T)$, which affords $U_{eff} = 226(4)$ cm^{-1} (325(6) K) and $\tau_0 = 1.3(3) \times 10^{-9}$ s with $R^2 = 0.997$.

Among several possibilities,[51] intermolecular dipolar interactions have been implicated as facilitating tunneling in mononuclear transition metal,[24] lanthanide,[5,52,53] and actinide[43,54] single-molecule magnets. To probe this possibility, magnetic measurements were performed on frozen

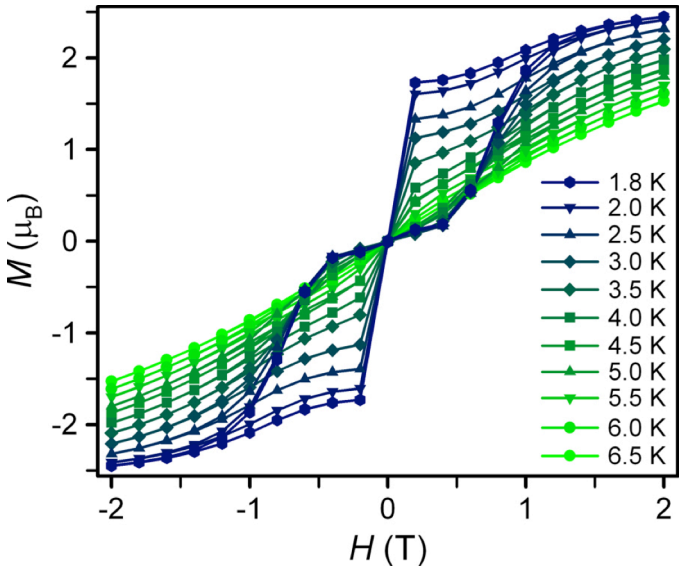


Figure 7.5. Plot of the magnetization (M) for **1** versus dc magnetic field (H). Data were collected at an average sweep rate of 50 Oe/s, by starting at $H = 0$ T, sweeping to $H = +2$ T, and then cycling to –2 T and back to +2 T. Data were obtained at 1.8 K first, and then collected with increasing temperature. Solid lines are guides for the eye. As the magnetic field is swept from 2 to −2 T and back, hysteretic behavior is clearly observed for $H_{dc} \neq 0$, indicating slow magnetic relaxation with relaxation times on the order of minutes for these fields. Waist-restricted magnetic hysteresis loops are observed for all data from 1.8 to 6.5 K owing to rapid tunneling once a measurement is taken at 0 T.

solutions of **1** in 2-methyltetrahydrofuran. The resulting ac magnetic susceptibility data reveal slowly relaxing magnetic moments completely analogous to the data obtained for microcrystalline samples (see Fig. 7.S4), offering proof of the molecular nature of the slow magnetization dynamics. Indeed, above 8 K, the temperature dependence of τ indicates a relaxation barrier for $[Fe(C(SiMe_3)_3)_2]^-$ in frozen solution that is identical to that observed in the crystals. For a 4 mM solution of **1**, the lowest concentration for which reliable data could be obtained, the relaxation times at low temperature are indeed somewhat slower than in the crystals, by as much as a factor of 2 at 10 K. There is, however, still a significant deviation from strict Arrhenius behavior at these low temperatures, indicating that dipolar interactions are not the sole facilitators of tunneling. It should be noted that geometric distortions in solution could also be a factor, as deviations from strict axial symmetry can induce mixing of the ground $M_J = \pm^7/_2$ levels and enable tunneling. Such an effect may also be operative to a lesser extent in the crystalline phase, given the slight deviation from linearity associated with the apparent C–Fe–C angle of 179.2(2)° and possible Renner-Teller vibronic activity reflected by the anisotropic thermal ellipsoids of the iron(I) ion. Magnetization data collected on the frozen solutions of **1** display waist-restricted hysteresis loops similar to those collected for the crystalline phase (see Fig. 7.S4). In this case, however, the loops remain slightly open at zero field, presumably due to the increased relaxation times observed upon elimination of dipolar effects.

7.4 Outlook and Conclusions

As exemplified with the linear iron(I) complex $[Fe(C(SiMe_3)_3)_2]^-$ (U_{eff} = 226 cm^{-1}), the foregoing results demonstrate that a two-coordinate transition metal complex with an odd electron count can behave as a single-molecule magnet with an extremely high spin reversal barrier in zero applied field. Importantly, the axial ligand field imposed at the transition metal center directs the ion toward a large magnetic anisotropy, leading to relaxation properties akin to those observed for lanthanide complexes, and suggesting that low-coordinate transition metal centers could potentially serve as replacements for lanthanides in hard permanent magnets. Future efforts will explore the effects of modifying the ligand field in related linear $S = {}^3/_2$ complexes, with particular emphasis on further enhancing magnetic anisotropy by bringing the d_{z2} orbital lower in energy and ensuring minimal quenching of the orbital angular momentum. In addition, we will investigate the possibility of mitigating tunneling pathways by engaging such metal centers in strong magnetic exchange interactions that create higher spin ground states, as recently demonstrated for lanthanide systems.[55,56]

7.5. Acknowledgements

This research was funded by the National Science Foundation through grant CHE-1010002. I thank Dianne J. Xiao, Annie T. Chantarojsiri, Gary J. Long, and Fernande Grandjean for assistance with acquisition and analyses of Mössbauer spectra. I also am grateful to Dr. Mihail Atanasov and Professor Frank Neese for lending their computational expertise to the analysis of $[Fe(C(SiMe_3)_3)_2]^-$. I thank Dr. Rita Nichiporuk for help collecting ESI/MS data. I thank Drs. Michael Nippe, Selvan Demir, and Meg Fasulo for fruitful discussions experimental assistance. I am also grateful to Professor J. R. Long for assistance throughout the study.

7.6. References and Notes

(1) Ishikawa, N.; Sugita, M.; Ishikawa, T.; Koshihara, S.-Y.; Kaizu, Y. *J. Am. Chem. Soc.* **2003**, *125*, 8694.
(2) Rinehart, J. D.; Long, J. R. *Chem. Sci.* **2011**, *2*, 2078.
(3) Gatteschi, D.; Sessoli, R.; Villain, J. *Molecular Nanomagnets*, Oxford University Press, Inc., New York, 2006.
(4) Branzoli, F.; Carretta, P.; Filibian, M.; Zoppellaro, G.; Graf, M. J.; Galan-Mascaros, J. R.; Fuhr, O.; Brink, S.; Ruben, M. *J. Am. Chem. Soc.* **2009**, *131*, 4387.
(5) Jiang, S.-D.; Wang, B.-W.; Sun, H.-L.; Wang, Z.-M.; Gao, S. *J. Am. Chem. Soc.* **2011**, *133*, 4730.

(6) Gonidec, M.; Biagi, R.; Corradini, V.; Moro, F.; De Renzi, V.; del Pennino, U.; Summa, D.; Muccioli, L.; Zannoni, C.; Amabilino, D. B.; Veciana, J. *J. Am. Chem. Soc.* **2011**, *133*, 6603.
(7) Sessoli, R.; Tsai, H. L.; Schake, A. R.; Wang, S.; Vincent, J. B.; Folting, K.; Gatteschi, D.; Christou, G.; Hendrickson, D. N. *J. Am. Chem. Soc.* **1993**, *115*, 1804.
(8) Sessoli, R.; Gatteschi, D.; Caneschi, A.; Novak, M. A. *Nature* **1993**, *365*, 141.
(9) Milios, C. J.; Vinslava, A.; Wernsdorfer, W.; Moggach, S.; Parsons, S.; Perlepes, S. P.; Christou, G.; Brechin, E. K. *J. Am. Chem. Soc.* **2007**, *129*, 2754.
(10) Yoshihara, D.; Karasawa, S.; Koga, N. *J. Am. Chem. Soc.* **2008**, *130*, 10460.
(11) Mannini, M.; Pineider, F.; Sainctavit, P.; Danieli, C.; Otero, E.; Sciancalepore, C.; Talarico, A. M.; Arrio, M.-A.; Cornia, A.; Gatteschi, D.; Sessoli, R. *Nature Mater.* **2009**, *8*, 194.
(12) Leuenberger, M. N.; Loss, D. *Nature* **2001**, *410*, 789.
(13) Ardavan, A.; Rival, O.; Morton, J. J. L.; Blundell, S. J.; Tyryshkin, A. M.; Timco, G. A.; Winpenny, R. E. P. *Phys. Rev. Lett.* **2007**, *98*, 057201.
(14) Stamp, P. C. E.; Gaita-Ariño, A. *J. Mater. Chem.* **2009**, *19*, 1718.
(15) Bogani, L.; Wernsdorfer, W. *Nat. Mater.* **2008**, *7*, 179.
(16) Atanasov, M.; Ganyushin, D.; Pantazis, D. A.; Sivalingam, K.; Neese, F. *Inorg. Chem.* **2011**, *50*, 7460.
(17) Freedman, D. E. *et al. J. Am. Chem. Soc.* **2010**, *132*, 1224.
(18) Harman, W. H.; Harris, T. D.; Freedman, D. E.; Fong, H.; Chang, A.; Rinehart, J. D.; Ozarowski, A.; Sougrati, M. T.; Grandjean, F.; Long, G. J.; Long, J. R.; Chang, C. J. *J. Am. Chem. Soc.* **2010**, *132*, 18115.
(19) Weismann, D.; Sun, Y.; Lan, Y.; Wolmerhäuser, G.; Powell, A. K.; Sitzmann, H. *Chem. Eur. J.* **2011**, *17*, 4700.
(20) Lin, P.-H.; Smythe, N. C.; Gorelsky, S. I.; Maguire, S.; Henson, N. J.; Korobkov, I.; Scott, B. L.; Gordon, J. C.; Baker, R. T.; Murugesu, M. *J. Am. Chem. Soc.* **2011**, *133*, 15806.
(21) Jurca, T.; Farghal, A.; Lin, P.-H.; Korobkov, I.; Murugesu, M.; Richeson, D. S. *J. Am. Chem. Soc.* **2011**, *133*, 15814.
(22) Vallejo, J.; Castro, I.; Ruiz-Garcia, R.; Cano, J.; Julve, M.; Lloret, F.; De Munno, G.; Wernsdorfer, W.; Pardo, E. *J. Am. Chem. Soc.* **2012**, *134*, 15704.
(23) Kramers, H. A. *Proc. R. Acad. Sci. Amsterdam* **1930**, *33*, 959.
(24) Zadrozny, J. M.; Long, J. R. *J. Am. Chem. Soc.* **2011**, *133*, 20732.
(25) Mossin, S.; Tran, B. L.; Adhikari, D.; Pink, M.; Heinemann, F. W.; Sutter, J.; Szilagyi, R. K.; Meyer, K.; Mindiola, D. J. *J. Am. Chem. Soc.* **2012**, *134*, 13651.
(26) Power, P. P. *Chem. Rev.* **2012**, *112*, 3482.
(27) Reiff, W. M.; LaPointe, A. M.; Witten, E. H. *J. Am. Chem. Soc.* **2004**, *126*, 10206.
(28) Reiff, W. M.; Schulz, C. E.; Whangbo, M.-H.; Seo, J. I.; Lee, Y. S.; Potratz, G. R.; Spicer, C. W.; Girolami, G. S. *J. Am. Chem. Soc.* **2009**, *131*, 404.
(29) Merrill, W. A.; Stich, T. A.; Brynda, M.; Yeagle, G. J.; Fettinger, J. C.; de Hont, R.; Reiff, W. M.; Schulz, C. E.; Britt, R. D.; Power, P. P. *J. Am. Chem. Soc.* **2009**, *131*, 12693.
(30) Zadrozny, J. M.; Atanasov, M.; Bryan, A. M.; Lin, C.-Y.; Rekken, B. D.; Power, P. P.; Neese, F.; Long, J. R. *Chem. Sci.* **2013**, *4*, 125.
(31) Atanasov, M. A.; Zadrozny, J. M.; Long, J. R.; Neese, F. *Chem. Sci.* **2013**, *4,* 139.

(32) (*a*) Bergbreiter, D. E.; Killough, J. M. *J. Am. Chem. Soc.* **1978**, *100*, 2126. (*b*) Evans, W. J.; Kozimor, S. A.; Ziller, J. W.; Kaltsoyannis, N. *J. Am. Chem. Soc.* **2004**, *126*, 14533.
(33) LaPointe, A. M. *Inorg. Chim. Acta.* **2003**, *345*, 359.
(34) *APEX2*, v. 2009 ; Bruker Analytical X-Ray Systems, Inc: Madison, WI, 2009.
(35) Sheldrick, G. M., *SADABS*, Version 2.03; Bruker Analytical X-Ray Systems, Inc.: Madison, WI, 2000.
(36) Altomare, A.; Burla, M. C.; Camalli, M.; Cascarano, G. L.; Giacovazzo, C.; Guagliardi, A.; Moliterni, A. G. G.; Polidori, G.; Spagna, R. *J. Appl. Cryst.* **1999**, *32*, 115.
(37) Sheldrick, G. M., *SHELXTL*, Version 6.12; Bruker Analytical X-ray Systems, Inc.: Madison, WI, 2000
(38) Farrugia, L. J. *J. Appl. Cryst.* **1999**, *32*, 837.
(39) Neese, F.; Wennmohs, F., *Orca; version 2.8*, An *ab initio*, DFT, and semiempirical SCF-MO package with contributions from U. Becker, D. Ganyushin, A. Hansen, D. G. Liakos, C. Kollmar, S. Kossman, T. Petrenko, C. Reimann, C. Riplinger, K. Sivalingam, E. Valeev, & B. Wezisla, Lehrstuhl fur theoretische Chemie, Bonn, Germany, 2010.
(40) Atanasov, M.; Ganyushin, D.; Sivalingam, K.; Neese, F. *Struct. Bond.* **2012**, *143,* 149.
(41) Atanasov, M.; Zadrozny, J. M.; Long, J. R.; Neese, F. *Chem. Sci.* **2013**, *4*, 139.
(42) Eaborn, C.; Hitchcock, P. B.; Smith, J. D.; Sullivan, A. C. *J. Chem. Soc., Chem. Commun.* **1983**, 827.
(43) Eaborn, C.; Hitchcock, P. B.; Smith, J. D.; Sullivan, A. C. *J. Organomet. Chem.* **1984**, *263*, C23.
(44) Eaborn, C.; Hitchcock, P. B.; Smith, J. D.; Sullivan, A. C. *J. Chem. Soc., Chem. Commun.* **1984**, 870.
(45) Al-Juaid, S. S.; Eaborn, C.; Hitchcock, P. B.; Izod, K.; Mallien, M.; Smith, J. D. *Angew. Chem. Int. Ed.* **1994**, *33*, 1268.
(46) LaPointe, A. M. *Inorg. Chim. Acta.* **2003**, *345*, 359.
(47) Stoian, S. A.; Yu, Y.; Smith, J. M.; Holland, P. L.; Bominaar, E. L.; Münck, E. *Inorg. Chem.* **2005**, *44*, 4915.
(48) Yu, Y.; Sadique, A. R.; Smith, J. M.; Dugan, T. R.; Cowley, R. E.; Brennessel, W. W.; Flaschenriem, C. J.; Bill, E.; Cundari, T. R.; Holland, P. L. *J. Am. Chem. Soc.* **2008**, *130*, 6624.
(49) Nakajima, Y.; Nakao, Y.; Sakako, S.; Tamada, Y.; Ono, T.; Ozawa, F. *J. Am. Chem. Soc.* **2010**, *132*, 9934.
(50) Carlin, R. *Magnetochemistry* (Springer-Verlag, Berlin, 1986).
(51) Gatteschi, D.; Sessoli, R. *Angew. Chem. Int. Ed.* **2003**, *42*, 268.
(52) Luis, F.; Martínez-Pérez, M. J.; Montero, O.; Coronado, E.; Cardona-Serra, S.; Martí-Gastaldo, C.; Clemente-Juan, J. M.; Sesé, J.; Drung, D.; Schurig, T. *Phys. Rev. B.* **2010**, *82*, 060403(R).
(53) Meihaus, K. R.; Rinehart, J. D.; Long, J. R. *Inorg. Chem.* **2011**, *50*, 8484.
(54) Rinehart, J. D.; Long, J. R. *Dalton Trans.* **2012**, *41*, 13572.
(55) Rinehart, J. D.; Fang, M.; Evans, W.; Long, J. R. *Nat. Chem.* **2011**, *3*, 538.
(56) Demir, S.; Zadrozny, J. M.; Nippe, M.; Long, J. R. *J. Am. Chem. Soc.* **2012**, *134*, 18546.

Table 7.S1. Crystal data for structure refinement of **1**.

Empirical Formula	$C_{38}H_{90}FeKN_2O_6Si_6$
Formula weight	934.61 g/mol
Temperature	100(2) K
Wavelength	0.71069 Å
Crystal System	Triclinic
Space Group	*P*–1
Unit Cell Dimensions	a = 12.809(5) Å, α = 63.410(5)°
	b = 15.271(5) Å, β = 79.118(5)°
	c = 15.651(5) Å, γ = 77.807(5)°
Volume	2660.3(16) Å^3
Z	2
Density (calculated)	1.167 Mg/m^3
Absorption coefficient	0.536 mm^{-1}
F_{000}	1018
Crystal color	Yellow-green
Crystal size	0.26 × 0.15 × 0.13 mm^3
θ range	2.51 to 26.06°
Index ranges	$-15 \le h \le 15$
	$-18 \le k \le 17$
	$-19 \le l \le 19$
Reflections collected	10551
Independent reflections	7215 [R_{int} = 0.0525]
Completeness to θ = 26.06°	99.3 %
Absorption correction	Multi-scan
Maximum and minimum transmission	0.8610 and 0.7478
Refinement method	Full-matrix least-squares on F^2
Data / restraints / parameters	9887 / 89 / 481
Goodness-of-fit on F^{2a}	1.088
Final R indices [I > 2σ(I) = 9887 data]^b	R_1 = 6.22 %, wR_2 = 13.85 %
R indices (all data, 0.80 Å)	R_1 = 9.67 %, wR_2 = 15.59 %
Largest diff. peak and hole	0.734 and –0.792 e.Å^{-3}

[a] GooF = $[\Sigma[w(F_o^2-F_c^2)^2] / (n-p)]^{1/2}$ where n is the number of reflections and p is the total number of parameters refined. [b] $R_1 = \Sigma||F_o|-|F_c|| / \Sigma|F_o|$; $wR_2 = [\Sigma[w(F_o^2-F_c^2)^2] / \Sigma[w(F_o^2)^2]]^{1/2}$

Table 7.S2. **a**. Energies (in cm^{-1}) of $S = {}^3/_2$ states and **b**. of the spin-orbit split components of the lowest ^4E state from CASSCF and NEVPT2 calculations of $[Fe(C(SiMe_3)_3)_2]^-$ with a geometry from X-ray diffraction data and accounting for the complete set of the 5 quintet and 45 triplet electronic states

	Electronic State[a]	*CASSCF*	*NEVPT2*	Configuration state function (%)
a	^4E	0	0	54 $d_{xy}d_{yz}d_{xz}$; 46 $d_{x2-y2}d_{yz}d_{xz}$
		27.8	49.0	46 $d_{xy}d_{yz}d_{xz}$; 54 $d_{x2-y2}d_{yz}d_{xz}$
	^4E	2676.4	3970.3	41 $d_{xy}d_{x2-y2}d_{yz}$; 21 $d_{xy}d_{yz}d_{z2}$; 21 $d_{x2-y2}d_{xz}d_{z2}$
		2742.6	4066.2	41 $d_{xy}d_{x2-y2}d_{xz}$; 21 $d_{xy}d_{xz}d_{z2}$; 21 $d_{x2-y2}d_{yz}d_{z2}$
	^4E	3119.7	5614.5	31 $d_{xy}d_{yz}d_{z2}$; 33 $d_{x2-y2}d_{xz}d_{z2}$; 18 $d_{xy}d_{xz}d_{z2}$; 14 $d_{x2-y2}d_{yz}d_{z2}$
		3171.6	5722.4	34 $d_{x2-y2}d_{yz}d_{z2}$; 33 $d_{xy}d_{xz}d_{z2}$; 18 $d_{x2-y2}d_{xz}d_{z2}$; 14 $d_{xy}d_{yz}d_{z2}$
	$^4A_1$	4353.5	6526.2	64 $d_{xy}d_{x2-y2}d_{z2}$; 31 $d_{yz}d_{xz}d_{z2}$
	^4E	16515.8	14344.5	43 $d_{xy}d_{x2-y2}d_{xz}$; 22 $d_{xy}d_{xz}d_{z2}$; 22 $d_{x2-y2}d_{yz}d_{z2}$
		16608.1	14442.5	44 $d_{xy}d_{x2-y2}d_{yz}$; 22 $d_{xy}d_{yz}d_{z2}$; 21 $d_{x2-y2}d_{xz}d_{z2}$
	$^4A_1$	17610.9	16239.5	67 $d_{yz}d_{xz}d_{z2}$; 33 $d_{xy}d_{x2-y2}d_{z2}$

b	E(1) ($M_J = \pm {}^7/_2$)	0	0
	E(2) ($M_J = \pm {}^5/_2$)	198.7	210.1
	E(3) ($M_J = \pm {}^3/_2$)	434.9	452.0
	E(4) ($M_J = \pm {}^1/_2$)	703.3	710.4

[a]Based on analysis using wavefunctions from an average over the 10 $S = {}^3/_2$ CASSCF calculation. Only composition of electronic states from different electronic configurations which exceed 10 % and only singly occupied d-orbitals are listed; non-listed are the other two doubly-occupied d-orbitals for each configuration state function, e.g. $d_{xy}d_{yz}d_{xz}$ implies a $|d_{xy}^1d_{yz}^1d_{xz}^1d_{x2-y2}^2d_{z2}^2|$ configuration state function.

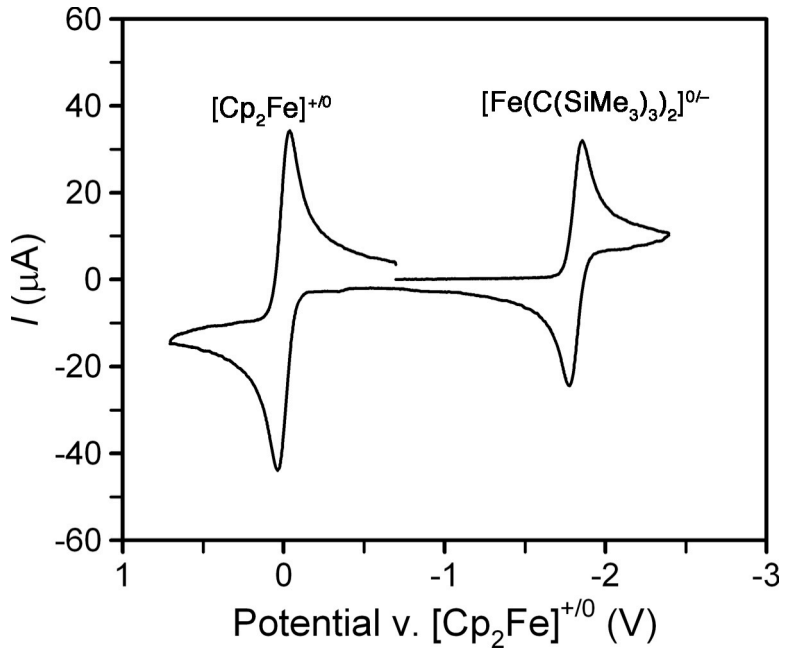


Figure 7.S1. Cyclic voltammogram of **1** in difluorobenzene solution at 298 K. Data were obtained with a platinum wire counter electrode, a silver sire reference electrode, and a glassy carbon working electrode and a scan rate of 100 mV/s.

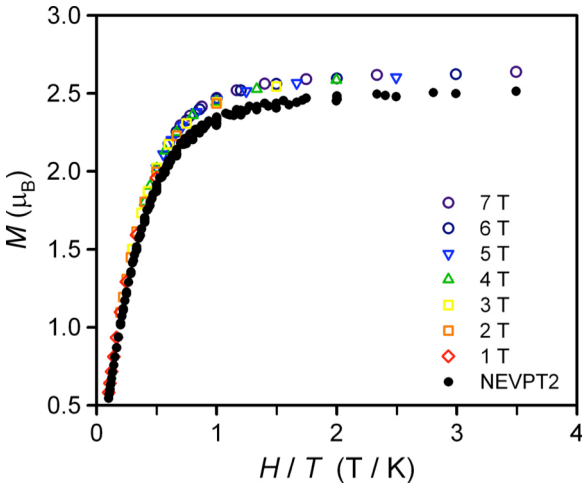


Figure 7.S2. Variable-temperature variable-field reduced magnetization data for **1.** Data were collected from 10 K to 2 K, cooling under an applied field of the given strength. Near-superimposability of the isofield lines typically indicates negligible magnetic anisotropy. Here, we see that they can also signify very large magnetic anisotropy. Reasonable agreement is observed between the data and simulated isofield lines with the electronic structure as detailed in the main text and Table 7.S2.

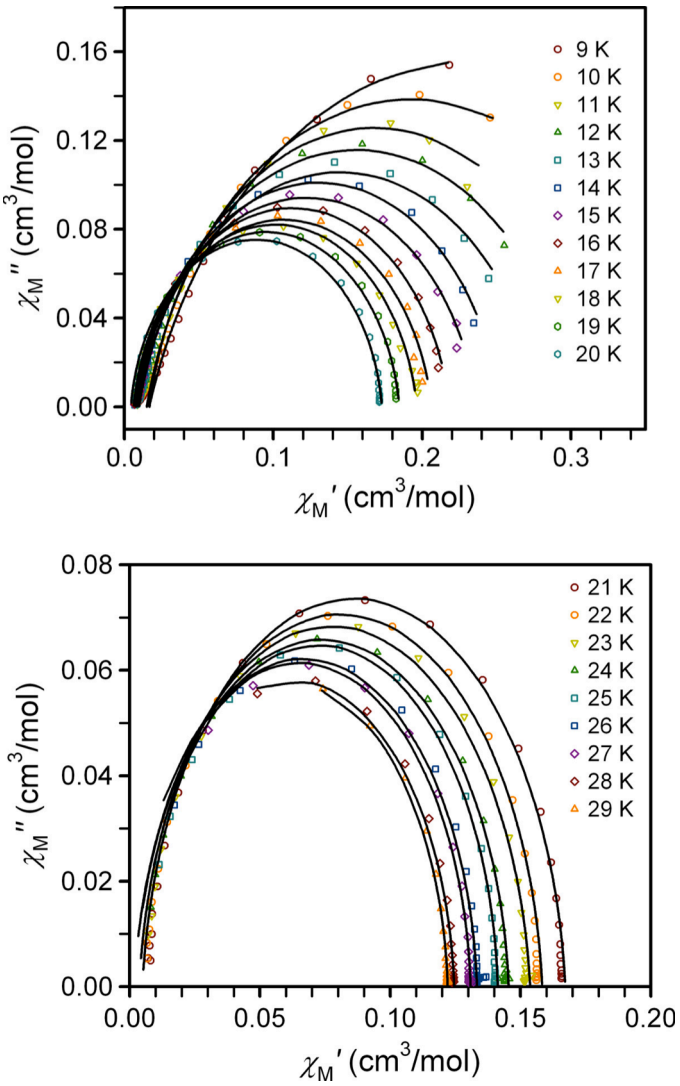


Figure 7.S3. Variable-temperature Cole-Cole plots for **1.** Top: data collected from 9 to 20 K. Bottom: data collected from 21 to 29 K. All data were collected under a 0 Oe applied dc field. Black lines represent fits to the data as detailed in the main text and the magnetic measurements experimental section.

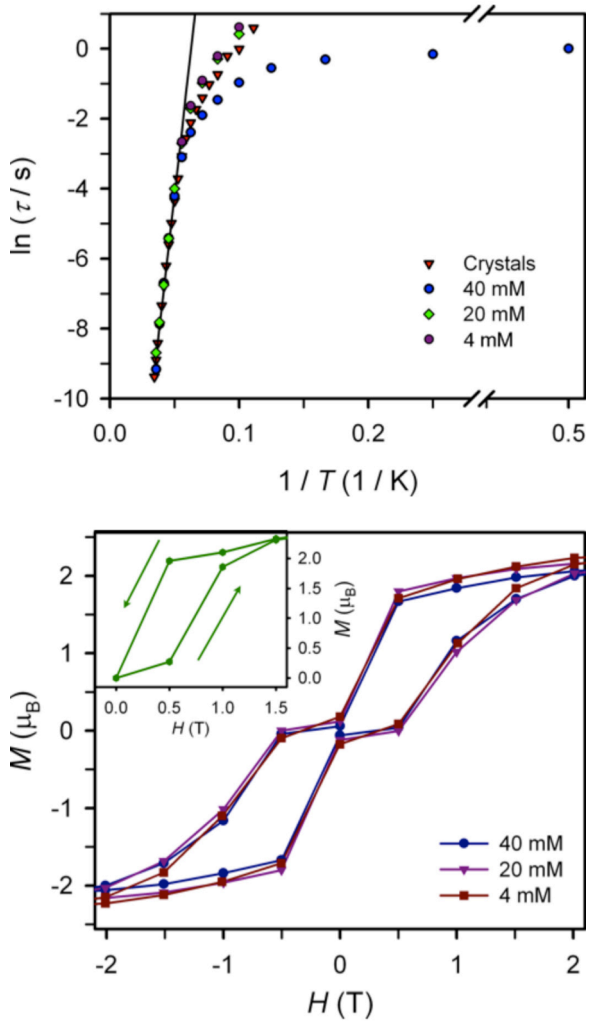


Figure 7.S4. **Top:** Variable-temperature relaxation time data for 40, 20, and 4 mM solutions of **1** in 2-methyltetrahydrofuran. The black line represents the expected temperature dependence of the magnetic relaxation time for an Orbach process with U_{eff} = 226 cm^{-1} and $\tau_0 = 1.3 \times 10^{-9}$ s . Slowing of the magnetic relaxation time at low temperature is attributed to a disruption of intermolecular dipole-dipole interactions which make magnetic relaxation facile. **Bottom:** Variable-field magnetization data collected on 40, 20, and 4 mM frozen solutions of **1** in 2-methyltetrahydrofuran. The average dc field sweep rate for data collection was 70 Oe/s. Inset: Demagnetization curve for crystalline **1** collected at an average 70 Oe/s field sweep rate. Green arrows indicate order of data acquisition, starting at H_{dc} = 0 T. Note the superimposability of the zero field data for crystalline **1** as opposed to the solution data.

Appendix 1: Additional Crystallographic Data for Chapter 2.

Table A1.1. Crystallographic Data[a] for $[(PY5Me_2)Co(MeCN)](PF_6)_2$ (**4**).

Empirical formula	$C_{72}H_{75}Co_2F_{24}N_{15}OP_4$
Formula weight	1864.189
T, K	140(2)
λ, Å	0.71703
Crystal system	Monoclinic
Space group	$P\,2_1/c$
a, Å	22.419(2)
b, Å	15.2490(13)
c, Å	24.564(2)
α, °	90
β, °	107.777(2)
γ, °	90
V, Å^3	7996.7(12)
Z	4
$\rho_{calculated}$, g/cm^3	1.516
μ, mm^{-1}	0.609
F_{000}	3797
Crystal dimensions	0.32 × 0.31 × 0.25 mm^3
θ range	2.15 to 20.82°
Index ranges	$-17 \le h \le 22$
	$-15 \le k \le 15$
	$-24 \le l \le 19$
Reflections collected	27405
Independent reflections	8345 [R_{int} = 0.0677]
Completeness to θ = 20.82°	99.70%
Data / restraints / parameters	8345 / 0 / 1100
Goodness-of-fit on F^2	1.055
Final R indices [$I > 2\sigma(I)$][b]	R_1 = 0.0574, wR_2 = 0.1390
R indices (all data)	R_1 = 0.1055, wR_2 = 0.1620
Largest diff. peak and hole	0.771 and –0.593 eÅ^{-3}

[a]Obtained with graphite-monochromated Mo Kα (λ = 0.71073 Å) radiation. [b]$R_1 = \Sigma||F_o| - |F_c||/\Sigma|F_o|$, $wR_2 = \{\Sigma[w(F_o^2 - F_c^2)^2]/\Sigma[w(F_o^2)^2]\}^{1/2}$.

Table A1.2. Crystallographic Data[a] for $[(PY5Me_2)Ni(MeCN)](PF_6)_2$ (**5**).

Empirical formula	$C_{72}H_{75}F_{24}N_{15}Ni_2OP_4$
Formula weight	1863.709
T, K	140(2)
λ, Å	0.71703
Crystal system	Monoclinic
Space group	$P\ 2_1/c$
a, Å	22.369(5)
b, Å	15.229(3)
c, Å	24.496(5)
α, °	90
β, °	107.777(4)
γ, °	90
V, Å^3	7946(3)
Z	4
$\rho_{calculated}$, g/cm^3	1.396
μ, mm^{-1}	0.655
F_{000}	3384
Crystal dimensions	0.34 × 0.24 × 0.18 mm^3
θ range	1.60 to 20.88°
Index ranges	$-22 \le h \le 22$ $-15 \le k \le 15$ $-24 \le l \le 24$
Reflections collected	30902
Independent reflections	8347 [R_{int} = 0.0591]
Completeness to θ = 20.88°	99.60%
Data / restraints / parameters	8347 / 0 / 1100
Goodness-of-fit on F^2	1.206
Final R indices [$I > 2\sigma(I)$][b]	R_1 = 0.0572, wR_2 = 0.1431
R indices (all data)	R_1 = 0.0866, wR_2 = 0.1560
Largest diff. peak and hole	0.780 and –0.454 eÅ^{-3}

[a]Obtained with graphite-monochromated Mo Kα (λ = 0.71073 Å) radiation. [b]$R_1 = \Sigma||F_o| - |F_c||/\Sigma|F_o|$, $wR_2 = \{\Sigma[w(F_o^2 - F_c^2)^2]/\Sigma[w(F_o^2)^2]\}^{1/2}$.

Table A1.3. Crystallographic Data[a,c] for [(PY5Me$_2$)Cu(MeCN)](PF$_6$)$_2$ (**6**).

Empirical formula	$C_{62}H_{56}Cu_2F_{24}N_{12}P_4$
Formula weight	1712.169
T, K	159(2)
λ, Å	0.71703
Crystal system	Triclinic
Space group	$P\,1$
a, Å	11.4070(6)
b, Å	12.7561(7)
c, Å	13.1823(7)
α, °	68.7890(10)
β, °	70.0600 (10)
γ, °	89.6880(10)
V, Å^3	1665.70(15)
Z	2
$\rho_{calculated}$, g/cm^3	1.671
μ, mm^{-1}	0.854
F_{000}	846
Crystal dimensions	0.30 × 0.26 × 0.07 mm^3
θ range	2.09 to 26.35°
Index ranges	$-11 \le h \le 14$
	$-9 \le k \le 15$
	$-13 \le l \le 16$
Reflections collected	10748
Independent reflections	7872 [R_{int} = 0.0390]
Completeness to θ = 25.41°	97.40%
Data / restraints / parameters	7872 / 3 / 938
Goodness-of-fit on F^2	0.948
Final R indices [$I > 2\sigma(I)$][b]	R_1 = 0.0353, wR_2 = 0.0804
R indices (all data)	R_1 = 0.0411, wR_2 = 0.0816
Largest diff. peak and hole	0.478 and –0.460 eÅ^{-3}

[a]Obtained with graphite-monochromated Mo Kα (λ = 0.71073 Å) radiation. [b]$R_1 = \Sigma||F_o| - |F_c||/\Sigma|F_o|$, $wR_2 = \{\Sigma[w(F_o^2 - F_c^2)^2]/\Sigma[w(F_o^2)^2]\}^{1/2}$. [c]Refinement of a twin component was accomplished via inclusion of the twin law [−1 0 0 0 −1 0 0 0 −1]. The final twin parameter refined to 0.5.

Table A1.4. Crystallographic Data[a] for $[(PY5Me_2)_4Co_4Re(CN)_7](PF_6)_5$ (**7**).

Empirical formula	$C_{133}H_{100}Co_4F_{30}N_{27}P_5Re$
Formula weight	3103.07
T, K	150(2)
λ, Å	0.71073
Crystal system	Monoclinic
Space group	C 2/c
a, Å	44.679(10)
b, Å	18.870(4)
c, Å	41.036(9)
α, °	90
β, °	107.277(3)
γ, °	90
V, Å^3	33036(13)
Z	8
$\rho_{calculated}$, g/cm^3	1.148
μ, mm^{-1}	1.253
F_{000}	12440
Crystal dimensions	0.48 × 0.18 × 0.12 mm^3
θ range	1.35 to 22.46°
Index ranges	$-32 \le h \le 48$ $-20 \le k \le 20$ $-44 \le l \le 38$
Reflections collected	67753
Independent reflections	21480 [R_{int} = 0.1107]
Completeness to θ = 22.46°	99.90%
Data / restraints / parameters	21480 / 411 / 913
Goodness-of-fit on F^2	1.047
Final R indices [$I > 2\sigma(I)$][b]	R_1 = 0.1022, wR_2 = 0.2607
R indices (all data)	R_1 = 0.1519, wR_2 = 0.2821
Largest diff. peak and hole	1.506 and –1.140 eÅ^{-3}

[a]Obtained with graphite-monochromated Mo Kα (λ = 0.71073 Å) radiation. [b]$R_1 = \Sigma||F_o| - |F_c||/\Sigma|F_o|$, $wR_2 = \{\Sigma[w(F_o^2 - F_c^2)^2]/\Sigma[w(F_o^2)^2]\}^{1/2}$. . [c]The poor quality of the data precluded anisotropic refinement of all atoms in the main body of this structure. All atoms were therefore modeled isotropic with the following exceptions: Re, Co, PF_6^- counterions not included in our disorder model. When necessary, PF_6^- counterions were constrained to ideal octahedral geometry. Disorder of PF_6^- counterions was modeled with the use of partial occupancies. We implemented SQUEEZE after we were unable to successfully model the disordered solvent within the structure. Importantly, we note that changes to both our solvent and counterion disorder models did not significantly change the main $[(PY5Me_2)_4Co_4Re(CN)_7]^{5+}$ moiety.

Table A1.5. Crystallographic Data[a,c] for $[(PY5Me_2)_4Ni_4Re(CN)_7](PF_6)_5$ (**8**)..

Empirical formula	$C_{133}H_{119}F_{30}N_{30}Ni_4OP_5Re$
Formula weight	3299.37
T, K	100(2)
λ, Å	1.54178
Crystal system	Triclinic
Space group	P –1
a, Å	12.0290(6)
b, Å	19.9232(9)
c, Å	32.0482(13)
α, °	80.202(3)
β, °	89.201(3)
γ, °	73.901(3)
V, Å^3	7267.2(60)
Z	2
$\rho_{calculated}$, g/cm^3	1.466
μ, mm^{-1}	3.479
F_{000}	3227
Crystal dimensions	0.15 × 0.06 × 0.04 mm^3
θ range	1.40 to 68.28°
Index ranges	$-14 \le h \le 14$
	$-15 \le k \le 22$
	$-37 \le l \le 38$
Reflections collected	70482
Independent reflections	24635 [R_{int} = 0.0699]
Completeness to θ = 68.28°	92.40%
Data / restraints / parameters	24635 / 166 / 1818
Goodness-of-fit on F^2	1.203
Final R indices [$I > 2\sigma(I)$][b]	R_1 = 0.0628, wR_2 = 0.1461
R indices (all data)	R_1 = 0.0809, wR_2 = 0.1528
Largest diff. peak and hole	1.809 and –1.299 eÅ^{-3}

[a]Obtained with graphite-monochromated Mo Kα (λ = 0.71073 Å) radiation. [b]$R_1 = \Sigma||F_o| - |F_c||/\Sigma|F_o|$, $wR_2 = \{\Sigma[w(F_o^2 - F_c^2)^2]/\Sigma[w(F_o^2)^2]\}^{1/2}$. [c]Given the $Ni^{II}_4Re^{IV}$ configuration of the cluster as dictated by magnetic measurements, 5 PF_6^- counterions are required in the structure. Given the 6 PF_6^- moieties located in the structure, we modeled some of them at partial occupancies with the use of free variables. Significant disorder of solvents of crystallization was impossible to model. SQUEEZE was implemented to account for these regions of electron density. We note that prior to the use of SQUEEZE, changes to our models of solvent and counterion disorder had little affect on the structure of the $[(PY5Me_2)_4Ni_4Re(CN)_7]^{5+}$ moiety.

Table A1.6. Crystallographic Data[a,c] for $[(PY5Me_2)_4Cu_4Re(CN)_7](PF_6)_4$ (**9**).

Empirical formula	$C_{123}H_{100}Cu_4F_{24}N_{27}Ni_4P_4Re$
Formula weight	2976.539
T, K	141(2)
λ, Å	0.71703
Crystal system	Triclinic
Space group	$P\,\bar{1}$
a, Å	18.7657(10)
b, Å	19.3343(10)
c, Å	22.5562(12)
α, °	113.0980(10)
β, °	97.2190(10)
γ, °	110.3760(10)
V, Å^3	6722.5(6)
Z	2
$\rho_{calculated}$, g/cm^3	1.542
μ, mm^{-1}	1.679
F_{000}	3126
Crystal dimensions	0.22 × 0.15 × 0.03 mm^3
θ range	1.03 to 25.41°
Index ranges	$-22 \le h \le 22$
	$-23 \le k \le 23$
	$-26 \le l \le 27$
Reflections collected	70338
Independent reflections	24454 [R_{int} = 0.0671]
Completeness to θ = 25.41°	98.60%
Data / restraints / parameters	24454 / 0 / 1648
Goodness-of-fit on F^2	0.921
Final R indices [$I > 2\sigma(I)$][b]	R_1 = 0.0503, wR_2 = 0.1021
R indices (all data)	R_1 = 0.0815, wR_2 = 0.1143
Largest diff. peak and hole	1.081 and –0.653 eÅ^{-3}

[a]Obtained with graphite-monochromated Mo Kα (λ = 0.71073 Å) radiation. [b]$R_1 = \Sigma||F_o| - |F_c||/\Sigma|F_o|$, $wR_2 = \{\Sigma[w(F_o^2 - F_c^2)^2]/\Sigma[w(F_o^2)^2]\}^{1/2}$. [c]In contrast to the previous M_4Re clusters, only 4 PF_6^- counterions were located in the difference Fourier map for this crystal structure. Severely disordered solvent molecules within the structure were accounted for using the SQUEEZE function. We note that prior to the use of SQUEEZE, changes in solvent disorder models did not change the main $[(PY5Me_2)_4Cu_4Re(CN)_7]^{4+}$ body.

Appendix 2: Additional EPR Interpretive Details for Chapter 3.

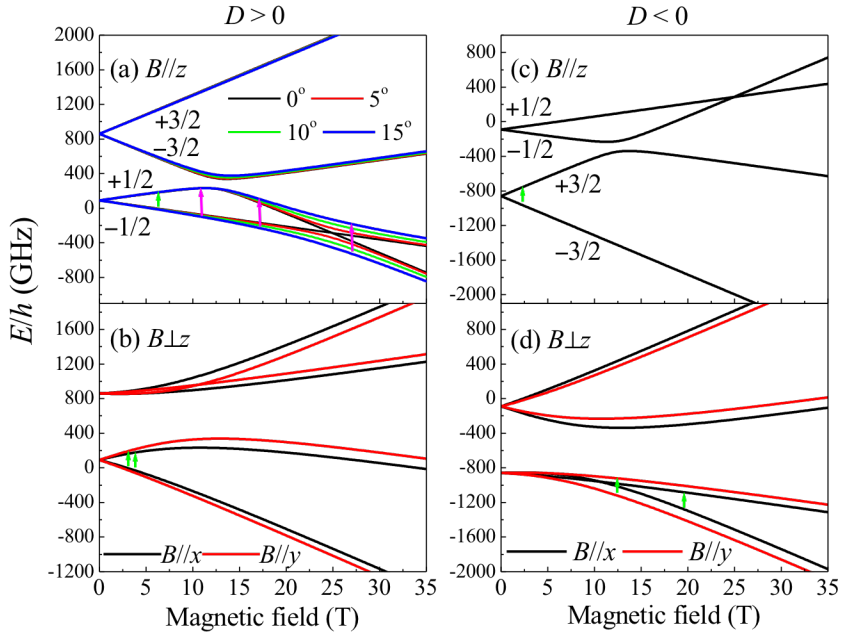


Figure A2.1. Simulations of the field parallel ($B//z$) and perpendicular ($B\perp z$) Zeeman diagrams of **1** for the two cases $D > 0$ [(a) and (b)] and $D < 0$ [(c) and (d)]. The employed Hamiltonian and the magnitudes of the parameters used in these simulations are given in the main text; (a) corresponds exactly to the lower inset to Fig. 3.2 in the main article, with the different curves representing successive 5^{o} misalignments of the applied field away from the parallel (z) orientation (black curve). The green vertical arrows correspond to allowed excitations of ~200 GHz from the ground state, thus denoting the locations of components of the low-temperature powder spectrum, i.e., one parallel component ($B//z$) and two perpendicular components ($B//x$ and $B//y$) which are split as a consequence of the rhombic E term. The vertical magenta arrows in (a) correspond to allowed excitations of ~330 GHz from the ground state, illustrating the three low-temperature resonances observed in Fig. 3.S3.

As can be seen in Fig. A2.1, panels (a) and (b) reproduce all of the features of the experiments remarkably well (see also Fig. 3.2 in Chapter 3). Although panels (c) and (d) were obviously generated using parameters optimized for the easy-plane ($D > 0$) case, they clearly illustrate the incompatibility of the easy-axis scenario. Indeed, it is impossible to find a set of physically realistic parameters that comes close to the experimental observations. For example, to reproduce the powder results would require both a significant reduction in the magnitude of D and an unphysical E ($> |D|/3$) parameter. Furthermore, although it is possible to produce a spectrum consisting of three ground state resonances for the $D < 0$, $B//x$ case, it again involves unphysical parameters that are also completely at odds with the magnetic measurements. Finally, we remark on the fact that the parameters obtained for the easy-plane case are rather well constrained by the combined multi-frequency powder and single-crystal EPR measurements. The powder measurements constrain the g tensor and E to some extent (though there is

interdependence of these terms), but are highly insensitive to D. On the other hand, the single-crystal measurements separately constrain D and E very well: D primarily determines the field location (~14 T) of the avoided crossing between the $m_S = +^1/_2$ and $-^3/_2$ states, while E determines the magnitude of the gap at the avoided crossing. Meanwhile, neither of these features is particularly sensitive to the field misalignment. Consequently, the location of the maximum at ~14 T in the main panel of Fig. 3.2 constrains D, while the curvature at this maximum determines E; it is the minimum at ~22 T that necessitates the 15° of field misalignment. Combining these results with the powder measurements then provides a stronger constraint on the g tensor. Overall, the obtained parameter set is quite reasonable for pseudo-tetrahedrally coordinated Co^{II}. Finally, we note also that the frequency dependence of the line widths and line shapes is in good accord with the simulations. In the vicinity of the avoided crossing at ~14 T and ~22 T, the dependence of the resonance frequencies on the applied field becomes very weak and non-linear. Thus, the curved positions on the blue simulation in Fig. 3.2 produce broad resonance, in contrast to the linear regions at high and low fields.

Appendix 3: Supplementary Information for Chapter 5.

Additional Magnetic Susceptibility Fitting Details.

It has been noted[1,2] that determination of the sign of D can often be difficult from fitting magnetic susceptibility data collected on powder samples. Often, equally good fits can be obtained for negative and positive D values of approximately the same magnitude. Therefore, fits were attempted on the $\chi_M T$ data of **1**-**4** where D was restrained to be positive and negative. The table below displays the best fits using a positive and negative D, as well as the individual R^2 factors describing the quality of the fit. For all complexes, the R^2 values indicate better fits for negative D values. For **3** and **4**, the difference in R^2 is substantial between the positive and negative D fits, while for **1** and **2** the difference is much smaller. On the basis of the slow magnetic relaxation at zero-field, the negative sign of D for **2** can likely be concluded to be correct. For **1**, however, the sign of D is ambiguous, as slow magnetic relaxation for pseudotetrahedral and octahedral Co(II) complexes with $D > 0$ under applied field is precedented.[3,4] The simulation of the isofield lines of **3** is in good agreement with the experimental data.[5]

	$D < 0$				$D > 0$			
	g_z	$g_{x,y}$	D (cm^{-1})	R^2	g_z	$g_{x,y}$	D (cm^{-1})	R^2
1	2.222	2.118	-11.3	0.9937	2.105	2.178	+10	0.9896
2	2.958	2.701	-23.8	0.9966	2.43	2.936	+24	0.9417
3	2.960	2.285	-62	0.9936	1.05	2.932	+55	0.466
4	2.953	2.165	-83	0.9907	1.01	2.87	+57	0.213

Of note is that the utilized hamiltonian, $\hat{H} = D\hat{S}_z^2 + \mu_B g\boldsymbol{S}\cdot\boldsymbol{H}$, does not include other common spin-hamiltonian terms. Specifically, the hamiltonian lacks a term that allows for a weak long range interaction between spin centers, typically parameterized with the term zJ', where z is the number of interacting neighbors and J' the magnetic coupling between them. Inclusion of zJ' in the fits had no effect. In fact, in all cases, the fits were made worse with a nonzero zJ'. An additional term that is typically included when modeling the anisotropy of mononuclear transition metal complexes is transverse anisotropy $\hat{H} = E(\hat{S}_x^2 - \hat{S}_y^2)$, where E is the transverse anisotropy term and $\hat{S}_x$ and $\hat{S}_y$ are spin operators. However, note that determination of this parameter, especially its sign, can be difficult from susceptibility data alone. Further, were our model hamiltonian incorrect, we would expect for a noticeable improvement to the fit to occur upon inclusion of E, but this is not the case. No significant improvement was observed after inclusion of E, but this does not mean that E is zero for these complexes. Rather, this suggests that a separate technique, EPR, would need to be employed to obtain an accurate value for E.

Additional Ligand-Field and AOM Fitting Details. The single-crystal polarized data obtained by Fukui et al.[6] allowed for the elucidation of the splitting among the orbital triplet terms that result from the tetragonal distortion from tetrahedral symmetry. The actual symmetry is likely lower still, as indicated by the additional splitting of the ^4E terms that they observed (see

Table A.3S4). However, our focus is on the magnetic properties of these complexes and the absence of rhombic (transverse) zero-field splitting (E) terms means attempts to make assignments with use of lower point group symmetries are not critically important. We employed the program DDNFIT to explore the parameter space of the single-electron d-orbital energies to see if any refinement of the originally reported parameters can be made. In all cases, $E(z^2) \equiv 0$. In some fits, $E(yz) \equiv E(xz)$ (i.e., the axial model; D_{2d} symmetry), while in others, rhombic orbital splitting ($E(yz) \neq E(xz)$, with, arbitrarily, $E(yz) < E(xz)$) was allowed (i.e., the rhombic model; C_{2v} symmetry). Representative d-orbital splittings for each of these models are presented in Table 5.S6. The main points are two-fold. The first is that fits to the spectra, in agreement with previous work, indicate that the ligand field strength of the S4 donor set, as represented by $10Dq$ (Δ_{tet}) -4200 cm^{-1} (the negative sign is for the tetrahedral geometry). The second point is that the energy of the lowest lying electronic excited state, $^4T_2(z)$, which is $^4B_2$ in D_{2d} ($^4A_2$ in C_{2v}), is crucial in determining the magnetic properties of these complexes, yet this energy cannot be determined from electronic absorption spectroscopy, as its energy is likely in the mid-IR region. Fukui et al. estimated this energy as 1000 cm^{-1} from the D and $g_{\|}$ values, but not independently.[6] Therefore, we employed two fitting methods: in one case the fits made use of this value, and in the other, this transition was ignored. As can be seen in Table 5.S4, this choice has little effect on the quality of fits to the higher energy, observed electronic transitions. The use of rhombic, rather than axial, orbital symmetry likewise has relatively little effect and the resulting rhombic orbital splitting ($E(xz) - E(yz) = 1400 - 1800$ cm^{-1}) seems larger than might be expected. Overall, as was originally found by Fukui et al.[6] it is possible to reproduce successfully the electronic transitions in **3**. Values calculated in Table S4 were calculated with DDN and the parameters (in cm^{-1}) given by Fukui et al.: $B = 590$ cm^{-1} (60% of the free-ion value; C is ignored as the calculation is only for spin quartet states), and single electron d orbital energies (in cm^{-1}): $E(d_{z2}) = 0$, $E(d_{x2-y2}) = 4140$, $E(d_{xy}) = 5140$, $E(d_{xz},d_{yz}) = 6850$. These d orbital energies may alternatively be described as (in cm^{-1}) $Dq = -421$, $\mu = 4140$, $\delta = 1710$, $V = 0$ (i.e., no rhombic orbital splitting).

The minimum AOM description for **1**-**4** is only σ bonding, as parameterized by ε_σ. We began with this simple description, as further described in Chapter 5, and utilized the general geometry depicted in Scheme A.3S1. We utilized only one bond distance for the Co–E bonds, corresponding to the mean values. It is possible to adjust the ε_σ value for n chemically identical ligands, L, by scaling each to the bond distance, r: $(\varepsilon_\sigma)_j$ (j = 2, ..., n) = $(\varepsilon_\sigma)_1 \times [r(M–L_1)^5 / r(M–L_j)^5]$. However, in the case of **3**, the maximum effect this would have would be a roughly 3% reduction in $(\varepsilon_\sigma)_j$ (using the shortest Co–S bond as $M–L_1$) so we will disregard this refinement for **3** as well as **1**, **2**, and **4**. One issue with the approach utilized here, which was explored at length by Fukui et al., is the concept of "misdirected valency", which had been promoted extensively by Gerloch and co-workers, i.e., that the M–L bond vector does not coincide directly with the σ-bonding MO/AO of L, and was handed by including two additional bonding parameters, $\varepsilon_{\pi\sigma\|}$ and $\varepsilon_{\pi\|}$, the former of which accounts for a σ-like interaction with the π-system of the ligand.[7] However, on the basis of their analysis Fukui *et al*. concluded that: "... the misdirection of the σ bonding is not a very important factor in the Co(II) complex." We therefore also disregard it here. We allowed our model to also incorporate π-bonding (donation) from the phenylchalcogenide ligands. In contrast to, e.g., a halido ligand, π-bonding from the Group 16 donors may be asymmetric ($\varepsilon_{\pi\|} \neq \varepsilon_{\pi\perp}$).[8] However, these $[Co(EPh)_4]^{2-}$ complexes have no clearly defined molecular plane on which to base asymmetry in π-bonding and the twist of the phenyl rings does not help in this regard either, as it is somewhat variable. Therefore, we employed

three approaches: a single, cylindrical π-bonding parameter, ε_π, for a given ligand set and anisotropic π-bonding allowing for two components which were parallel (in this case, π-bonding involving d_{z2}, d_{x2-y2} and none involving d_{xy}) and perpendicular (π-bonding involving d_{xy} and none involving d_{z2}, d_{x2-y2}) to the molecular z (S_4) axis. We also must consider the molecular geometry, using the crystal structures determined here. Table A.3S2 presents the relevant metrical parameters for **1** – **4**. The geometrical model employed is as shown in Scheme A.3S1. The approximate S_4 axis (D_{2d} symmetry) is taken as the z axis (to define θ), and the vector in Co-E1 direction normal to z is taken as the x axis (to define ϕ). The distribution of E ligands in the ϕ plane does not follow ideal geometry, but is close enough for our purposes. This can be seen by the listing of torsional angles for **3** in Table A.3S3, which shows that the C_3 axis that would exist along each Co-E bond in T_d symmetry is reasonably well maintained (120 ± 5°).

A return to the LFT analysis highlights more specifically the significance of the d-orbital energy splitting. The fits of **3** gave a Racah parameter B = 580 – 585 cm^{-1}; equal to 60% of the free-ion value.[9] For the calculation of zero-field splitting, it is worthwhile to include the spin doublet excited states as well. Therefore, we now include the Racah parameter C, set also to 60% of the free-ion value,[10] giving C = 2470 – 2490 cm^{-1}. Lastly, a value of ζ = 320 cm^{-1}, likewise 60% of the free-ion value,[11] is included. As an example, if we apply the rhombic orbital splitting model determined for **3** and using the estimation of $^4A_2 \rightarrow {}^4T_2(z) \approx 1000$ cm^{-1}, a zero-field splitting of 63.2 cm^{-1} is calculated, which is remarkably close to the value determined from our fitting of the susceptibility and magnetization data. This calculation is crude, thus one should avoid placing too much import on its result, but nevertheless this demonstrates that tuning of the energy of the lowest lying excited state is the overarching factor in determining the value of D.[12,13] This method could be applied to the phenoxo and phenylselenido complexes, but, as discussed above, the uncertainty in the energy of the crucial $^4T_2(z)$ level gives us little confidence in the results. The clearest conclusion from the LFT analysis is that the Racah B parameter decreases in the order E = O > S > Se, demonstrating that the contribution to D from the ^4P free-ion term is least for **1** and **2** (E = O), greater for **3** and greatest for **4** (E = Se).

References

(1) Kahn, O. Molecular Magnetism, John Wiley & Sons, New York, 1993
(2) M. P. Shores, J. J. Sokol, J. R. Long, J. Am. Chem. Soc. 124 (2002) 2279-2292.
(3) Zadrozny, J. M.; Liu, J.; Piro, N. A.; Chang, C. J.; Hill, S.; Long, J. R. *Chem. Commun.* **2012**, *48,* 3927.
(4) Vallejo, J.; Castro, I.; Ruiz-García, R.; Cano, J.; Julve, M.; Lloret, F.; De Munno, G.; Wernsdorfer, W.; Pardo, E. *J. Am. Chem. Soc.* **2012**, *134*, 15704.
(5) Zadrozny, J. M.; Long, J. R. *J. Am. Chem. Soc.* **2011**, *133*, 20732.
(6) Fukui, K.; Masuda, H.; Ohya-Nishiguchi, H.; Kamada, H. *Inorg. Chim. Acta* **1995**, *238*, 73.
(7) Deeth, R. J.; Duer, M. J.; Gerloch, M. *Inorg. Chem.* **1987**, *26*, 2573,
(8) Schäffer, C. E. *Struct. Bonding* **1968**, *5*, 68.
(9) Brorson, M.; Schäffer, C. E. *Inorg. Chem.* **1988**, *27*, 2522.
(10) Bendix, J.; Brorson, M.; Schäffer, C. E. *Inorg. Chem.* **1993**, *32*, 2838.

(11) The contribution to D from the spin doublet excited states, the lowest of which lie at ~10,500 cm^{-1} in this calculation, appears not to be significant. Application of a Racah C value 100-fold larger than appropriate, as to render the spin doublet states irrelevant, gives $D = -60.1$ cm^{-1}.

(12) Another possible deficiency of the LFT used here is that the contribution to D from spin-spin coupling (D^{SSC}) is not considered. This can be a problem when the SOC contribution to the total D value (D^{SOC}) is small in magnitude (e.g., $|D| < 5$ cm^{-1}), such as commonly found in e.g., Mn(II) (see, e.g., Ganyushin, D.; Gilka, N.; Taylor, P. R.; Marian, C. M.; Neese, F. *J. Chem. Phys.* **2010**, *132*, 144111.; Duboc, C.; Collomb, M.-N.; Neese, F. *Appl. Magn. Res.* **2010**, *37*, 229.) However, in the present case, the D values are large in magnitude from the SOC contribution being correspondingly large, so that the neglect of D^{SSC} is relatively immaterial.

Scheme A.3S1. Relevant angles used for AOM analysis. The *x*-axis has the same ϕ as the Co–E_4 bond. The *y*-axis is oriented along the viewing direction, and has the same ϕ as the Co–E_1 bond.

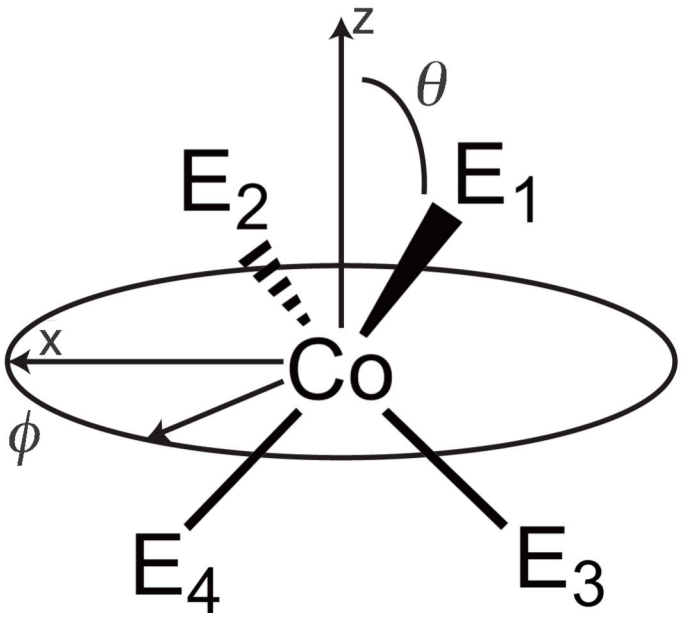


Table A.3S1. Observed and calculated d-d excitation energies for $[Co(SPh)_4]^{2-}$ as observed in **3**.

Band Assignment[a]	Observed Transitions		Calculated[d]	
	Ref. 17[b]	This work[c]	Ref. 17	This work
$^4A_2 \rightarrow {}^4T_2$				
($^4B_1 \rightarrow {}^4B_2$) (*z*)	~1000 [f]		1000	(980; *80*)
($^4B_1 \rightarrow {}^4E$) (*x*, *y*)	~5000		4854	(4922; *4933*)
[$^4A_2 \rightarrow {}^4A_1$] (*z*)	~1000 [f]	---		[950; *780*]
[$^4A_2 \rightarrow {}^4B_1$, $^4B_2$] (*x*, *y*)	< 5000, 5130	4290, 5000		[4143, 5203; *4207*, *5107*]
$^4A_2 \rightarrow {}^4T_1(^4F)$				
($^4B_1 \rightarrow {}^4E$) (*x*, *y*)	7100		7360	(7351; *7340*)
($^4B_1 \rightarrow {}^4A_2$) (*z*)	8400		8207	(8204; *8216*)
[$^4A_2 \rightarrow {}^4B_2$, $^4B_1$] (*x*, *y*)	6600, 7600	5970, 7600		[7335, 7359; *7292*, *7464*]
[$^4A_2 \rightarrow {}^4A_2$] (*z*)	8400	8160		[8181; *8156*]
$^4A_2 \rightarrow {}^4T_1(^4P)$				
($^4B_1 \rightarrow {}^4E$) (*x*, *y*)	13 850		14 046	(13 989; *13 981*)
($^4B_1 \rightarrow {}^4A_2$) (*z*)			15 343	(15 229; *15 247*)
[$^4A_2 \rightarrow {}^4B_2$, $^4B_1$] (*x*, *y*)	13 400, 14 300	13 420, 14 430		[13 783, 14 099; *13 648*, *14 385*]
[$^4A_2 \rightarrow {}^4A_2$] (*z*)	15 350	15 310		[15 260; *15 210*]

[a]Band assignments are grouped under their idealized tetrahedral geometry label; assignments in parentheses are assuming a D_{2d} symmetry, assignments in brackets are assuming a C_{2v} symmetry. [b]From single-crystal polarized UV-Vis spectra [17]. [c]From diffuse-reflectance spectra.

Table A.3S2. Metrical parameters used for the AOM analysis of tetrakis(arylchalcogenato)cobalt(II) complexes: CoE_4 (E = O, S, Se) coordination sphere distances (Å) and angles (degrees).

Complex	Co–E_i distances (Å); [mean, (std. dev.)]	E_i–Co–E_j angles (º); those used for θ in AOM in italics; [mean, (std. dev.)][a]
1, $(Ph_4P)_2[Co(OPh)_4]$ [b]	1.955, 1.965, 1.974, 1.958; [1.963(8)]	*106.81*, 106.02, 111.40, 104.12, 104.42, *122.86*; [109.27(7.15)]
2, $K(Ph_4P)[Co(OPh)_4]$ [c]	1.959	*67.35*, 133.83
3, $(Ph_4P)_2[Co(SPh)_4]$ [d]	2.319, 2.329, 2.314, 2.331; [2.323(8)]	*119.61*, 97.35, 113.98, 112.48, 98.34, *116.27*; [109.67(9.48)]
4, $(Ph_4P)_2[Co(SePh)_4]$ [e]	2.436, 2.437, 2.425, 2.429; [2.432(6)]	*114.95*, 97.74, 116.89, 120.95, 94.25, *113.55*; [109.72(10.98)]

[a] The S_4 axis defines the *z* axis; θ for the AOM is defined by the angle from this axis to a given E ligand. One of the Co-E vectors (normal to *z*) is chosen as the *x* axis; ϕ for the AOM is defined by the angle from this axis to a given E ligand. See Scheme S1. [b] This work. [c] This work. The complex has crystallographic four-fold symmetry. [d] Data taken from Fukui et al. (CSD code: ABTHCO01). [e] This work. [h]

Table A.3S3. Torsional angles relevant to AOM analysis of **3**.

i, j, k in S_i–Co–S_j–S_k Torsional angle	Angle (deg.)
1–2–3	113.23
1–2–4	123.76
1–3–2	126.34
1–3–4	121.37
1–4–2	127.72
1–4–3	112.06
2–1–3	121.12
2–1–4	115.81
2–3–4	112.29
2–4–3	120.22
3–1–4	123.08
3–2–4	123.01
mean	120.00
standard deviation	5.41

Table A.3S4. AOM geometrical parameters for fits, as well as fitted AOM parameters for **1-4**.

	1		**2**		**3**		**4**	
E1 (θ, ϕ)	(53.40°, 0°)		(33.68°, 0°)		(59.80°, 0°)		(57.48°, 0°)	
E2 (θ, ϕ)	(53.40°, 180°)		(33.68°, 180°)		(59.80°, 180°)		(57.48°, 180°)	
E3 (θ, ϕ)	(118.57°, 90°)		(146.32°, 90°)		(121.86°, 90°)		(123.22°, 90°)	
E4 (θ, ϕ)	(118.57°, 270°)		(146.32°, 270°)		(121.86°, 270°)		(123.22°, 270°)	
	σ-only	σ and π	σ-only	σ and π[a]	σ-only	σ and π	σ-only	σ and π
B (cm^{-1})	768	775	-	402	580	523	478	483
ε(σ) (cm^{-1})	3175	3850	-	7880	3450	4520	3780	3690
ε(π∥) (cm^{-1})	-	995	-	2650	-	1080		-90
ε(π⊥) (cm^{-1})	-	0	-	0	-	0		0

[a]The large ε(σ) likely suggests this fit problematic.

Appendix 4: Magnetization Fitting Details for Chapter 6

Originally, I had planned to evaluate this index based on deviations from the Brillouin function. I tried, using $S = {}^1/_2$ and variable g for each data set, but in all cases the Brillouin function did not adequately represent a master function with which we could compare superimposability. Instead I used eq (S1) as a fitting equation, which would be weighted to fit the three highest-T data of the 1 T data set and the three lowest-T data of the 7 T set. The values of c_1, c_2, c_3, c_4, and the exponent n, determined from these fits are given in Table 2.

$$M = \left(\frac{c_1 \left(\frac{H}{T} \right)^n}{c_2 \left(\frac{H}{T} \right)^n + c_3 \left(\frac{H}{T} \right)} \right) + c_4 \qquad \text{(S1)}$$

The experimental magnetizations were compared with these ideal, master functions, and the superimposability index, R_σ, was then defined according to eq (S2). The master functions for each complex are plotted as black lines in Figs. S1 – S6.

$$R_\sigma = \sum_i \frac{(M_{\text{exp},i} - M_{calc,i})^2}{M_{\text{exp},i}} \qquad \text{(S2)}$$

Fitted coefficients and exponents for derivation of Σ_σ, the superimposability index.

Complex	c_1	c_2	c_3	c_4	n	R_σ
1	1.492	0.748	0.081	1.08	3.34	0.029
2	1.487	0.658	0.075	1.01	3.13	0.027
3	2.048	1.018	0.112	0.75	3.08	0.013
4	4.969	3.428	0.494	0.73	3.16	0.062
5	6.094	3.734	0.395	0.44	2.93	0.005
6	5.788	4.354	0.865	0.62	3.38	0.135

Appendix 5: Supplementary Information for Chapter 7.

Additional Mössbauer Interpretive Details. The asymmetry observed in the quadrupole doublet of the room temperature Mössbauer spectrum of **1** indicates that the compound exhibits either an anisotropy in the recoil-free fraction, the Goldanskii-Karyagin effect,[1,2,3,4] or a non-random orientation of the crystallites in the absorber, i.e. texture,[4,5] or slow paramagnetic relaxation effects.[6,7,8] In the first two cases one would expect the same line width but differing areas for the two components of the quadrupole doublet, whereas in the third case one would expect differing line widths with the same area for the two components of the quadrupole doublet.

The anisotropy in the two-coordinated linear bonding observed about the Fe(I) ion in **1** could possibly lead to a Goldanskii-Karyagin asymmetry[1-4] in the Mössbauer spectrum. As a consequence, we have fit the Mössbauer spectrum of **1** with a major quadrupole doublet with differing component areas and the same line width. This fit yields an increase in reduced χ^2 of 10 percent as compared with the fit with a major quadrupole doublet with the same component area and differing line widths. This increase in χ^2 seems to rule out the presence of both Goldanskii-Karyagin asymmetry[1-4] and texture,[4,5] as the cause of the asymmetry in the major doublet. This conclusion is consistent with the x-ray structural results obtained at 100 K, which show relatively little anisotropy in the thermal factors of the Fe(I) ion. Further the equivalent isotropic thermal factor of 0.0162(2) $Å^2$ observed at 100 K is perfectly normal for an iron cation at this temperature.

The asymmetry in the 295 K spectra of $Fe(C(SiMe_3)_3)_2$ and **1** (see Supplementary Fig. S3) is a strong indication that both compounds are exhibiting slow paramagnetic relaxation on the Mössbauer timescale. An estimate of this timescale is given by the Larmor precession time of the nuclear magnetic moment about the internal hyperfine field, $\tau_L = 1.34 \times 10^{-7}/H_{int} = \sim 1.34 \times 10^{-9}$ s for $H_{int} = \sim 100$ T. As a consequence, the 295 K spectra have been fit with a relaxation profile[9] and the fits shown in Figure 2 and Supplementary Figure S3 correspond to relaxation of the internal hyperfine field, H_{int}, assumed to be in the absence of relaxation 152 and 63.97 T for $Fe(C(SiMe_3)_3)_2$ and **1**, parallel to the principal axis of the electric field gradient, which is taken to be the linear coordination axis.

We have carried out a fit of the Mössbauer spectrum of **1** in terms of slow paramagnetic relaxation[9] of the hyperfine field, $H_{int} = 63.97(1)$ T, which has been obtained from a fit of the 5 K spectrum of **1**, as is discussed in the text of the paper and shown in Figure 2. In general, H_{int} is given by $H_{int} = H_{Fermi} + H_{dip} + H_{orb}$, where H_{Fermi}, H_{dip}, and H_{orb} represent the Fermi contact, dipolar, and orbital contribution to the internal hyperfine field. If we assume, as was reported earlier,[10] that $H_{Fermi} = -38$ T for $S = {}^3/_2$ and at most $H_{dip} = +24$ T, a value doubled that suggested earlier because the magnitude of the quadrupole interaction in **1** is larger than that observed in $Fe(C(SiMe_3)_3)_2$, the H_{orb} contribution is 80 T in **1**, as compared to 191 T in $Fe(C(SiMe_3)_3)_2$.

Computational Details. Multireference calculations (CSSCF and NEVPT2) of the energy levels of $[Fe(C(SiMe_3)_3)_2]^-$ were computed based on the X-ray geometry using def2-TZVP basis set and corresponding auxiliary functions def2-TZVP/C and the resolution of the identity option. The full manifold of electronic multiplets spanned by the nominal $3d^7$ configuration of iron(I) in the complex have been computed using state averaging over the 10 quartets ($S = {}^3/_2$) and the 40 doublet ($S = {}^1/_2$) states. Sample state-specific calculations did not yield results which differed much from the adopted computational protocol. Such calculations sometimes suffer from a lack

of convergence at the CASSCF level. CASSCF wavefunctions were rotated and purified following the implementation by K. Sivalingam available in the current version of ORCA.[11] The *ab-initio* based ligand field method utilized here has been described in detail previously.[12,13]

CASSCF energies of quartet d-d transitions are compared with NEVPT2 results in Supplementary Table S3. Doublet states start with 17000 (CASSCF) and 16000 (NEVPT2). The ground state is ^{4}E and aside from the spin ($S = {}^3/_2$ instead of $S = 2$ of $Fe(C(SiMe_3)_3)_2$) are of the same orbital nature $(d_{xy}, d_{x2-y2})^3$ as for $Fe(C(SiMe_3)_3)_2$. The 5 × 5 ligand field matrix V (eq.S1)

$$V = \begin{bmatrix} V_{xy,xy} & V_{xy,yz} & V_{xy,z2} & V_{xy,xz} & V_{xy,x2-y2} \\ V_{yz,xy} & V_{yz,yz} & V_{z2,yz} & V_{xz,yz} & V_{yz,x2-y2} \\ V_{z2,xy} & V_{z2,yz} & V_{z2,z2} & V_{xz,z2} & V_{x2-y2,z2} \\ V_{xz,xy} & V_{xz,yz} & V_{xz,z2} & V_{xz,xz} & V_{x2-y2,xz} \\ V_{x2-y2,xy} & V_{x2-y2,yz} & V_{x2-y2,z2} & V_{x2-y2,xz} & V_{x2-y2,x2-y2} \end{bmatrix} \qquad \text{(S1)}$$

and the Racah parameter of 3d-3d inter electronic repulsion *B* have been obtained from the best fit of the 10 × 10 ligand field plus inter electronic repulsion matrix HLFIR written down in the basis of the configuration state functions in a parametric form (eq.S2) to numerical form of the corresponding matrix resulting from a CASSCF or from the diagonally corrected (for dynamical correlation) NEVPT2 results (eq.S3, after removal of the arbitrary energy gauge origins (see below).

Equation (S2) was derived using electronic basis functions (Slater determinants, in this case identical with the configuration state functions, i.e. eigenfunctions of the total spin operators $\hat{S}^2$ and $\hat{S}_z$ for $S = M_s = {}^3/_2$) for three electrons in a standard order $|d_{xy}^+ d_{yz}^+ d_{z2}^+>$, $|d_{xy}^+ d_{yz}^+ d_{xz}^+>$, $|d_{xy}^+ d_{yz}^+ d_{x2-y2}^+>$, $|d_{xy}^+ d_{z2}^+ d_{xz}^+>$, $|d_{xy}^+ d_{z2}^+ d_{x2-y2}^+>$, $|d_{xy}^+ d_{xz}^+ d_{x2-y2}^+>$, $|d_{yz}^+ d_{z2}^+ d_{xz}^+>$, $|d_{yz}^+ d_{z2}^+ d_{x2-y2}^+>$, $|d_{yz}^+ d_{xz}^+ d_{x2-y2}^+>$, $|d_{z2}^+ d_{xz}^+ d_{x2-y2}^+>$; eq.S2 is also valid for the here considered d^7 Fe^I complex after changing sign in front of the V_{ij} one electron ligand field matrix elements (i,j = d_{xy},d_{yz},d_{z2},d_{xz},d_{x2-y2}).

$$
\begin{bmatrix}
V_{xy,xy}+V_{yz,yz}+ & V_{xz,z2} & V_{z2-y2,z2}+3\sqrt{3}B & -V_{xz,yz} & -V_{x2-y2,yz} & 0 & V_{xz,xy} & V_{x2-y2,xy} & 0 & -3B \\
V_{z2,z2}-12B & & & & & & & & & \\
V_{xz,z2} & V_{xy,xy}+V_{yz,yz}+ & V_{x2-y2,xz} & V_{z2,yz} & 0 & -V_{x2-y2,yz} & -V_{z2,xy} & 0 & V_{x2-y2,xy} & 0 \\
 & +V_{xz,xz}-15B & & & & & & & & \\
V_{x2-y2,z2}+3\sqrt{3}B & V_{x2-y2,xz} & V_{xy,xy}+V_{yz,yz}+ & 0 & V_{z2,yz} & V_{xz,yz} & 0 & -V_{z2,xy} & -V_{xz,xy} & -3\sqrt{3}B \\
 & & +V_{x2-y2,x2-y2}-6B & & & & & & & \\
-V_{xz,yz} & V_{z2,yz} & 0 & V_{xy,xy}+V_{z2,z2}+ & V_{x2-y2,xz} & -V_{x2-y2,z2}+3\sqrt{3}B & V_{xy,yz} & 3B & 0 & V_{x2-y2,xy} \\
 & & & +V_{xz,xz}-12B & & & & & & \\
-V_{x2-y2,yz} & 0 & V_{z2,yz} & V_{x2-y2,xz} & V_{xy,xy}+V_{z2,z2}+ & V_{xz,z2} & 6B & V_{xy,yz} & 0 & -V_{xz,xy} \\
 & & & & +V_{x2-y2,x2-y2}-12B & & & & & \\
0 & -V_{x2-y2,yz} & V_{xz,yz} & -V_{x2-y2,z2}+3\sqrt{3}B & V_{xz,z2} & V_{xy,xy}+V_{xz,xz}+ & 0 & 3\sqrt{3}B & V_{xy,yz} & V_{z2,xy} \\
 & & & & & +V_{x2-y2,x2-y2}-6B & & & & \\
V_{xz,xy} & -V_{z2,xy} & 0 & V_{xy,yz} & 6B & 0 & V_{yz,yz}+V_{z2,z2}+ & V_{x2-y2,xz} & -V_{x2-y2,z2} & V_{x2-y2,yz} \\
 & & & & & & +V_{xz,xz}-3B & & & \\
V_{x2-y2,xy} & 0 & -V_{z2,xy} & 3B & V_{xy,yz} & 3\sqrt{3}B & V_{x2-y2,xz} & V_{yz,yz}+V_{z2,z2}+ & V_{xz,z2} & -V_{xz,yz} \\
 & & & & & & & +V_{x2-y2,x2-y2}-12B & & \\
0 & V_{x2-y2,xy} & -V_{xz,xy} & 0 & 0 & V_{xy,yz} & -V_{x2-y2,z2} & V_{xz,z2} & V_{yz,yz}+V_{xz,xz}+ & 0 \\
 & & & & & & & & +V_{x2-y2,x2-y2}-15B & \\
-3B & 0 & -3\sqrt{3}B & V_{x2-y2,xy} & -V_{xz,xy} & V_{z2,xy} & V_{x2-y2,yz} & -V_{xz,yz} & 0 & V_{z2,z2}+V_{xz,xz}+ \\
 & & & & & & & & & +V_{x2-y2,x2-y2}-12B
\end{bmatrix}
\tag{S2}
$$

The arbitrary energy gauge origin for the diagonal matrix elements has been eliminated by subtracting the $H_{LFRI}(1,1)$ from $H_{LFIR}(i,i)$, i=1 to 9 leading to the following expressions for the diagonal matrix elements: 0, $V_{xz,xz} - V_{z2,z2} - 3B$, $V_{x2-y2,x2-y2} - V_{z2,z2} + 6B$, $V_{xz,xz} - V_{yz,yz}$, $V_{x2-y2,x2-y2} - V_{yz,yz}$, $V_{xz,xz} - V_{z2,z2} - 3B$, $V_{xz,xz} + V_{x2-y2,x2-y2} - V_{yz,yz} - V_{z2,z2} + 6B$, $V_{xz,xz} - V_{xy,xy} + 9B$, $V_{x2-y2,x2-y2} - V_{z2,z2} - 3B$, $V_{x2-y2,x2-y2} - V_{xy,xy}$, $V_{xz,xz} + V_{x2-y2,x2-y2} - V_{xy,xy} - V_{z2,z2} - 3B$, $V_{xz,xz} + V_{x2-y2,x2-y2} - V_{yz,yz} - V_{xy,xy}$. Applying the formalism from refs 12 and 13 provides the following symmetric AILFT matrix (S3) derived from the NEVPT2 results. Eq. S3 is a superposition of two separate,

$$\mathbf{H}_{\mathbf{LFIR}} = \begin{bmatrix} 0 & 3 & 3980 & -20 & 109 & 0 & -61 & -27 & 0 & -2271 \\ -19 & -7391,-7112 & -51 & -42 & 0 & 109 & -61 & 0 & -27 & 0 \\ 3718 & -123 & 1797,1627 & 0 & -42 & 20 & 0 & -61 & 61 & -3934 \\ -10 & -54 & -13 & 40,260 & -51 & 3887 & 72 & 2271 & 0 & -27 \\ 66 & -8 & -66 & 3 & 2247,2186 & 3 & 4542 & 72 & 0 & 61 \\ 14 & 140 & -17 & 3621 & 64 & 1786,1518 & 0 & 3934 & 72 & 61 \\ -94 & -81 & 31 & 72 & 4574 & -40 & 5632,5133 & -51 & -46 & -109 \\ -32 & -7 & -41 & 1750 & 120 & 3668 & -32 & 16,247 & 3 & -20 \\ -39 & -23 & 29 & -43 & 5 & 25 & -42 & -37 & -7393,-7234 & -42 \\ -1762 & 25 & -3664 & -25 & 59 & 61 & -121 & -66 & -8 & 29,138 \end{bmatrix} \quad \text{(S3)}$$

diagonal matrices. Black values are *ab initio* results, while red values correspond to the analogous matrix calculated using the LF parameters of V, eq. S4 and B = 757 cm^{-1} after insertion into eq. S2. A least squares fit of the LF parameters from eq. S2 plus B (a total of 16 unknowns) to the over-complete numerical data set (54 matrix elements) given by the NEVPT2 results of the matrix eq.S3 resulted in the LF matrix eq.S4 yielding also the value of the parameter B = 757 cm^{-1}.

$$V(NEVPT2) = \begin{array}{c} \begin{matrix} |d_{xy}\rangle & |d_{yz}\rangle & |d_{z2}\rangle & |d_{xz}\rangle & |d_{x2-y2}\rangle \end{matrix} \\ \begin{bmatrix} -2743 & -72 & -61 & 61 & 27 \\ -72 & -804 & 42 & -21 & 109 \\ -61 & 42 & -5905 & -3 & -46 \\ 61 & -21 & -3 & -695 & 51 \\ 27 & 109 & -46 & 51 & -262 \end{bmatrix} \end{array} \quad \text{(S4)}$$

Diagonalization of the matrix S4 yields energies of orbitals 0, 3153, 3286, 5109 and 5219 cm^{-1} with their assignment using the eigenfunctions to $|d_{z2}>$, $|d_{xy}>$, $|d_{x2-y2}>$, $|d_{yz}>$ and $|d_{xz}>$, respectively. They have been used to construct ligand field orbital energy plot for $[Fe(C(SiMe_3)_3)_2]^-$ (Figure 7.1c).

As follows from the very small standard deviations (σ = 162 cm^{-1}) between *ab initio* (eq. S3 given in black color) and calculated (listed in red color) values, the parametric ligand field model is remarkably consistent with the *ab initio* results yielding a reasonable data reduction from 54 to a total of 16 parameters. These results also yield valuable information about the ligand field in the most general form (general AILFT). Further analysis using various parameterization schemes are possible. They are prone to the problem of over parameterization in the case of complex hetero ligand complexes. A similar procedure using the CASSCF results yields considerably smaller ligand field splitting (eq.S5) (yielding after diagonalization ligand

field energies 0(d_{z2}), 2241(d_{xy}), 2315(d_{x2-y2}), 3924 (d_{yz}), 4007(d_{xz})), B = 944 cm^{-1}, (σ = 151 cm^{-1}). Comparison between CASSCF and NEVPT2 data deduced in such a way shows the important role of dynamical correlation for the studied complex.

$$V(CASSCF) = \begin{bmatrix} -3645 & -80 & -44 & 79 & 14 \\ -80 & -1986 & 32 & 2 & 120 \\ -44 & 32 & -5896 & -4 & -36 \\ 79 & 2 & -4 & -1896 & 63 \\ 14 & 120 & -36 & 63 & -3576 \end{bmatrix} \quad \text{(S5)}$$

References

(1) (a) Goldanskii, V. I. *et al*. *Dokl*. *Phys*. *Chem*. *(Engl*. *Transl*.*)* **1963**, *147,* 766; (b) Karyagin, S. V. *Dokl*. *Akad*. *Nauk SSSR* **1963**, *148,* 1102.

(2) Spiering, H. In *Mossbauer Spectroscopy Applied to Inorganic Chemistry;* Long, G. J., Ed., Plenum: New York, 1984; Vol. 1, pp 77-170.

(3) Chandra, R.; Ericsson, T. *Hyperfine Interact*. **1979**, *7*, 229.

(4) Grandjean, F.; Long, G. J.; Benson C. G.; Russo, U. *Inorg*. *Chem*. **1988**, *27*, 1524.

(5) Grenèche, J. M.; Varret, F. *J . Phys., Lett*. **1982**, *43*, L233.

(6) (*a*) Tjon, J. A.; Blume, M. *Phys*. *Rev*. **1968**, *165*, 446. (*b*) Blume, M.; Tjon, J. A. *Phys*. *Rev*. **1968**, *165*, 456.

(7) Mørup, S. In *The Time Domain in Surface and Structural Dynamics*; Long, G. J.; Grandjean, F., Kluwer: Dordrecht, 1988; pp. 321-333.

(8) Wickman, H. H.; Wertheim, G. K. In *Chemical Applications of Mössbauer Spectroscopy*, Goldanskii, V. I.; Herber, R. H., Academic Press: New York, 1968; pp. 548-621.

(9) Dattagupta, S.; Blume, M. *Phys*. *Rev B* **1974**, *10*, 4540.

(10) Reiff, W. M.; LaPointe, A. M.; Witten E. H. *J*. *Am*. *Chem*. *Soc*. **2004**, *126*, 10206.

(11) Neese, F.; Wennmohs, F., *Orca; version 2.8*, An *ab initio*, DFT, and semiempirical SCF-MO package with contributions from U. Becker, D. Ganyushin, A. Hansen, D. G. Liakos, C. Kollmar, S. Kossman, T. Petrenko, C. Reimann, C. Riplinger, K. Sivalingam, E. Valeev, & B. Wezisla, Lehrstuhl fur theoretische Chemie, Bonn, Germany, 2010.

(12) Atanasov, M.; Ganyushin, D.; Sivalingam, K.; Neese, F. *Struct*. *Bond*. **2012**, *143*, 149.

(13) Atanasov, M.; Zadrozny, J. M.; Long, J. R.; Neese, F. *Chem*. *Sci*. **2013**, *4*, 139.